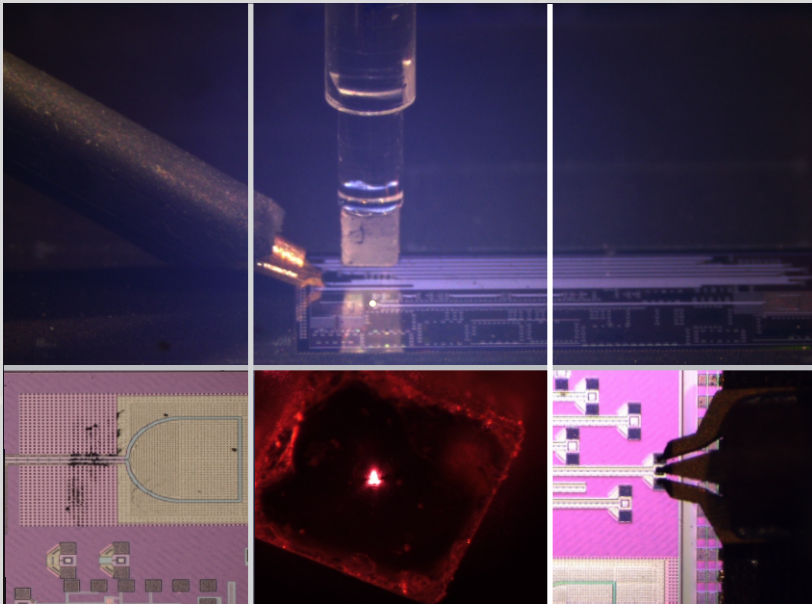


On-wafer Characterization of MM-wave and THz Circuits Using Electrooptic Sampling

Mehran Jamshidifar



Höchstfrequenztechnik
und Quantenelektronik



On-Wafer Characterization of MM-Wave and THz Circuits Using Electrooptic Sampling

Von der Naturwissenschaftlich-Technischen Fakultät der
Universität Siegen

zur Erlangung des akademischen Grades
Doktor der Ingenieurwissenschaften
(Dr.-Ing.)

genehmigte
DISSERTATION

vorgelegt von

M.Sc. Mehran Jamshidifar

aus Khorram Abad

1. Gutachter: Prof. Dr.-Ing. Peter Haring-Bolívar
 2. Gutachter: Prof. Dr.-Ing. Jörn Schmedt auf der Günne
- Vorsitzender: Prof. Dr.-Ing. Joachim Ender

Tag der mündlichen Prüfung: 04. Oktober 2016

Band 7 aus der Schriftenreihe
Höchstfrequenztechnik und Quantenelektronik
Prof. Dr.-Ing. Peter Haring Bolívar
Naturwissenschaftlich-Technische Fakultät
Universität Siegen
57068 Siegen

urn:nbn:de:hbz:467-10849

Gedruckt auf alterungsbeständigem holz- und säurefreiem Papier

*To the memory of my father,
To my beloved mother and wife*

Abstract

THz, the electromagnetic spectrum lying between millimeter waves and optics, is nowadays widely utilized in the applications such as material inspection, medicine, explosives detection and astronomy. Although optical and photonic based systems for generating THz waves can fully cover the upper band of the THz spectrum (from several THz to far infrared), they are inefficient at lower frequency bands i.e., mm-waves, and at the same time inappropriately bulky for portable applications. In contrast, recent progress in solid states electronics in conjunction with aggressive scaling of devices are promising to facilitate the future availability of THz systems realized as compact and cheap all-electronic solutions. THz microelectronics is an increasingly relevant field of activities, therefore.

Without concerning about the challenges in the design and fabrication of such devices, their performance needs to be characterized with systems faster than the device itself; therefore, we face with limitations. Recently, the measurement bandwidth of microwave network analyzers equipped with extension modules has extended beyond 1 THz. However, their calibration is a challenging task and performing a full band measurement, due to a need for waveguide components, considerably increases the cost and time of measurement. Systematic errors in system calibration due to lack of precise models for devices at THz frequencies are also remarkable drawbacks of this approach. An eligible alternative for these systems is the use of electrooptic and photoconductive sampling which rely on optical and photonic approaches. These techniques with the help of femtosecond pulse lasers provide a very broadband measurement system far beyond today's electronic devices bandwidth without suffering from the challenges of the electronic approach. In particular electrooptic sampling with non-contact probing can also perform useful high resolution near field scanning of devices.

The aim of this thesis is to demonstrate the electrooptic sampling for the characterization of mm-wave and THz electronic devices. To this end, an extremely broadband (microwave to THz) device, which is a 65-nm CMOS nonlinear transmission line (NLTL), is used as the device under test. Before showing the measurement results for this device, the advances in THz electronics as well as their common the characterization techniques are reviewed. For the characterization, a rather compact EOS experimental setup featured with a large dynamic range, high sensitivity and high spatial resolution is presented. In the measurement phase, it is shown that what challenges in particular for the characterization of a nonlinear device we may face to and which scenarios can be used to overcome them. The relative jitter in EOS, known as the most prohibiting factor for achieving a high measurement bandwidth, is resolved with a novel synchronization technique called Laser Master Laser Slave (LM-LS). This is achieved by feeding the DUT with a microwave signal which is generated from the comb harmonics of the femtosecond

laser. Since the signal is sampled by the laser itself, EOS provides a fully coherent heterodyne detection which helps to significantly increase the detection bandwidth of the system from 50 GHz up to 300 GHz which is presently restricted by the DUT fabrication technology i.e. the 65-nm CMOS. Furthermore, it is shown that for nonlinear devices, measurement with EOS can outperform traditional microwave network analyzer measurements and in particular it can detect hidden features like conversion losses which may not be observed by electronic techniques. In the end by performing photoconductive measurements for the DUT, a good comparison between electrooptic and photoconductive sampling in terms of their detection bandwidth and image resolution is demonstrated.

Zusammenfassung

THz, das elektromagnetische Spektrum, das zwischen Millimeterwellen und Optik liegt, ist weit verbreitet in Anwendungsgebieten wie Materialinspektion, Medizin, Entdeckung von Sprengstoffen und Astronomie. Obwohl auf Optik und Photonik basierende Systeme für Generation von Terahertz-Wellen die oberen Bandbreiten des THz-Spektrums vollig abdecken können, sind sie ineffizient in den unteren Frequenzbändern, wie etwa dem mm-Wellenbereich, und gleichzeitig sind ihre Größen ungeeignet für tragbare Anwendungen. Im Gegensatz dazu versprechen die aktuellen Fortschritte in der Festkörper Elektronik in Verbindung mit einer aggressiven Skalierung von Bauelementen, die zukünftige Verfügbarkeit von THz Systemen, als kompakte und preiswert voll-elektronische Lösungen. Daher ist die THz Mikroelektronik ein zunehmend relevantes Arbeitsfeld.

Unabhängig von den Herausforderungen in Design und Fabrikation von THz Komponenten, müssen deren Leistungsfähigkeit mit Hilfe von Instrumenten charakterisiert werden, die schneller sind als die Komponente selbst, daher stößt man hier an Grenzen. Die aktuellen Messbandbreiten von Mikrowellen-Netzwerkanalysatoren, die mit Erweiterungsmodulen ausgestattet worden sind, gehen bereits über 1 THz hinaus. Jedoch ist ihre Kalibrierung aufwendig und Messungen über die volle Bandbreite erhöhen, wegen der Notwendigkeit von Wellenleiterkomponenten, wesentlich die Kosten und den Zeitaufwand. Die systematischen Fehler in der Kalibrierung der Systeme, auf Grund des Mangels an präzisen Modellen für Komponenten im THz Frequenzbereich, sind ebenfalls ein bedeutender Nachteil dieses Ansatzes. Eine gute Alternative für diese Systeme ist elektrooptisches oder photokonduktives Abtasten, welche nicht elektronisch arbeiten sondern optik- und photonik-basiert sind. Diese Techniken stellen mit Hilfe von Femtosekunden-Lasern Breitbandmesssysteme zur Verfügung, welche die Bandbreite der heutigen elektronischen Messgeräte bei weitem übertreffen, ohne durch die Herausforderungen von elektronischen Ansätzen beschränkt zu werden. Insbesondere durch das elektrooptische Abtasten mit Hilfe von kontaktlosen Proben können wertvolle, hochauflösende Nahfeld-Scans von Komponenten durchgeführt.

Das Ziel dieser Dissertation ist die Charakterisierung von mm-Wellen und THz Komponenten mit Hilfe des elektrooptischen Abtastens zu demonstrieren. Zu diesem Zweck wird eine extrem breitbandige (von Mikrowellen bis zu THz) Komponente, eine 65-nm CMOS nichtlineare Diodenleitung, als DUT genutzt. Bevor die Messungsergebnisse für das Gerät gezeigt werden, werden sowohl die Fortschritte in der THz-Elektronik als auch deren häufigsten Charakterisierungsmethoden vorgestellt. Der für die Charakterisierung verwendete relativ kompakte elektrooptische Aufbau, welcher eine große Dynamik, hohe Sensitivität und hohe räumliche Auflösung aufweist, darauf folgend präsentiert. Der anschließende Abschnitt beschreibt die Messungen und zeigt mit welchen Herausforderungen,

insbesondere bei der Charakterisierung von nichtlinearen Komponenten, man konfrontieren wird und welche Szenarios als Lösung genutzt werden können. Der relative Jitter im elektrooptischen Abtasten, der meist am stärksten einschränkende Faktor für die Erreichung hoher Messbandbreiten, wird mit Hilfe einer neuartigen Synchronisationstechnik, dem sogenannten Laser Master Laser Slave (LM-LS), entgegengewirkt. Dies ist durch die Versorgung des DUT mit Mikrowellensignal, die aus dem Harmonik-Kamm des Femtosekunden-Lasers generiert wird, erreicht. Da das Mikrowellensignal mit dem gleichen Laser abgetastet wird, erhöht das voll kohärente, elektrooptische Abtasten die Detektionsbandbreite von zuvor 50 GHz auf bis zu 300 GHz, was die derzeitige Grenze auf Grund der DUT Fabrikationstechnologie (65-nm CMOS) ist. Ausserdem wird gezeigt, dass elektrooptisches Abtasten für nichtlineare Komponenten die traditionellen Mikrowellenmessmethoden übertreffen kann. Insbesondere detektiert elektrooptisches Abtasten versteckte Eigenschaften, wie Umwandlungsverlusten, die nicht mit elektronischen Messungen beobachtet werden können. Abschließend demonstrieren die Messungen mit einem Photokonduktivdetektor eine gute Vergleichbarkeit von elektrooptischen und photokonduktiven Abtasten, insbesondere in Bezug auf Detektionsbandbreite und Bildauflösung.

Acknowledgement

The work leading to these results was supported with funding by the European Community's 7th Framework Programme under grant agreement no: FP7-224189, ULTRA project.

Foremost, I would like to deeply thank and appreciate Prof. Dr.-Ing. Peter Haring-Bolívar, my first supervisor, who gave me work permission in the institute of high frequency and quantum electronic at the University of Siegen. Without his support and never-ending helps, this work would not have been possible. I am proud of him that I have been supervised with such a great person with brilliant, broad and in-depth knowledge. I will never forget his positive influence in whole my life. I give my special thanks to Prof. Jörn Schmedt auf der Günne as my second supervisor and the second reviewer of my thesis. I am also grateful to Prof. Dr.-Ing. Joachim Ender for being the chair of the final oral exam and giving useful comments to improve the writing of is work. I would like to express my gratitude to Prof. Dr.-Ing. Otmar Loffeld, the head of Zentrum für Sensor System (ZESS), for all his direct and indirect helps in increasing my scientific capabilities while I was IPP member at ZESS. Particularly, annual and semester presentations under his management and organized by Dr. Stefan Knedlik and Dr. Holger Nies, have helped me to organize this work better. I am grateful to Dr. Lorenzo Tripodi (at that time Philips) for provision of the nonlinear transmission line. I owe my deepest gratitude to Dr. Gunnar Spickermann for his hours of effort in the lab to improve the experimental setup and the use of his program modules which allowed accelerating this work at the highest pressure time of the ULTRA project. I also learned a lot from his great knowledge and experience in optics. I express my thanks to Dr. Heiko Schäfer Eberwein for the fabrication of a photoconductive switch and spell and grammar correction of the ULTRA project reports. I would like to thank Dr. Robert Sczech my office-mate, for making a good atmosphere at the workplace during this research. We had lots of good time with discussions about many scientific and nonscientific things and he helped me to have better understanding of the German language and culture as well as scientific topics. I would like to thank all our institute members: Dr. Volker Warnkross, Dr. Rainer Bornemann, Dr. Christian Debus, Dr. Anna Katharina Wigger, Daniel Stock, Andreas Neuberger, Matthias Kahl,

Christoph Süßmeier, Tran Tuan Anh Pham, and Christian Weisenstein. I also thank our institute secretor Mrs. Heike Brandt for on time handling of my work contracts and paper works. I appreciate my friend Moe Rahnema for the spell and grammar checking of this dissertation. I also say thank you to our IT technician Armin Kütke, our web developer Tobias Gläser, and the secretary of ZESS Mrs. Silvia Niet-Wunram. Last but not least, the deepest gratitude goes to my wife Maria, who without losing sight of life supported me to complete this work.

Related Publications

Parts of this work were published in the following

Peer reviewed Journal papers:

- M. Jamshidifar and P. H. Bolívar, “Diminishing relative jitter in electrooptic sampling of active mm-wave and THz circuits”, *Optics Express* 21 (4), 4396-4404, 2013.
- M. Jamshidifar, G. Spickermann, H. Schäfer, and P. H. Bolívar, “ 200-GHz bandwidth on wafer characterization of CMOS nonlinear transmission line using electro-optic sampling”, *Microwave and Optical Technology Letters* 54 (8), 1858-1862, 2012.

Peer reviewed conference papers:

- M. Jamshidifar, G. Spickermann, and P. H. Bolívar, “MM-Wave Dispersion Characteristics of a Nonlinear Transmission Line Measured by Electrooptic Sampling “, 41st international conference on Infrared, Millimeter, and Terahertz Waves (IRMMW-THz), 2016.
- M. Jamshidifar and P. H. Bolívar , “Extremely Low-Jitter and Ultra-Broadband Electrooptic Sampling System for NearField Sensing of Active and Passive Sub-THz Electronic Devices” 38th international conference on Infrared, Millimeter, and Terahertz Waves (IRMMW-THz), 2013.
- M. Jamshidifar, G. Spickermann, H. S. Eberwein, and P. H Bolívar, “ Low-Jitter Electrooptic Sampling of Active mm-Wave Devices up to 300 GHz” European Microwave Conference (EuMC),2013.

Abbreviations

AC	Alternative current	MWatt	Mega-watt
AM	Amplitude modulation	mWatt	milliWatt
BRF	Birefringence filter	NA	Not available
CMOS	Complementary metal oxide semiconductor	NVNA	Nonlinear vector network analyzer
CPW	Coplanar waveguide	P.S (PS)	Photoconductive switch
CW	Continuous wave	PC	Photoconductive
dB	deciBel	PLL	Phase locked loop
DC	Direct current	PM	Phase modulation
DUT	Device under test	PSM	Polarization state modulation
EO	Electrooptic	QCL	Quantum cascade laser
EOS	Electrooptic sampling	RF	Radio frequency
EWB	Extremely wideband	RH-NLTL	Right handed nonlinear transmission line
FREOS	Free-running EOS	RMS	Root mean square
fsL	Femtosecond laser	RTD	Resonant tunneling diode
GRIN	Gradient index	SEM	Scanning electron microscope
GSG	Ground-signal-ground	SNR	Signal to noise ratio
GVD	Group velocity dispersion	TDS	Time domain spectroscopy
HBT	Heterojunction bipolar transistor	TEM	Transversal electromagnetic mode
HEMT	High electron mobility transistor	THz	Terahertz
HFSS	High frequency structures simulator	VCO	Voltage controlled oscillator
HR	High reflection or high resolution	VNA	Vector network analyzer
HRS	High resolution and sensitivity	VSWR	Voltage standing wave ratio
HS	High sensitivity	Xtal	Crystal
IF	Intermediate frequency		
IMPATT	IMPact ionization Avalanche Transit-Time		
IQ	In- quadratic (phase)		
LH-NLTL	Left handed nonlinear transmission line		
LM-LS	Laser master laser slave		
LM-MS	Laser master microwave slave		
LNA	Low noise amplifier		
LO	Local oscillator		
LTL	Linear transmission line		
LTL	Nonlinear transmission line		
m-HEMT	Metamorphic high electron mobility transistor		

Contents

1. Introduction.....	1
2. THz Waves and THz Electronics	5
2.1 THz waves and their applications.....	5
2.2 Photonic and optical based THz	6
2.2.1 Photoconductive pulse THz emitter.....	6
2.2.2 Optical rectification.....	7
2.2.3 Photo-carrier mixing.....	7
2.2.4 Quantum Cascade Laser (QCL)	7
2.3 Electronic THz sources.....	8
2.3.1 Narrowband THz wave generation	9
2.3.2 NLTL for ultra-broadband THz wave generation	12
2.4 A short theory of NLTL and its THz range design considerations	13
2.4.1 Selection of varactors.....	13
2.4.2 Left and right handed NLTLs	15
2.4.3 The host microwave transmission line	16
2.4.4 NLTL Circuit model, dispersion and characteristics impedance.....	17
2.4.5 Bandwidth consideration.....	19
2.4.6 Common applications of NLTL	19
2.5 THz detectors and sensors.....	22
3. Characterization of mm-Wave and THz Devices	25
3.1 Common electronic instrumentation	25
3.1.1 Measurement bandwidth of the system	28
3.1.2 Cost efficiency.....	28
3.1.3 On-wafer measurement.....	28
3.1.4 Measurement of nonlinear devices.....	29
3.1.5 Dynamic range.....	29
3.1.6 Magnitude and Phase stability	29
3.1.7 Other measurement challenges.....	31
3.2 NLTL based network analyzer	31
3.3 Photonic instrumentation	32
3.3.1 Photoconductive (PC) probing.....	33
3.3.2 Electrooptic Sampling (EOS)	36
4. Electrooptic Sampling Theory	41
4.1 Ti: Sapphire femtosecond pulsed laser	41
4.2 Electrooptic effect and electrooptic crystals.....	44
4.2.1 Linearity of electrooptic	47
4.2.2 Crystal selection for EOS sampling of mm- wave and THz devices	49
5. Electrooptic Setup.....	57
5.1 Schematic diagram of the setup.....	57

5.1.1 The pigtailed electrooptic probe	58
5.1.2 The photoconductive switch	59
5.1.3 Wafer probe station and the EOS setup mechanics	63
5.1.4 Microwave probe	65
5.1.5 Grating pair for optical fiber dispersion compensation	65
5.2 Challenges using fiber-pigtailed probe	67
5.2.1 Glass birefringence inside the fiber	67
5.2.2 Low Optical damage threshold.....	67
5.3 Modification of setup and using non-pigtailed probe	68
5.3.1 Non-pigtailed probe assembly	69
5.3.2 Examination of different crystals as probe tip	70
5.3.3 Synchronization of the setup	70
5.3.4 Setup calibration.....	71
6. EOS Measurement of a 65-nm CMOS NLTL	73
6.1 DUT.....	73
6.1.1 All-electronic CMOS NLTL based transceiver	74
6.1.2 The 65-nm CMOS NLTL	75
6.2 EOS measurements.....	77
6.2.1 Longitudinal scan.....	77
6.2.2 Transversal scan	78
6.2.3 Vertical scan	79
6.3 Simulation of a linear transmission line structure	80
6.3.1 The simulated structure	81
6.3.2 The simulation results	82
6.4 Comparison between simulation and measurements.....	84
6.4.1 Transversal scan	84
6.4.2 Vertical scan	85
6.5 Measurement of an NLTL terminated with an on-chip antenna.....	85
7. Measurement Challenges, Errors, and Jitter	87
7.1 Measurement errors and challenges	87
7.1.1 Comparison of EOS with electronic microwave measurements.....	87
7.1.2 Self-reference detection using spectrum analyzer vs. lock-in amplifier	89
7.1.3 Investigation on errors in lock-in measurements.....	93
7.1.4 Jitter in the frequency domain.....	94
7.1.5 Jitter in the time domain	94
7.1.6 Characterization of the lock-in amplifier errors	95
7.2 Synchronization techniques	96
7.2.1 Free running EOS system.....	96
7.2.2 Microwave Master- Laser Slave (MM-LS).....	96
7.2.3 Laser Master- Microwave Slave (LM-MS).....	97
7.2.4 Laser Master- Laser Slave (LM-LS).....	98
8. Laser Master-Laser Slave Synchronization	99
8.1 Mechanism of LM-LS synchronization.....	100

8.2 Providing the IF signal for superheterodyne LM-LS	102
8.2.1 The use of amplitude modulator	102
8.2.2 The use of IQ modulator	103
8.3 Measurements with LM-LS	106
8.3.1 Harmonic measurement.....	106
8.3.2 Longitudinal scan and the effect of relative jitter.....	107
9. Optical Network Analysis Measurements	111
9.1 Device under test	111
9.2 Scanning of the NLTLs.....	112
9.3 Measurement results	114
9.3.1 VSWR for the higher harmonics	117
9.3.2 NLTL dispersion	120
10. Photoconductive Probing vs. EOS	123
10.1 The photoconductive probe and the setup	123
10.2 Measurement results	124
10.2.1 Harmonic scan	125
10.2.2 Transversal scan	126
10.2.3 Longitudinal scan.....	126
10.2.4 Field mapping.....	127
11. Conclusion	131

1. Introduction

THz waves with the electromagnetic spectrum lying between microwave and optics are nowadays widely used in many applications such as material inspection, explosive detection, medicine and astronomy. This interest has motivated scientists to explore new methods for generation and detection of THz waves. THz waves can be generated with different techniques, and more conventional ways are based on optics and photonic. The use of femtosecond laser in conjunction with photoconductive antennas to emitting THz waves and quantum cascade lasers are examples. These methods suffer from drawbacks such as the need for costly and bulky instruments like lasers or cryogenic cooling systems which make them inappropriate for portable applications. Alternatively, electronic approaches for realizing THz systems have great advantages as illustrate compact and cheap solutions for future availability of THz waves. Despite these outstanding advantages, it is extremely challenging to push electronic devices to operate at very high frequencies of THz. Fortunately recent development in electronic technology and scaling has opened new doors in this field. Recently THz electronic devices have been made using ultrafast Schottky diodes with the cut-off frequency in a range of tens of THz or ultrafast transistors such as InP-HEMT whose f_{\max} lies in THz range. On the other side, targeting THz waves with electronics has also made significant progress in the development of mm-waves devices and expanded the high frequency market.

By increasing the speed of electronic devices towards THz range, their characterization poses new challenges as we need instruments faster than the devices under test (DUTs). In a worst case scenario, if one makes a device faster than the conventional instruments, he/she should look for another characterization alternative. The good news is that newly fabricated high speed devices can also be utilized in instrumentation, as recently have been demonstrated by Schottky diode based extended modules [1] in network analyzers. This has extended their

measurement bandwidth beyond 1 THz which covers more than the required bandwidth of the most today's ultrafast electronics. Although this is very favorable, these kinds of instruments are in their infancy and need improvement. Notably, since at THz frequencies it is extremely difficult to precisely model device contact probes and calibration kits, systematic errors in measurements can be increased. Another drawback of using these instruments is the high cost of setup components and time consuming measurements. This can be imagined for a full-band measurement of an ultra-broadband device, as with this approach one needs to perform band-to-band measurements by changing waveguide sets and performing several times of calibrations.

In contrast to the electronic systems, the photonics and optical approaches such as photoconductive (PC) probing and Electrooptic Sampling (EOS) offer an ultra-broadband measurement bandwidth from DC to several THz. These systems also require much less calibration of the setups during measurements which lead to having fewer errors. Also in comparison to electronic approach, they present interesting features such as near field sensing and imaging with the use of a contactless positionable probe. In particular, EOS using an electrooptic (EO) crystal probe with very high spatial resolution and almost a flat frequency response in the detection is a superior solution for ultrafast electronic devices characterization. These unique properties of EOS are the motivation to use it in this thesis.

The history of EOS refers to 1983 where Valdmanis et al. [2] for the first time introduced it using the picosecond lasers. It was more development after the invention and the use of the femtosecond pulse lasers in the 90 s which highly extended the measurement bandwidth of EOS for the purpose of ultrafast electronic characterization. It can be assumed that a typical 100 fs of laser pulse-width theoretically guarantees measurement bandwidth up to 10 THz which is much beyond the operating frequency of today's electronics. In other words, since the 90 s, EOS as an ultrafast optical approach is capable to measure THz devices. However, there were not such devices available at that period of time. The recent progress in increasing the operating frequency of electronic devices towards THz can be a strong convincing reason to use this high speed technique for their characterization.

The main objective of this work is to characterize an all-electronic THz device which is designed based on Nonlinear Transmission Line (NLTL), in the framework of ULTRA project [3]. This device acting as a harmonic generator can be used for frequency up/down-conversion in a superheterodyne transceiver for the applications such as mm-wave or THz spectroscopy. The device was designed by Philips [4] as our project partner and fabricated using the 65-nm CMOS technology at TSMC® [5].

Since in this work both DUT and characterization methods are important, before demonstrating results, the state-of-the-art in THz electronics and their common ways of characterization are reviewed. In follow-up, the principle and theory of NLTL as an ultra-broadband THz DUT is also introduced and theoretically described. Since this device is theoretically designed to operate from microwave to THz, therefore, an ultra-broadband characterization system like EOS is required. On the other hand, the device itself can also be used to figure out the limitations of the EOS in terms of measurement bandwidth.

Most of the previous works have shown a very broadband EOS for the characterization of passive components in the pump-probe regime and only a few attempts have been made for active nonlinear components. This work, by differentiating between EOS for passive and active components, highlights why reaching an ultrahigh-bandwidth in the latter is much challenging than another. In contrast to pump-probe EOS for passive components such as transmission lines, in CW excitation of nonlinear devices, we may lose most of the potential of system bandwidth due to facing with jitter and more specifically, at higher frequencies the signal to noise degrades drastically. Resolving these challenges, which for years has remained as the major prohibiting factor in EOS, is targeted in this work. Accordingly, the most critical part of jitter which is relative jitter between the source and the sampling laser pulse is studied and finally with a novel approach fully resolved. It can be said that this solution, called laser master laser slave (LM-LS) configuration, for the first time is introduced here for the integration with EOS. This scheme makes the system fully coherent and allows recovering an ultra-broad measurement bandwidth.

2. THz Waves and THz Electronics

2.1 THz waves and their applications

The term “THz” refers to a range of the electromagnetic spectrum which is located between millimeter wave and infrared optics. The availability of this part of the spectrum has made attractions to use it in spectroscopy and future ultra-broadband communication systems. For example, the non-ionizing imaging and scanning of the human body is highly demanded for both security and medical diagnosis and THz is a real solution for that. Biological studies, remote sensing, aerospace discovery, material inspection, explosives detection and imaging of industrial products have nowadays become a very common application of THz waves [6]–[8]. In recent years, the so-called THz-gap has been bridged by pushing the gap from both the microwaves and the optics sides. Today, the question is not how to generate THz, but how to realize THz emitters or detectors in a compact, easy to use and cost-effective commercial manner. In this regard, many techniques for generating and detecting THz waves have been introduced. In the following sections of this chapter, as an introduction, common *solid state* and *photonic approaches* of the generating and detecting THz waves is shortly reviewed which persuades us to move forward to the electronic schemes.

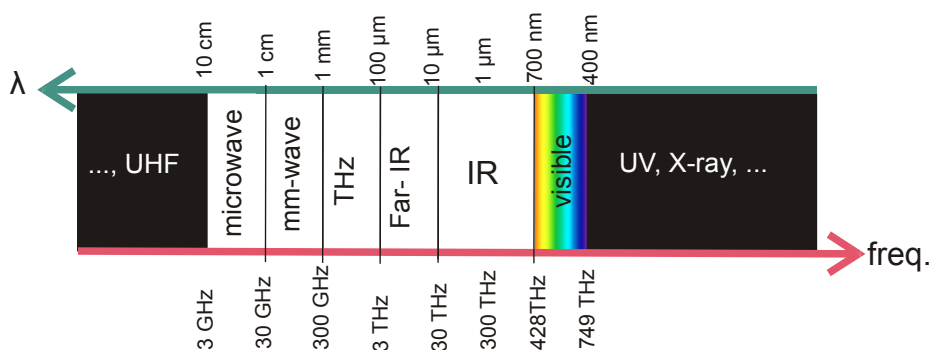


Figure 2.1 The electromagnetic spectrum highlighted for THz

2.2 Photonic and optical based THz

The term “THz gap” is a reminder that THz was hard to achieve or may only be generated at low power, but this has proven not to be the case nowadays as the amount of radiated power can vary in a very broad range from microwatts to MWatts. In this regard, while low power systems are appropriate for lab-scale applications such as material inspection and imaging, remote sensing and future communication systems based on THz require very high power solutions to compensate the path losses. In general, based on the amount of emitted power and the application, THz generators can be classified into three categories as follows

- Very high power THz, with nearly 1 MW which can be generated by Gyrotrons [9]–[11], klystrons or traveling wave tubes (TWTs)[7], [8], [12] and usually they work at lower THz bands towards mm-waves.
- High power THz with emitting several Watts which can be generated with the aid of free electron lasers [10],[13].
- Medium and low power THz (less than tens of milli-Watts) which can be generated using laser and solid states.

In the following sections more common methods of generating THz are explained.

2.2.1 Photoconductive pulse THz emitter

This method is more convenient and relatively easy which is mostly used in the time domain spectroscopy (TDS)[8] systems. The mechanism of generating THz waves is as follows: a femtosecond laser pulse illuminates a photoconductive Auston switch [14] which is deposited on a relatively fast semiconductor substrate like GaAs. The absorbed photons of the laser generate carriers including electron and holes which are accelerated by the bias voltage applied to the electrodes as shown in Figure 2.2. The semiconductor response to the optical pulse of the laser matters as for example, shorter the carrier lifetime generates a shorter THz pulse and the emitter efficiency can be affected by the mobility of the carriers. With a photoconductive emitter, depending on the emitter and the laser pulse width, several THz [15] of bandwidth

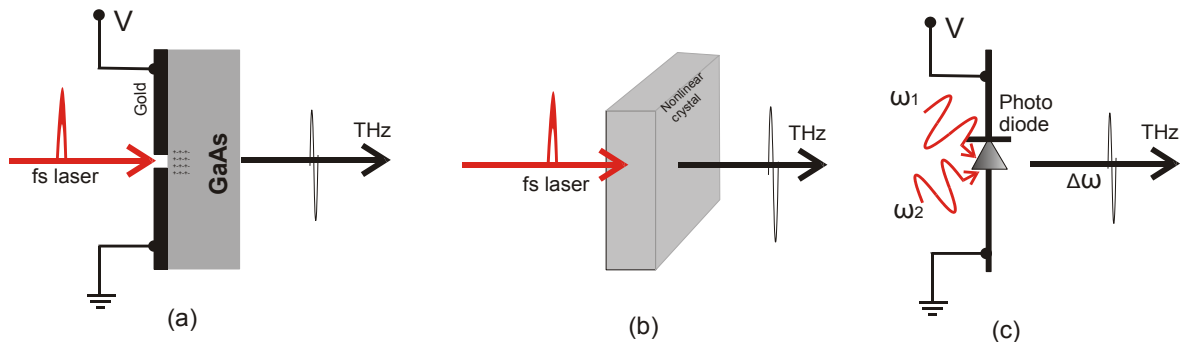


Figure 2.2 (a) Photoconductive THz emission, (b) optical rectification and (c) photo-carrier mixing

can be achieved. A major drawback of this scheme is a very low conversion efficiency of the optical energy to THz and typically pumping a photoconductive emitter with 1 Watt of the optical power will generate only sub-milli-Watt of the THz power.

2.2.2 Optical rectification

In this technique, a nonlinear optical crystal like LiNbO₃ can be used to generate THz waves based on the second order nonlinear polarization effect [16], determined by $p = \chi(E)E$ where

$$\chi(E) = \chi_1 + \chi_2 E + \chi_3 E^2 + \dots \quad (2.1)$$

is the material susceptibility. The THz waves can be generated by optical mixing of two different wavelengths of CW lasers or the intrinsic spectrum of a single femtosecond (fs) pulse [17], [18]. In the latter, each wave component in the spectrum band of $\Delta\lambda$, due to the nonlinearity of the medium, mixes with the rest resulting in new photon generation in the THz range. More clearly, two wavelengths λ_1 and λ_2 with the offset frequency of $\Delta\omega = \omega_1 - \omega_2$, which lies in the THz range are mix with each other to generate a THz signal. The method of optical rectification is known as the most broadband THz wave generation scheme ever. However, the amount of the emitted power is limited by the very small electrooptic coefficient of the crystal. Figure 2.2 (b) shows a very simple schematic of this scheme.

2.2.3 Photo-carrier mixing

Comparable to the optical rectification, this scheme in principle also needs two wavelengths to generate a beat frequency at THz range. Despite this similarity, it uses a different mechanism of photonic mixing usually using two CW lasers as shown in Figure 2.2 (c). Assuming two laser beams at optical frequencies of ω_1 and ω_2 , the mixed signal can be derived as:

$$\begin{aligned} & |E_1| \cos(\omega_1 t) \times |E_2| \cos(\omega_2 t) \\ &= \frac{1}{2} |E_1| |E_2| [\cos[(\omega_1 - \omega_2) t] + \cos[(\omega_1 + \omega_2) t]] \end{aligned} \quad (2.2)$$

while the beat frequency of $\Delta\omega = \omega_1 - \omega_2$ lies in the THz frequency range and the sum of the frequencies remains in the optical range much beyond the optical frequency used. The latter term is rejected by the low pass filtering of the photo mixer.

2.2.4 Quantum Cascade Laser (QCL)

QCLs are solid-state sources of THz frequencies based on band gap engineering which was introduced at Bell labs in 1994 [19]. They can generate average power levels much greater than one mWatt [20], [21], very advantageous in imaging and scanning. The main drawback of this method is the complexity of the semiconductor heterostructure and usually the need for a cryogenic temperature to have an efficient

performance. To build up a QCL, the bandgap structure of semiconductor material must be reengineered. For example, for GaAs, which has a bandgap at infrared (800 nm), inter-sub-band gaps or in other words, quantum wells are required. This can be realized by placing thin periodic layers of materials such as AlGaAs in a form of super-lattice composition. The thickness of the layers tunes the emitted wavelength. Figure 2.3 shows the mechanism of THz wave radiation in a QCL [22] [23].

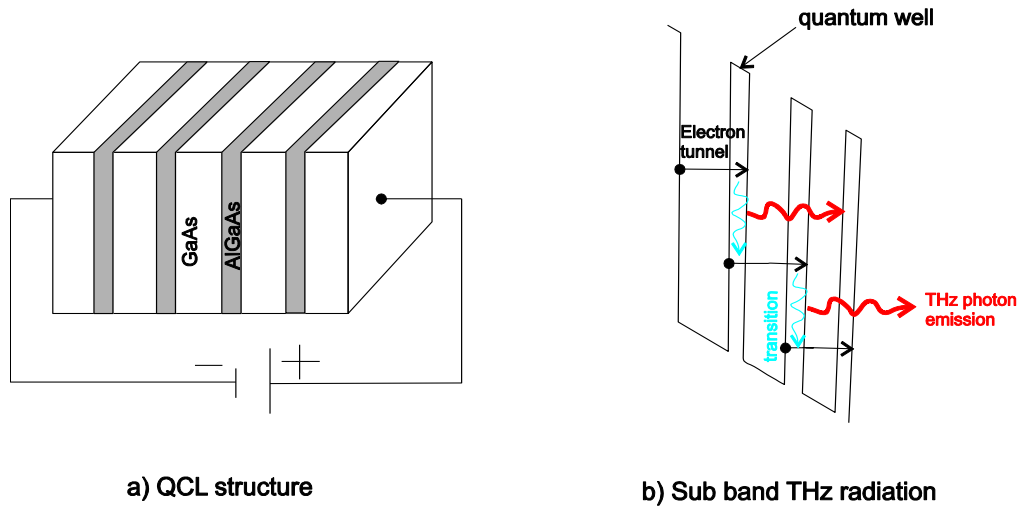


Figure 2.3 Schematic of multilayer structure for generation of quantum wells in a quantum cascade laser (a) and (b) mechanism of THz wave radiation from sub-bands.

2.3 Electronic THz sources

A drawback of most of the techniques presented before is that they operate in lab-scale and may need expensive and bulky lasers or cryogenic cooling systems. On the contrary, the electronic approach is an alternative which can make the availability of THz waves in a cheap, compact and massive industrial solution. In this approach, people from the microwave side are attempting to increase the performance of the electronic devices to make them operational at THz range as recently several devices and systems have been demonstrated. Despite a huge interest, unfortunately, this approach suffers from certain technology limitations. Although the aggressive scaling can help to increase the speed of the devices, it is still limited by the carrier drift-velocity saturation and reduces the tolerance of devices in power handling. For example, even a very low power applied at the gate of a field effect device, which has only tens of nanometer length can harm it. However, these limitations should not be disappointing as researchers have found several ways to improve them.

Since the scope of this work is to characterize THz electronic devices, recent advances in THz electronics are significantly important for us. Therefore, in the next sections of this chapter, the literature is reviewed in this regard.

2.3.1 Narrowband THz wave generation

Direct oscillation at THz frequencies

One way of generating THz waves is to make a direct oscillation at THz frequencies by applying a DC bias to a Resonant Tunneling Diode (RTD) [24]. Looking at I-V curves of a typical RTD depicted in Figure 2.4, the negative differential resistance is identified as the origin of this oscillation. Unfortunately, the efficiency of this scheme is very low and only a very small portion of the power at THz range can be radiated. In [25] the main reason for this low power efficiency is attributed to the narrow voltage range in the negative resistance area (see Figure 2.4) which makes the output power defined by $P = \Delta I \times \Delta V$ small. Moreover, the semiconductor used must be

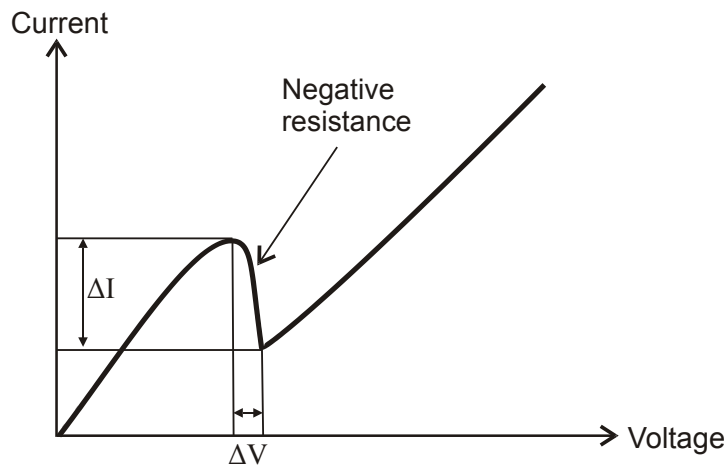


Figure 2.4 I-V curve of a typical resonance tunneling diode

engineered carefully to be operational at the THz frequencies.

Frequency multipliers (diode only)

Another scheme which is more conventional is the use of frequency multiplication. In this approach, a microwave signal drives a circuit which includes a chain of frequency multipliers and finally generates THz wave as schematically shown in Figure 2.5. The multiplier element can be an ultrafast diode e.g. a Schottky, and for

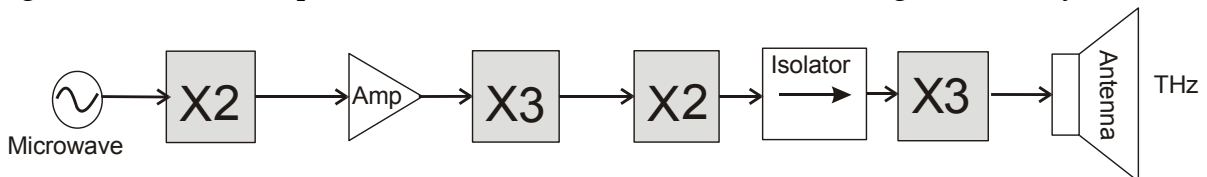


Figure 2.5 A typical diode based all-electronic THz transmitter with Schottky diode multiplier chain. Inspired from RPG ®.

achieving higher power at the output, the signal may be amplified in the primary stages using ultrafast transistors such as III/V heterojunction bipolar transistor (HBT), HEMT or metamorphic HEMT (mHEMT).

Diodes can operate at very high frequencies and have already commercially been adapted to THz systems [26], [27]. IMPATT (IMPact ionization Avalanche Transit-Time) diode, Gunn diode, RTD (resonant tunneling diodes) and SBD (Schottky barrier diodes) are widely used in these kinds of technologies. The major drawback of using diodes in a frequency multiplier is their passive upconversion (mixing) mechanism, as they exhibit no gain. This shortage results in a very large conversion loss as with pumping power of hundreds of milli-Watts a THz signal with only a few microwatts can be achieved [8], [28]. If such a multiplier is being used for down conversion of a receiving signal, due to the lack of having a low noise amplifier (LNA) at THz frequencies in the first stage, the signal to noise ratio (SNR) dramatically degrades. Moreover, designing Schottky diode based multipliers at frequencies above 2 THz is a challenge due to the size of the chip and the waveguide dimension in reaching sufficient matching [28]. Figure 2.6 shows layout and scanning electron microscope (SEM) image of a THz multiplier.

Combined frequency multipliers

Since pure diode based THz wave generation suffers from having no gain and large conversion losses, the attempt in this approach is made to compensate this shortage with the use of ultrafast transistors in the primary or intermediate stages of the multiplier chain. To this end, increasing the speed of the transistors as high as possible is helpful in making them operational at mm-wave or even THz frequencies, where the power for a diode in a multiplier circuit becomes the bottleneck. This requires a significant increase of some key characteristic such as the unit current gain

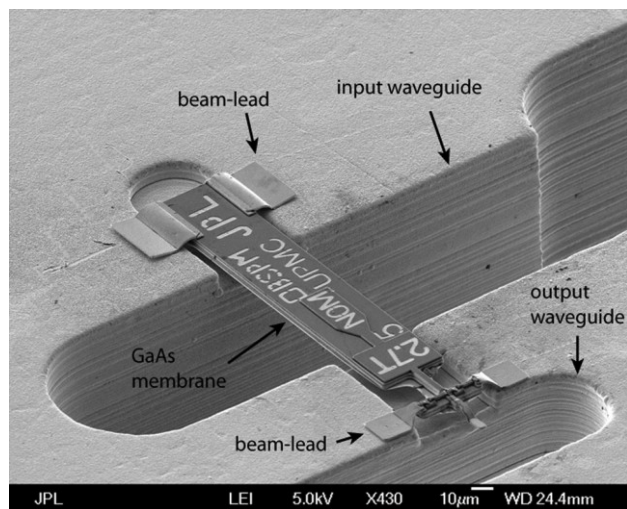
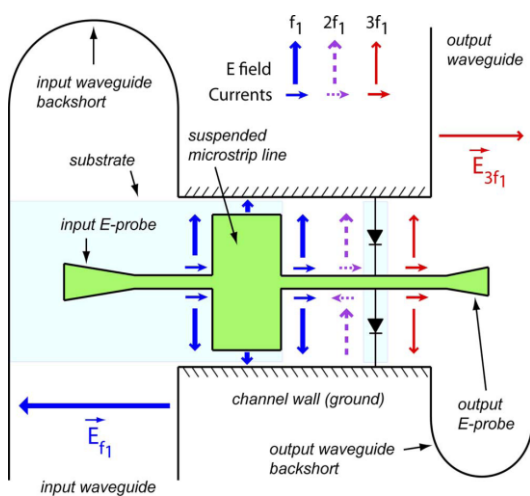


Figure 2.6 Layout (left) and SEM image (right) of a 2.7 THz frequency tripler chip. Reproduced with permission from [28].

cut-off frequency (f_T) and the maximum frequency of oscillation (f_{max}) of a transistor. As a rule of thumb in a field effect transistor $f_T \sim \frac{g_m}{2\pi C_{gs}}$ can be increased by increasing both the mobility (μ) of the semiconductor carriers to enhance g_m as well as reducing the gate length to reduce the device size and achieving a smaller C_{gs} . A technique to achieve a f_{max} greater than 1 THz was addressed in [29] which is performed by using InP- HEMT structure.

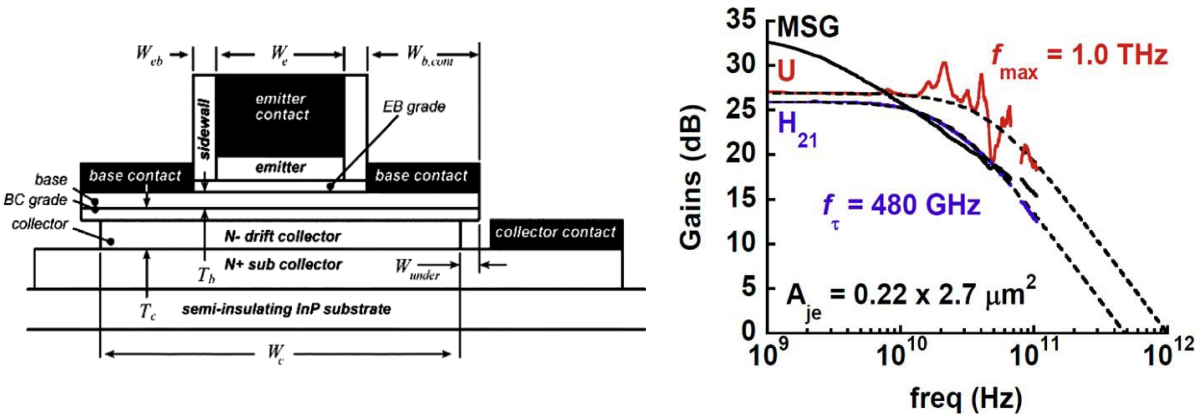


Figure 2.7. An InP HBT device (left) and prospective f_{max} (right) of this technology. Reproduced with permission from [29] and [33].

Similarly, the bandwidth of Bipolar Junction Transistors (BJTs) has been subjected for improvement. Exclusively with SiGe HBT technology $f_{max} > 860$ GHz [30]–[32] and even 1 THz has been achieved [33] as shown in Figure 2.7. This is resulted from band diagram of SiGe which allows electrons emitted from emitter passing very quickly through base and collector depletion layers. A scaling technology roadmap with $f_{max} = 2.8$ THz with InP HBT technology, called 3 THz generation is also addressed in [34].

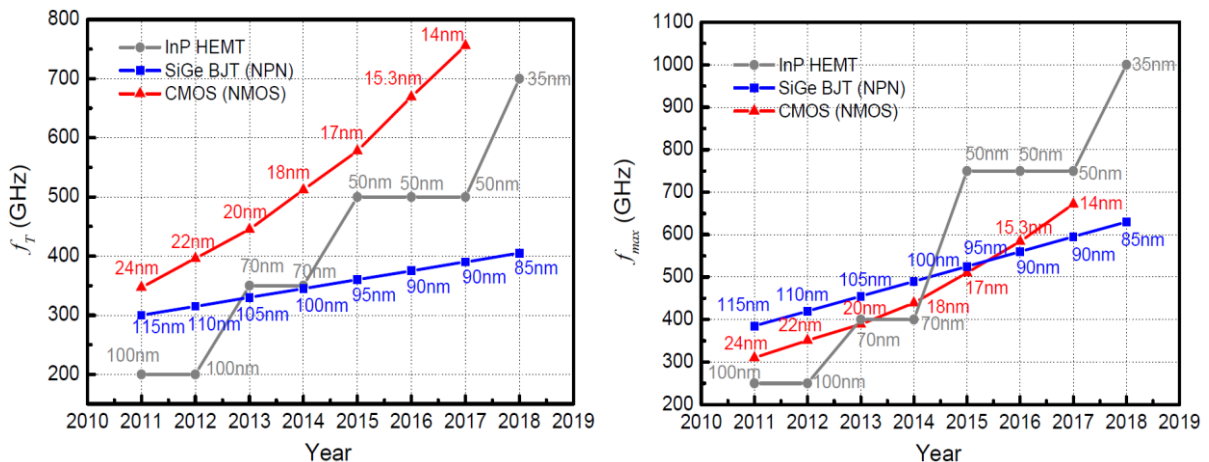


Figure 2.8 Road map of transistor technology for both f_T and f_{max} [35]

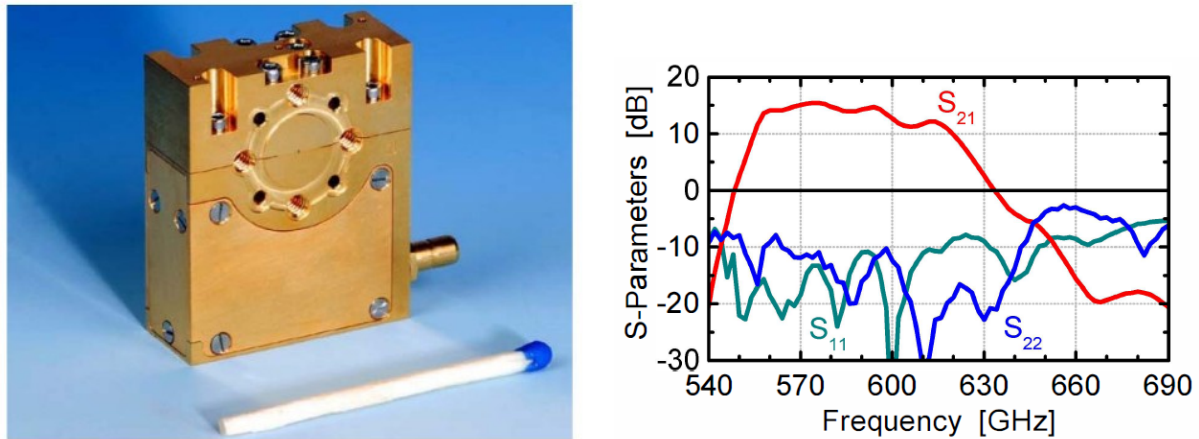


Figure 2.9. A viewgraph of a LNA operating at 600 GHz and its frequency response. Reproduced with permission from [38].

All of the utilized technologies in the field of THz electronics are pushing to demonstrate a higher profile. The diagrams depicted in Figure 2.8 shows the state-of-the-art increase of f_T and f_{max} based on the used technologies [35].

For a transistor used as an amplifier, the operation frequency is much smaller¹ than f_{max} and f_T , and hence it is very challenging to have an amplifier at mm-wave or THz frequencies. Despite this fact, recent mm-wave and THz amplifiers such as a 25 dB of gain at 325 GHz [36], more than 16 dB at 460 GHz [37], and interestingly an LNA with 12 dB of gain at 600 GHz [38]–[41] using 35-nm mHEMT, were demonstrated by the Fraunhofer Institute [42] in Germany as the cutting edge technology of actively generating THz waves (see Figure 2.9).

2.3.2 NLTL for ultra-broadband THz wave generation

Another interesting approach for all-electronic THz is to use nonlinear transmission lines (NLTLs). An NLTL, in general, is a synthetic microwave (mm-wave) transmission line which can be realized by periodically loading of nonlinear elements such as varactors on a host transmission line e.g., a coplanar waveguide (CPW) as shown in Figure 2.10. By feeding a CW microwave signal to this structure, the nonlinear functionality of varactors distorts the signal and hence, helps to generate

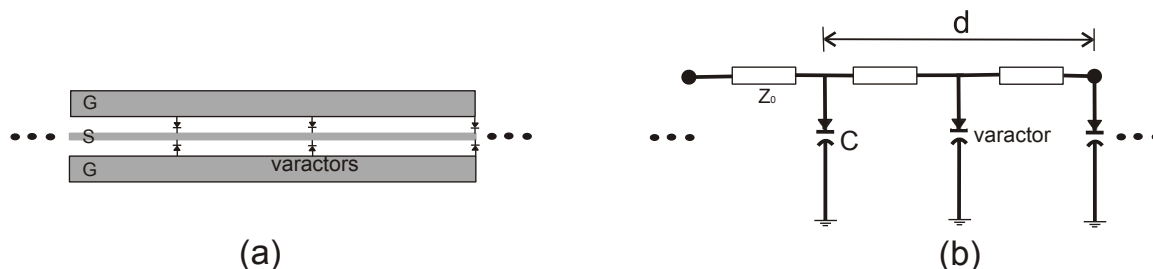


Figure 2.10. A schematic of (a) CPW based NLTL and (b) its circuit model

¹ Usually, 10 times smaller than f_T

harmonics.

In contrast to the diode based passive approach, which generally generate only few harmonics with rather high losses, this scheme can generate all sequential harmonics frequencies from the fundamental to THz with a higher efficiency [44]. As a demonstration, all-electronic THz spectroscopy system based on NLTL in GaAs technology with a bandwidth larger than 1 THz was addressed in [45] (see Figure 2.11). Based on application and the required bandwidth, an NLTL module can be fabricated with different technologies such as CMOS [4], [46], [47], HBT or HEMT [48], [49] which is a significant advantage for integration with MMICs. As NLTL is an ultra-broadband DUT which is suitable for EOS measurement, it is described in more detail in the following sections.

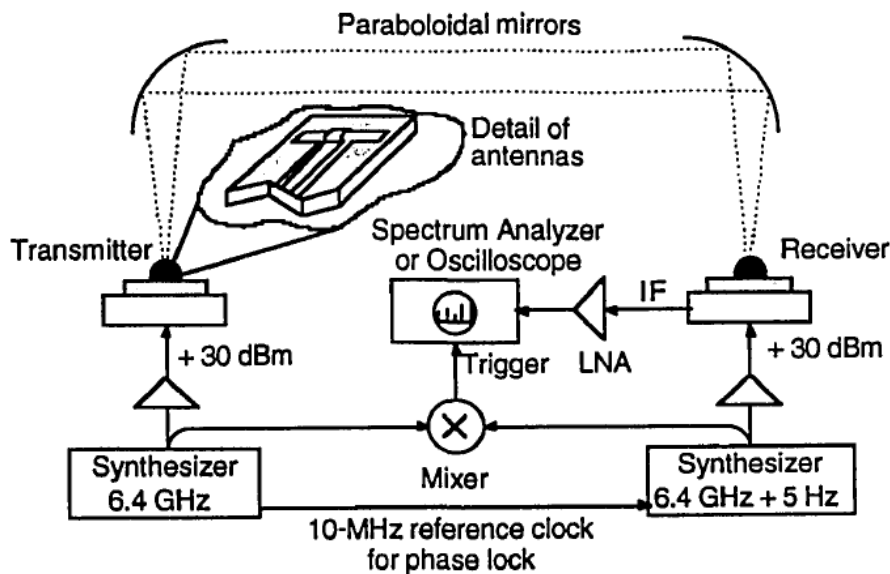


Figure 2.11 All-electronic GaAs NLTL based THz transceiver for spectroscopy. The NLTL is integrated with a silicon lens antenna. Reproduced with permission from [45].

2.4 A short theory of NLTL and its THz range design considerations

Since both the host transmission line and incorporated varactor are key elements in an NLTL design, their effect on the overall performance of the final device, in particular, at high frequencies is theoretically described as follows.

2.4.1 Selection of varactors

A varactor is a voltage controlled capacitance which can be realized using a PN junction. By applying a variable reverse bias voltage to the junction, it modulates the length of depletion region, and changes the junction capacitance according to $C(V) = \epsilon A/t(V)$, where ϵ is the permittivity of the semiconductor used, t is the

voltage dependent variable length of depletion region and A is cross section area of the junction respectively.

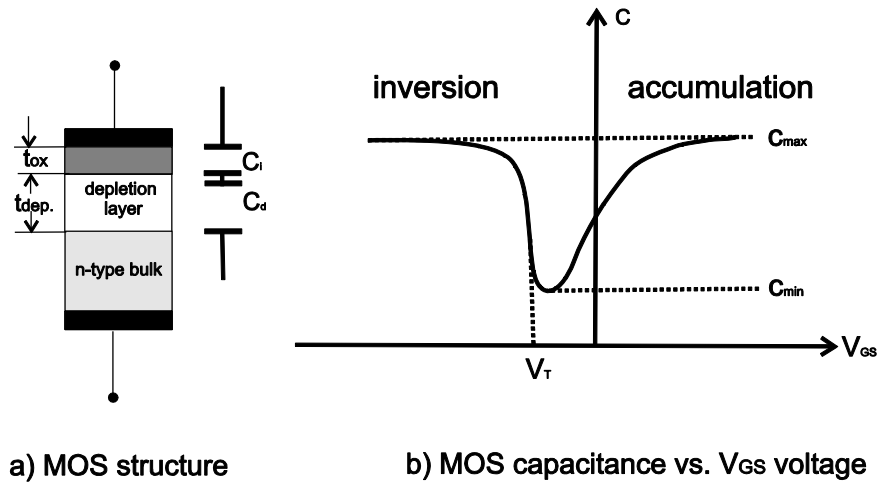


Figure 2.12 (a) A structure and schematic diagram of a MOS varactor and (b) capacitance variation as a function of bias voltage. Figure adapted by author from [51].

It is notable that any diode with reverse bias can be used but for ultra-high speed and THz applications, Schottky and resonant tunneling diodes (RTD) in III-IV technology are preferred. The latter can also amplify the signal by its negative differential resistance. Another alternative, which is more convenient for designers and rather cheaper in the technology, is CMOS varactor. A broad range of application from a multi-gigahertz voltage controlled oscillators (VCOs) to millimeter wave NLTLs [4], [46] have been addressed using these kinds of varactors. Also, the scaling of CMOS technology has made new varactors which are more attractive for ultrafast designers [50].

Since CMOS varactor is frequently mentioned in this work, at this point it is good to describe its principle of work and functionality. To this end, Figure 2.12

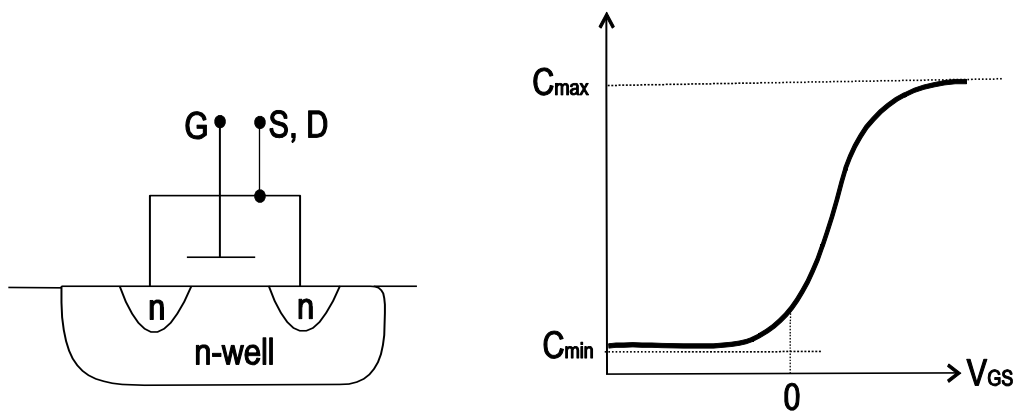


Figure 2.13 A MOS varactor configuration without inversion of the carriers. Figure adapted by author from [51].

portrays a typical MOS capacitance [51] in which the gate and bulk are connected to the applied bias voltage. Insulators, including silicon dioxide layer, with a thickness of t_{ox} , and a part of n-type bulk silicon (with a thickness of t_{dep}), are sandwiched between these electrodes.

For this MOS varactor, the capacitance varies with voltage principally in three regimes of operation so-called, *inversion*, *depletion* and *accumulation* as shown in Figure 2.12 (b). In the inversion state, where $V < V_T$, the minority carriers from the bulk are attracted by the bias of the gate to the lower plate of the silicon dioxide layer and since $C_d = 0$, the C_i only takes part of the structure capacitance. In this case, the capacitance is maxima. By increasing the voltage to the range of $V_T < V < V_{FB}$ ¹, the junction operates in the depletion mode and the capacitance decreases due to enhancing the depletion region length of t_{dep} . and the total capacitance yields:

$$C_{total} = \frac{C_i C_d}{C_i + C_d} \quad (2.3)$$

For $V > V_{FB}$ the majority carriers of the bulk again attract to the lower plate and *accumulation* takes place which again increases the capacitance to C_i value.

To achieve a monotonic response of the varactor to the applied voltage, some manipulation for controlling the inversion state is required. Figure 2.13 shows a kind of MOS varactor designed for this goal in which the source and gate are connected, and the inversion has been minimized by doping the bulk semiconductor.

Theoretically, the transfer function of these kinds of varactors for 130-nm CMOS is a hyperbolic tangent function given by:

$$C(V) = C_0 + C_1 \tanh\left(\frac{V - V_0}{V_1}\right) \quad (2.4)$$

and depending on technology, the parameters can change. For instance, typical values for IBM 8RF 130-nm technology are $V_0 = 0$, $V_1 = 0.5$ V, and $C_1 = 0.75 C_0$ [52]. It is noteworthy to state that by scaling of CMOS, this mathematical model of varactors becomes more inaccurate due to additional parasitic effects.

2.4.2 Left and right handed NLTLs

NLTL can be classified in either right or left handed design based on the arrangement of varactors on the host transmission line. As shown in Figure 2.14 (a), a typical right handed NLTL (RH-NLTL) can be illustrated by placing varactors in shunt branches of the circuit ladder along microwave transmission line. This kind of NLTL is more conventional and can be used for pulse shaping or as a distributed phase shifter.

In contrast to RH-NLTL, a dual design is called left-handed (LH-NLTL). In this configuration, varactors are incorporated in series branches of the transmission line ladder as depicted in Figure 2.14 (b). The term “left handed” is chosen since it behaves with anomalous dispersion and negative refractive index. In an LH-NLTL, the group and phase velocity are in the opposite direction and this property is useful

¹ V_{FB} stands for flat band voltage.

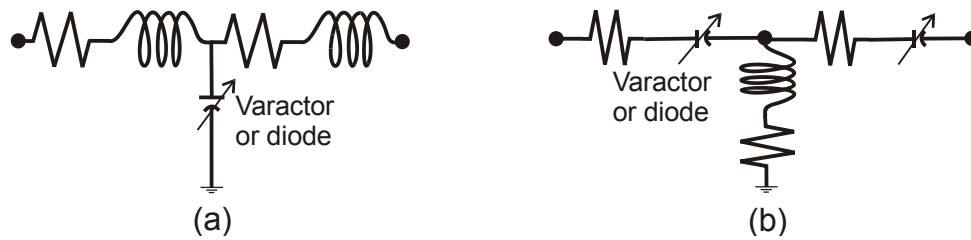


Figure 2.14 Schematic of (a) left handed and (b) right handed NLTL

for designing meta-materials and phase shifters [52]–[56]. In harmonic generation application of NLTLs, in comparison to RH-NLTL, it gives higher harmonic conversion efficiency with a shorter length as reported in [55] and shown in Figure 2.15. This gain is achieved at the expense of larger phase mismatch. Despite this significant advantage, integration of series varactors (diodes) with planar transmission lines (e.g. CPW) is cumbersome as one would need to connect both ends of the varactors (diodes) to the signal line. This configuration necessitates making a bi-planar signal line that may increase losses at high frequencies. Since dealing with LH-NLTL is too far from the scope of this work and our DUT is an RH-NLTL device, for simplicity hereafter the term “NLTL” *only* refers to an RH-NLTL.

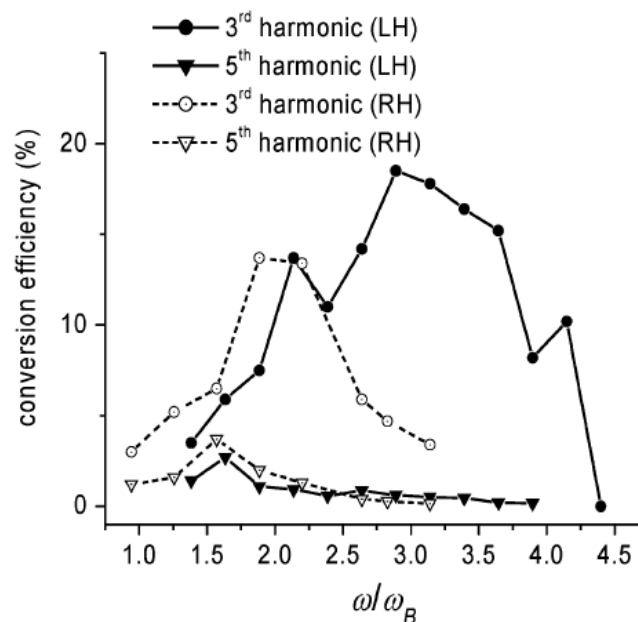


Figure 2.15 A comparison of conversion efficiency between right and left handed NLTLs. Reproduced with permission from [56].

2.4.3 The host microwave transmission line

Any microwave or mm-wave transmission line such as microstrip line, slot line and CPW can be used as a host structure for an NLTL design. Amongst all, CPW is more

convenient for design because of its quasi TEM broadband performance, more accurate design models, less parasitic effects and radiation losses, as well as a good compatibility with MIMICs [58]. Beside all of these advantages, it can also be fabricated with a simpler process by only one substrate side metallization which makes it appropriate for on-wafer probing.

2.4.4 NLTL Circuit model, dispersion and characteristics impedance

The Periodic structure of an NLTL and the “T” circuit model of its unit cell are shown in Figure 2.16. Neglecting parasitic inductance and resistance of varactor, it adds up a parallel capacitance C_v to the unloaded line capacitance C_0 at each unit cell. Assuming N sections of this unit cell to forms a final NLTL, therefore, the network

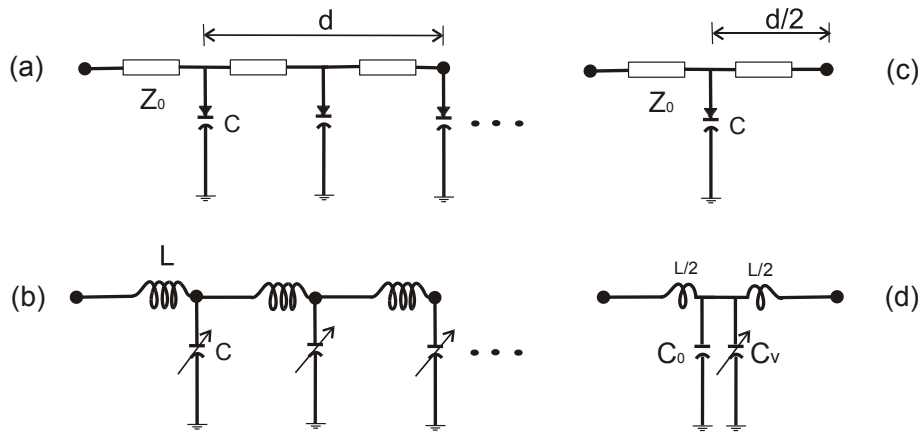


Figure 2.16 Transmission line model of (a) an NLTL and (b) an NLTL unit cell including varactor as a lumped element, (c) lossless LC equivalent circuit NLTL and (d) unit cell

ABCD transfer matrix results in a straight forward formulation for the behavior of the structure [49], [59]. Accordingly, for an arbitrary section number n , the ABCD matrix is given by:

$$\begin{pmatrix} V_n \\ I_n \end{pmatrix} = \begin{pmatrix} A & B \\ C & D \end{pmatrix} \begin{pmatrix} V_{n+1} \\ I_{n+1} \end{pmatrix} \quad (2.5)$$

On the other hand, from the circuit theory, the ABDC matrix of a unit cell shown in Figure 2.16 (c), which is a transmission line with the length of d connected to a shunt capacitance with normalized admittance of $b = \frac{\omega C}{Y_0}$, yields

$$\begin{pmatrix} A & B \\ C & D \end{pmatrix} = \begin{pmatrix} \cos \frac{\theta}{2} & j \sin \frac{\theta}{2} \\ j \sin \frac{\theta}{2} & \cos \frac{\theta}{2} \end{pmatrix} \begin{pmatrix} 1 & 0 \\ j b & 1 \end{pmatrix} \begin{pmatrix} \cos \frac{\theta}{2} & j \sin \frac{\theta}{2} \\ j \sin \frac{\theta}{2} & \cos \frac{\theta}{2} \end{pmatrix} \quad (2.6)$$

where $\theta = kd$ and k is the propagation constant of the *unloaded* transmission line. Propagation constant of the unit cell due to added shunt capacitance of C_v (see Figure 2.16 (d)) is modified to $\gamma = \alpha + j\beta$ and therefore,

$$\begin{pmatrix} V_n \\ I_n \end{pmatrix} = \begin{pmatrix} V_{n+1}e^{\gamma d} \\ I_{n+1}e^{-\gamma d} \end{pmatrix} \quad (2.7)$$

By comparing to Eq. (2.5) we have

$$\begin{pmatrix} V_n \\ I_n \end{pmatrix} = \begin{pmatrix} A & B \\ C & D \end{pmatrix} \begin{pmatrix} V_{n+1} \\ I_{n+1} \end{pmatrix} = \begin{pmatrix} V_{n+1}e^{\gamma d} \\ I_{n+1}e^{-\gamma d} \end{pmatrix} \quad (2.8)$$

$$\begin{pmatrix} V_n \\ I_n \end{pmatrix} = \begin{pmatrix} A - e^{\gamma d} & B \\ C & D - e^{-\gamma d} \end{pmatrix} \begin{pmatrix} V_{n+1} \\ I_{n+1} \end{pmatrix} \quad \text{or} \quad (2.9)$$

and for a nontrivial solution, $AD - BC + e^{2\gamma d} - (A + D)e^{\gamma d} = 0$. Since in a reciprocal network, which is a case here for a unit cell, $AD - BC = 0$, therefore, with substituting Eq. (2.6) in this equation

$$\cosh(\gamma d) = \frac{A + D}{2} = \cos(kd) - \frac{b}{2} \sin(kd) \quad (2.10)$$

This equation, so-called dispersion relation, shows the relation between the NLTL and the unloaded transmission line propagation constants. Assuming no losses for the network ($\alpha=0$), Eq. (2.10) leads to

$$\cos(\beta d) = \cos(kd) - \frac{b}{2} \sin(kd) \quad (2.11)$$

On the other side, if one considers varactors as lumped elements which locally add up a voltage dependent capacitance to the line, in a very simple approach, phase velocity and consequently delay per-section yield

$$V_{ph} = \frac{1}{\sqrt{L(C_0 + C_v(V))}}, \tau = \sqrt{L(C_0 + C_v(V))} \quad (2.12)$$

which shows a voltage dependency for the wave velocity and phase. Consequently, from the transmission line theory [59], the characteristics impedance of NLTL can be calculated as

$$Z_{NLTL} = \sqrt{\frac{L}{C_0 + C_v(V)}} \quad (2.13)$$

To get a feeling of the overall impedance for the NLTL, the average value of the varactor capacitance can be used as

$$C_{Avg} = C_0 + \frac{\int_{V_L}^{V_H} C_v(V)}{V_H - V_L} \quad (2.14)$$

where V_H and V_L indicate the highest and lowest voltage levels of the propagating signal, respectively.

2.4.5 Bandwidth consideration

NLTL¹ is a lowpass structure, and its bandwidth can be drastically limited by the technology and design. The cutoff frequency of a varactor which is a key factor in achieving the highest frequency of the design is given by:

$$f_d = \frac{1}{2\pi r_d C_d} \quad (2.15)$$

where r_d and C_d are the diode (varactor) series resistance and capacitance respectively. Albeit faster devices are favorable, selection of technologies such as CMOS can make a tradeoff between cost and performance of the NLTL. Recent progress in the high speed CMOS varactors [46] shows a cutoff frequency more than 500 GHz. However, it is still far below a multi-THz cutoff frequency of GaAs Schottky diodes [45],[60]. Therefore, implementing an NLTL with Schottky diodes strongly enhances its operational bandwidth, as van der Weide [61] in 1994 addressed an electrical pulse as short as 450 fs with this approach. Another obstacle for an NLTL to reach its highest bandwidth arises from its periodic nature. Although the distributed network of an NLTL in comparison to resonate matching networks exhibits much more broadband behavior [48], [60], its periodic structures can also limit its bandwidth by the structure Bragg frequency. The term ‘‘Bragg frequency’’ was suggested due to the similarity of NLTL periodic structure to periodic lattice structures which can be characterized with X-ray. The Bragg resonant frequency [48] of an NLTL can be defined as

$$f_B = \frac{1}{\pi\sqrt{LC_{Avg}}} \quad (2.16)$$

which is a frequency at which the structure signal transmission (S_{21}) reduces to zero. In other words, at Bragg frequency, the impedance of NLTL exhibits a short circuit behavior and beyond this frequency, the wave cannot propagate on the structure in a normal way. The NLTL impedance with respect to the Bragg frequency [60] is given by

$$Z_0 = \sqrt{\frac{L}{C}} \times \sqrt{1 - \frac{\omega^2}{\omega_B^2}} \quad (2.17)$$

2.4.6 Common applications of NLTL

There are lots of applications for NLTLs such as pulse compression [50], [51], soliton and high power shock waves generation [52], [53], pulse amplification [54], phase

¹ RH-NLTL since LH-NLTL is a high pass structure.

shifter [55], [56], frequency selectors [55], [57], and high-speed measurement systems with sub picosecond resolution [49]. The latter has recently been demonstrated by Anritsu® for the development of a network analyzer extension module [53], [58]. In the following section, the mechanism of NLTL for pulse shaping and soliton generation is described.

Shock wave generation

Shortly before, in Eq. (2.12) we saw that varactors impose a voltage-dependent phase velocity for the traveling signal on NLTL. This unique property of NLTL is a key factor for pulse compression or shock wave generation. The mechanism is as follows: for a pulse which is propagating on an NLTL, the peak can travel slower (faster) than its trough, and consequently its fall (rise) time steepens. For a signal which is propagating on NLTL, at each section (unit cell) it receives a phase shift and step by step becomes sharper in the edge as shown in Figure 2.17. It is worth to mention that to enhance the Bragg frequency and achieve a shorter fall (rise) time; large characteristics impedance for the host transmission line is required. Implementing CPW with very high characteristics impedance with CMOS faces with technological limitations and become unfeasible. For this reason, usually typical impedance values between 75-100 Ω [44], [60] are acceptable. One drawback of having large impedance for the host transmission line is its large intrinsic inductance which implicitly produces conductive dissipations and hence, reduces the NLTL power handling efficiency.

It should be pointed out that although for a high impedance host transmission line, we have a mismatch with a 50 Ω loads, this can be compensated by the capacitance of varactor itself. In other words, a part of the large inductance of the unloaded line vanishes by the varactors capacitances.

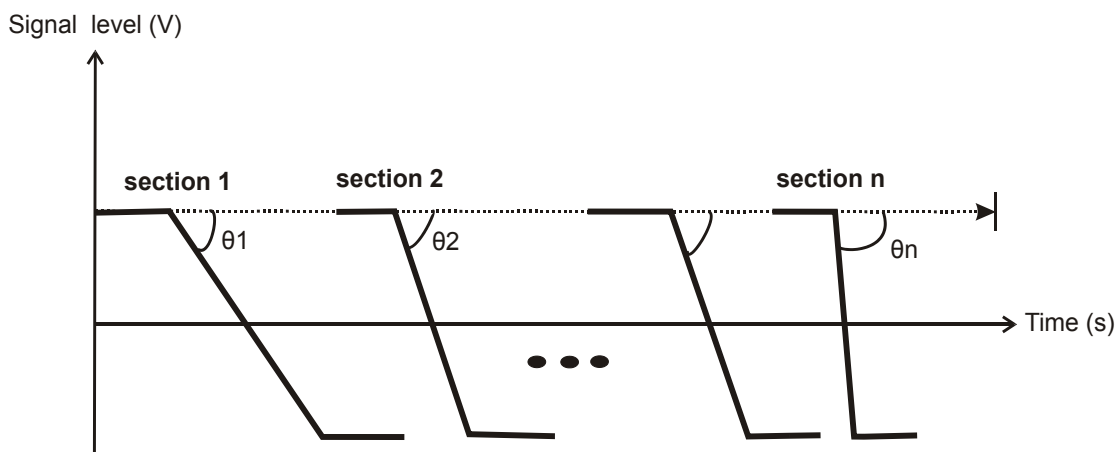


Figure 2.17 NLTL as a pulse compressor for shock wave generation. The pulse by passing through the NLTL periodic sections becomes sharper in fall time ($\theta_n > \theta_{n-1} > \dots > \theta_1$). Figure adapted by author from [48].

Theoretically, increasing the number of periodic sections N of an NLTL results in sharper pulse, however, the skin-effect and radiation losses of CPW also hamper this goal by decaying the amplitude of the propagating signal. Having in mind that the radiation loss of a CPW at frequencies close to 1 THz can increase with a rate of 10 dB/mm [62], therefore the longer the line larger the decay of the voltage and consequently resulting in less swing range for the varactor capacitances. The dissipation due to the parasitic resistance of varactors can also act in the same way [49]. A trade of scenario, therefore, for a designer should be incorporating many high-performance small devices at short intervals and reducing losses by shortening the length of NLTL. Ideally, a well-designed NLTL can only be limited in bandwidth by the fundamental properties of the utilized varactor time constant shown in Eq. (2.15) and the Bragg frequency.

Soliton generation

The functionality and behavior of an NLTL can be expressed by its fundamental

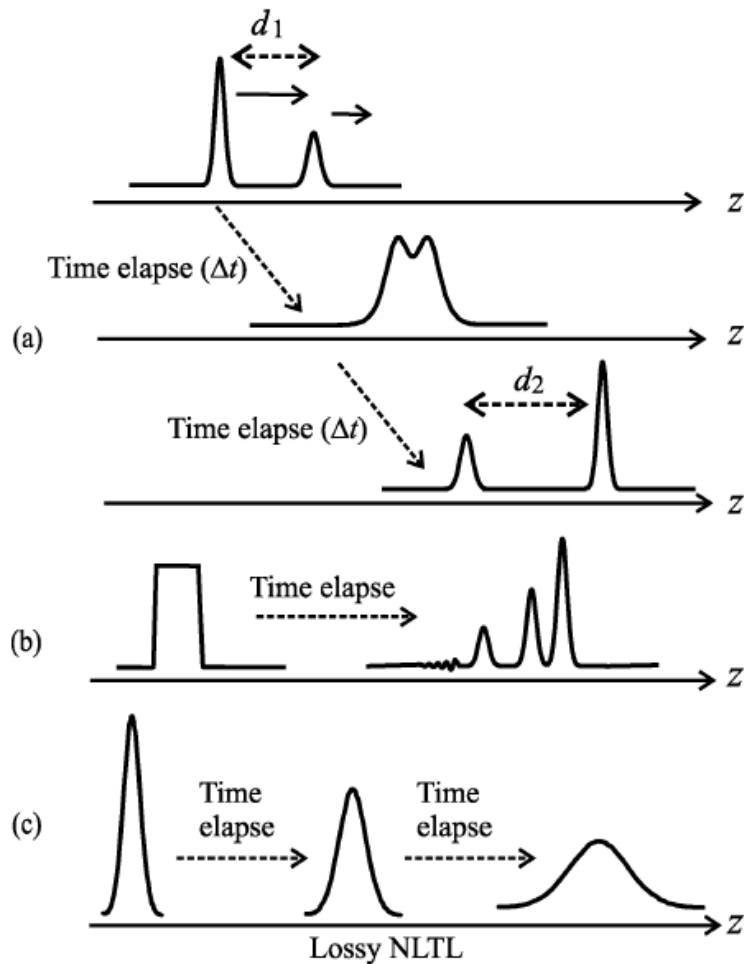


Figure 2.18 Soliton wave generation and propagation on an NLTL. (a) the speed of soliton depends on its amplitude, (b) mechanism showing how a soliton is generated from an input pulse and (c) traveling of a soliton on a lossy line. Reproduced with permission from [70].

characteristics including dispersion (attributed to the periodicity of unit cells) and nonlinearity of varactors. The dispersion and nonlinearity play contrary roles. For a propagating wave on an NLTL, dispersion broadens the pulse while the nonlinearity compresses. At the balance between these two effects, the final behavior of the system can be identified. Much below the Bragg frequency¹, NLTL shows small dispersion which makes it appropriate for shockwave generation [60]. This regime of operation has the highest attraction for us as our DUT is accordingly designed. By approaching to the Bragg frequency, the NLTL behaves very dispersive and becomes suitable for soliton generation [48], [60], [63]–[68], in which the energy of the input pulse can be distributed over one or few decomposed pulses, resulting in a very high amplitude pulse. Nahata et al. [69] have investigated on amplification of very short pulses using NLTL with this approach. An electrical soliton [70], similar to optical frequency solitons in fiber optics, is an interaction between dispersion and nonlinearity, as sketched in Figure 2.18. If there is no loss for an NLTL, the amplitude of soliton can be increased orders of magnitude larger than that for the input pulse.

2.5 THz detectors and sensors

So far, common ways of generating THz waves have been mentioned, but on the other side, the detection of THz waves with a good and highly sensitive detector which can compensate the lack of the power of the emitter, is highly demanded. Interestingly, many THz generators can also be utilized as detectors. However, some changes might be needed. Photoconductive Auston switch, integrated with a THz antenna for time domain spectroscopy (TDS) of THz detection is a good example. In comparison to the GaAs based emitter, here the semiconductor used, must be faster in response to the optical pulse. For this reason, materials such as low temperature grown GaAs (Lt- GaAs), which in contrast to intrinsic GaAs indicates much less carrier lifetime, can be used. Zheng et al. [21], with this scheme, have demonstrated electrical transient as short as 360 fs corresponding to 1.25 THz of 3-dB bandwidth, and a carrier lifetime of 150 fs, as well as 7% quantum efficiency.

Detecting of THz signals by means of electronics has also attracted attention. Fortunately, since the electronic detection of THz wave works in a low power regime [6], the power handling challenge which was already mentioned in this chapter, is not a crucial issue. However, the new challenge here is noise reduction and sensitivity improvement.

EOS working in a heterodyne system is another scheme of detecting of THz waves. In this technique an electrooptic crystal senses the THz electric field based on the Pockels effect. As will be seen later on, in next chapters of this work, this method is highly broadband which is fully applicable for the ultrafast electronic characterization.

¹ For $f < \frac{f_{\text{Bragg}}}{2}$

A category of THz detectors, which is a bit far from this work, are temperature based components like Bolometer [71]–[73], Golay cell and thermopiles. These detectors principally absorb THz wavelengths according to black body radiation and convert it to an electric signal. Although these THz sensors have been widely used in THz imaging, because of their incoherent and slow response, they are inappropriate for heterodyne applications.

3. Characterization of mm-Wave and THz Devices

In the previous chapter, the state-of-the-art electronic generation of THz waves and more specifically NLTL approach were mentioned. Regardless of the difficulties in making THz devices, their characterization is the next challenging issue as it requires very high-speed instrumentation. In the range of mm-wave and THz, two main characterization methods including electronics and photonics are used which are discussed in this chapter.

3.1 Common electronic instrumentation

Electronic based measurement systems such as spectrum analyzer, network analyzers and sampling oscilloscope are widely used for the characterization of high speed devices. For the latter, there is a limitation in the temporal resolution and spectrum analyzers only measure the power of a signal without giving information about the phase. In contrast, Vector Network Analyzers (VNAs) are capable of measuring both the amplitude and phase of the signal. In microwaves and millimeter wave, the S-parameters using transmission and reflection of a signal (see Figure 3.1) are used for the full characterization of a multiport device and in this regard VNAs

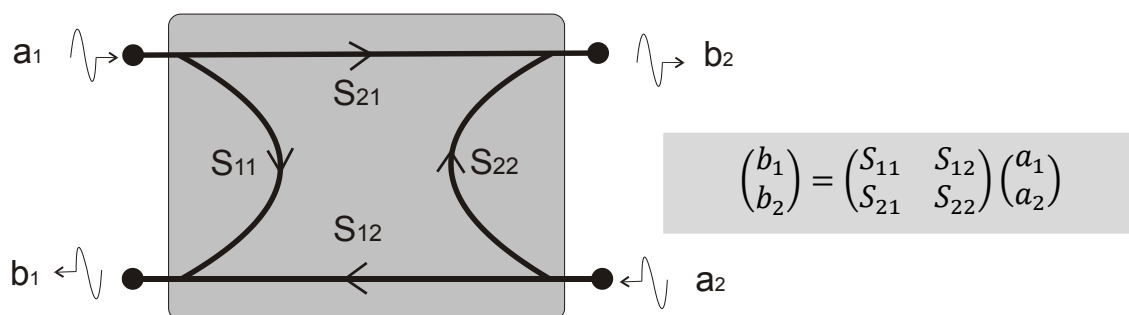


Figure 3.1 S-parameters of a two-port network where a and b show the incident and reflected voltages at a port respectively.

are perhaps the most appropriate electronic measurement solution. The phase information of the S-parameters helps to figure out the behavior of devices in terms of time delay and the phase (group) velocity. VNAs are also applicable for the characterization of passive devices such as RF cables, filters, isolators, attenuator, connectors, adaptors, antennas and active devices like power amplifiers and mixers.

To date, most of modern VNAs can characterize devices in a frequency range up to 70 GHz [1], [74], [75]. The problem emerges when a DUT works at higher frequencies where we need faster internal components inside the instruments.

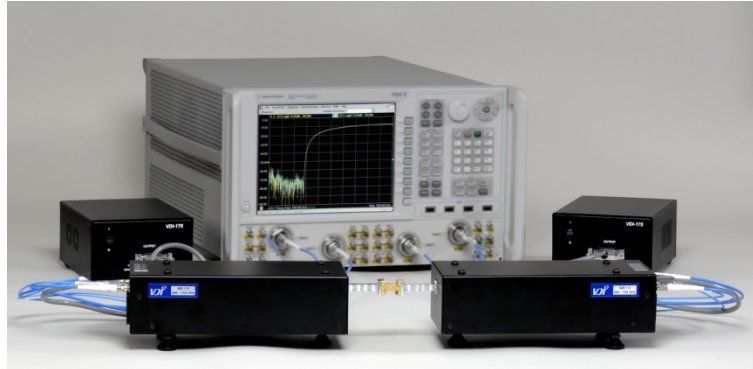


Figure 3.2 VDI THz extension modules for network analyzers. Reproduced with permission from [26].

Recently, a large enhancement in the measurement bandwidth of VNAs has been achieved by equipping them with extension modules. These modules have pushed VNAs to work in the lower THz frequency bands (Upper bands of the mm-waves) by mixing and upconverting the frequency of the source using harmonic mixers.

Recently Agilent® Technologies in cooperation with Virginia Diodes [26] VDI® have demonstrated a new extension module operational up to 1.1 THz [1], [26], [76]. Other competitor vendors like Radiometer Physics (RPG®) [27] and OML® [77] are also demonstrating relevant products. A view of VNA extension module and block diagram showing its operation is depicted in Figure 3.2 and Figure 3.3 respectively. As shown in the block diagram, two harmonic mixers with identical

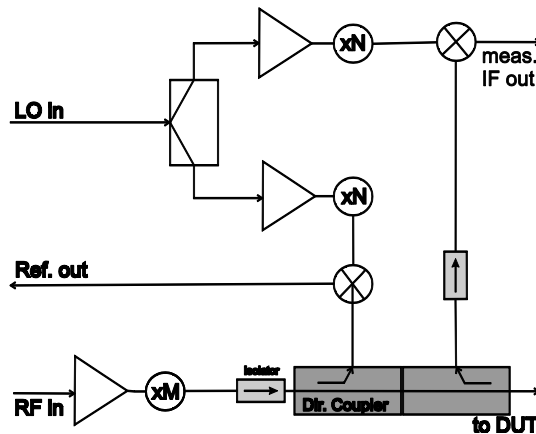


Figure 3.3 Schematic diagram of VDI extension modules. Figure adapted by author from [76].

functionalities are used to upconvert the signal of the generator in the transmitter side, and simultaneously downconvert the RF response of the DUT in the receiver. The system is configured as a heterodyne detector with RF, LO and IF and the signal is finally translated to an IF for signal processing and S-parameters analysis. In the following sections the features and functionalities of the extension modules from Virginia diodes®, combined with a VNA from Agilent® as a cutting edge technology in the THz electronic characterization, are introduced.

Table 3.1 Standard waveguide bands for mm-wave and THz range. Source from [78].

Military name	IEEE name	Frequency range (GHz)
WR-15	WM-3759	50–75
WR-12	WM-3099	60–90
WR-10	WM-2540	75–110
WR-08	WM-2032	90–140
WR-06	WM-1651	110–170
WR-05	WM-1295	140–220
WR-04	WM-1092	170–260
WR-03	WM-864	220–330
WR-02	WM-570	330–500
WR-1.5	WM-380	500–750
WR-1.0	WM-250	750–1100

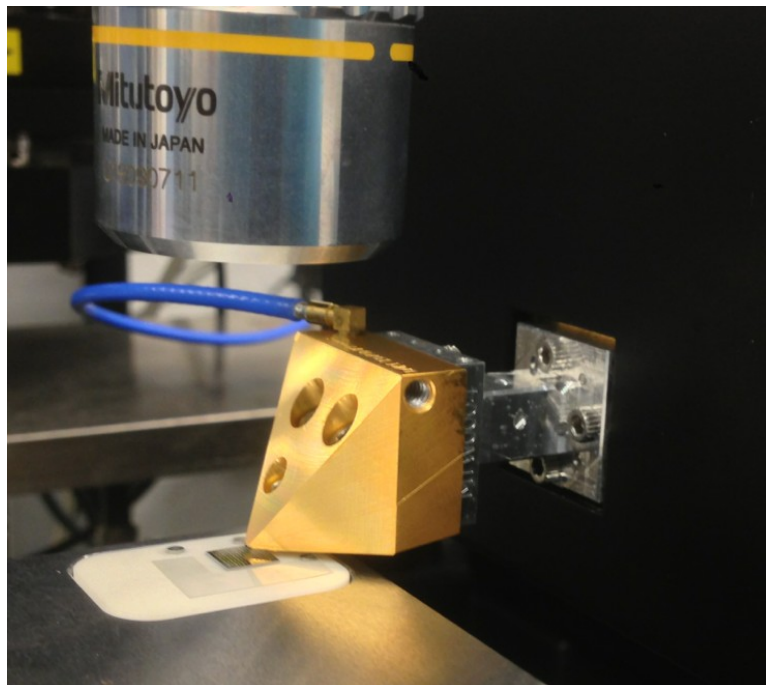


Figure 3.4 . A THz probe for wafer test. Reproduced with permission from [79].

3.1.1 Measurement bandwidth of the system

Measurement bandwidth of this combination has exceeded 1 THz. Although this is an enormous achievement in the electronic bandwidth, for a full-band measurement in the THz range, a set of banded waveguides as listed in Table 3.1 [76], as well as their relevant components, are required.

3.1.2 Cost efficiency

The need of banded waveguide for an ultra-broadband measurement makes the system extremely expensive and at the same time measurement with such systems is a time-consuming procedure. Moreover, this can also bring errors in the measurements due to replacing setup components from one measurement band to another. Also, for the case of on-wafer probing, additional finances for the band limited THz probes, precise probe positioners, and probe stations [78], [80] needs to be considered (see Figure 3.4 and Figure 3.5).

3.1.3 On-wafer measurement

Measurement in wafer-level and before dicing is very important for testing tape outs without consuming time and money for packaging prototyped. These kinds of measurements are now electronically, up to 1.1 THz is feasible using VDI® extension

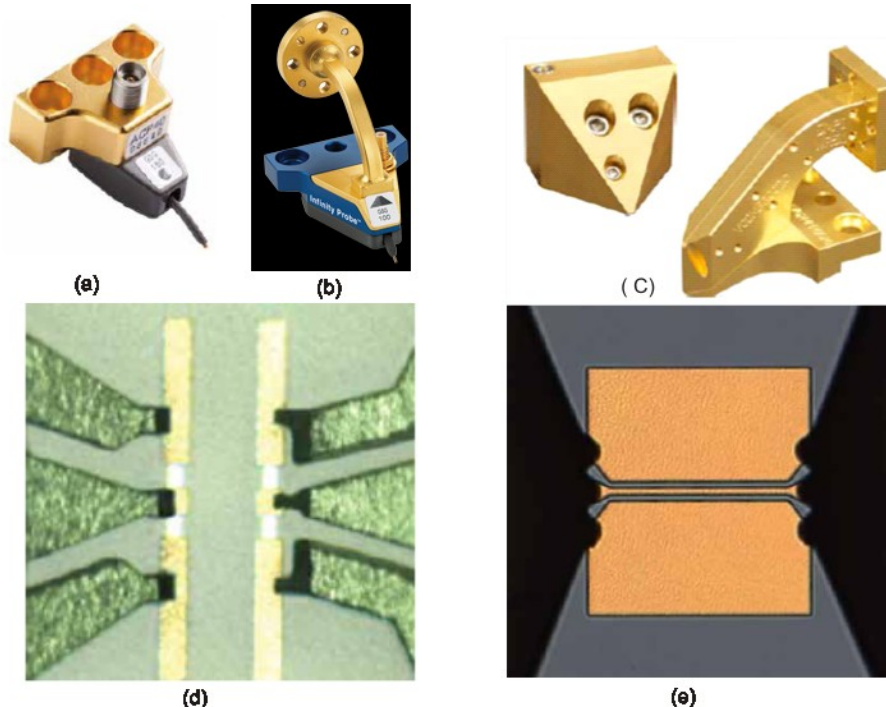


Figure 3.5 View graph of Cascade Microtech ® wafer probes for different frequency bands from microwave to THz. (a) coaxial to CPW transition, (b) waveguide to CPW, (c) waveguide mechanics for THz probes up to 1.1 THz, (d) tips for a and b and (E) Tips for C. Figure adapted by author from [78].

modules and various wafer probes (see Figure 3.5) for instance from Cascade Microtech® [78] or GGB® [80]. These probes are contact probes which are applicable only for a port based measurements and the risk of damage due to mechanical deformation or strain is high. Moreover, achieving a precise calibration for measurement is also a challenge.

3.1.4 Measurement of nonlinear devices

Since the s-parameters can only determine linear performance of devices, Agilent Technologies®, in contrast, have recently introduced X-parameters for nonlinear VNA (NVNA) measurements. X-parameters are being used to assess the performance of nonlinear devices in both small and large signal regime. DUT can be an amplifier which is working at a saturated 1 dB gain compression point, an NLTL or any other nonlinear component. Basically, in an NVNA, S-parameters are measured over harmonics of the signal and hence the X- parameters can be extracted.

3.1.5 Dynamic range

To measure a weak signal at THz frequency with high accuracy and without hitting the noise level, a high dynamic range measurement system is required. VDI® [81] has addressed manufacturing of high dynamic range transceivers applied in their extension modules. However, the dynamic range decreases with increasing the frequency with a slope of more than 80 dB over the system full band (see Figure 3.6).

3.1.6 Magnitude and Phase stability

Other important parameters in the VNA measurement are the magnitude and phase stability. These factors are strongly affected by increasing the temperature, jitter or noise of the system. With this respect, Table 3.2 summarizes the specification of

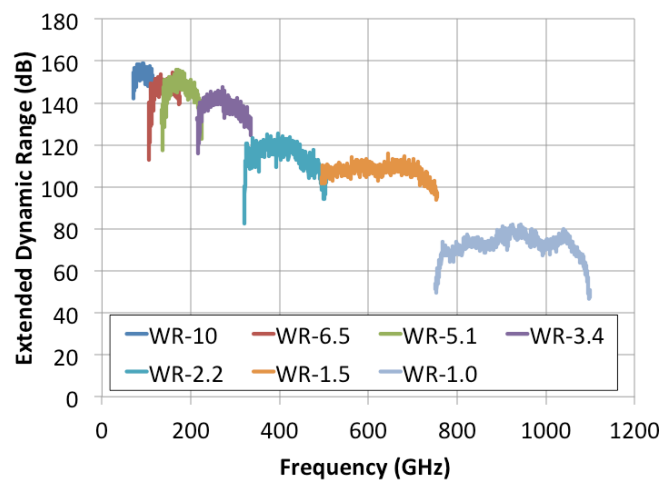


Figure 3.6 Dynamic range of VDI® extension modules over waveguide bands. The measured bandwidth for the dynamic range is 10 Hz. Reproduced with permission from [81].

VDI® extension modules. Despite a good magnitude stability (less than 1 dB over the full band), the phase drifts from 2 to 15 degrees. The main reason of this can be attributed to increasing jitter due to increasing the frequency or harmonic number as the jitter at n^{th} harmonic is n times larger than that at the first harmonic.

Regardless of the additional phase drift by temperature, this instability can decrease the accuracy of measurements by bringing more than 4% errors which cannot be resolved by averaging. This phase noise degrades the image quality in imaging applications of the extension modules

Table 3.2 VDI® Vector Network Analyzer (VNA) extenders for different bands and their specifications. Source [26]

Waveguide	WR 15	WR 12	WR 10	WR 8.0	WR 6.5	WR 5.1	WR 4.3	WR 3.4	WR 2.8	WR 2.2	WR 1.5	WR 1.0
Frequency band (GHz)	50-70	60-90	75-110	90-140	110-170	140-220	170-260	220-330	260-400	325-500	500-750	750-1100
Dynamic Range (BW=10Hz,dB,typ)	120	120	120	120	120	120	115	115	100	100	100	60
Dynamic Range (BW=10Hz,dB,min)	100	100	100	100	100	100	100	100	80	80	80	40
Magnitude Stability (±dB)	0.15	0.15	0.15	0.15	0.25	0.25	0.3	0.3	0.5	0.5	0.8	1
Phase Stability (±deg)	2	2	2	2	4	4	6	6	8	8	10	15
Test Port Power (dBm, standard/high power)	6/13	6/10	6/10	0	0	-6	-6	-9	-16	-17	-25	-35
Test Port Input Limit (dBm,saturation/damage)	16/20	16/20	16/20	16/20	9/20	9/20	-3/13	-4/13	-10/13	-10/13	-19/13	-20/13

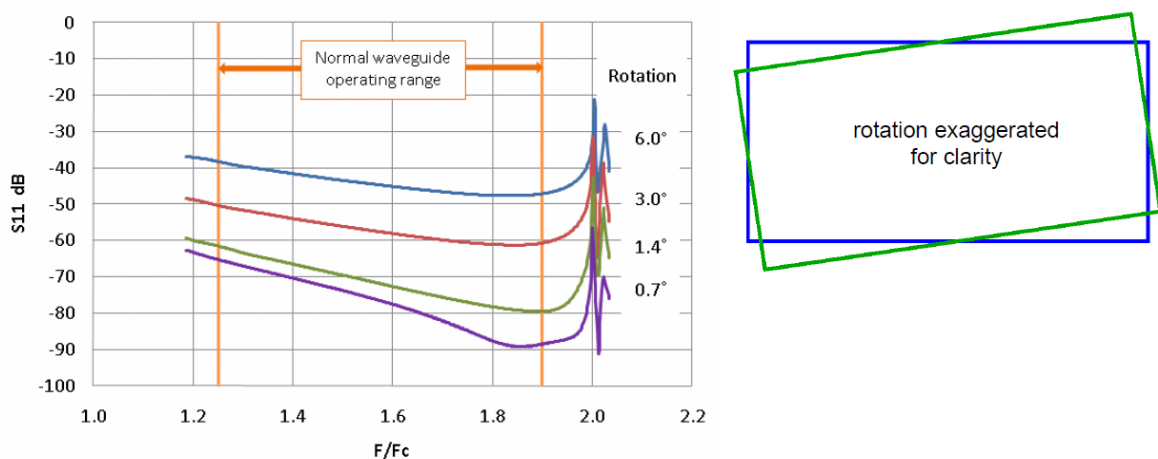


Figure 3.7 The effect of mechanical E and H misalignment on waveguide measurement. Reproduced with permission from[84].

3.1.7 Other measurement challenges

Although mm-wave and THz range measurement using VNAs is an attractive state-of-the-art technique, but since it is in its infancy, there is a need for improvement. De-embedding of measurements is a big challenge as there is no precise and verified model for fixtures at THz frequencies [82], [83]. Also a small disorientation of E and H plane due to mechanical displacement and misalignment of the waveguide flanges[84] can influence measurements by changing the waveguide electrical length as shown in Figure 3.7. This can bring systematic errors to the measurements which cannot easily be eliminated [82], [83]. In addition, by replacing the waveguide components which is unavoidable for a full-band measurement, any other change such as moving cables can destabilize the phase of the measurement and deteriorate its repeatability. It needs to be highlighted here that most of these challenges are attributed to the nature of electronic measurement systems and not necessarily the instruments.

3.2 NLTL based network analyzer

Basically fast electronic components, which can generate millimeter or THz wave, may also be applied for detection. Accordingly, high performance Schottky diode harmonic mixers have been used in both transmitter and receiver side of VDI® VNA extension modules. NLTL also can be considered as an alternative and elegant approach. In comparison to diode based mixer systems, it takes advantage of generating all harmonics¹, with higher conversion efficiency.

An NLTL can be used as a core element in an ultrafast sampling oscilloscope [85] due to generating a short fall (rise) time sampling pulse. In 1993 Shakouri et al. [86], [87] and later on others [88]–[93] introduced prototypes of active mm-wave and THz probes based on NLTL sampling bridges. Figure 3.8 shows one of these probes with typical measurement results demonstrating a sub picosecond temporal resolution with 3 dB bandwidth of 516 GHz [88].

In this broadband VNA, one of the NLTLs, upconverts the RF signal from the VNA signal generator and delivers a sequence of harmonics up to THz range to a DUT via a broadband directional sampler circuit. A sampling bridge including pair of Schottky diodes and hold capacitance is used to mix the transmitted (reflected) signal from the DUT with a signal which has already been generated by another identical NLTL driven by a local oscillator (LO) at $f_{LO} = f_{RF} + f_{IF}$. The superheterodyne system can finally translate the response of the DUT to an IF and hence, measured by baseband circuitry and oscilloscope. Obviously, in this system both RF and LO must be synchronized together, for example with a 10 MHz reference trigger. As a commercially update of available instruments base on NLTL, recently Anritsu® [94] has introduced a new VNA working up to 110 GHz. This instrument is principally

¹ As far as power allows us.

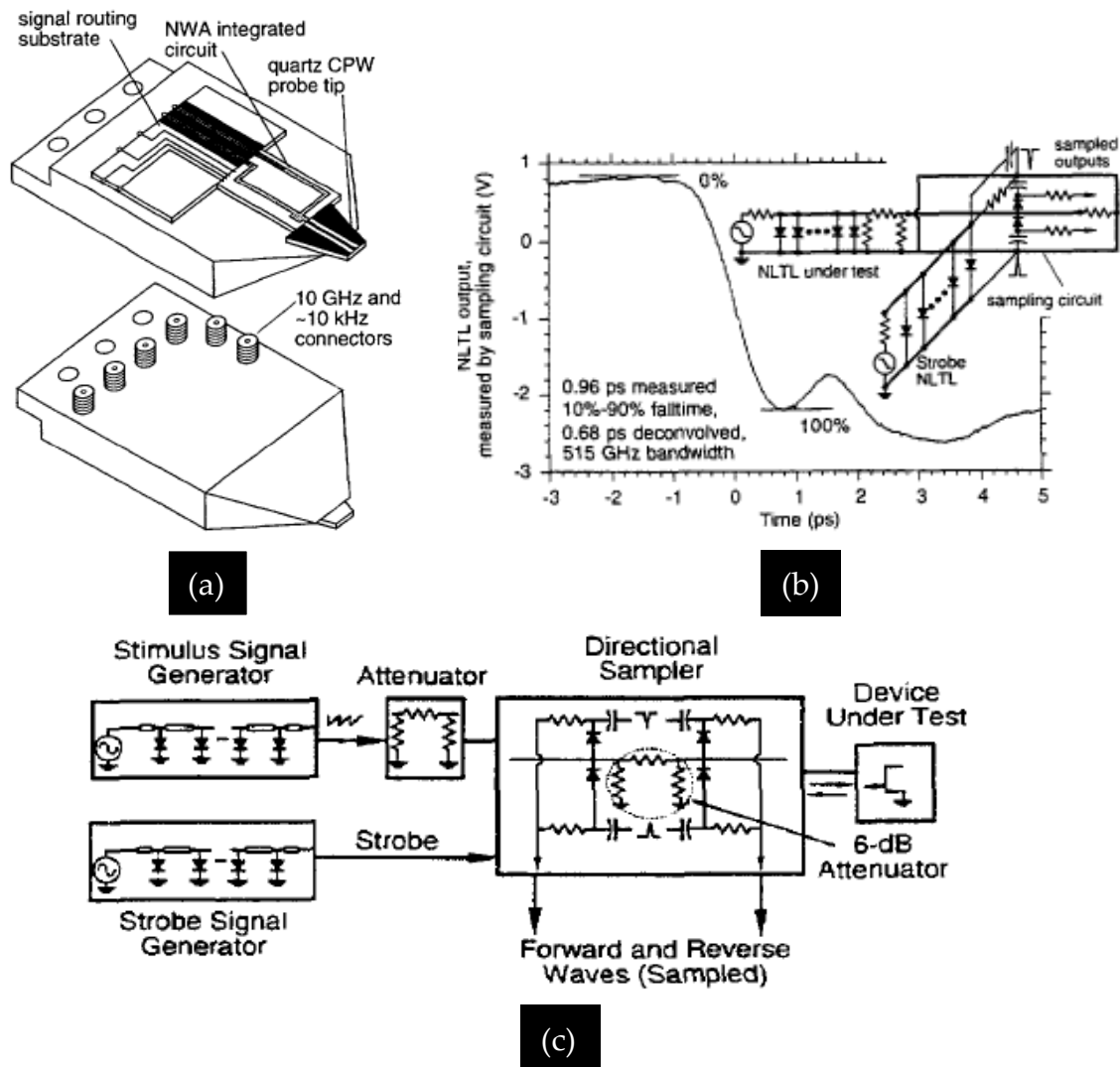


Figure 3.8 An NLTL based VNA probe. (a) The probe, (b) circuit diagram of the probe including NLTL sampling bridges and a measurement data up to 516 and (c) broadband directional coupler for the probe. Reproduced by permission of the Institution of Engineering & Technology [90].

working based on the equivalent time sampling also known as under sampling¹ and its schematic diagram is shown in Figure 3.9. In this diagram, the LO works at a frequency much lower the RF signal given to the DUT. The LO drives NLTL and the output generated sharp pulse is then used as a time-gating to downconvert the RF signal to an IF. The Shorter the pulse width results in broader the measurement bandwidth and higher the efficiency.

3.3 Photonic instrumentation

As mentioned earlier, electronic instruments due to lowpass behavior of internal electronics have a limited bandwidth. In contrast, optics with a highpass behavior

¹ Also called harmonic sampling or super-Nyquist sampling.

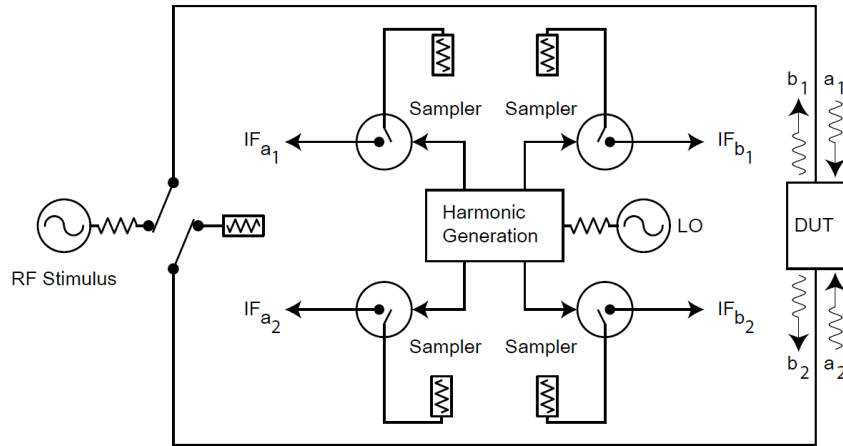


Figure 3.9 A schematic diagram of NLTL based network analyzer working up to 110 GHz from Anritsu®. Reproduced with permission from [94].

can be combined with photonics for ultrafast device characterization. In this regards, two common photonic based methods, including photoconductive (PC) detection and electrooptic sampling (EOS), which have shown the most attraction in literature and are relevant to the scope of this work are explained.

3.3.1 Photoconductive (PC) probing

One of the photonic approaches in the characterization of ultrafast devices is PC probing which operates based on gating with the use of an Auston [95] switch. A very short laser pulse opens the gate, by hitting the switch, and samples the signal arrived at the gate position. The short duration of the laser pulse guarantees ultra-wide bandwidth of the measurement system, but for optimum performance the semiconductor of the switch should be fast enough to respond to the laser pulse.

A faster response of a PC probe can be achieved by the semiconductor shorter carrier life time and higher mobility. Many people in semiconductor material engineering have tried to improve the impulse response of photoconductive switches [96]–[105]. Picosecond time resolution using Silicon on sapphire was reported in [106], [107] and more attractively sub-picosecond resolution with LT-GaAs as one of the fastest materials ever, was achieved [98], [108]–[110]. This material is very suitable for THz PC antenna applications as was used to detect beyond 60 THz bandwidth in free space TDS [111].

The PC sampling of THz devices can be performed in two different ways including contact and non-contact-probing. In contact probing, PC sampling gates can be integrated with DUT [105] in a monolithic design or used as an external contact probe [112] to touch DUTs. For the purpose of mm-wave and THz range characterization, another PC switch as a source of a short pulse should also be implemented in the same way. Therefore, in this approach, a pair of switches for generating and detecting the pulse is required. To realize such a system, the semiconductor has to be photoconductive. For example silicon based switches are not

recommended due to having indirect bandgap and suffering from slowness due to long carrier lifetime of the used semiconductor.

In contrast, GaAs (LT-GAAs) is a well-known semiconductor for this application as for example the S-parameters measurements with GaAs based PC probing of active devices has been addressed in [104], [113]–[124]. If incorporating PC switches on the same wafer which holds DUT is not possible, an interface like bonding wiring can be used. However, this additional fixture can influence the measurements. Figure 3.10 shows a typical contact PC probing setup in which switches PC₁, PC₂, PC₃ and PC₄ are connected to a DUT. A femtosecond laser activates the PC₁ which is connected to a DC bias and hence, a THz pulse launches on the host transmission line of the DUT. The PC₂ also samples this pulse as the DUT

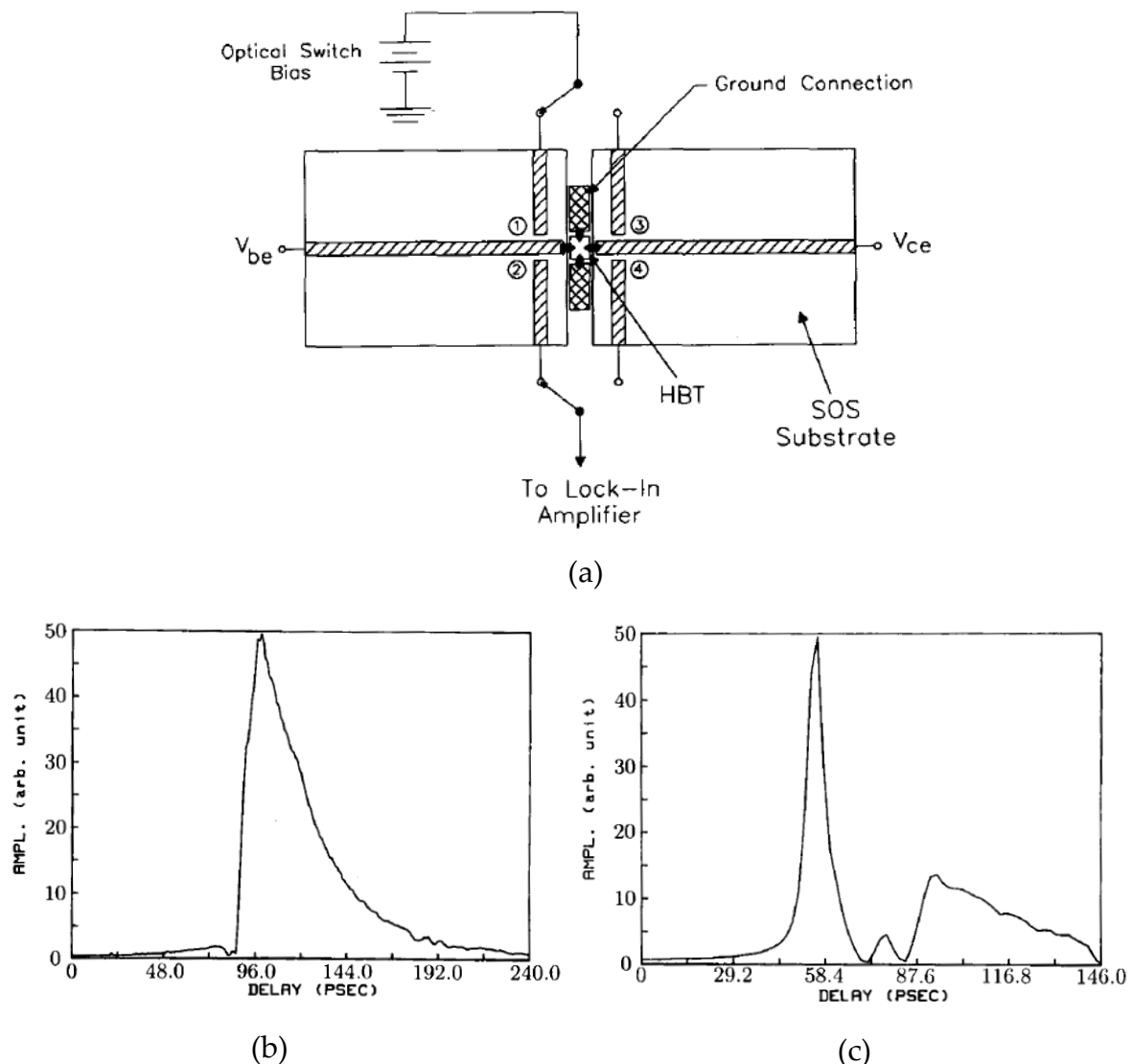


Figure 3.10 Contact photoconductive probing for mm-wave and THz device characterization (a) schematic diagram of a HBT transistor as DUT integrated with 4 photoconductive switches. Input pulse for device is generated by switch PC₁. (b) The sampled input signal at PC₂ and (c) the transmitted pulse sampled at PC₄. Reproduced with permission from [120].

input port. This switch is used for S_{11} measurement for the reflected wave from the DUT by a proper time windowing. To measure S_{21} , the pulse passing through the DUT can be sampled by either PC_3 or PC_4 at the time of arrival. Because the setup operates in the time domain, by proper time windowing, multiple reflections from the sampled signal in a post process can be eliminated. This is an interesting advantage of the time domain systems over the frequency domain measurements as the latter needs directional couplers to distinguish between transmitted and reflected signals. Moreover, time-gating at any switch in this coherent detection can be performed by controlling the time delay between source and sampler with a precise linear stage. Despite these advantages, one major drawback of contact PC probing is the invasiveness of the probes on the DUT. However, by computational methods and de-embedding it can also be minimized.

Another type of PC probing is contactless in which the PC is mounted on a positionable support and can measure the internal nodes of devices. Richard. K. Lai et al. [101], [125] have fabricated a low noise and high sensitivity PC probe and its SEM¹ picture is shown in Figure 3.11. This probe is pigtailed with an optical fiber. Waechter et al. [126] and recently Nagel et. al [127], [128] have introduced PC probes as THz detectors. In Chapter 10 experimental results for mm-wave measurements of an NLTL performed by such a commercial PC probe are demonstrated.

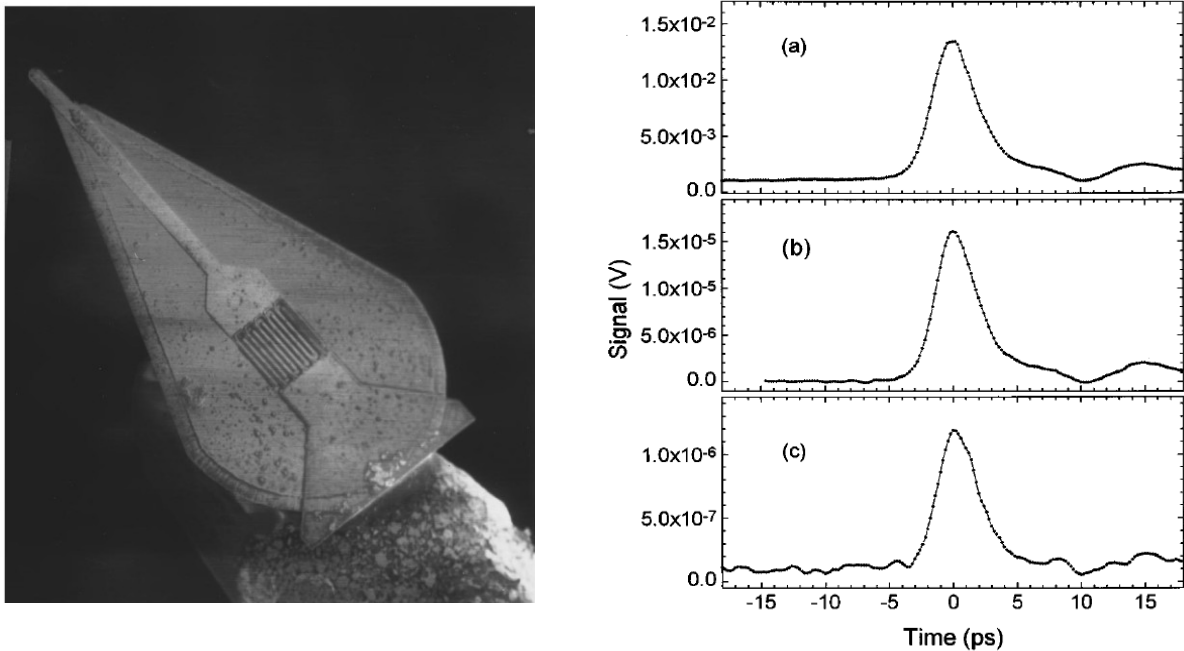


Figure 3.11 Scanned electron microscopy of a contactless fiber-mounted epitaxial lift-off LT-GaAs photoconductive probe and its measurements for different laser powers and modulation frequencies “(a) 2 mW and 1 kHz, (b) 200 μ W and 10 kHz, and (c) 2 mW and 50 kHz”. Reproduced with permission from [125].

¹ Scanning Electron Microscope

3.3.2 Electrooptic Sampling (EOS)

EOS is also an interesting photonic method for the ultrafast device characterization. A very simple schematic of this superior technique is shown in Figure 3.12. This typical setup which works in the pump-probe mechanism, in which, the PC probe launches a short pulse on a transmission line, and the EO crystal probe detects the pulse using the Pockels¹ effect. The probing laser beam, which is reflected from a high reflection coating at the bottom facet of the EO crystal, is modulated by this electric pulse and therefore, can be used for field detection. EOS with ultra-broadband measurement bandwidth is a promising method to assess the performance of very broadband electronic devices much beyond that for the electronics instrumentation. With a nonmetallic and contactless probe, it also takes advantage over the PC probing due to handling larger bandwidth and less invasiveness to DUTs.

Since EOS is the main measurement method used in this work, at this time it is necessary to review the state-of-the-art in this field.

Passive vs. active devices characterization

Since DUT can impact differences in achieving the highest measurement bandwidth of the systems, before explaining the achievement in the literature, it is necessary to draw a distinction between EOS used for the characterization of passive vs. active devices.

Most reputed literature has focused on the characterization of passive devices such as transmission lines in the pump-probe scheme. In this regime, a mm-wave (THz), similar to a case that was mentioned in PC contact probing, can be generated by transient response of a DC biased Auston PC switch to a femtosecond laser pulse. The generated short electrical pulse travels on the transmission line, and hence its coherent measurement at different positions on the line can be carried out using an EO probe (see Figure 3.12). In other words, the pulse response of transmission lines

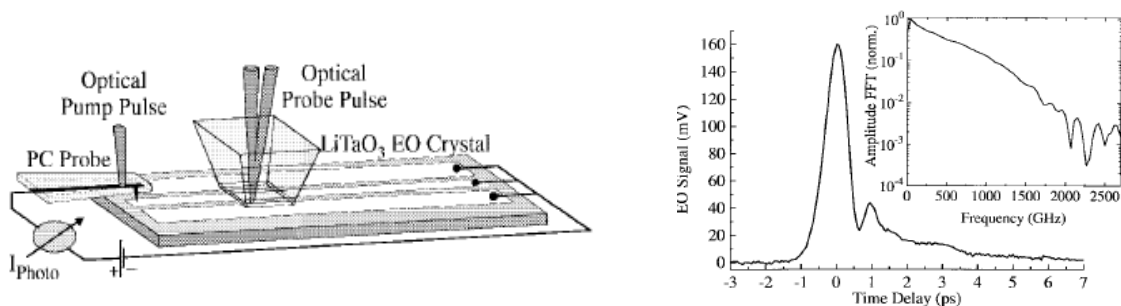


Figure 3.12 EOS characterization of passive devices (CPW). Schematic of the simplified setup (left) and measurement results beyond 1 THz (right). Reproduced with permission from [133].

¹ The Pockels effect is described in detail in next chapter.

can be measured for the analysis such as the line dispersion and attenuation.

The story for EOS measurement of active devices [129]–[133] is not as straightforward as that for passives. For an active device, such a short pulse with an uncalibrated power, not only may harm the device but also can lead us to a wrong understanding of the device performance. Because the response of a nonlinear system to a short pulse is not meaningful, therefore, CW feeding and the frequency domain measurement of the device is more appropriate. This is exactly a case for NLTL measurements and hence, EOS with such a capability is an appropriate technique for its characterization. However, at higher frequencies smaller signal to noise ratio and increased jitter may cause challenges.

Advances in EOS at a glance

Following to this short description of passive and active characterization, now it is a time to explain what has been so far achieved in the literature of EOS measurements.

In 1983 the first idea of EOS was introduced by Valdmanis [2], [134], [135] and later on Kolner et al. [136] shown preliminary results. Since that time several groups have tried to improve EOS capability. In 1986 Rodwell et al. [129] introduced direct (internal) EOS in contrast to external probing. The availability of the femtosecond laser in the 1990s in conjunction with improvement in semiconductor scaling gave an opportunity to demonstrate EOS for larger bandwidths than before. Frankel and others [62], [109], [113], [115], [134], [137]–[141] beside study of the probe invasiveness have shown a quantitative bandwidth of their setups in both pulse and CW excitation of circuits. They measured a large bandwidth by applying thinner EO crystals for the probe and utilizing high-speed DUTs (both passive and active). With

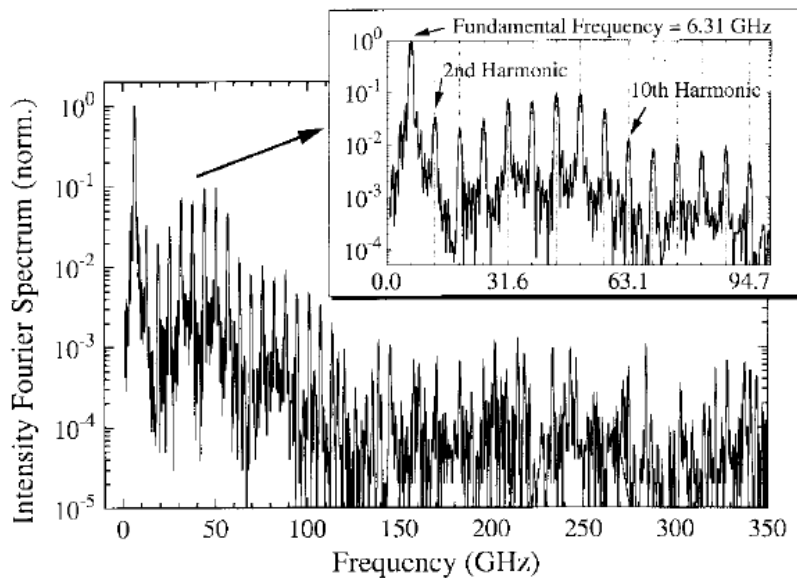


Figure 3.13. EOS Measurement of harmonics of a CW excited GaAs NLTL up to 150 GHz above noise level. The fundamental is at 6.31 with 25 dBm of power. Reproduced with permission from [133].

this regards, in 1996 they addressed a bandwidth of 100 GHz for active devices and 700 GHz for passives [140].

Similarly, Heiliger [142], Pfeifer and others [107], [133], [143] also reported photoconductive generation of the pulse in CPWs and demonstrated ultra-broad bandwidth of EOS for the passive characterization. Gibony et al. [144] have performed measurements on NLTL structure to demonstrate large measurement bandwidth of EOS in CW mode of circuit excitation and has introduced the effect of jitter in their measurement. Pfeifer et al. in 1996 measured a GaAs NLTL up to 150 GHz [133] as shown in Figure 3.13. They also introduced microwave master and laser slave synchronization technique for EOS. To the best of our knowledge, this measurement to date is the highest measurement bandwidth for CW excited circuits. Regarding improving in EO probe performances, Whitaker and others [145]–[151] developed different optical fiber pigtailed LiTaO₃ and GaAs probes for freely

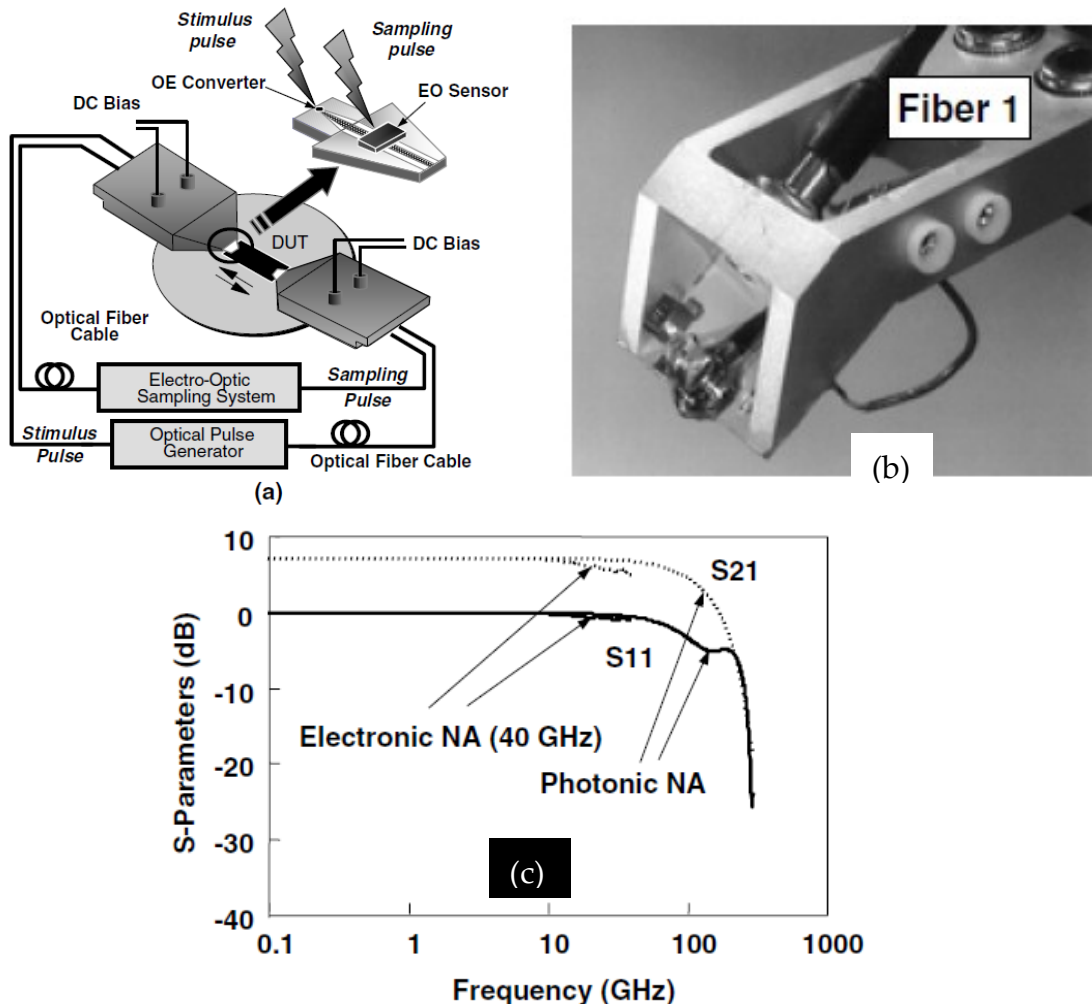


Figure 3.14. An EO probe integrated with a photoconductive THz emitter used for the characterization of mm-wave devices. (a) the setup and schematic of probe, (b) a photograph of the probe and (c) S-parameter measurement of a HEMT transistor.

Reproduced with permission from [156].

positioning of the measurements and reported improvement in sensitivity but at the expense of a reduction in the bandwidth. Chandani [152] also introduced his fiber base GaAs probe. A low-invasive probe was introduced by Lee et al. [149] and in 2008 Meignien et al. [153] introduced a two port EOS capable of distinguishing between the forward or reverse traveling directions of signals on transmission lines. To our knowledge since the end of the 1990s, no significant changes in EOS setups in terms of bandwidth enhancement or jitter reduction has been addressed, but many groups over the world have demonstrated measurements of different devices which cannot be scaled in a unique format for a meaningful comparison. It is notable to say that limitations of EOS in the CW mode of excitation still is an open issue and perhaps the most challenging topic in EOS for THz range measurements, which from our point of view is Jitter, has not been resolved. Later on, in the experimental results, solutions for reducing jitter in EOS will be presented.

On wafer probing

Near field sensing of devices is useful for the device characterization and imaging. Although the near field sensing with microwave resonator probes can be used for material and circuit characterization, they are inefficient at millimeter waves and THz frequencies. At these very high frequencies, electronic probing can be performed only with contact probes at circuit ports and as it was mentioned before in this chapter, they are expensive, and have other drawbacks. Alternatively, the photonic PC (*noncontact*) probing and EOS can be used. The latter, which is more relevant to this work, was frequently reported by several groups such as Pfeifer et al. [107] and Young et al. [154]. They separately demonstrated near field mapping of antennas and resonators, however, not at THz but microwaves and lower mm-wave frequencies. Interestingly, Nagatsuma et al. [155], [156] in 2002, by combining PC and EOS, introduced a photonic measurement probe integrated with an optical based VNA for on-wafer device characterization. In this configuration the PC switch generates a short pulse and after propagating through DUT, EO probe performs the sampling. This probe and the demonstrated results for a HEMT transistor, as well as a comparison to the electronic VNA measurement are portrayed in Figure 3.14.

Internal EOS

In general, there are two different ways of EOS called external and internal or direct and indirect [157] which are schematically shown in Figure 3.15. In contrast to external EOS, in internal EOS, the substrate of DUT itself is used as an EO sensor and therefore it takes advantage of being noninvasive to DUTs. Interestingly, in [158]–[162] this outstanding property of direct EOS can be used to investigate on invasiveness¹ of the external EOS probes.

¹ Invasiveness of probes is described in detail in next chapter.

Despite this big advantage, the direct method suffers from several disadvantages as follows:

- It necessitates using EO substrate for DUTs. This drawback excludes silicon based circuits to be measured. However, it privileges GaAs based devices.
- Characterization of DUTs in the Pump–probe system needs two different wavelengths for pump and probe as shown in Figure 3.15. In this case, the wavelength of the pump beam must be smaller than the bandgap of GaAs (850 nm) to be able to generate carriers in the substrate, while at the same time the probe must be tuned to a wavelength larger than this bandgap. Two different wavelengths from a single laser source can be obtained using nonlinear optics at the cost of more complexities.
- The last but not least disadvantage of internal EOS is that the laser has to be reflected from the metallic parts of the DUT and the field at the gaps cannot be measured properly. It should be noted that this is a contrast to the external probing in which a high reflection dielectric layer at the bottom facet of the probe is used. Also, the accuracy of measurements can be affected by the Fabry-Pérot etalon resonance of the substrate for the probe beam.

Far Field Sensing

Mostly in this chapter the focus was on EOS for near field detecting and device characterization, in which electrooptic probe approaches devices. It is noteworthy to mention that EOS can also be used for far field measurements like in a TDS. In contrast to near field, it detects the field component of a plane wave which is transmitted from an antenna.

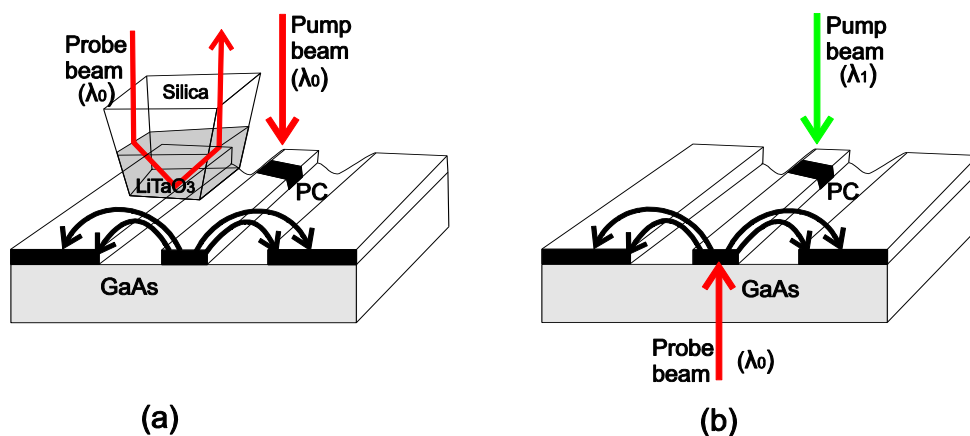


Figure 3.15 (a) Indirect and (b) direct electrooptic sampling. Direct pump–probe EOS needs two laser wavelengths λ_0 and λ_1 .

4. Electrooptic Sampling Theory

As discussed in the previous chapter, electrooptic sampling (EOS) using femtosecond laser (fsL) offers a very broadband measurement system for the electronic devices characterization. In such a system, the near field of active or passive electronic components can be detected and sampled by an fsL pulse based on electrooptic the Pockels effect inside the EO crystal. Since the attention is paid to characterization of ultra-broadband mm- wave and THz devices, and the ultra-short laser pulse has given this capability to EOS, briefly the mechanism of femtosecond laser pulse generation and more in detail the principles of electrooptic effect and EOS are described in the following sections.

4.1 Ti: Sapphire femtosecond pulsed laser

The Solid state ultra-short pulse laser using Ti: Sapphire crystals was for the first time introduced in 1986 [163] and was improved in the last decades. Nowadays the technology is affordable to generate pulses less than 6 fs with milli-Watts of power to hundreds of femtosecond with several watts [163]. Since this short pulse determines the bandwidth of EOS, its mechanism of generation in principle is described. It should be pointed out that the explanation of the femtosecond laser in this chapter is only dedicated to the case of MIRA Ti: Sapphire laser used in our EOS system and

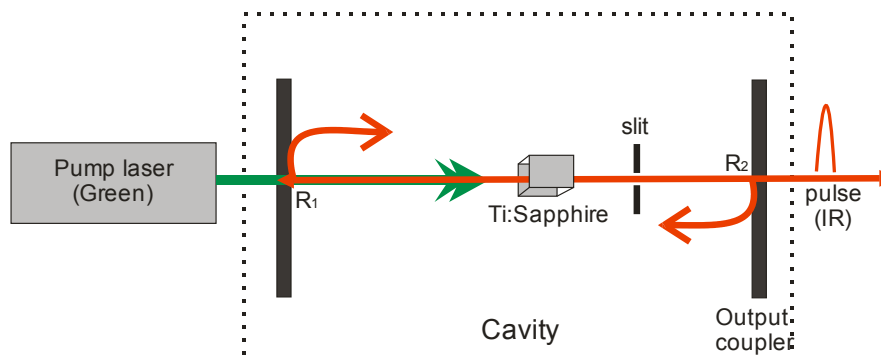


Figure 4.1 A very simplified schematic of a laser cavity for ultra-short pulse emission with passive mode locking.

necessarily should not be extrapolated to any other fsL.

As depicted in Figure 4.1, to generate a femtosecond pulse a cavity with a gain media is needed. Gain media inside the cavity is required to compensate losses, and to have a non-damping resonance for the optical beam. Ti: Sapphire ($\text{Ti}^{3+}:\text{Al}_2\text{O}_3$) is a crystal which is commercially available and has been used as gain medium for fsLs. The crystal is mechanically very stable and can tolerate very high temperature up to 2040°C. It can absorb photons at 400-600 nm and perform the fluorescence amplification from 680 nm-1100 nm with a maximum intensity peak at 800 nm [164]. In the absence of the pump laser (normal condition), atoms of the crystal are stabilized in their low energy state and by absorbing photons from a pump laser, they get excited to energetic state and stimulate or emit light. Under this circumstance, they amplify the light instead of absorption and therefore the gain medium is formed. The mirrors are used for the cavity bouncing and a birefringence filter (BRF)¹ can restrict the wavelength of operation. A pair of prisms¹ inside the cavity can be used to compensate group velocity dispersion of ultra-short pulse as it passes through optical components. The laser runs in the CW mode and longitudinal modes start lasing when the cavity length becomes exactly an integral number of the emitted light half-wavelength i.e. $L = n\lambda/2$, where L is the half-length of the cavity. Since n is not strictly defined, many different wavelengths can resonate coherently as modes of the cavity. In the mode-locked state, a short pulse of the light bounces back and forth inside the cavity and a small fraction of the light escapes from the output coupler which is in principle a partially transparent mirror (see Figure 4.1). The cavity round trip length $2L$ defines the laser repetition rate given by: $f = c/2L$ where c is the velocity of light in the free space. For the Mira laser the nominal repetition rate is around 76 MHz that can be tuned in the range of ± 1 MHz by changing the cavity length with the internal mirrors. It is worth to notify that the repetition rates up to 77 GHz with few millimeter cavity length is achievable with ND:YVO₄ laser [165]. Whenever the modes are fully locked, a very short pulse starts to emit.

The mode locking mechanism can be implemented in both passive and active ways, but the active mode locking usually generates longer pulse width and needs external electronic circuitry and synchronization [163]. In this way, the optical shutter is controlled by electronics and opens up at the arrival time of the pulse to the gain medium and closes again. The timing between electronic and the optical pulse must be precisely matched to have a short pulse [163]. In other words, the modulating frequency must be accurately set equal to the laser repetition rate. Since the length of the cavity can slightly vary with the temperature, the electronic precise follow-up

¹ Not shown in Figure 4.1.

compensation system like a PLL has to be implemented. Without facing with complexity and challenges of active mode locking, alternatively, passive mode lock using a so-called “saturable absorber” in the cavity can be obtained which also takes advantage of generating shorter pulse [163]. In this case, the key of the shutter is in the hand of the pulse itself that can open whenever arrives, no matter sooner or later than its expected arrival time. This authority is given by a saturable absorption key feature which indicates that the losses of the material used can adapt to the intensity of the incident light. Since in the pulse mode, the peak power is much larger than that for CW mode, the material opens the gate to the peak power to pass and attenuates the CW. Some materials such as organic dyes show this property but unfortunately they are very wavelength dependent, generally are in liquid form and must frequently be refreshed by flowing. The MIRA system [164] has resolved this problem by another approach using the combination of nonlinear Kerr lens effect inside the crystal, and slitting the light. With the Kerr lens effect, the beam diameter in mode-locked becomes smaller than that in CW state due to larger peak power. Therefore, using a slit (see Figure 4.1) the CW can be blocked while the mode locked pulse passes freely. Figure 4.2 shows how the Kerr lens effect makes Self-focusing inside Ti: Sapphire crystal. The refractive index of crystal varies spatially with the light intensity profile making a gradient index (GRIN) lens according to the following equation

$$n(I) = n_0 + n_1 \times I \quad (4.1)$$

where n and I are the optical refractive index and the light intensity respectively.

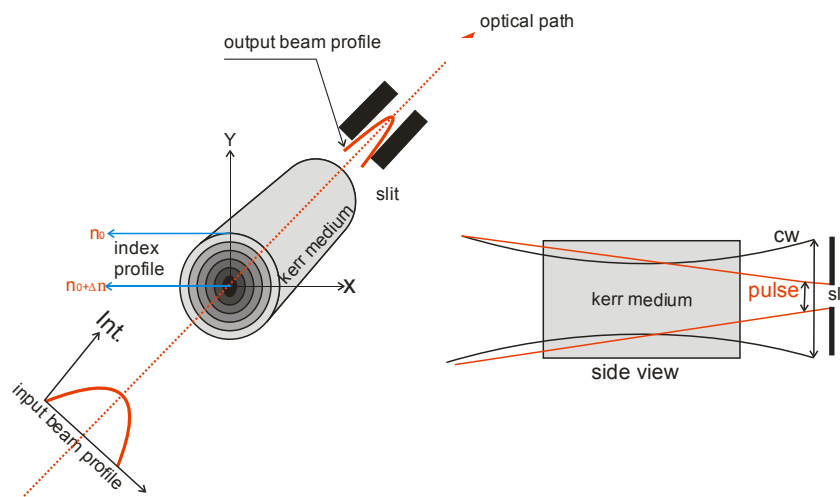


Figure 4.2 Nonlinear Kerr effect (Kerr lens) plus slit to form a mode locked ultra-short laser pulse.

Notably, Kerr lens is formed only at the center of beam profile inside the Ti: Sapphire crystal due to extreme intensity of the light.

4.2 Electrooptic effect and electrooptic crystals

Besides fsL, EO crystal which samples electric field is another key component in the EOS. Before demonstrating that how optical beam and electric field interact with each other in EO crystals, it is necessary to explain the electromagnetic waves propagation in anisotropic media [167], [168].

For an isotropic dielectric material exposed to an electromagnetic wave, $\vec{D} = \epsilon_0 \vec{E} + \vec{P}$ where \vec{P} is polarization vector defined by $\vec{P} = \epsilon_0 \chi \vec{E}$ and $\chi = \epsilon_r - 1$ is the electric susceptibility or equally $\vec{D} = \epsilon_0 \epsilon_r \vec{E}$. The permittivity ϵ in isotropic materials is a scalar; therefore \vec{D} and \vec{E} are parallel vectors. The refractive index $n = \sqrt{\epsilon}$ also remains constant and independent of the applied electric field. In contrast, some EO crystals are anisotropic and at optical frequencies show nonlinear polarization behavior. This property can be reflected as crystal birefringence, in which the refractive index by discriminating between polarization components let them travel with different velocities. Any birefringence crystal at least has one extra-ordinary mode in which the pair vectors (\vec{D} , \vec{E}) as well as wave vector \vec{K} and ray vector (pointing) \vec{S} are not parallel as shown in Figure 4.3. Based on the number of extraordinary axes, an EO crystal can be uniaxial or biaxial. The optical refraction index of an EO crystal can be expressed by an index ellipsoid determined by

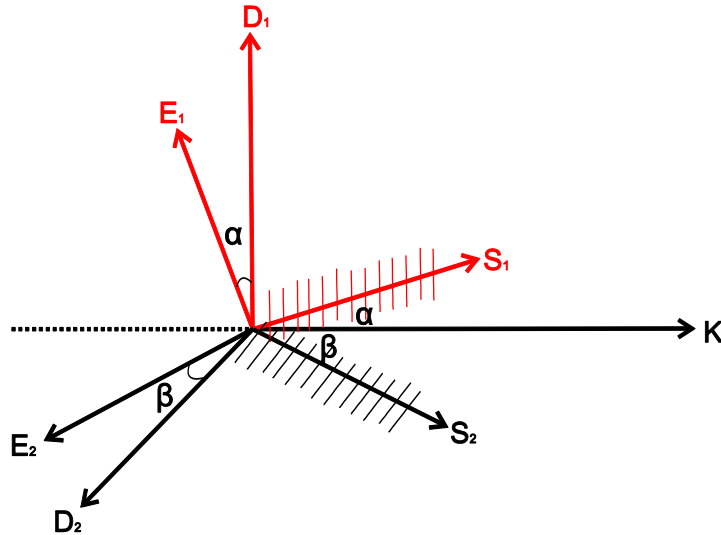


Figure 4.3 A biaxial EO crystal field and wave vector components. There are two extraordinary axes S_1 and S_2 . Figure adapted by author from [167].

$$\frac{x^2}{n_x^2} + \frac{y^2}{n_y^2} + \frac{z^2}{n_z^2} = 1 \quad (4.2)$$

where X, Y and Z are crystal principal axes. As shown in Figure 4.4, special cases of biaxial are isotropic, with no extraordinary axis ($n_x = n_y = n_z$), and uniaxial when having one extraordinary ($n_z = n_e$) and two ordinary $n_x = n_y = n_o$ axis. In an EO crystal both n_o and n_e vary with respect to applied external electric field according to

$$n(E) = n_0 + a_1 \cdot E + \frac{1}{2} a_2 E^2 + \dots \quad (4.3)$$

The second term of the right hand is known as the *Pockels effect* which is a linear variation of refractive index resulted from the second order nonlinear polarization vector of $\vec{P} = \epsilon_0(\chi_1 \vec{E} + \chi_2 \vec{E} \vec{E} + \dots)$ [167]. The Pockels effect is the basis of electrooptic sampling and modulation of the optical laser beam. The 3rd term in Eq. (4.3)

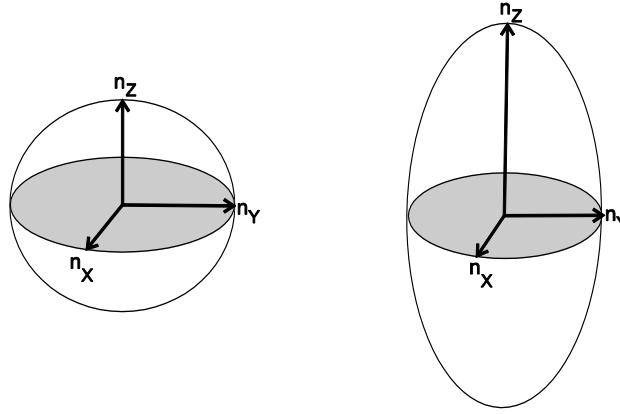


Figure 4.4 Index ellipsoid for (left) an isotropic material and (right) a uniaxial crystal

represents the nonlinear *Kerr effect* and higher orders are neglected. In particular the Kerr effect is applicable in optical mixing to up (down) convert and generate harmonics of optical wavelengths (frequencies) and self-focusing (Kerr lens) for generating femtosecond pulse that was already explained.

In case when X, Y and Z are not in the same direction of principal axes of the crystal, index ellipsoid can be expressed by

$$\frac{x^2}{n_1^2} + \frac{y^2}{n_2^2} + \frac{z^2}{n_3^2} + 2 \frac{yz}{n_4^2} + 2 \frac{xz}{n_5^2} + 2 \frac{xy}{n_6^2} = 1 \quad (4.4)$$

where $n_1 = X$, $n_2 = Y$ and $n_3 = Z$ are principal axes. Assuming the applying an external electric field of $\vec{E} = E_x \vec{x} + E_y \vec{y} + E_z \vec{z}$ to the crystal, the Pockels effect adds up the differential terms of

$$\begin{pmatrix} \Delta\left(\frac{1}{n^2}\right)_1 \\ \Delta\left(\frac{1}{n^2}\right)_2 \\ \Delta\left(\frac{1}{n^2}\right)_3 \\ \Delta\left(\frac{1}{n^2}\right)_4 \\ \Delta\left(\frac{1}{n^2}\right)_5 \\ \Delta\left(\frac{1}{n^2}\right)_6 \end{pmatrix} = \begin{pmatrix} r_{11} & r_{12} & r_{13} \\ r_{21} & r_{22} & r_{13} \\ r_{31} & r_{32} & r_{33} \\ r_{41} & r_{42} & r_{43} \\ r_{51} & r_{52} & r_{53} \\ r_{61} & r_{62} & r_{63} \end{pmatrix} \begin{pmatrix} E_x \\ E_y \\ E_z \end{pmatrix} \quad (4.5)$$

to the unbiased refractive index, where r_{ij} [pm/V] are EO coefficients of a 6×3 matrix which is a simplified form of EO tensor due to zero symmetrical elements. To better understanding the EO effect, it is better to illustrate an example for the case of LiTaO₃ crystal. To this end, Figure 4.5 shows an X-cut LiTaO₃ which is a $3m^1$ uniaxial crystal and its differential refractive index is expressed by

$$\begin{pmatrix} \Delta\left(\frac{1}{n_1}\right)^2 \\ \Delta\left(\frac{1}{n_2}\right)^2 \\ \Delta\left(\frac{1}{n_3}\right)^2 \\ \Delta\left(\frac{1}{n_4}\right)^2 \\ \Delta\left(\frac{1}{n_5}\right)^2 \\ \Delta\left(\frac{1}{n_6}\right)^2 \end{pmatrix} = \begin{pmatrix} 0 & -r_{22} & r_{13} \\ 0 & r_{22} & r_{13} \\ 0 & 0 & r_{33} \\ 0 & r_{51} & 0 \\ r_{51} & 0 & 0 \\ -r_{22} & 0 & 0 \end{pmatrix} \begin{pmatrix} E_x \\ E_y \\ E_z \end{pmatrix} \quad (4.6)$$

where $n_1 = n_2 = n_o = 2.176$ are ordinary, $n_3 = n_e = 2.180$ is extraordinary axis and initial values $n_4 = n_5 = n_6 = 0$, while EO coefficients are $r_{13} = r_{23} = 7.5, r_{33} = 33.0, r_{51} = 20.0$ and $r_{22} = 1.0$, all in [pm/V] [169], [170]. By applying an external electric field in the Z direction, therefore $E_x = E_y = 0$ whereas $E_z \neq 0$, and finally the index ellipsoid in Eq. (4.4) yields

$$\left(\frac{1}{n_o^2} + r_{13}E_z\right)x^2 + \left(\frac{1}{n_o^2} + r_{13}E_z\right)y^2 + \left(\frac{1}{n_e^2} + r_{33}E_z\right)z^2 = 1 \quad (4.7)$$

The deviation of refractive indexes including $\Delta(1/n_o)^2 = r_{13}E_z$ and $\Delta(1/n_e)^2 = r_{33}E_z$ is very small in comparison with their initial values and according to the approximation of $\Delta n = -\left(\frac{n^3}{2}\right) \cdot \Delta\left(\frac{1}{n}\right)^2$ the new refractive indexes yields

$$n_{o1} \approx \left(n_o - \frac{1}{2}n_o^3 r_{13}E_z\right) \text{ and } n_{e1} \approx \left(n_e - \frac{1}{2}r_{33}E_z\right) \quad (4.8)$$

In a real condition, if an optical beam with polarization in the XZ plane (see Figure 4.5), expressed by $E_{in} = E_0 e^{i\omega t} (\vec{x} + \vec{z})$ travels through the crystal in the Y direction, the phase of the X and Z field components changes according to

¹ Crystal symmetry axis

$$\vec{E} = E_0 e^{i(\omega t - k_x y)} \vec{x} + E_0 e^{i(\omega t - k_z y)} \vec{z} \quad (4.9)$$

where $k_x = \frac{2\pi n_x}{\lambda}$ and $k_z = \frac{2\pi n_z}{\lambda}$ are wave numbers for the ordinary and extraordinary axis respectively (see the ellipsoid in Figure 4.5). The difference in the X and Z components velocities, determines an elliptical polarization state for the output optical beam and at the output of the crystal (Y= L), where L is the crystal length, differential phase retardation can be expressed by $\Gamma = (k_x - k_z)l$, and finally

$$\begin{aligned} \Gamma &= \frac{2\pi l (n_x(E_z) - n_z(E_z))}{\lambda} \\ &= \frac{2\pi l}{\lambda} \left[\left(n_0 - \frac{1}{2} n_o^3 r_{13} E_z \right) - \left(n_e - \frac{1}{2} n_e^3 r_{33} E_z \right) \right] \\ &= \frac{2\pi l}{\lambda} \left[(n_0 - n_e) - \frac{1}{2} (n_e^3 r_{33} - n_o^3 r_{13}) E_z \right] \\ &= \Gamma_0 + \Delta\Gamma \end{aligned} \quad (4.10)$$

where Γ_0 shows the crystal background (intrinsic) birefringence and $\Delta\Gamma$ represents differential *retardation* due to the applied electric field. This property is used as the basis of EOS.

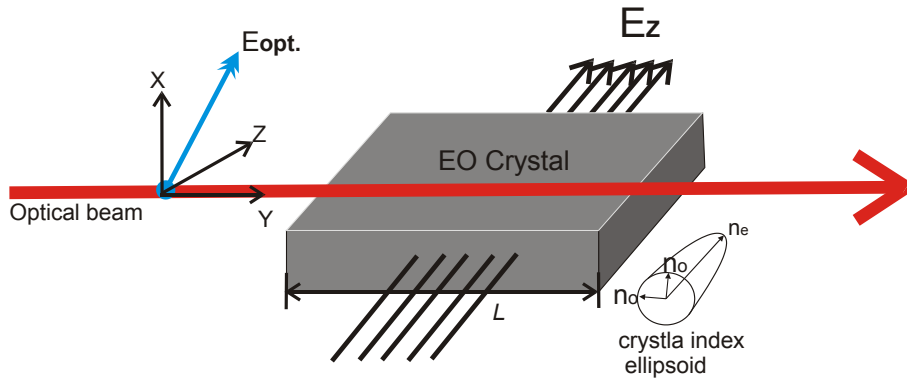


Figure 4.5 Schematic of an X-Cut LiTaO₃ crystal and its EO modulation. X and Y are ordinary axes and Z is extraordinary.

4.2.1 Linearity of electrooptic

The electric field induced modulation and demodulation of an optical beam is the basis of EOS and therefore, a linear response to the electric field is mandatory. Based on the Pockels effect, in an EO crystal, the electric field can modulate an optical beam in three different ways including: amplitude modulation (AM), phase modulation (PM) and polarization state modulation (PSM). Due to having a simple mechanism of detection, PSM or in other words, intensity modulation is preferred [171]. This is schematically shown in Figure 4.6. The input polarizer ($\lambda/2$ plate) is required to rotate the input laser beam polarization and align it with the angle θ to the crystal index ellipsoid axis. Immediately after the half wavelength plate, there are two orthogonal polarization components aligned in the direction of n_e and n_o of the crystal. By

passing the optical beam through the crystal, these two components have a phase difference according to (4.10). Also, the optical intensities at the crystal input and

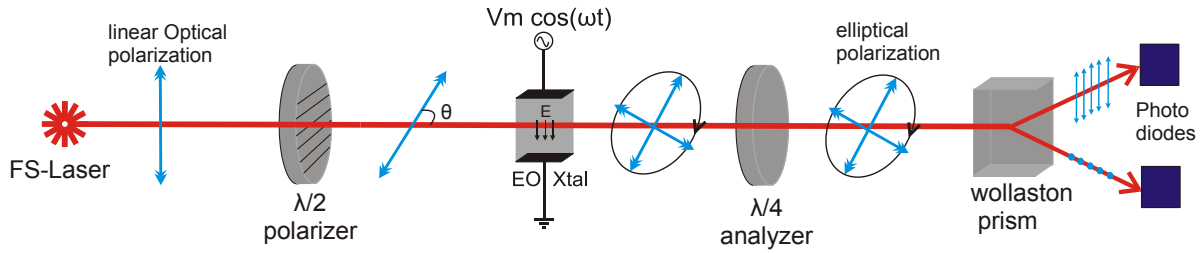


Figure 4.6 The mechanism of EO intensity modulation and detection

output are given by

$$I_{in} \propto |E_x(0)|^2 + |E_z(0)|^2 = 2|E_0|^2 \tag{4.11}$$

$$I_{out} \propto |E_x(l)|^2 + |E_z(l)|^2 = 2|E_0|^2 \sin^2 \frac{\Gamma}{2}$$

yields a transmission factor of $\frac{I_{out}}{I_{in}} = \sin^2 \frac{\Gamma}{2}$ which is plotted in Figure 4.7. To have a linear approximation of the function, a phase bias at the operating point $\Gamma_0 = \frac{\pi}{2}$ is needed which can be realized either by applying a voltage (electric field) bias or optical bias using a $\lambda/4$ plate as the latter is shown in Figure 4.6. The orthogonal polarization components of the modulated laser beam which contain the information of interest can be separated by a Wollaston prism and hence, be detected by a pair of balanced photodiodes. The photodiodes are configured in a differential way which reduces the laser amplitude noise and at the same time gives 3 dB of gain [15].

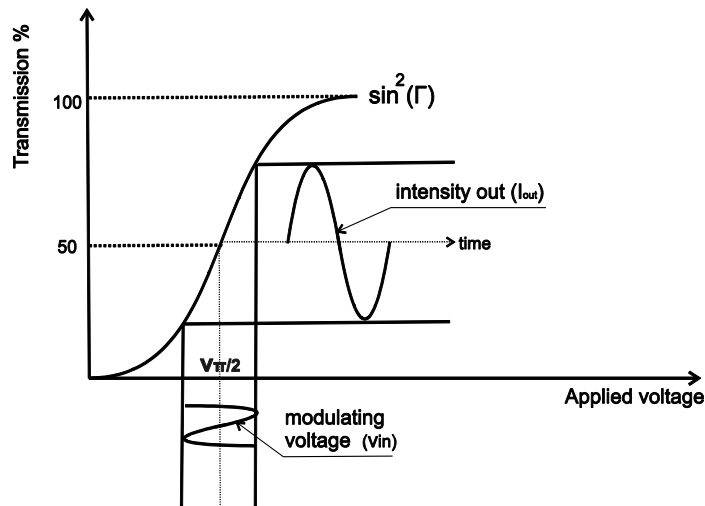


Figure 4.7 Transmission functions of the intensity modulator used in EOS. To have linearity the optimum operating point is biasing at 50% transmission. Figure adapted by author from [170].

Assuming the applied modulating electric field given by $E_z = E_m \sin \omega_m t$, according to Eq. (4.10),

$$\Gamma = \Gamma_0 + \Delta\Gamma = \frac{\pi}{2} + \Gamma_m \sin \omega_m t$$

while

$$(4.12)$$

$$\Gamma_m = -\frac{1}{2}(n_e^3 r_{33} - n_o^3 r_{13})E_m$$

and for small values of $\Gamma_m \ll 1$, the transmission factor yields

$$\frac{I_{out}}{I_{in}} = \sin^2 \frac{\Gamma}{2} \approx \frac{1}{2}[1 + \Gamma_m \sin \omega_m t]$$

$$(4.13)$$

which indicates that the *intensity* of the laser is *linearly* proportional to the applied electric field.

4.2.2 Crystal selection for EOS sampling of mm- wave and THz devices

For EOS, depending on the application one can use an EO crystal such as ZnTe, LiTaO₃, LiNbO₃, Ga As, GaP, KD*P and KTP. By choosing a crystal and depending on its orientation, X, Y or Z components of the electric field vector can be detected. For example, LiTaO₃ and LiNbO₃ are sensitive to the tangential field components (E_x and E_y in Figure 4.8) while BSO [154] is sensitive to the normal component (E_z). Therefore, to measure all components, it is necessary to use either two different crystals as shown in Figure 4.8 or rotate the probe to an orientation which can sense the desired field component. The latter solution needs significant changes in the arrangement of

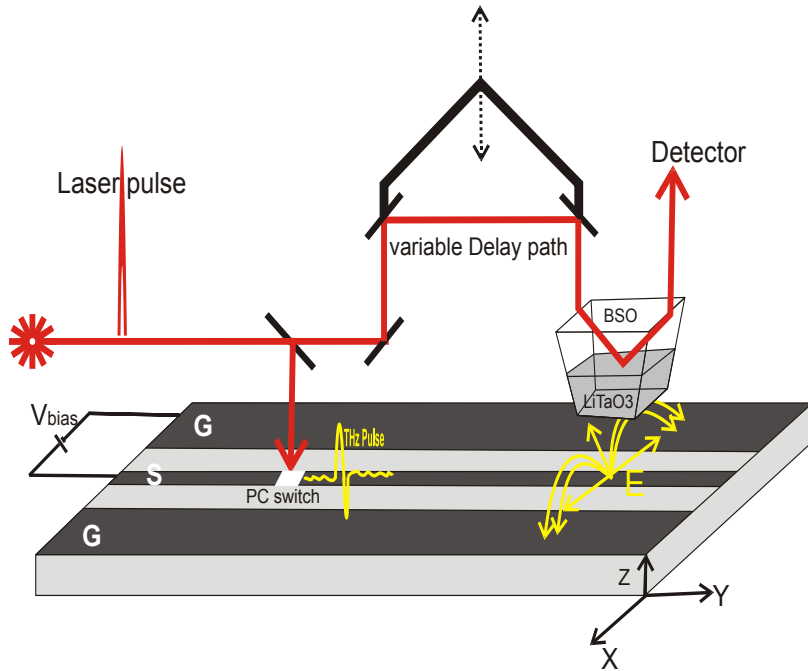


Figure 4.8 Schematic diagram of an EOS setup for near field sensing of ultrafast devices. The EO probe with two crystals is used to detect tangential component of electric field E_x by LiTaO₃ and normal component of E_z by BSO.

experimental EOS setup and detecting all field components with a same setup van be very time-consuming.

In our setup, it has been targeted to characterize ultrafast devices which are usually CPW based circuits (see Figure 4.8). Since CPW slot width (the distance between signal and ground lines) is very small¹ for our DUTs, the tangential x-component of the electric field has a very high intensity. Moreover, this electric field component can be precisely calibrated as we have the CPW slot width and its applied voltage. At the same time, the EO crystal firstly needs to be transparent at our optical wavelength (800 nm). Secondly, it should have a large electrooptic coefficient and thirdly, be very less invasive to the electric field of DUTs. Based on these considerations, finding a crystal which fulfills all our requirement seems to be impossible or at least difficult. With this regards, LiTaO₃ is a well-qualified crystal for all of the above requirements except the invasiveness. Also, it has a high mechanical stability, high temperature tolerance and a high phonon resonances at 6.3 THz [172] which is far beyond our operation frequencies. Therefore, a compromise was made to use this crystal in the setup.

Electrooptic Probe Invasiveness on DUTs

LiTaO₃ probe can invade DUTs by perturbing of their near field. The reason is the high permittivity ($\epsilon_r= 41-43$) [173] of the material which capacitively loads DUTs. If one insists on selecting LiTaO₃, he/she should choose a probe with a small footprint in comparison to DUTs. This helps to maximally reduce the probe invasiveness. In our measurement setup, size of DUTs are on the order of tens of micrometer and therefore, a probe with the size of focused laser spot ($\approx 10 \mu\text{m}$ diameter) can be an

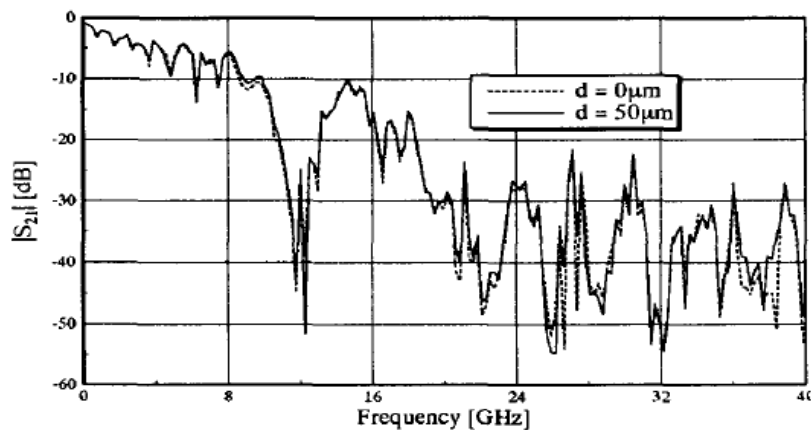


Figure 4.9 Network analyzer measured S -parameters of a circuit invaded by an external EO probe as a function of probe distance to the circuit. The behavior of the circuit almost remains unchanged over the measured frequencies showing negligible invasion of the probe on the DUT. A reason for that is very small footprint of the LiTaO₃ crystal. Reproduced with permission from [160].

¹ Tens of micrometer

optimum choice. Due to extreme difficulties in cutting and handling the material such small footprint is hard to be feasible. On the other hand, the thicker the probe gives larger the signal and therefore, it is required to come to a tradeoff between the probe invasiveness and sensitivity.

A number of researchers have tried to formulate the LiTaO₃ invasiveness in different ways. For example, in [160] the comparative results of network analyzer S-parameters measurement and direct¹ EOS measurements in the presence of an external LiTaO₃ probe over a microwave circuit was demonstrated as shown in Figure 4.9. This experiment shows almost no influence on the *overall* performance of the circuits i.e., shift in the resonance or the characteristic impedance of the device. However, local field perturbation is unavoidable. About 10% of invasiveness was also addressed by Frankel et al. [174]. Nevertheless, this cannot be extrapolated to other cases if one does not consider the comparative size of DUTs and probes. The work in [159] with direct EOS, has demonstrated an optimum low invasive distance for the external probes from DUT. However, their results might be influenced by the Fabry-Pérot etalon resonance [175] of an established cavity consisting of the lower facet of the probe and surface of DUT. Despite the above suggestions, it is necessary to emphasize that finding a formulation for invasiveness of probe is not trivial and results of one study necessarily cannot be used to another investigation as it is a case study which strongly depends on the size of probes, the geometry of DUTs and the frequency of operation.

Organic and Polymer Electrooptic Crystals

Some recent work such as [176]–[178] have focused on the organic electrooptic materials to reduce the probe invasiveness. An example is ionic salt crystal (DAST) which has a large electrooptic coefficient and at the same time very low permittivity. Despite this advantages, unfortunately, this material shows large nonlinearity and static birefringence [179]. Moreover, it can be dissolved in water content and needs a full control of humidity around the setup [172]. Also, the EO Polymers reported in [180]–[183] are good candidates for noninvasive broadband detection [172] due to having a low relative permittivity (ϵ_r between 2-4) and no vibrational phonon resonance. Unfortunately, there are also other drawbacks for these kinds of EO materials. For instance, they may need to be poled to remove their centro-symmetry. Furthermore, suppression of the cross polarization to make them sensitive to only one field component and degradation with response to the temperature [172], [182] might also be a big challenge of using them. For comparison, several common crystals are listed in Table 4.1.

¹ Direct and indirect EOS were described in previous chapter

Table 4.1 A comparison between few EO polymers and inorganic crystals commonly used as EOS probe materials. Source from [172]

Material	Wavelength λ (nm)	Refractive index $n(\text{optical})$	Electrooptic coefficient r_{ij} (pm/V)	$n^3 \times r_{ij}$	ϵ_r	Figure of merit $(n^3 \times r_{ij})/\epsilon_r$
LiTaO ₃	633	2.180	33	340	43	7.9
BSO	633	2.54	5.0	82	56	1.5
GaAs	900	3.60	1.1	51	13.2	3.9
PBLG	800	1.58	1.5	6.0	2.13	2.8
LD3	800	1.577	13.2	52	2.6	20

Phase matching considerations

In THz detection, the mismatch between the optical and THz beam velocities inside the EO crystal can degrade signal detection. Therefore, in order to increase SNR, constructive overlap between the optical and THz wave is necessary. A factor which

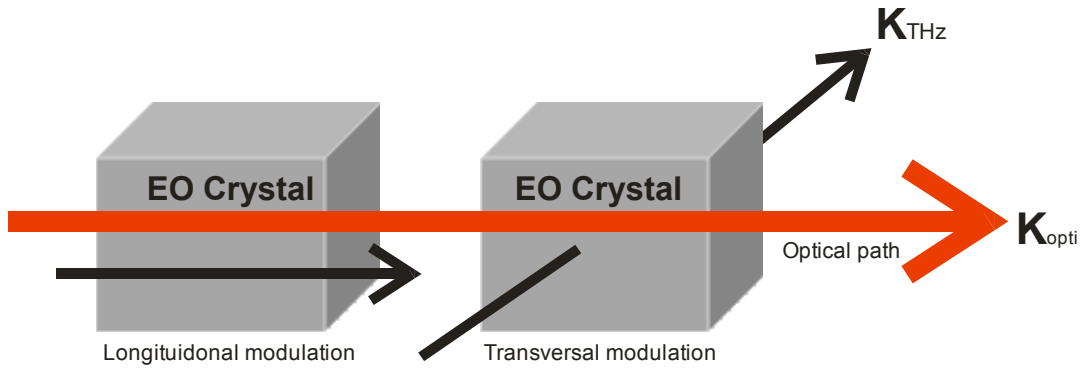


Figure 4.10 Depending on the application of an EO crystal; it can modulate both longitudinal and transversal electric field. LiTaO₃ is commonly used for transversal detection and ZnTe is proper for longitudinal.

determines this mismatch is defined by the *coherent length*, which is a length that the phase difference between the optical *group* velocity and the THz wave *phase velocity* yields $\pi/2$. The coherent length is mathematically given by

$$l_c(\omega_{THz}) = \frac{\pi c}{\omega_{THz} |n_{opt-eff}(\omega_o) - n_{THz}(\omega_{THz})|} \tag{4.14}$$

where

$$n_{opt-eff} = n_{optic}(\omega_o) - \lambda_{opt} \left| \frac{\partial n_{opt}}{\partial \lambda} \right| \lambda_{opt}$$

where c is the velocity of light in free space, n is the refractive index, ω_0 is the optical and ω_{THz} is THz frequency respectively. This parameter can strongly limit the detection bandwidth of THz waves. From Eq. (4.10), apparently, larger the length of the crystal linearly increases the phase retardation and the detected signal, but prior to that the coherent length which is frequency dependent already restricts this enhancement.

To achieve the largest possible bandwidth, the crystal thickness should be carefully adapted to the coherent length. From Eq. (4.14), at 1 THz, the coherent length is calculated as 50 μm for LiTaO₃ and 1 mm for ZnTe. At the first glance, this result may convince us to use ZnTe instead of LiTaO₃, but it should be noticed that the coherent length is defined only for the longitudinal and not the transversal mode of EO detection (see Figure 4.10) which is a case in our EOS setup. Therefore, fortunately, the issue of the coherence length does not play a significant role. Even if one considers the coherent length, our typical 25-50 μm thick crystal still fulfills our required bandwidth.

Crystal figure of merit

As already mentioned, a crystal with a larger EO coefficient for higher sensitivity, and with a low permittivity for low invasiveness is favorable. Based on this criterion, a figure of merit (FOM) was defined for few common crystals as summarized in Table 4.1. It shows that LiTaO₃ is the best choice in inorganic crystals in this regard. It should be mentioned that the sensitivity of 340 in this table is only valid for the PM method of detection in which only one polarization component is used, but for the PSM which is usually used in EOS, having two polarization components degrades this factor to 262 as reported in [184].

It can be argued that the situation even becomes worse if one refers to the exact retardation formulas for the sensitivity of Δn in Table 4.2. It shows that its

Table 4.2 A comparison between most typical EO inorganic crystals commonly used in EOS. Source from [169], [172], [184].

Xtal	Symmetry	λ (nm)	Ref. index (optical)	Electrooptic coeff. (r_{ij}) [pm/V]	Sensitivity Δn	ϵ_r	FOM [172] ($n^3 \times r_{ij}$)/ ϵ_r	Detection mode	Coupling factor (T) from air
LiTaO ₃	3m	633	$n_e=2.180$, $n_o=2.180$	$r_{33}=33$, $r_{13}=7.5$	$\frac{1}{2}(n_e^3 r_{33} - n_o^3 r_{13})$ $= \frac{262}{2} = 131$	43	3.0	Transver- sal	26%
GaAs	$\bar{4}3m$	900	$n=3.60$	$r_{41}=1.1$	$\frac{1}{2}(n^3 r_{41} + n^3 r_{41}) = 51$	13	3.9	Longitud- inal or Transve- sal	43%
ZnTe	$\bar{4}3m$	633	$n=2.99$	$r_{41}=4.3$	$\frac{1}{2}(n^3 r_{41} + n^3 r_{41}) = 115$	10	11.5	usually longitud- inal	48%

sensitivity decreases by a factor of 2 and reaches to 131. Nevertheless, it still remains on the top of the table for its high sensitivity. Unfortunately, due to the high

permittivity and hence, less coupling factor¹ of LiTaO₃, it degrades based on the defined figure of merit and ZnTe dominates. For more understanding of this issue a short selection guide for commonly used EO crystals is summarized in Table 4.2.

Crystal electromagnetic coupling efficiency

Another important factor in selecting of an EO crystal is the electromagnetic coupling factor. It is defined by the transparency of the material for THz waves. The reflection of the incoming THz wave at the material-air boundary hampers its detection by the crystal. The transmission (T) and reflection (\mathcal{R}) for the electric field of a THz wave from medium 1 to medium 2 (see Figure 4.11) at their interface are given by

where n_i is the refractive index of the medium i at THz frequencies. Apparently, the

$$\mathcal{R} = \left| \frac{n_1 - n_2}{n_1 + n_2} \right|, T = 1 - \mathcal{R} = \left| \frac{2n_1}{n_1 + n_2} \right| \quad (4.15)$$

higher the permittivity ($n_2 \gg n_1$) of the crystal, the less the electromagnetic coupling we have. The coupling from air ($n_1 = 1$) to some well-known crystals are listed in Table 4.2 which shows that LiTaO₃ is the worst candidate in this regard. Since Eq.(4.15) is known for a plane wave at far field, one may argue about its validity for the case of near field, but the finite element simulation using Ansys® HFSS of a real structure including our DUT and a crystal with dimensions of 1000×1000×50 μm^3 which is placed 5 μm above the DUT (see Figure 4.12), roughly confirms our estimation. The calculated tangential electric field inside a 50 μm thick crystal shows an *average* coupling factor of 15% for LiTaO₃ and 39% for ZnTe in comparison to 100% of free space (see Figure 4.13).

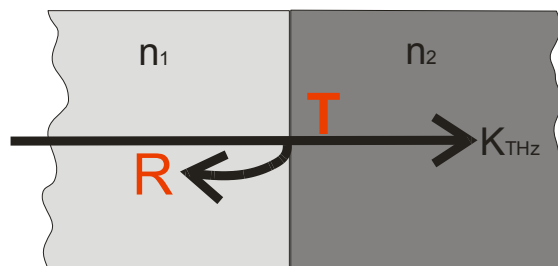


Figure 4.11 Reflection of THz waves and the electromagnetic coupling between two mediums.

¹ Coupling factor is explained in next sub-section.

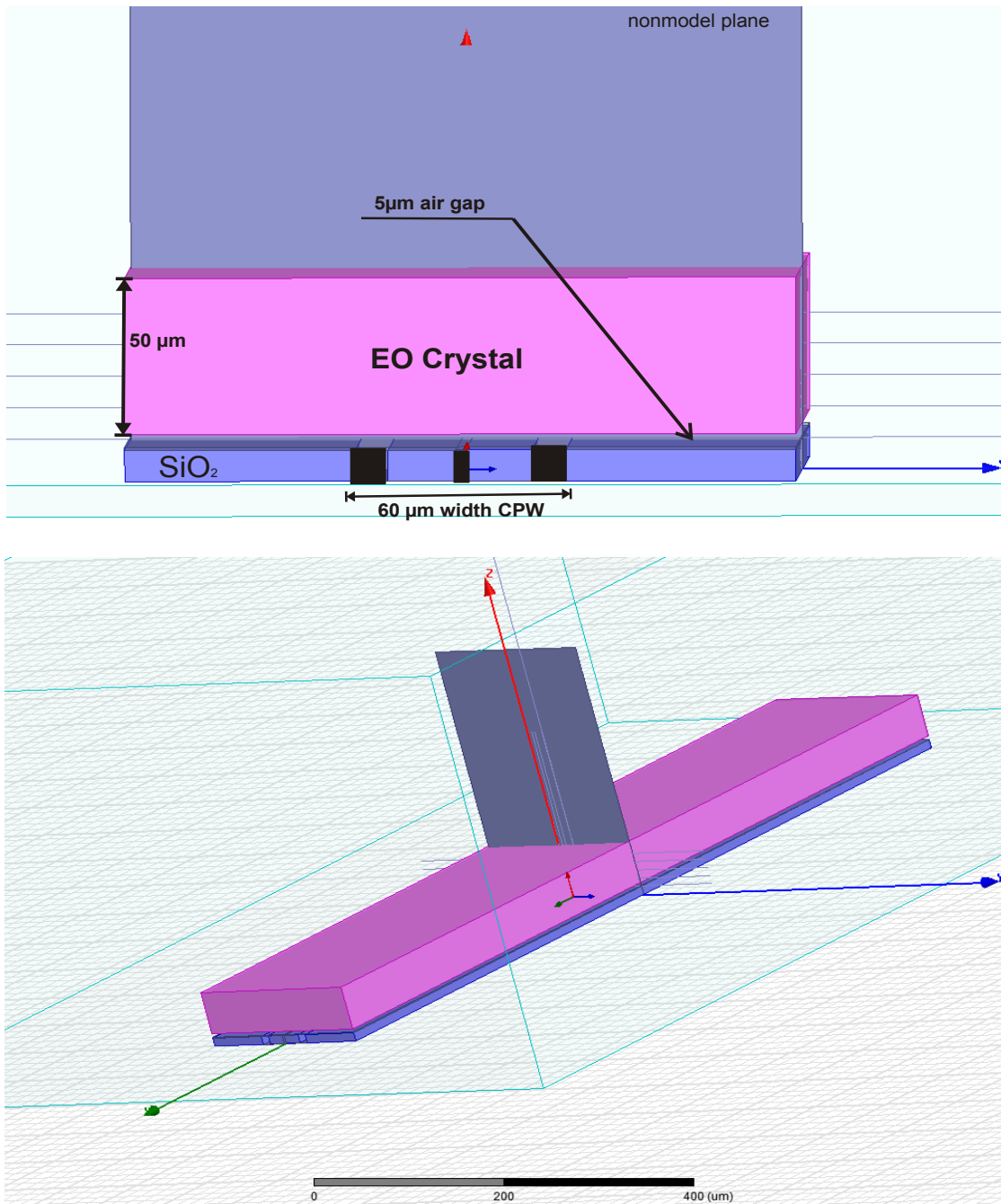


Figure 4.12 DUT structure in the presence of a 50µm thick EO crystal. (Top) side view and (bottom) overall view

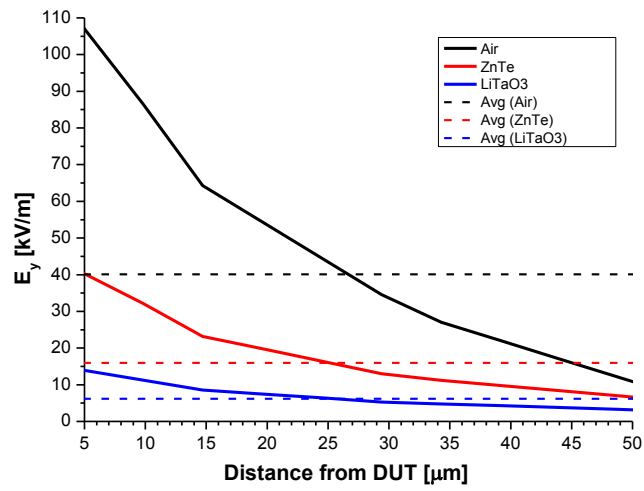


Figure 4.13 The simulated tangential electric field as a function of vertical distance from the CPW structure @ 200 GHz in air, ZnTe, and LiTaO₃.

5. Electrooptic Setup

To carry out the ultra-broadband characterization of the electronic circuits, an EOS system with the following features was built up:

- Ultra-wideband measurement bandwidth, potentially from DC to THz, based on electrooptic sampling with a femtosecond laser source.
- Contactless EO probing for internal chip characterization without the need for having dedicated contact pads or ports.
- Freely positionable probe to allow near field mapping of DUTs.

The setup was first equipped with an optical fiber pigtailed EO crystal, but after facing challenges that are explained later in this chapter, it was reconfigured to a so-called non-pigtailed approach. In the following section, the probe and setup, as well as their functionalities are demonstrated.

5.1 Schematic diagram of the setup

As shown in Figure 5.1 a femtosecond laser beam is divided into two beams with a beam splitter. One beam is used as a probe beam and another as a synchronization

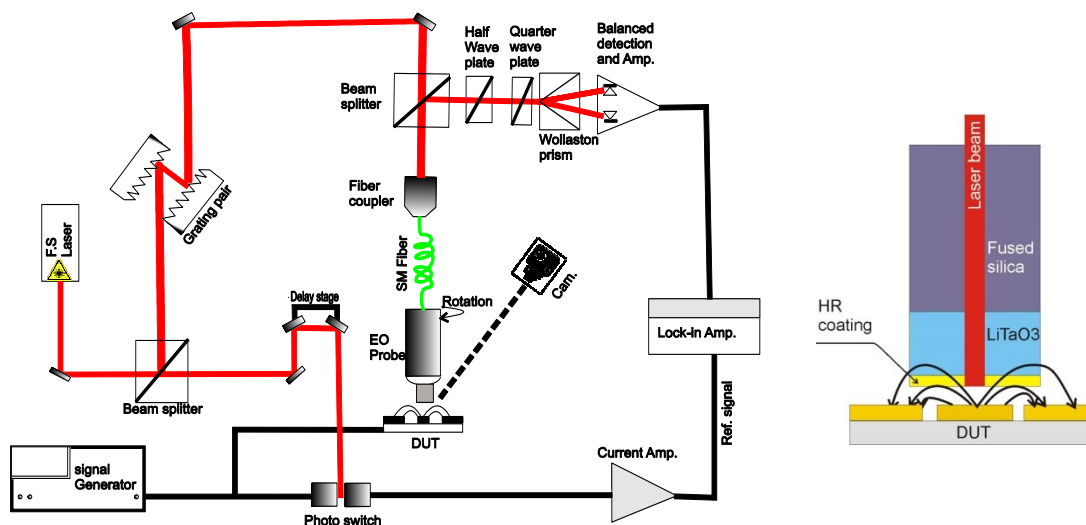


Figure 5.1 Schematic diagram of the EOS setup (left) and detail of the EO probe tip (right)

beam for heterodyne detection. Obviously, synchronization of a heterodyne system is very critical, therefore, in EOS, the laser as sampler should be synchronized with the sampled signal of DUTs. Since the laser is an optical system and DUT is driven by a microwave generator, hence, a component for conversion of the optical to an electric signal is required. This can be achieved using a PC Auston switch which is specifically designed to operate at microwave frequencies. The PC switch plays the role of a harmonic mixer that mixes the microwave frequency with the higher harmonics of the laser repetition rate. Assuming the laser repetition frequency of f_l (typically 75 MHz) and f_m as the microwave frequency, the output frequency of photo switch mixer is $\Delta f = f_m - n \times f_l$, where n is the laser harmonic number (see Figure 5.1). This offset frequency Δf can easily be adjusted in the range of kHz or MHz and used as external trigger signal for the lock-in amplifier. This offset frequency can be stabilized at a reference frequency f_r (usually between 10 kHz to 100 kHz) (not shown in Figure 5.1)¹ from an external signal generator using a PLL system. While the laser is synchronized to the microwave generator, the probe beam samples the signal of DUT with an electrooptic crystal based on the Pockels effect which was explained in the previous chapter. The reflected laser beam from a highly reflective (HR) coating at the bottom facet of the LiTaO₃ crystal (see Figure 5.1 -right) which is modulated by the electric field of DUT is then separated from the incident beam by another beam splitter. This beam hence, by passing through a $\lambda/4$ plate and a Wollaston prism is prepared for the intensity detection with the aid of electronics including a pair of balanced photodiodes, a low noise current amplifier and either a lock-in amplifier or a data acquisition. The delay stage provides a time delay between the sampling laser beam and the sampled signal. The grating pair in the setup is used for dispersion compensation of the fiber-based EO probe which is explained later in this chapter. To understand the system characteristics in the following sections, key components of the setup are described in detail.

5.1.1 The pigtailed electrooptic probe

The most crucial component of the system is the EO probe, consisting of a fiber coupled LiTaO₃ crystal [150], [152] which samples the electric field from DUTs. The amplitude and phase of the DUT electric field can thereby be detected from the modulation of the optical polarization state of the reflected laser beam. As mentioned in the previous chapter, LiTaO₃ is advantageous over other crystals and its application has frequently been addressed [113], [115], [133]. Nevertheless, it is not the best choice due to its high invasiveness². The crystal has a 50 μm (25 μm) thickness and is placed on a 0.9 mm \times 0.9 mm fused silica support. This combination, hence, is glued to a GRIN lens which is pigtailed with a 780-HP Nufern [185] fiber. This allows an efficient optical coupling and focus of the probe laser beam at a diameter less than 10 μm at the probe tip. The pigtailed optical fiber, shown in

¹ See MM-LS in Chapter 7 for detail.

² See Chapter 4.

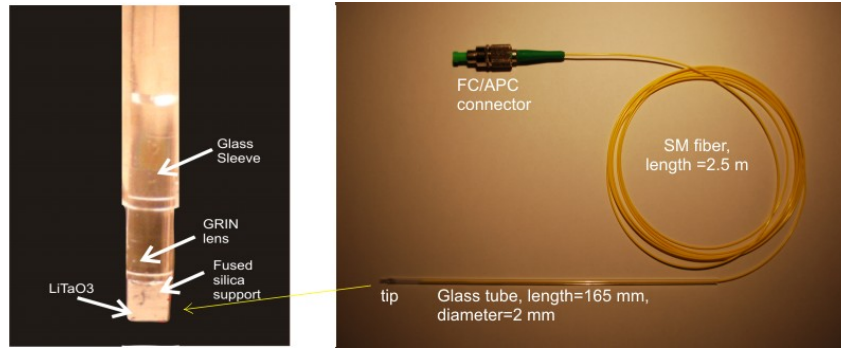


Figure 5.2 The fiber pigtailed EO probe with 50 μm thick crystal and the detail of the tip.

Figure 5.2, provides flexible maneuver and positioning of the probe in the setup. Since passing the femtosecond laser pulse through this fiber faces dispersion, a dispersion compensation unit consisting of a grating pair is integrated with the setup. This combination provides a laser pulse width < 200 fs at the probe tip where the THz signal is detected and theoretically ensures a detection bandwidth up to 5 THz ($\sim 1/200$ fs). For comparison, without this compensation, a 2.5 m length fiber would deliver broader than 5 ps laser pulses, which theoretically limits the system bandwidth to frequencies below 200 GHz.

5.1.2 The photoconductive switch

A typical Auston [95] PC switch is made of a semiconductor substrate (or a photoconductive thin film on a substrate), on which metallic electrodes are deposited in a form of a 50Ω microstrip line. By illumination of laser beam on the gap between two electrodes of microstrip transmission line, the semiconductor absorbs photons and generates an enormous number of electron and hole pairs. The number of generated carriers, evidently, depends on the semiconductor material quantum efficiency and the laser beam power. As long as these charge carriers are alive, the switch is turning on and conducting (low resistance state), otherwise it remains in off-state (high resistance). Using this mechanism, the harmonics of the laser

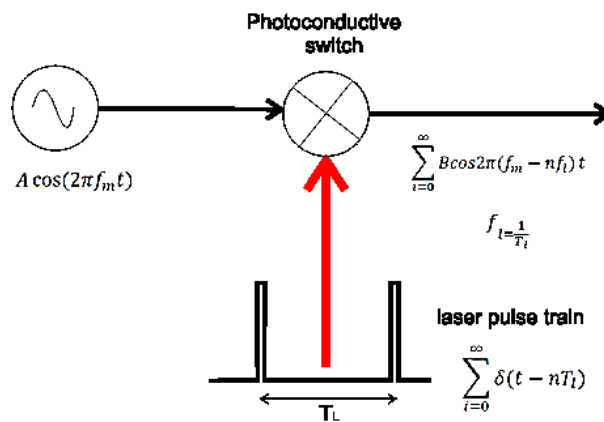


Figure 5.3 Harmonic mixing of a microwave signal and laser pulse.

repetition rate can mix with a microwave signal which is fed to the switch as shown in Figure 5.3. As the switch has to efficiently work at the microwave (6-20 GHz) frequencies, high frequency considerations must be taken into account. For this reason, the switch operation in *off* and *on* states needs to be characterized.

The current density of the switch in both *on* and *off* cases can be described by

$$\mathbf{j} = \mathbf{j}_c + \mathbf{j}_d \quad (5.1)$$

where,

$$\mathbf{j}_c = \sigma \cdot \mathbf{E} \quad \text{and} \quad \mathbf{j}_d = \frac{\partial \mathbf{D}}{\partial t} = -j\omega\epsilon\mathbf{E} \quad (5.2)$$

are conduction and displacement current densities respectively. Also, for n and p carriers the conductivity is

$$\sigma = \sigma_n + \sigma_p = q\mu_n n + q\mu_p p \quad (5.3)$$

where μ is the mobility and q is the electron charge quanta. In *off*-state, \mathbf{j}_d is dominated because of the capacitive coupling and by illuminating the switch (on-state), the conduction current rapidly increases due to existing of the carriers, and this state lasts until carriers recombine. A detailed balance of photoconductive switch dimensions and the carrier lifetime (i.e. material choice) is needed to deliver a high efficiency and a good on/off ratio. In our design, intrinsic GaAs with a carrier lifetime of the order of 10^{-9} to 10^{-8} s was used. This is sufficiently short, in comparison to the

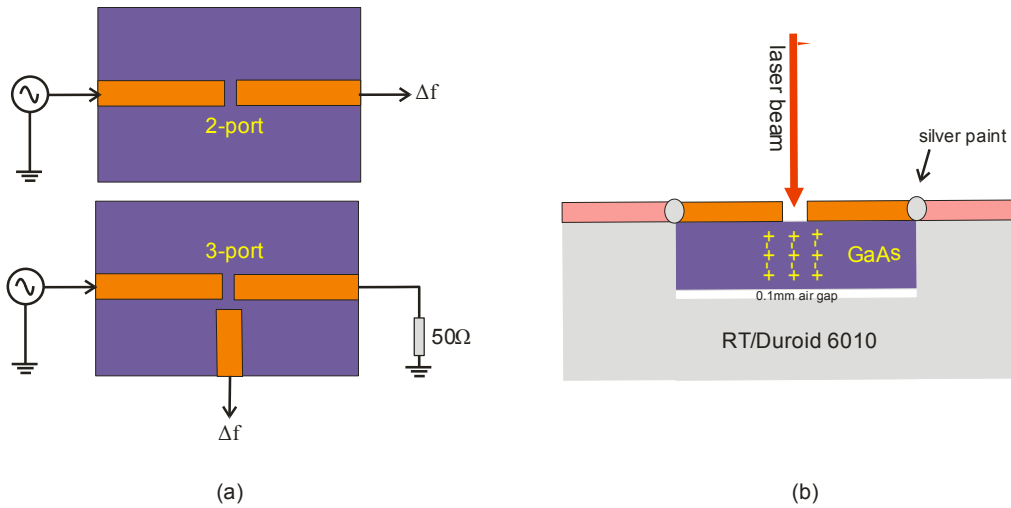


Figure 5.4 The photoconductive switch using intrinsic GaAs ($\epsilon_r=10.9$) substrate and deposited by a gold layer with thickness of 250nm 50Ω transmission line. (a) Two port and three port configuration, (b) the cross section of the switch which is embedded in RT/Duroid 6010 ($\epsilon_r=10.2$, $h=1.29$ mm) substrate.

laser repetition period¹ 1.3×10^{-8} and long compared with the microwave signal period 1.67×10^{-10} ($f = 6$ GHz). At first sight, it seems that, with this characteristic, the switch is not fast enough, however, in reality, the carrier lifetime is shorter than that for the theoretical values due to metal to semiconductor transitions and surface recombination.

The dimensions of the photoconductive switch are chosen to maximize the photoconductive switch efficiency. Assuming driving the photoconductive switch with 0 dBm microwave signal power, for a gap length of $g = 50 \mu\text{m}$, an average electron transit time of the order of $\tau_{tn} \approx \frac{g}{\mu \cdot E} = 2.9 \times 10^{-9}$ is estimated [170].

In theory, the response of switch to the femtosecond pulse is exponential with decay equal to the total carrier lifetime (i.e., the average for the material). The switch mixes the femtosecond pulse with microwave signal (V_{RF}) and hence, the output signal yields $V_{IF} = V_{RF} \times g(t)$, where $g(t)$ is the time gating function in response to the femtosecond laser pulse. A worst case scenario can be calculated using a recombination carrier lifetime of $\tau_n = 10^{-8}$ s close to the period of the laser $T_L = 1.33 \times 10^{-8}$ s, but two order of magnitude longer than the microwave signal period. Even with this long decay time, the short rise time $g(t)$ enables sampling of the microwave signal resulting in a kHz range beat frequency (see Figure 5.3). Evidently, for sampling higher frequencies, e.g. at mm-wave, it is therefore, crucial to design an appropriate switch with a high presence of surface and doping induced bulk recombination sites to reduce the effective carrier lifetime [186]. As discussed in Chapter 3, Lt-GaAs carrier lifetimes is down to few hundreds of fs [98]. However, this drastically can decrease the photoconductive switch efficiency due to much smaller mobility.

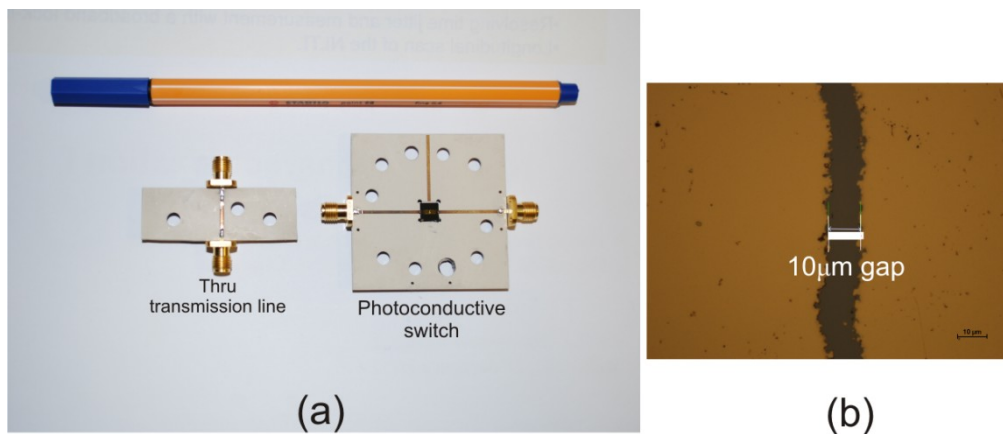


Figure 5.5 (a) Fabricated photoconductive switch mounted on substrate plus a test 50Ω transmission line, (b) a micrograph of a $10 \mu\text{m}$ -gap of the switch. The gap is simple and not interdigitated.

¹ Repetition frequency of the laser $f = 76$ MHz

Our photoconductive switch was realized by deposition of a gold microstrip lines with $50\ \Omega$ characteristics impedance on a $6\times 6\ \text{mm}^2$ GaAs piece of wafer and hence with silver paint connected to $50\ \Omega$ line on a $5\ \text{cm}\times 5\ \text{cm}$ RT/Duroid 6010 ($\epsilon_r=10.2$, $h=1.27\ \text{mm}$) substrate. This combination allows mounting the switch on standard optical mounts in the setup. Figure 5.4 shows the design strategies and cross section of the embedded photoconductive switch. A thin layer (0.1 mm) of air between GaAs and RT/Duroid 6010, as surface roughness, has been taken into account for impedance calculations of the microstrip line. Several configurations of switches with different gap lengths were fabricated, and only one sample is shown in Figure 5.5.

From the circuit model, in off-state, the switch acts as a series capacitance (for the gap) and two shunt capacitance from the metal edges to the back ground plane side of the microstrip line. The gap size plays a significantly important role in particular in off-state. The larger the gap, the less the coupling capacitance and hence, the larger isolation of the switch in off-state we have. In on-state, the switch acts like a conductor and the gap size, as well as the laser beam power intensity govern the amount of absorbed photons. The coupling in both states for different switches is given in Table 5.1. From these results, it can be seen that a 3-port $20\ \mu\text{m}$ gap switch has the highest isolation in off-state, but in on-state also it might have a low value of the coupling because of a mismatch caused by the loading of a stub on the 3rd port of the switch. The next highest insertion loss (4 dB) in off-state is given for $50\ \mu\text{m}$ gap, realized with a two-port switch.

A successful operation of PC switches could be demonstrated after several photoconductive switch optimization cycles. The quality and stability of the output

Table 5.1 Experimental results of different photo switches

Photo switch	High frequency test insertion loss (dB) (off-state)	High frequency test (on-state)	Low frequency test 10 kHz, 1 V p-p (off-state)	Low frequency test 10 kHz, 1Vp-p(on-state)
$50\ \Omega$ transmission line (RT/Duroid 6010 substrate)	0.5	NA	NA	NA
$5\ \mu\text{m}$ gap switch - 2 port	1,6	Harmonic unachievable or difficult to achieve	Current amplifier output less than 2 mV	Current amplifier output 8 Vp-p, (distorted waveform)
$20\ \mu\text{m}$ gap switch -2 port	2,4	NA	NA	NA
$20\ \mu\text{m}$ gap 3-port	9,5	NA	NA	NA
$50\ \mu\text{m}$ gap switch- 2-port	4,0	Clear difference signal	Current amplifier output less than 2 mV	Current amplifier output 20 Vp-p, saturated

Note: Gain of current amplifier is $10^5\ \text{V/I}$

signal (Δf) of the 50 μm gap two-port PC switch were measured using a spectrum analyzer and the result is shown in Figure 5.6. It can be seen that at $\Delta f = 30$ kHz the spectrum of the signal is narrow and approximately 60 dB above the noise level. The sideband level at the 2nd harmonic is a measure of the signal deviation from an ideal sine wave which is -35 dB lower than the peak value.

Figure 5.7 also shows the DC test of different switches vs. the bias voltage using Keithley® 4200 semiconductor characterization system. It reveals that the 50 μm -gap switch in on- state has almost 4 orders of magnitude gain at 1 V bias voltage and has the highest isolation in off-state.

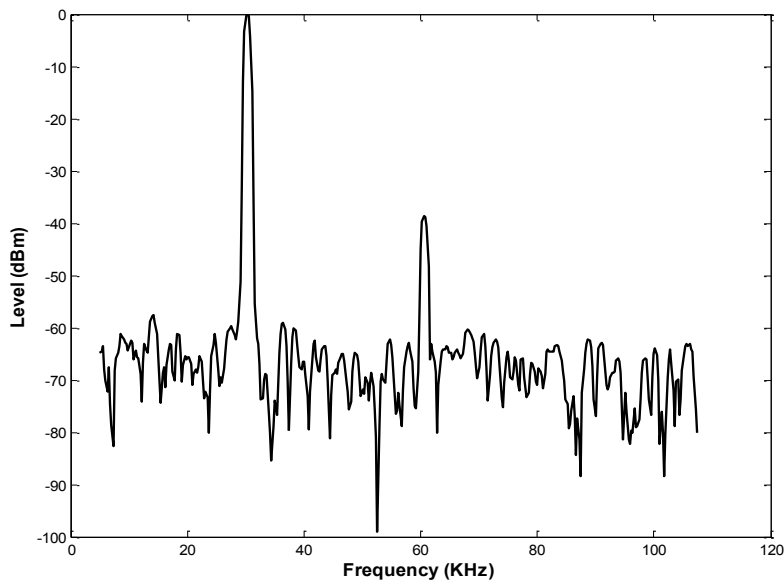


Figure 5.6 Spectrum of Δf achieved from mixing a 6 GHz signal with the laser pulses. The photoconductive mixing switch has 50 μm -gap.

5.1.3 Wafer probe station and the EOS setup mechanics

The EOS system was implemented with high precision motorized stages and a manual wafer probe station, in order to allow:

- The flexible and reproducible exchange of different DUTs with a vacuum chuck
- A rotary stage to change the orientation of dies on wafer depending on the position of microwave probe positioner which feeds the DUTs.
- A microwave probe station consisting of a Cascade Microtech® GSG (ground-signal-ground) probes and probe positioner for microwave feeding of circuits.
- A DC micro probe and probe positioner to bias the wafer (applicable when devices are driven by a built-in oscillators or biased transistors).

- Motorized XYZ stages with submicron resolution and traveling range of 20 cm to allow the on-wafer scanning of signals (mapping and precisely reproducible positioning on the circuit)
- Very high resolution objective and camera capable of distinguishing 3 μm size object at 3 cm of the working distance with a good field of view which enables

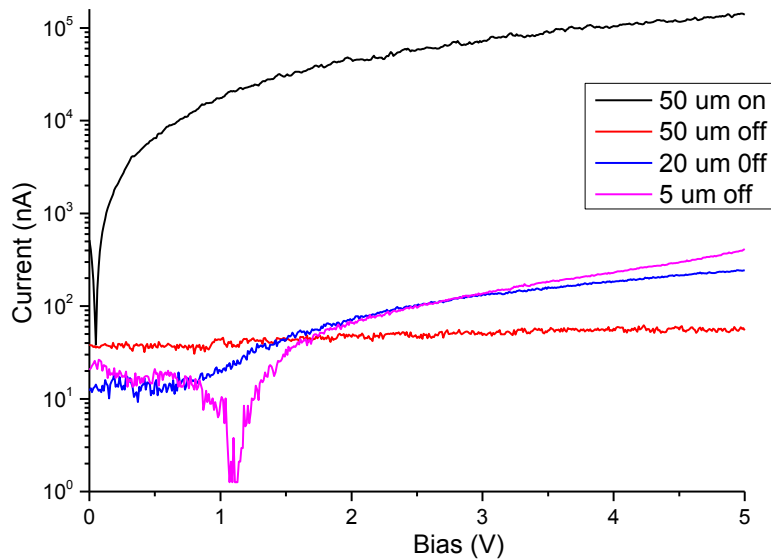


Figure 5.7 DC test of 5 μm , 20 μm , and 50 μm -gap 2-port switches in off-state and for a 50 μm -gap switch in on-state

zoom on small devices and precise positioning of microwave GSG and EO probe to contact DUTs.

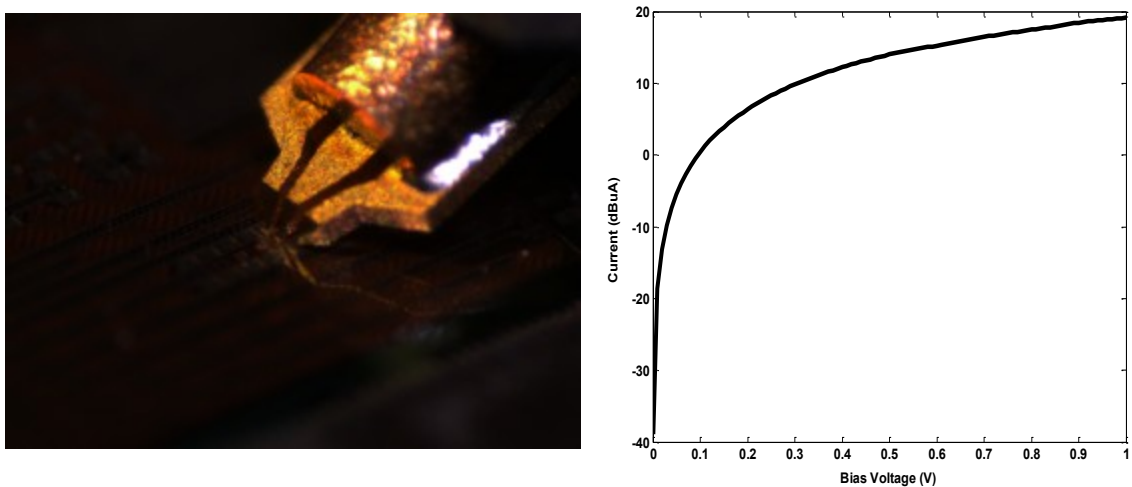


Figure 5.8 Touching 30 μm ×30 μm bonding pads with the microwave GSG probe and the resulted IV curve from the DC test of the contact.

5.1.4 Microwave probe

To feed the microwave signal to our DUTs, a microwave GSG probe is used. The probe is from Cascade Microtech® [78] with 75 μm pitch. The possibility of touching tiny ($30\ \mu\text{m} \times 30\ \mu\text{m}$) bonding pads with this probe was also examined using the Keithley 4200 series semiconductor characterization system. This was performed by applying 1 V DC bias to the device and limiting the current to 100 μA . Figure 5.8 shows a view of the probe tip in contact with a DUT and the demonstrated result of this test. The incremental response of the current to voltage ensures a successful contact to the small bonding pads.

5.1.5 Grating pair for optical fiber dispersion compensation

As mentioned earlier in this chapter, the EO probe is pigtailed with an optical fiber. The fiber dispersion can broaden the femtosecond laser pulse and hence, its

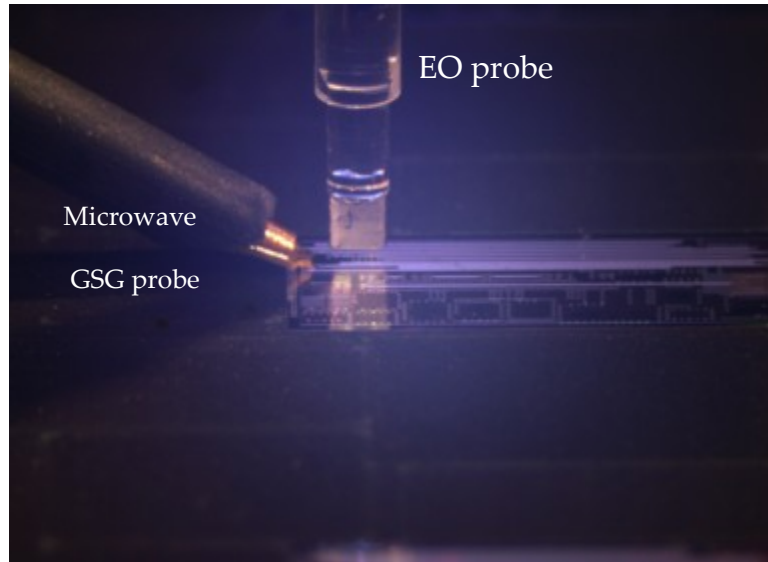


Figure 5.9 A close up view of the EO probe over the wafer

compensation is necessary. According to Sellmeier equations, refractive index of an optical material such as optical fiber can be expressed [187] by

$$n^2(\lambda) - 1 = \lambda \left(\frac{A_1}{\lambda^2 - B_1^2} + \frac{A_2}{\lambda^2 - B_2^2} + \frac{A_3}{\lambda^2 - B_3^2} \right) \quad (5.4)$$

where $A_i, B_i, i=1, 2, 3$ are constants and λ is the optical wavelength. The second order of the phase function $\varphi(\omega)$ derivative, which contains most dispersion of the fiber, is given by

$$\frac{\partial^2 \varphi_F}{\partial \omega^2} = \frac{\lambda^3}{2\pi c^2} \frac{\partial^2 n}{\partial \lambda^2} l = \varphi''_F l \quad (5.5)$$

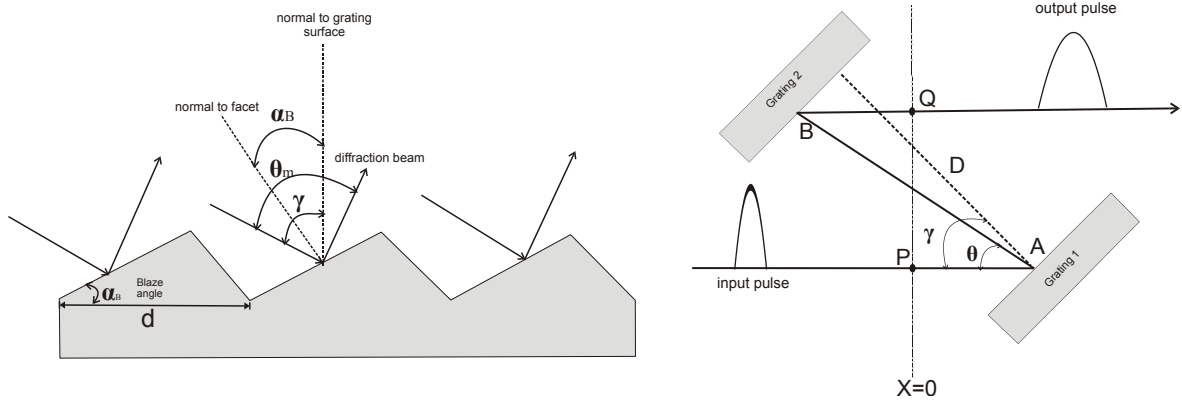


Figure 5.10. Grating for dispersion compensation. (left) principle of operation and (right) mechanism of dispersion compensation. Figure adapted by author from [187].

where L is the length of the optical fiber and ϕ_F'' is its group velocity dispersion (GVD) per unit length. Higher order dispersion components, in this case, are not considered as they are rather small and cannot be compensated by a grating pair, but with a pair of prisms. For a normal dispersive material like glass, GVD is positive and can be equalized or at least minimized with a negative dispersion value from the grating pair. The compensation can be achieved by tuning the distance between a grating pair which is mounted immediately before a fiber coupler in the setup (see the schematic of Figure 5.1), which provides coupling of the optical beam from free space to the fiber. The grating compensation dispersion can be calculated from grating equations, and the beam path geometry shown in Figure 5.10. For a diffraction grating

$$d[\sin(\gamma) + \sin(\theta - \gamma)] = m\lambda \quad (5.6)$$

where γ is the incident angle with respect to the normal direction to the grating surface, θ is the angle between the incident and the *refracted* beam and m is an integer indicating the refraction order [187], [188]. From the geometry

$$p = \overline{PABQ} = c \frac{\partial \varphi_2}{\partial \omega} = d \frac{1 + \cos(\theta)}{\cos(\gamma - \theta)} \quad (5.7)$$

and using

$$\frac{\partial^2 \varphi_G}{\partial \omega^2} = \left(-\frac{1}{2} \frac{m^2 \lambda^3}{\pi c^2 d^2} \left[1 - \left(\frac{m\lambda}{d} - \sin(\gamma) \right)^2 \right]^{-\frac{3}{2}} \right) \times D = \phi_G'' D \quad (5.8)$$

where ϕ_G'' is the grating GVD and D is the distance between the pair. The final cost function of the system which must be minimized is $\phi_{total}'' = \phi_F'' l + \phi_G'' D$ [187]. The Nufern® fiber has GVD of $\phi_F'' = 40.8 \text{ fs}^2/\text{mm}$, and for length of fiber $L = 2.5 \text{ m}$, the grating parameters of $m = 1$, $d = 833.33 \text{ nm}$ (1200 groove/mm), $\lambda = 800 \text{ nm}$ and $\gamma = 26^\circ$

the $\phi''_G = 1303 \text{ fs}^2/\text{mm}$. Accordingly, an optimum distance of $D = 7.8 \text{ cm}$ between the grating pair was calculated. The optical auto-correlator measured pulse at the end of fiber, where the probe is placed, was 150 fs and a deviation of 25 fs from the initial laser pulse width of 125 fs was observed and it is still much shorter than what we need.

5.2 Challenges using fiber-pigtailed probe

Using the pigtailed-probe in the setup, we may face with the following challenges.

5.2.1 Glass birefringence inside the fiber

A drawback using a pigtailed EO probe is the birefringence property of the glass (inside the fiber) which causes rotation of the laser beam polarization. Any change in the beam polarization state, caused by the strain or bending of the fiber, misaligns the optical polarization to the crystal axis and can degrade the detected signal or saturates the low noise amplifiers. Therefore, it must be compensated either by using a role of fiber as reported in [163] or rotating of incoming polarization by a $\lambda/2$ plate in a motorized or manual way.

5.2.2 Low Optical damage threshold

Another drawback of using a pigtailed-probe is the use of optical glue in the probe assembly as an adhesive for connecting fiber to the GRIN lens. This glue can be burned out by increasing the optical power more than 30 mW or even with a lower power in a longer exposure time. It was experienced that after a certain time, the sensitivity of the probe degrades due to the absorbing of the optical power in the glue. Finding this problem was not a trivial as the checking of the optical beam at the tip of the probe was not possible due to HR coating at the probe tip. Also, as degradation of the reflected beam from the probe tip caused by losing coupling into the fiber could mislead us to increase the input optical power which was harmful to

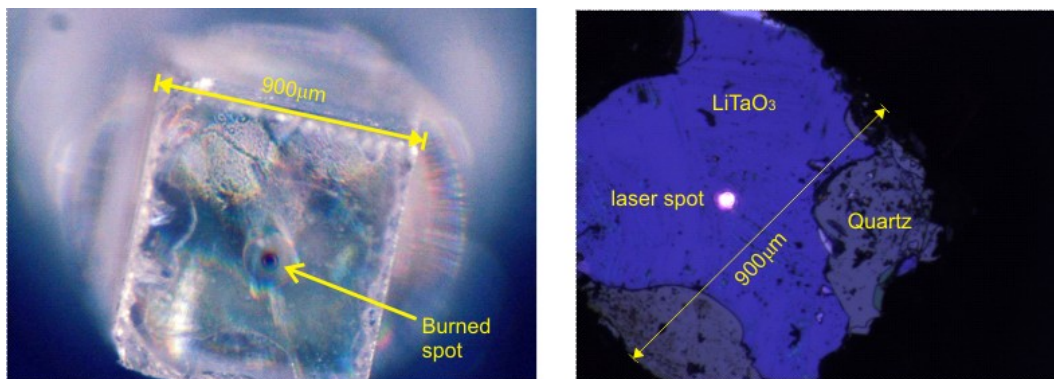


Figure 5.11 View of the EO probe from the bottom facet. (left) burned optical glue and blocking the laser beam and (right) an operational probe.

the probe. Evidently, Figure 5.11 shows the damage of the probe glue which was experienced in our setup by slightly increasing the power from the threshold (30 mw) to get a better reflected beam. The probe was killed; however, due to a large damage threshold of the LiTaO₃ crystal, fortunately, the probe was reusable. These drawbacks convinced us to use the EO crystal with another probe assembly, so-called non-pigtailed probe which is demonstrated in next section.

5.3 Modification of setup and using non-pigtailed probe

By the optical damage of the pigtailed-probe, the setup was modified to free space detection approach, and its schematic diagram is shown in Figure 5.12. In contrast to the previous approach, in this setup, a single mode polarization maintaining (PM) fiber is used which is not glued to the EO crystal. Similar to the pigtailed probe, this approach provides freely positioning laser beam for the XYZ stages which enables scanning of DUTs. The fiber has minimum dispersion at our laser 800 nm wavelength, and its PM property ensures stable polarization which is necessary for EOS. The beam from the fiber is coupled out with another fiber coupler, and the collimated beam again fully stabilized in polarization using a polarizer plate. This optical beam is given to a $\lambda/2$ plate to align beam polarization with respect to EO crystal probe orientation. With the aid of a spherical lens with the focal length of 25 mm, this beam is then focused to the upper facet of the GRIN lens. The GRIN lens

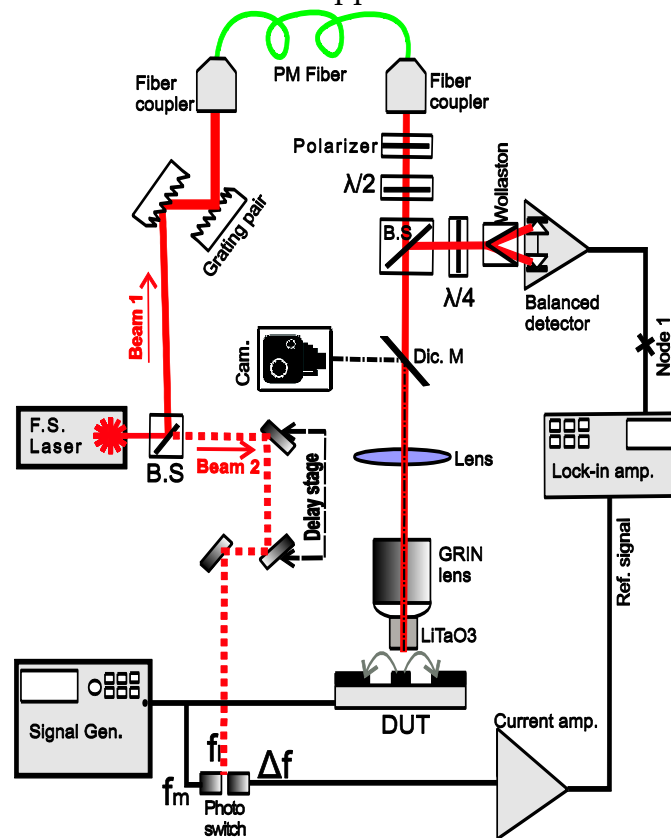


Figure 5.12 Schematic diagram of the free space setup. The fiber is just used to bring laser on the stages and not connected to the EO probe. Reproduced with permission from [189].

transfers a smaller laser spot image (5 μm diameter) from the upper facet to the lower facet, where the crystal is glued enabling high spatial resolution for scanning. The camera vision of wafer is provided via a dichroic mirror. A view of this setup is shown in Figure 5.13. This configuration of the probe assembly has resolved problems of the pigtailed-probe because it has:

- higher damage threshold as the fiber is not glued to the probe. This allows using much more laser power which can increase the SNR for the detection.
- stabilized beam polarization due to the use of PM fiber which ensures freely scanning of the wafer without concerning of the polarization misalignment.

Nevertheless, there are also minor disadvantages such as:

- more complexity of the setup and requirement of additional optical components to focus the laser beam in a diameter $< 10 \mu\text{m}$.
- the vision of the DUTs via a dichroic mirror which can make confusion with reflected images. However, this can be resolved by mounting the camera in oblique view with less visibility of the spot beam.

5.3.1 Non-pigtailed probe assembly

The new assembled probe similar to the pigtailed one consists of a LiTaO_3 crystal with dimensions of $900 \mu\text{m} \times 900 \mu\text{m} \times 50 \mu\text{m}$ mounted on a $500 \mu\text{m}$ -thick fused silica which is glued to a GRIN lens. The GRIN lens then is placed inside an Eppendorf, and all this combination is mounted on rotation stage (see Figure 5.13). Unlike the pigtailed-probe, in this case, fiber is not directly connected to the probe assembly as described shortly before (the description for Figure 5.12). The rest of the probe functionality is similar to the pigtailed one.

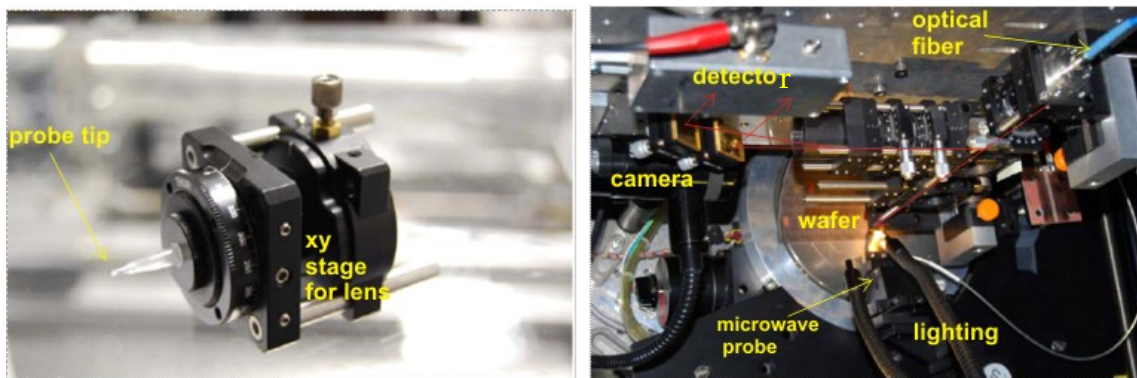


Figure 5.13 The assembled non-pigtailed probe (left) and a view of the setup (right). The red arrows show the optical path.

5.3.2 Examination of different crystals as probe tip

As discussed in Chapter 4, ZnTe is a crystal with theoretical minimum invasiveness for EOS. Its real functionality is compared with X and Z cut LiTaO₃. The Z-cut LiTaO₃ crystal has smaller electro optic coefficient than that for X-cut (1 vs. 20). The setup was first calibrated by a low frequency electric field measured on a 3 mm-gap slot line with the applied voltage of 150 V modulated by 15 kHz lock-in oscillator. In this

Table 5.2 EOS at kHz range frequencies with different crystals

Crystal	Crystal thickness (μm)	Detected signal (mV)	Equivalent detected signal for a 50 μm - thick crystal
LiTaO ₃ (x-cut)	50	65.1	65.1
LiTaO ₃ (z-cut), on 1mm fuses silica, HR coated on the bottom side	30	7.5	12.5
ZnTe <110> on 0.5mm fuses silica no coating	20	4	10

experiment, unlike LiTaO₃, the ZnTe crystal contains no high-reflective (HR) coating at the bottom facet; therefore, it is required to measure the signal at the reflecting metallic edges. The results are summarized in Table 5.2 which confirms that the X-cut LiTaO₃ is the most sensitive crystal and the good electromagnetic coupling for the ZnTe plays a minor role. This is a good affirmative experiment for the right selection of LiTaO₃ crystal in our experimental setup.

Table 5.3 Summary of setup synchronization mechanisms

All data @10 kHz mixing frequency	Software monitoring and control	Hardware (PLL)
Actuator Input	± 600 mV with a ratio of 150 Hz/mV	± 600 mV with a ratio of 150 Hz/mV
Accuracy	± 200 Hz	± 20 Hz
Measurement with Lockin-Amp.	Yes	Yes
Absolute Sync.-State	No, but overnight measurement possible as lock-in follows frequency	Yes, but still bound to asynch.

5.3.3 Synchronization of the setup

The setup was synchronized for long time measurements. The frequency drift of the Δf signal¹ in the range of few kHz during several hours was observed. This frequency drift is very slow which can be compensated in two different ways. One method is to use a soft controlled PLL system including monitoring of the frequency drift by a

¹ Resulted from the mixing of microwave signal and the laser pulse.

lock-in amplifier and synthesizing its proportional error signal by a Keithley® which is controlled by the LabVIEW software. This voltage is then given to the laser cavity mode-lock-starter-butterfly to follow-up the Δf deviations. This method is only applicable for the case of having *slow jitter*. Another method of synchronization is hard PLL controlling, by which much faster jitter can be compensated. In Table 5.3 a comparison of these two methods is reported.

5.3.4 Setup calibration

The probe detected signal was calibrated using a 3mm-gap slot line, and the measurement results are given in Table 5.4. The setup shows an excellent sensitivity of 1.3 V/m and a large dynamic range of more than 80 dB. The dynamic range can even be increased from the upper side to half voltage of the crystal but the detection is limited by the sensitivity on the lower side.

Table 5.4 Specification of the calibrated setup

Electric field	Detected EOS signal	Comments
115 kV/m	150 mV	Maximum observed signal
333 V/m	434 μ V	1 V applied on the slot line
1,3 V/m	1,7 μ V	Minimum detectable signal @ 1s integration

6. EOS Measurement of a 65-nm CMOS NLTL

In the previous chapter, the EOS setup featured with a very good sensitivity and a large dynamic range was demonstrated. Since the main objective of this work within the ULTRA project is to characterize an integrated fully electronic THz (mm-wave) transceiver based on NLTL, therefore, the devices output signal is subjected to broadband EOS measurements.

6.1 DUT

As shown in Chapter 2, NLTL is an interesting approach of generating millimeter and THz waves. It was also emphasized that these kinds of devices are difficult to be characterized with electronic instrumentation due to their ultra-broad band behavior. In contrary, they are very suitable for EOS measurements.

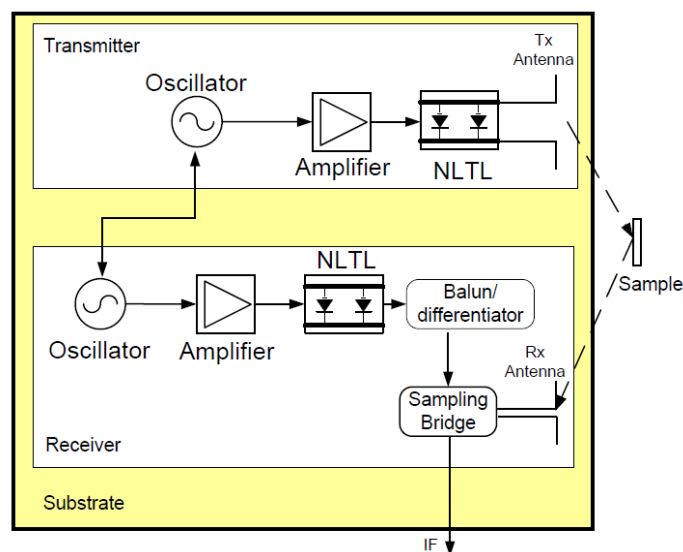


Figure 6.1. A diagram of Aleph THz transceiver for spectroscopy. Reproduced with permission from [46].

6.1.1 All-electronic CMOS NLTL based transceiver

In the framework of ULTRA project our partners from Philips® designed a 65-nm CMOS NLTL [46], [190] as a pilot for fully electronic generation and detection of the THz waves with the silicon technology. This module hence can be used in imaging

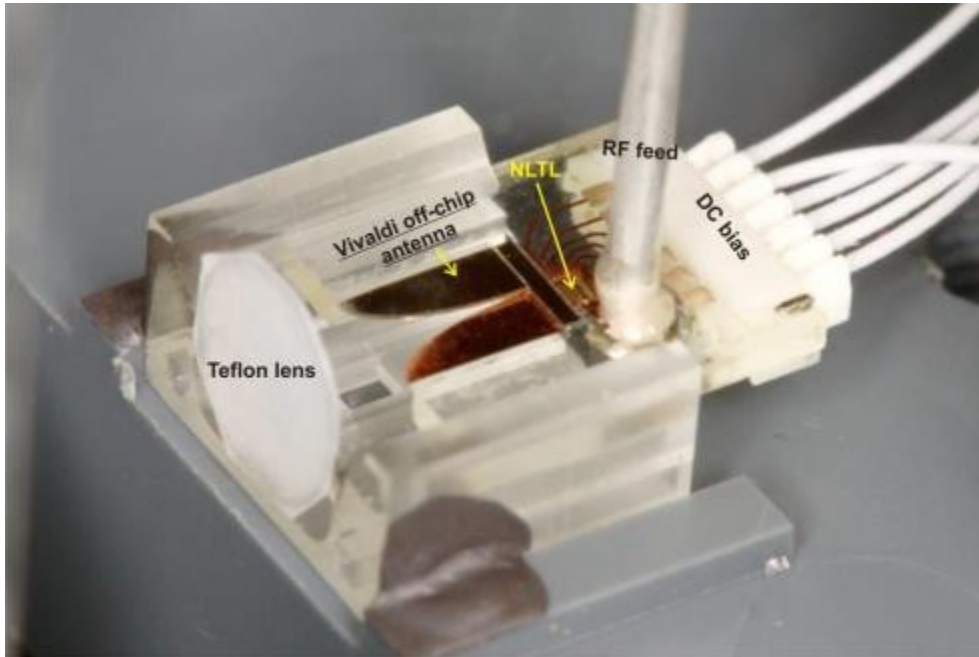


Figure 6.2 A close-up view of Aleph transmitter

and spectroscopy for material inspection and medical applications. A general block diagram of the system, as well as a close-up view of the transceiver module is shown in Figure 6.1 and Figure 6.2 respectively. In the transmitter, a microwave signal from an on-chip oscillator is first amplified and then compressed in the fall (rise) time by an NLTL. The extreme wide-band signal hence is emitted by a broadband antenna. In a reflection setup, if we put a sample in the path of this wave, some of the

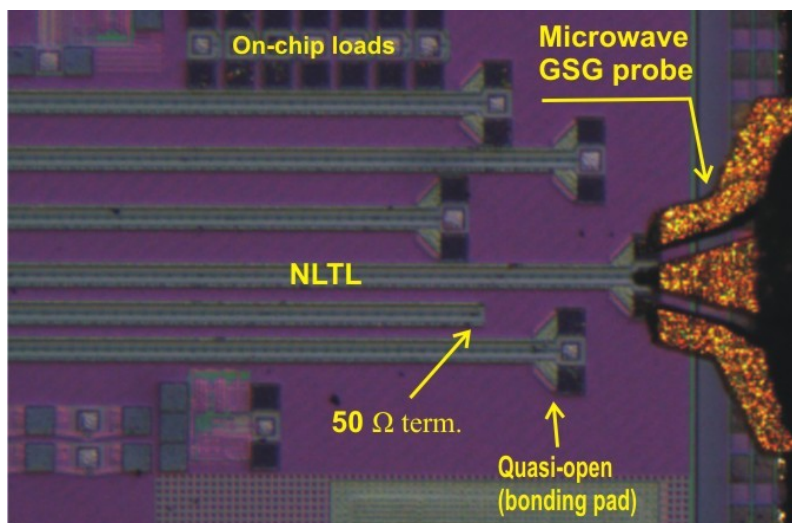


Figure 6.3 A micrograph of the die including NLTL and other devices

frequencies can be absorbed by the sample (due to resonances of its molecular structure) and the rest are reflected to the receiver antenna. To sample the signal, a superheterodyne mechanism is required; therefore, an integrated oscillator in the receiver generates a microwave signal with an offset frequency of Δf with respect to the transmitter oscillator. Similar to the transmitter, the receiver NLTL also generates a short pulse from this signal which is then used to drive a diode bridge for time gating of the received signal. The detected IF signal is later on processed by a DSP to figure out the finger print of the sample or material. A full operation and detail of the circuitry of the transceiver are beyond the scope of this work and the focus will be on the characterization of the NLTL as the broadband hart of the systems. Therefore, the NLTL design and performance is shortly demonstrated in the following sections.

6.1.2 The 65-nm CMOS NLTL

A micrograph of the chip is shown in Figure 6.3. It consists of different devices including NLTLs with open and $50\ \Omega$ load terminations as well as calibrating devices including on-chip load, short and open (LSO) terminations. A simplified layout of the NLTL is shown in Figure 6.4 which is a grounded CPW host structure with 190 periodic sections, each of which consists of a shunt CMOS varactor.

The structure was designed in Philips simulations were performed using *Cadence Spectre*[®]. Figure 6.5 shows the schematic diagram of this design. For simulation of these kinds of structures, there is a lack of existing single software¹ which can perform both the electromagnetic simulation as well as having a well verified library of components (such as CMOS varactors) at mm-wave and THz

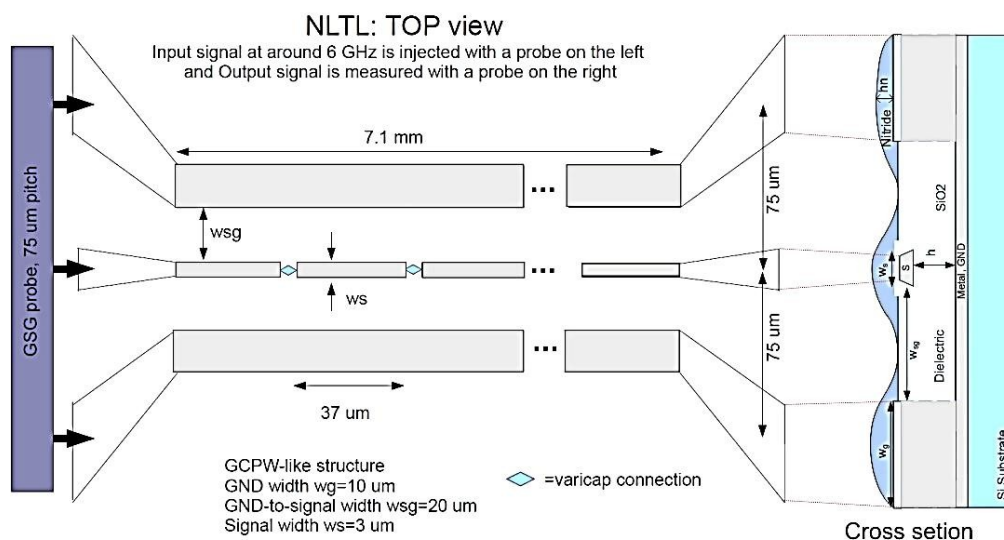


Figure 6.4 Top and cross section view of the NLTL lay out. The figure adapted by author from the ULTRA project internal reports.

¹ At the time of writing this dissertation.

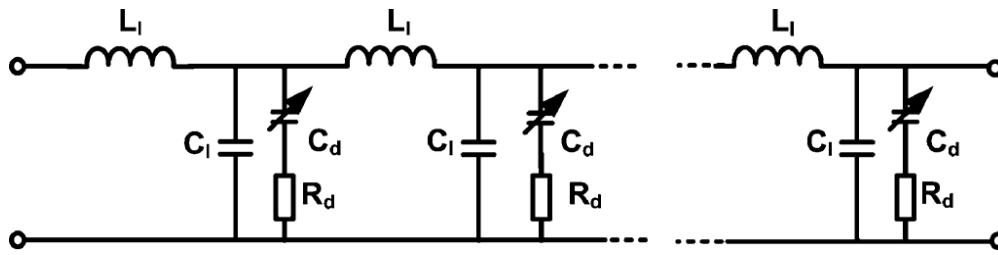


Figure 6.5. Schematic diagram of the NLTL periodic sections. Reproduced with permission from [190].

frequencies. Since the Cadence Spectre® is incapable of carrying out full-wave electromagnetic simulations for the transmission lines; therefore, the host CPW was simulated with IE3D® software and imported as a block into the Cadence Spectre®, and hence, combined with varactors to form an NLTL unit cell as shown in the schematic of Figure 6.5. The full schematic diagram of the design consists of 190 NLTL unit cells. The host passive CPW has a characteristic impedance of 82Ω , but the complete NLTL, by loading varactors, will show 50Ω and therefore, it is matched to a microwave signal generator impedance.

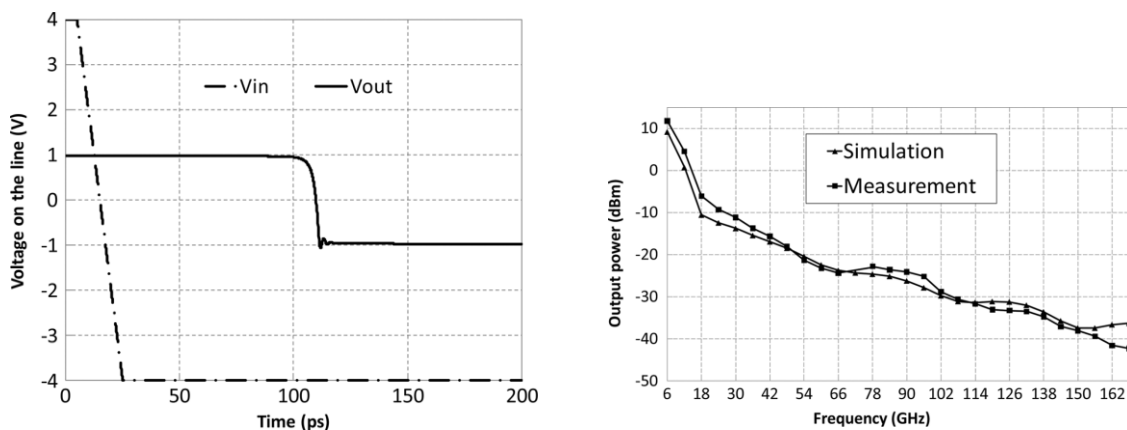


Figure 6.6. The NLTL simulation and microwave probing measurements results. The left side shows simulation in the time domain and how NLTL sharpens the fall time of the input signal. The input is a 6 GHz with 18 dBm of power signal. Reproduced with permission from [190].

The peak voltage of the generator before source impedance of 50Ω is set to 4 V; hence at the input of the line, after 50Ω impedance of the voltage source, the peak is 2 V. The input is a sine wave whose frequency can vary from 6 GHz to 10 GHz and even go higher. The inductance of varactors, due to its negligible effect was excluded from the simulations. Figure 6.6 show the time and frequency domain simulation results of the NLTL as well as microwave contact probing measurements. The microwave signal by passing through each NLTL section is getting sharper in the

fall time and forms a *quasi shock wave*¹, or in other words, generating harmonics. It is notable to mention that, reaching THz frequencies by CMOS is very optimistic and the lack of having precise models for the CMOS varactors at mm-wave and THz frequencies may lead us to inaccurate result.

6.2 EOS measurements

The NLTL was characterized by the EOS setup and the following measurements were performed.

6.2.1 Longitudinal scan

A 50 Ω terminated NLTL was fed by 18 dBm power of a microwave signal at 10 GHz, and the device output signal is measured. The IF² signal is set to 10 kHz therefore, up to 24th harmonic which is limited by the lock-in input frequency range (i.e. 240 kHz lock-in bandwidth) can be measured. The 24th harmonic or in other words, 240 kHz

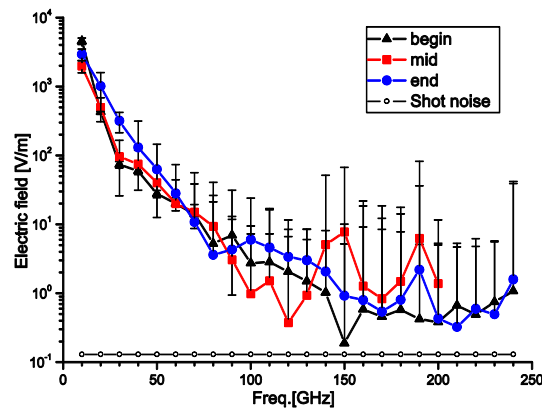


Figure 6.7 Measurement at the beginning, middle and end of a 7.1 mm long NLTL

signal at the lock-in is a true translation of 240 GHz from the DUT. One may select this IF at a lower frequency to enable scanning more harmonics with the lock-in, but the flicker noise from the laser, for the IF below 10 kHz, hampers this achievement. The result of this scan for the beginning, middle and end of the NLTL, as well as the shot noise level of the system are shown in Figure 6.7. The error bars in the graph reveal a large standard deviation or decrease of SNR by increasing the harmonic number (frequency). The highest field for the *first harmonic* is located at the beginning of the line (close to generator and microwave GSG probe) and by approaching the end, conversion of this power to higher harmonics can be seen. However, at some harmonics, the signal at the beginning of the line is stronger than that at the middle or end. With the observed large amount of deviation (error bars) the signal falls into

¹ See NLTL in Chapter 2.

² Δf from the photoconductive switch of the setup shown in Chapter 5.

the shot noise level. The shot noise for a balanced photo diode detector can be calculated from [191] given by

$$\sqrt{\frac{2\overline{\Delta I_{SN}^2}}{B}} = \sqrt{2 \times 2qI_0} A/\sqrt{Hz}$$

where $\overline{\Delta I_{SN}^2}$, B, q and I_0 are average RMS current of the shot noise, measurement bandwidth, elementary charge and current of each photodiode respectively. The factor 2 in both sides of the equation represents the current for two balanced photodiodes in the setup¹. The current of each photo diode is measured at 450 μ A and taking into account the current amplifier gain of $G=10^5$, hence, the shot noise equivalent voltage at lock-in yields $V_{shot\ noise} = 10^5 \times 2\sqrt{qI_0} = 1.7 \times 10^{-7} V/\sqrt{Hz}$ and based on setup calibration data, it is translated to an electric field equal to 0.13 V/m.

6.2.2 Transversal scan

At the end of the line, where the load is located, transversal sampling scan was performed in incremental steps of 10 μ m, while the probe tip was placed 10 μ m above the DUT. With an acceptable SNR, the measurements were limited up to 10th harmonics (100 GHz). As depicted in Figure 6.8, a remarkable asymmetry in the electric field distribution around the signal line is observed. For harmonics more than 4th, the signal peak shifts from the right side to the left side which can be interpreted as frequency dependent field distribution on the NLTL. Notably, even far at 400 μ m lateral distance from the NLTL signal line, the signal still can be detected. This is resulted from the small distance between neighboring devices on the wafer die which induces crosstalk. A guess for the field asymmetry was attributed to the asymmetric

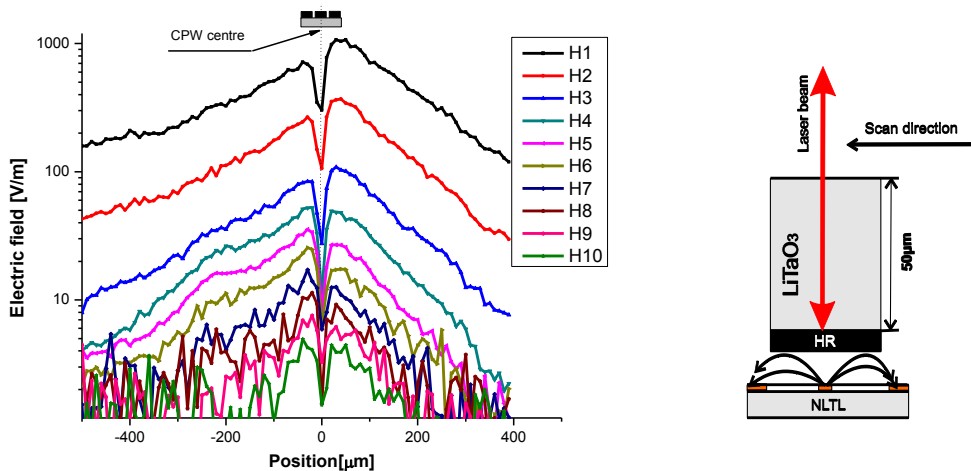


Figure 6.8 Transversal scan of a 50 Ω terminated NLTL (left) and the mechanism of the scan (right). H_i , where $i=1,2,3,\dots$ is an indication for harmonic number i . The reference position (0) is the center of CPW (signal line).

¹ See the schematic of the setup in Chapter 5

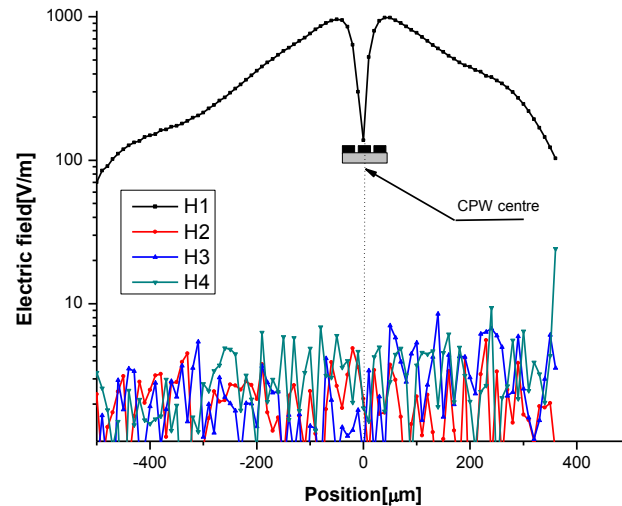


Figure 6.9 Transversal scan of an on-wafer linear transmission line (LTL) with identical dimensions to the host CPW of the NLTL. H_i , where $i=1,2,3,\dots$ is an indication for harmonic number i . The reference position (0) shows the signal line of the CPW.

arrangement of varactors to one side of the CPW signal line, but our measurement for a symmetric design also shows this field asymmetry. Alternatively, a suggestion was to check the influence of vias which are incorporated on a CPW for feeding varactors. For this reason, a linear CPW line on the chip with identical design to the NLTL but including no varactors and vias, was subjected to scan. The results of these measurements are shown in Figure 6.9. Evidently, in contrast to the NLTL measurements, the field distribution is symmetric around the signal line, and apparently, there is no signal for the harmonics as it has to be. This field distribution intensifies our guess that the field asymmetry can be caused by the vias with a length of about $10\ \mu\text{m}$ which is comparable to the CPW structure dimensions (signal strip width of $w=3\ \mu\text{m}$ and slot $s=20\ \mu\text{m}$). These vias with vertical current distribution can change field distribution of CPW and consequently perturb the line propagation modes.

6.2.3 Vertical scan

To investigate on the strength of the DUT, the vertical scan (in the z -direction) at the end of the NLTL was performed. In these measurements, the EO probe tip was lifted up in $5\ \mu\text{m}$ steps and the detected signal amplitude was measured. Figure 6.10 depicts results of this vertical scan. The graph shows the measurement in a linear (left axis) and log scale (right axis) at the 10 GHz fundamental. An evanescent field decay of approximately $20\ \text{dB}/50\ \mu\text{m}$ can be observed.

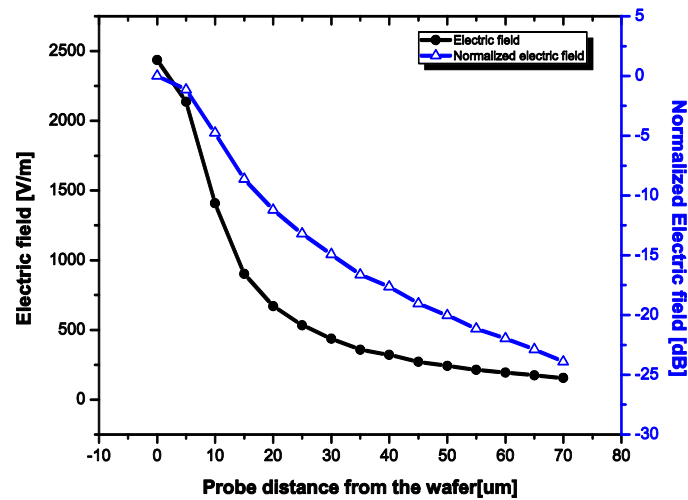


Figure 6.10 Vertical scan of the NLTL performed by lifting up the EO probe tip from the NLTL in $5\mu\text{m}$ steps. The graph shows the actual measurement in linear (left axis) scale and normalized in log scale (right axis)@10 GHz. The measured data are normalized to the maximum detected signal @ 5μ distance of the EO probe from the device.

6.3 Simulation of a linear transmission line structure

As it was shown in Figure 6.7, for the 10 GHz fundamental, the highest detected electric field¹ at a perpendicular Z distance of $\approx 5\mu\text{m}$ from the DUT is around 4800 V/m which is seen at the beginning of the line. On the other side, the NLTL CPW slot width is $20\mu\text{m}$ and by applying a 16 dBm power microwave signal, considering a 50

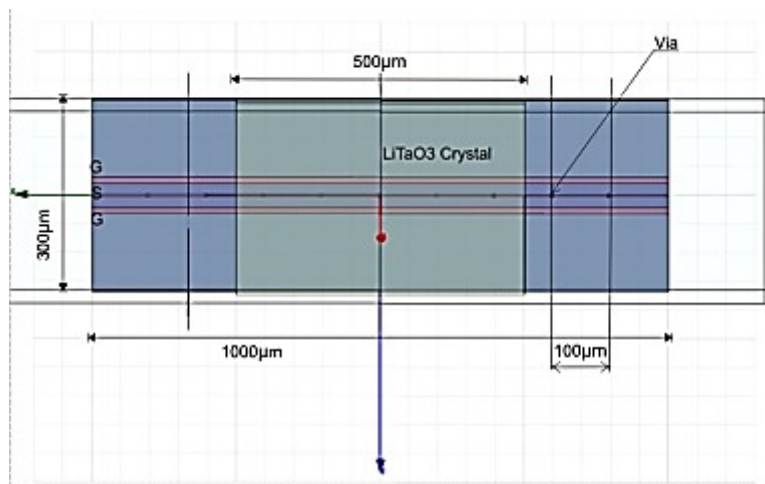


Figure 6.11 Top view of the simulated LTL including vias and LiTaO₃ crystal placed at a level of $5\mu\text{m}$ above the structure

¹ Tangential component of the field between signal and ground line of the NLTL CPW

Ω impedance for the NLTL, the expected RMS voltage is 1.41 V. With a rough calculation, this leads to $E = 1.411/20 \mu\text{m} = 70.5 \text{ kV/m}$ which is about 15 times larger than our measured value. To investigate this issue, and figure out if there is any frequency dependency for the radiated electric field of the device, passive structure¹ of the NLTL was simulated with the finite element based ANSYS-HFSS[®] electromagnetic simulator.

6.3.1 The simulated structure

This structure, which here is called LTL², is a CPW with vias just like the NLTL, but excluding the varactors. The simulation also takes into account real measurement

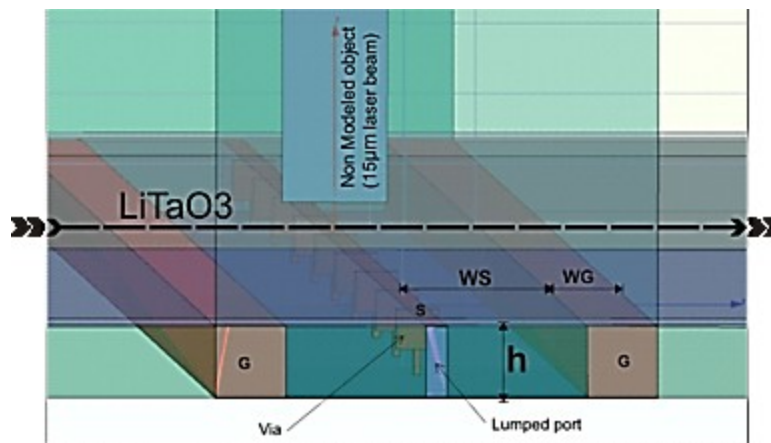


Figure 6.12 The cross section of the simulated structure and vias configuration. $WS = 20 \mu\text{m}$, $WG = 10 \mu\text{m}$, $S = 3 \mu\text{m}$, $h = 10 \mu\text{m}$ and the distance between two sequential vias is $100 \mu\text{m}$.

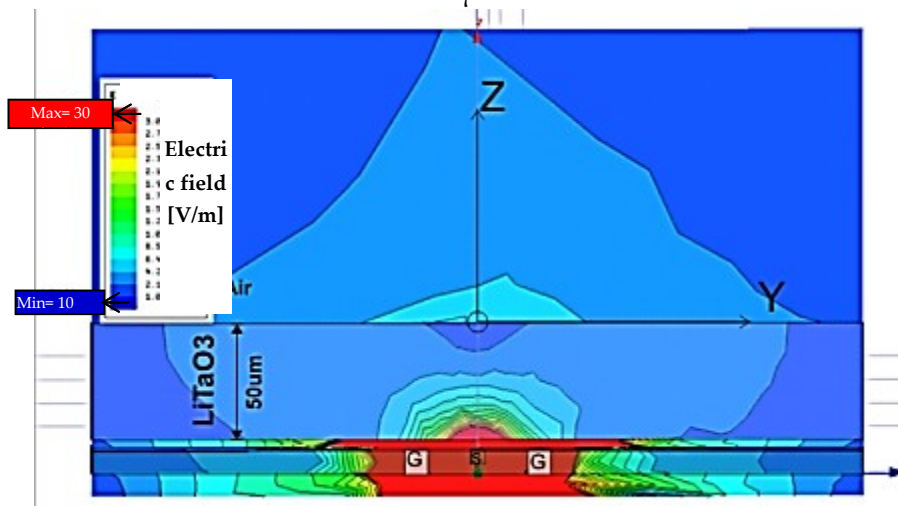


Figure 6.13 Total (tangential + normal) radiated electric field from the structure. Inside the crystal the field is much weaker than that in outside due to the high permittivity of the crystal and less electromagnetic coupling from the air.

¹ CPW including no varactor but vias

² Linear Transmission Line

conditions in presence of the detecting LiTaO₃ probe which is held above the device. The structure is consisting of:

- A CPW transmission line with dimensions identical to the fabricated NLTL: e.g., WG= 10 μm, S= 3 μm, WS= 20 μm, h= 10 μm except a shorter length of 1 mm instead of actual 7.1 mm which is chosen to reduce the simulation run time.
- A LiTaO₃ electro-optic crystal with $\epsilon_r= 41$ and $\tan\delta= 0.00001$ is placed 5 μm above the structure to include the invasiveness of the probe in the simulation.
- Vias with the identical dimension of the fabricated NLTL but in larger intervals to simplify the structure and to reduce the simulation run time as well. The distance between two vias is 100 μm, and there is a gap at the end of each via (close to the back ground plane of the CPW) to represent the vacant position of varactors.
- The simulation is performed with a finite ground plane.

Figure 6.11 and Figure 6.12 show the top view and the cross section of the simulated structure respectively.

6.3.2 The simulation results

A full-wave analysis of the structure at 10, 50, 90, 130, 170 and 210 GHz was performed using ANSYS-HFSS®. Assuming a fundamental frequency at 10 GHz, this simulation shows the behavior of the structure at 5th, 9th, 13th, 17th and 21st harmonics. The applied voltage at the lumped input port for all harmonics is set to 1 V. Figure 6.13 shows the simulated radiated electric field of the structure. It can be seen that due to the large permittivity of the LiTaO₃ ($\epsilon_r= 41$) crystal, the penetrated field inside the crystal is much weaker than that in air. This fact reveals that the field attenuation inside the crystal must seriously be considered while compared with the measurement results.

A simulated tangential electric field (E_y) of the structure is also shown in Figure 6.14. The scan is in the Y direction (the coordination of Figure 6.13). At each Y position, the field is integrated and averaged over 50 μm electro-optic LiTaO₃ crystal thickness in the Z direction. It can be observed that except at 130 GHz which might be a resonance frequency for the structure, the electric field for the higher frequencies is larger than that at the fundamental frequency.

An explanation for this observation can be attributed to the radiation or antenna effect of the structure. In other words, for the smaller wavelengths, the structure tends to be a bigger antenna. For example, the wavelength inside the crystal with $\epsilon_r = 41$ at $f= 210$ GHz yields $\lambda_g = \frac{\lambda_{air}}{\sqrt{\epsilon_r}} = 223 \mu\text{m}$ while the lateral size of the structure, which is the distance between two outer edges of the CPW ground strips, is 63 μm. This size is larger than $\lambda_g/4$, which is a size of monopole antenna.

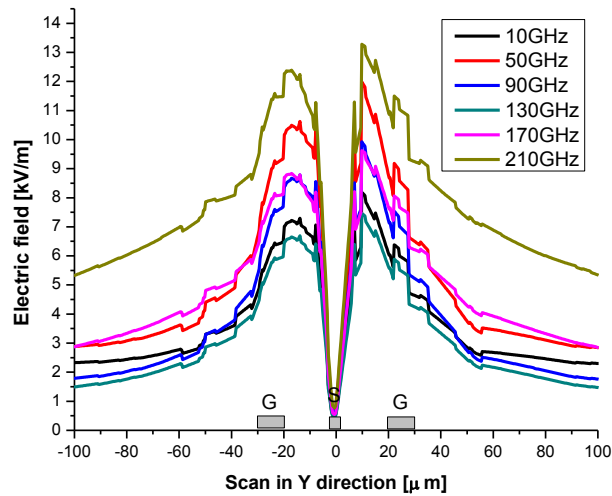


Figure 6.14 Simulated tangential (Y component) electric field inside electro-optic LiTaO_3 crystal placed $5\mu\text{m}$ above the structure.

In Figure 6.15, a comparative simulation is shown for the structure in the *absence*¹ of LiTaO_3 crystal. It can be observed that the field in air is roughly one order of magnitude larger than that inside the LiTaO_3 crystal. This is also shown in dB scale in Figure 6.16 showing approximately a 20 dB weaker field inside the crystal than the radiated field in air. Excluding this attenuation factor for the field inside the crystal, the behavior looks pretty similar except a little deviation at 90 GHz which might be

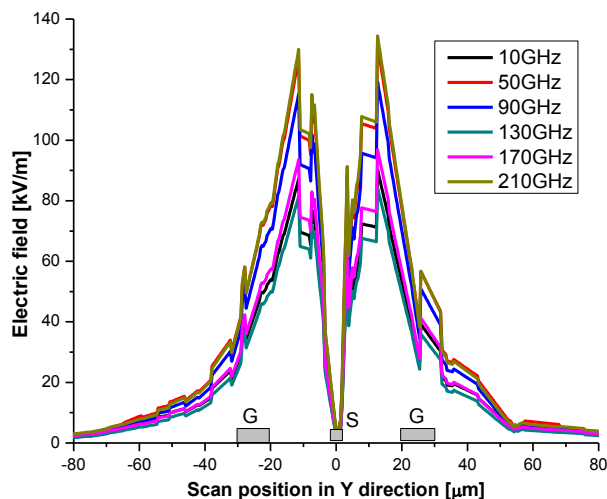


Figure 6.15 Simulated tangential electric field for the structure in the absence of LiTaO_3 crystal

¹ The crystal is replaced by air.

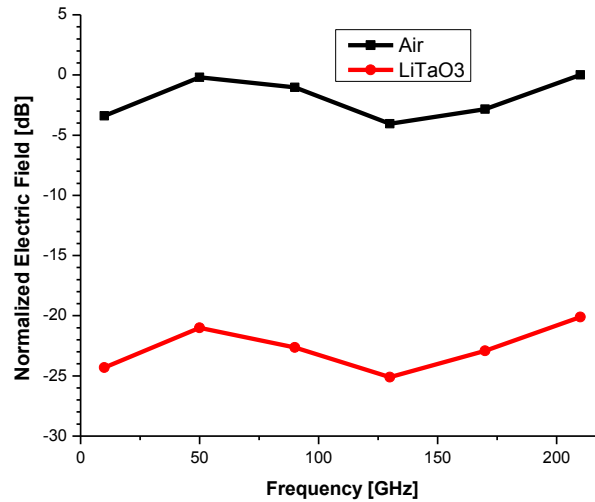


Figure 6.16 The electric field attenuation as a function of frequency inside a 50 μm thick LiTaO₃ crystal which is placed 5 μm above the structure. Air refers to the case for the absence of the crystal.

caused by an unknown structure resonance. Based on these simulation results one order of magnitude weaker electro-optic signal from the roughly calculated electric field is expected as seen in the measurements.

6.4 Comparison between simulation and measurements

6.4.1 Transversal scan

Figure 6.17 shows comparison between simulation of the averaged electric field inside a 50 μm thick electro-optic LiTaO₃ crystal and the EOS measurements at the

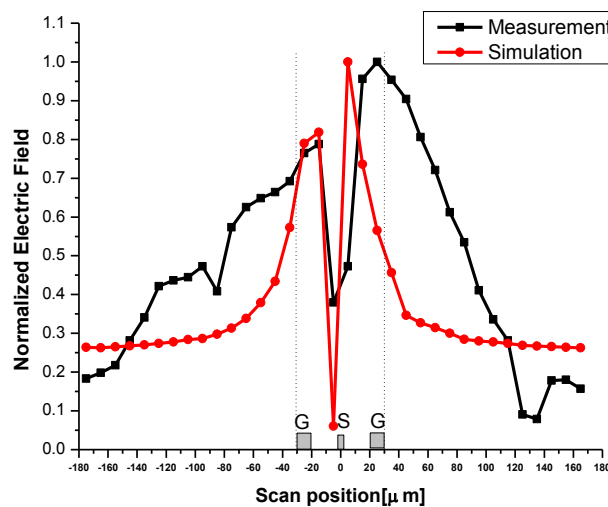


Figure 6.17 Simulation of the averaged electric field inside a 50 μm thick electro-optic LiTaO₃ crystal placed 5 μm above the NLTL and compared with the recorded EO measurements @ 10 GHz.

10 GHz fundamental. The comparison demonstrates nearly a good agreement between the simulation and the measurement inside¹ the structure region. However, outside the structure the deviation is large. This can be attributed to crosstalk from the neighboring devices on the wafer. Moreover, it must be notified that each measurement point is the average of the electric field inside the laser beam size (approximately 15 μm) and this was fully considered and adapted in the simulation results.

6.4.2 Vertical scan

The diagram of Figure 6.18 shows a simulated vertical scan of the evanescent electric field inside the LiTaO₃ crystal at 5th, 9th, 13th, 17th and 21st harmonics of the 10 GHz fundamental frequency. The scan range is from 5 to 50 μm along the Z-direction. The simulation reveals a decay of approximately 30 dB for the evanescent electric field inside the LiTaO₃ crystal at 10 GHz. This decay varies slightly for the higher harmonics due to more radiation from the structure, as already discussed. A comparison between measurements of Figure 6.10 and these simulation results shows 10 dB of less decay for the measurement which can be caused by the crosstalk of other structures on the wafer which are not included in this simulation.

6.5 Measurement of an NLTL terminated with an on-chip antenna

Within the *ULTRA* project, two different solutions for implementing an antenna integrated with an NLTL were planned. One approach was to use a monolithic

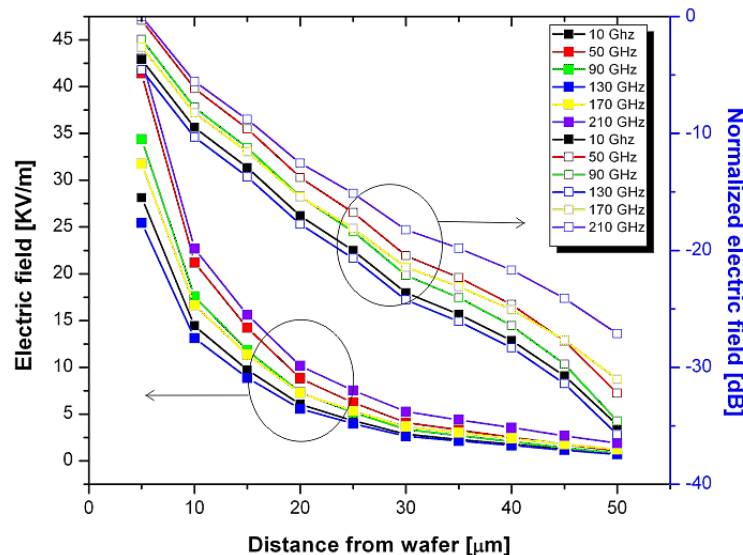


Figure 6.18 Simulated vertical scan of the evanescent electric field inside the LiTaO₃ crystal @ 5th, 9th, 13th, 17th and 21st harmonics of a 10 GHz fundamental frequency.

¹ The term "Inside structure" refers to the lateral distance between outer edges of two ground strips.

solution where the antenna is integrated with an NLTL on a single CMOS chip and therefore, inter-chip connections, which are usually the challenging issues at high frequencies, can thereby be avoided. On the other side, the on-chip antenna needs a large area on the CMOS chip, and dramatically increases the cost of fabrication. Therefore, a solution using an external Vivaldi antenna (see Figure 6.2) was scheduled separately and integrated with NLTL chip via an inter-chip connect.

The monolithic antenna solution, the so-called extremely wideband (EWB) wine shaped slot antenna on a 725 μm thick low resistivity silicon ($10 \Omega\cdot\text{cm}$) substrate was analyzed in [192] and its micrograph is shown in Figure 6.19. This antenna features omnidirectional radiation patterns over the operation frequency range [4], however, its radiation suffer from high losses and unwanted substrate modes in the silicon substrate. As the output power of the NLTL at higher frequencies is very small, therefore, an antenna with an improved performance is required. This was a reason that Vivaldi off-chip antenna was preferred in the final fabrication of the transmitter.

Nevertheless, EOS measurements for the monolithic antenna were also performed. The intention for choosing this antenna is not to measure its radiation pattern or efficiency, but to detect larger radiating field of the NLTL at higher frequencies and increase SNR. Accordingly, the results are also demonstrated in Figure 6.19. The intensity of the detected electric field over the antenna at 10 GHz (main harmonic) is 6 times larger than that for the NLTL terminated with a 50 Ω on-chip load. This is a convincing reason that in the next measurements, most of the results are performed for this device. Moreover, it can be seen that after the 12th harmonic (120 GHz) the signal hits the shot noise floor.

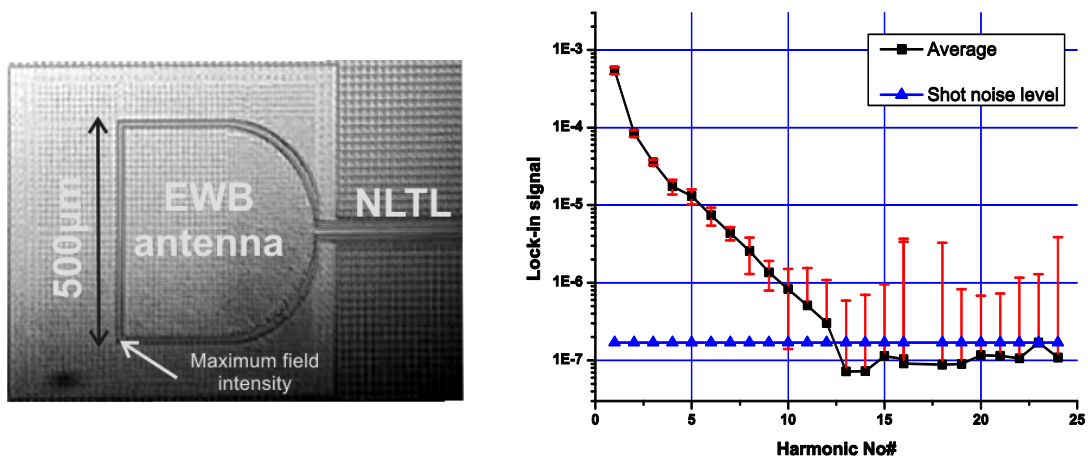


Figure 6.19 The On-chip antenna (left) and its measured electric field (right) up to 240 GHz. Error bars show standard deviation.

7. Measurement Challenges, Errors, and Jitter

In the previous chapter, primary measurements of the NLTL with the EOS were shown. In this chapter, first EOS results are compared with electronic measurements and then it is tried to figure out the errors and challenges. Jitter in the system is studied, and synchronization techniques to explore solutions in reducing the measurement errors are explained.

7.1 Measurement errors and challenges

EOS measurement results can contain unforeseen artifacts and errors and hence, there is a need for their verification. While the errors and challenges are recognized, one can look for solutions to enhance the EOS setup performance. To this end, it is good to take a closer look at the NLTL measurement results firstly.

7.1.1 Comparison of EOS with electronic microwave measurements

Figure 7.1 shows a micrograph of a two-port NLTL under measurement with GSG microwave probes. In this mechanism, one GSG coaxial to coplanar probe feeds the NLTL at the input port, and the output signal is collected by another probe and hence, given to a microwave spectrum analyzer. There is a difference between this

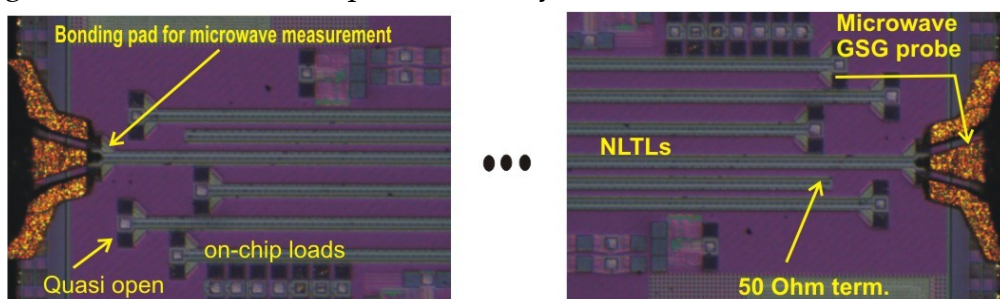


Figure 7.1 A micrograph showing how two GSG probes can measure the signal of the NLTL. The terminated line is used for the EOS and single port microwave measurements.

microwave approach and EOS as in this probing, we detects the output *power* of an NLTL with a matched and calibrated GSG probe while the EOS measures the *evanescent electric field* from a $50\ \Omega$ terminated NLTL. For the EOS, firstly, the evanescent field distribution over the line as a function of frequency has to be known. This was investigated by simulation as shown in the previous chapter that radiation at higher frequencies can gain from the structure antenna effect. Although this is important, it does not significantly influence harmonic measurements as it gives a maximum 4 dB of gain at 21st harmonics in comparison to the fundamental. Therefore, all power calculations are performed by neglecting this effect. Secondly, unlike microwave probing, the EOS does not discriminate between the transmitted and the reflected wave in case of having a mismatch on the NLTL at a specific frequency. To quantify this impact, further measurements of the signal propagation along the line with the investigation of the standing wave contributions inside the NLTL is necessary. This is explained in detail in Chapter 9. Despite these differences, both microwave and EOS collected data can anyhow be compared by considering a fully impedance matched NLTL, and converting the tangential electric field component to its equivalent voltage and power on the CPW structure.

Since the microwave measurements¹ were performed at 6 GHz input fundamental frequency with 16 dBm of power, therefore, the EOS also carried out for the harmonics of this frequency. It is notable to say that to overcome the cable losses and deliver the proper amount of power to the input port of the NLTL; it was necessary to amplify the microwave signal.

Figure 7.2 depicts the EOS measurement at the end of a $50\ \Omega$ terminated line in comparison to the microwave GSG probing up to the 30th harmonic (180 GHz). A

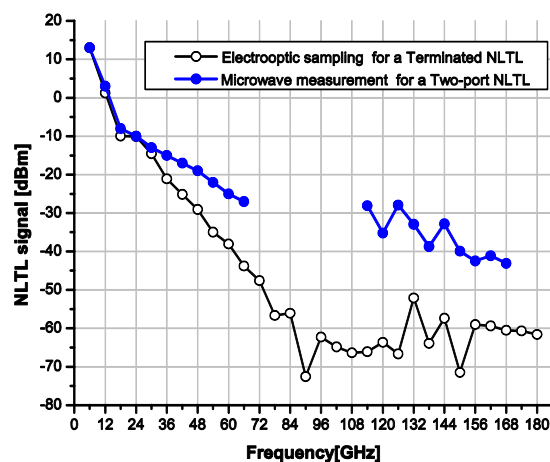


Figure 7.2 A comparison between electronic microwave measurement of an open line for the microwave probing and an EO sampling for a $50\ \Omega$ terminated line up to the 30th harmonic (180 GHz) of a fundamental Input signal @6 GHz and 16 dBm of power.

¹ From ULTRA project partners

good agreement between these two measurement methods until the 5th harmonic (30 GHz) can be observed and after this point deviation increases with increasing the frequency. For a meaningful comparison of the results, this issue has to be resolved in further investigations.

7.1.2 Self-reference detection using spectrum analyzer vs. lock-in amplifier

Since a large deviation between EOS and microwave measurements, in particular for harmonics higher than 5th was observed, it is tried to investigate on the downconverted signal of the NLTL i.e., after photodiode detection in the setup. Instead of using a lock-in amplifier, this signal is measured by a baseband (kHz range) HP35665A spectrum analyzer. This instrument is featured by a large dynamic

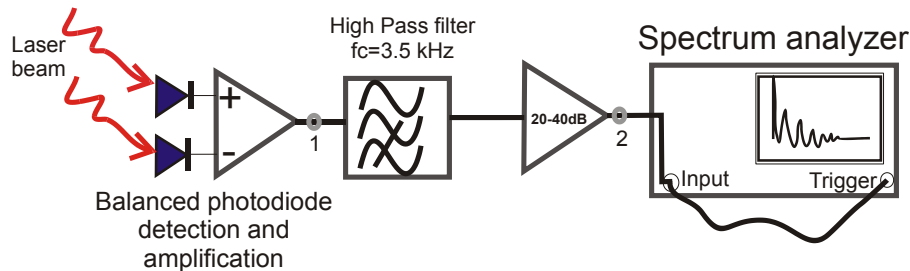


Figure 7.3 Schematic diagram of spectrum analyzer detection setup. The signal also is used as trigger to form self-reference detection.

range of more than 100 dB and a bandwidth up to 100.2 kHz. Figure 7.3 depicts a schematic of the modified detection scheme using the spectrum analyzer in the setup. In this configuration first the output signal of the balanced detector¹, used in the EOS measurement setup, is given to an analog Butterworth highpass filter with a cutoff



Figure 7.4 Downconverted replica of the NLTL output signal. The device is driven @ 10 GHz with 18 dBm of power. The compression of the signal rise time demonstrates the functionality of the NLTL.

¹ For more detail of detection, see full schematic of the setup in Chapter 5.

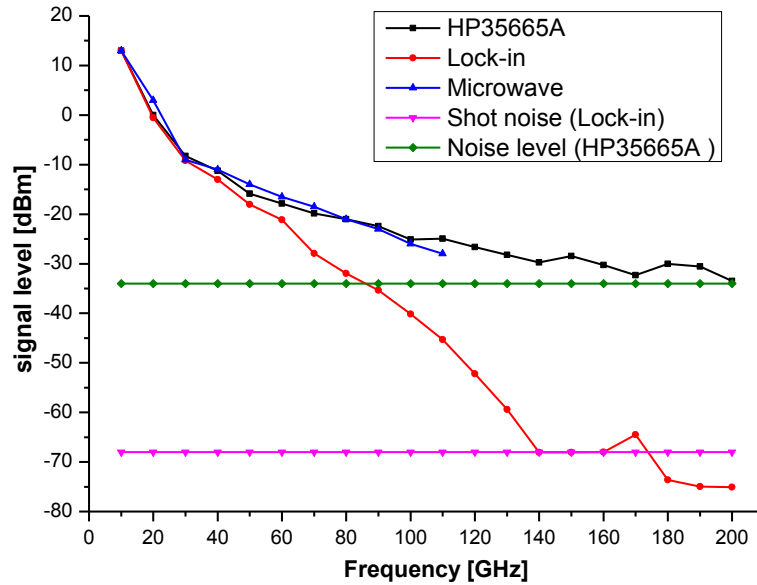


Figure 7.5 Measurement of NLTLs with three different detection methods including microwave probing, auto reference EOS with a spectrum analyzer, and EOS with a lock-in amplifier. The NLTLs are fed by 18 dBm @10 GHz fundamental. After the 5th harmonic the lock-in measurements deviates from the other methods.

frequency of $f_c = 3.5$ kHz and 48 dB/decade roll-off. The filter strongly blocks the DC background signal and the flicker noise, enabling to use an IF smaller than 10 kHz (typically 5 kHz). This allows envisaging more harmonics on full span 102.4 kHz bandwidth of the spectrum analyzer. This signal, after amplification of 20-40 dB is given to both the *input channel* and the *external trigger* of the spectrum analyzer to have a so-called self-reference detection scheme.

This down converted NLTL signal also on the oscilloscope as depicted in Figure 7.4 shows a amplitude of 3.3 V_{p-p}. A compression in the rise time (faster the slew rate) of the sine wave is resulted from the voltage-dependent wave velocity on the NLTL, caused by varactors. The sine wave deformation, including the time compression, the deceleration of positive peaks and acceleration of negative peaks, are interpreted as the generation of higher harmonics in the frequency domain.

Figure 7.5 compares three different measurement methods used within this project including microwave probing, EOS with lock-in amplifier detection, and EOS with spectrum analyzer. To draw a conclusion, the measurement for the lock-in reveals the same behavior observed in the previous measurements, and there is again a big deviation between this approach and the other methods for the frequencies nearly above 60 GHz (6th harmonic of the fundamental 10 GHz and higher). Furthermore, the graph also reveals that in a measurement up to 200 GHz, the other two measurement methods are also in a very good agreement. However, after 110 GHz (11th harmonic) no electronic measurement was available at the time of measurement. Due to this fact, the reason for the measurement deviation can be attributed to the working procedure of the lock-in amplifier. The lock-in detection

error can also be increased by the system timing jitter which increases with the harmonic number.

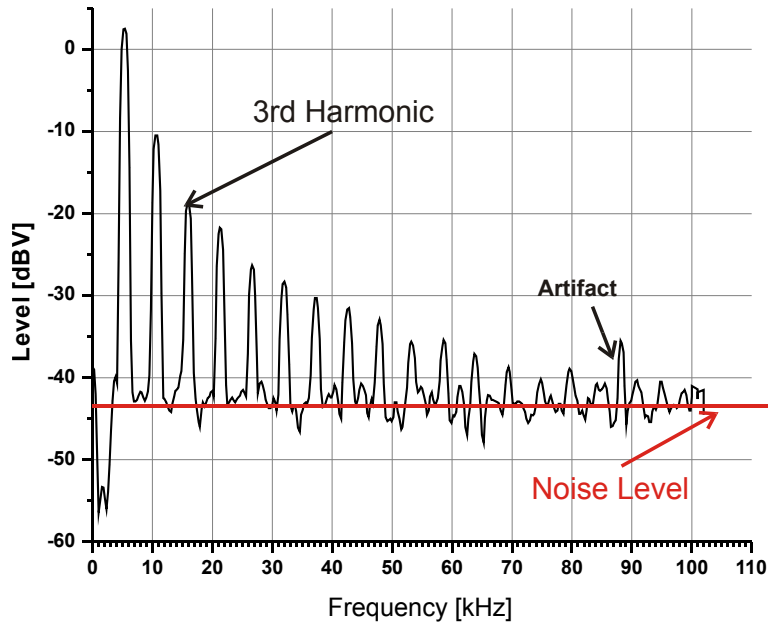


Figure 7.6 Measurement of the NLTL downconverted signal with a baseband spectrum analyzer. After 20th harmonic (equal to 200 GHz at the RF level) the measurement hits the system noise level. There is an artefact at 88 kHz due to an oscillation of the high gain baseband current amplifier.

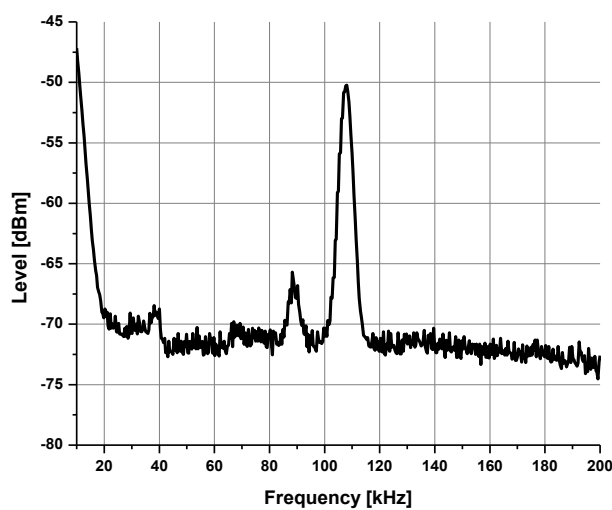


Figure 7.7 The spectrum of the output signal of the baseband current amplifier without any input signal (@node 1 in Figure 7.3). Oscillations from the amplifier are observed at 40, 88 and 108 kHz.

Although due to system timing jitter the measurement with the spectrum analyzer is more reliable and fits better to the microwave probing, unfortunately, its bandwidth is limited by the noise level. The noise level drastically increases due to the significantly larger measurement bandwidth of the spectrum analyzer. In this scheme, the bandwidth is 102.4 kHz and compared to the lock-in $BW_{lock-in} = 10$ Hz (for $TC^1 = 100$ ms), 40 dB of the higher noise level can be expected according to

$$\frac{N_{Spec.Analyser}}{N_{lock-in}} = 20 \log \left(\sqrt{\frac{BW_{Spec.Analyser}}{BW_{lock-in}}} \right)$$

This relative noise is calibrated at the level of -35 dBm and shown in Figure 7.5. The increase of the noise level deteriorates the sensitivity and dynamic range of this method and strongly limits the system detection bandwidth. This situation can apparently be seen from Figure 7.5 as at 200 GHz (20th harmonic) and beyond, the signal goes under the level of the noise floor. The spectrum of the detected signal is also depicted in Figure 7.6. This time, to view all harmonic on full span of the spectrum analyzer, the reference signal which corresponded to the fundamental is set to 5 kHz. The observed peak at 88 kHz assumed to be an artifact. To prove this, the output of the current amplifier is measured by another wideband spectrum analyzer (Advantest R3131A) while the NLTL is disconnected from the microwave generator and there is no reference signal. The result is shown in Figure 7.7, and at 40 kHz, 88 kHz, and 108 kHz we have oscillations of the current amplifier. The peak at 108 kHz fortunately, is out of the measurement range of the baseband HP35665A spectrum analyzer. Notably, the oscillation at 40 kHz is small in comparison to signal and hence, dissolves into the measurement signal.

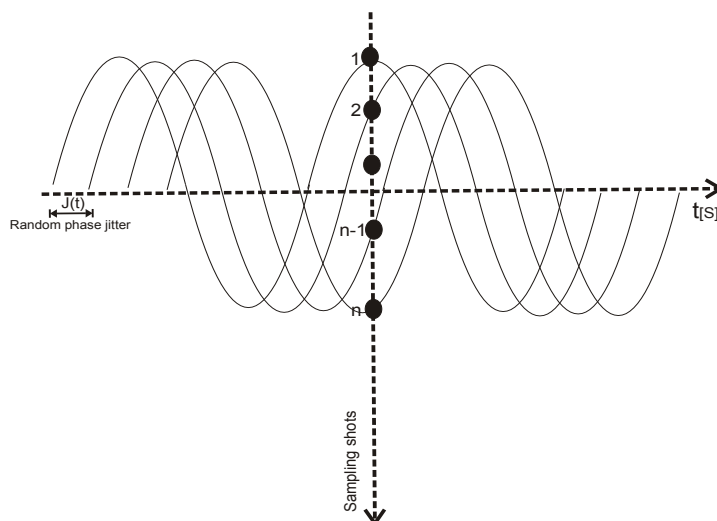


Figure 7.8 A sketch to illustrate measurement of a jittery signal with the lock-in amplifier

¹ Time-constant

7.1.3 Investigation on errors in lock-in measurements

The observed error with the lock-in amplifier detection can be caused by the *timing*

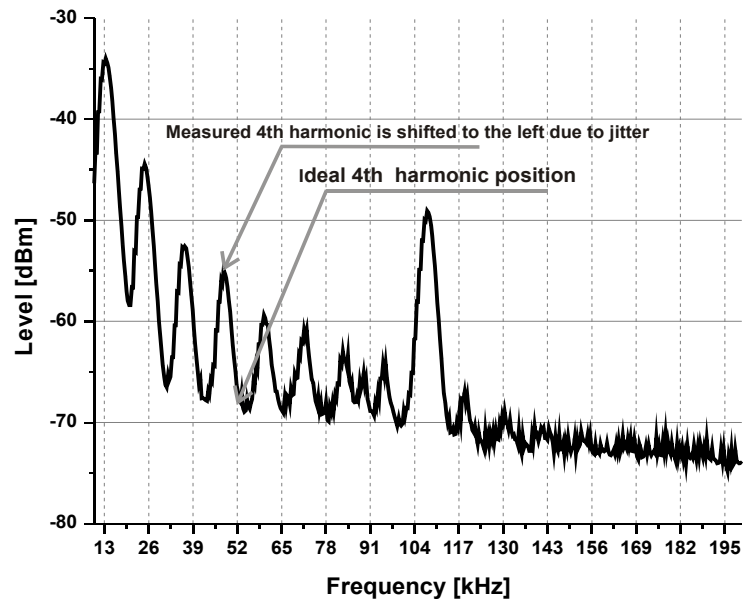


Figure 7.9 Frequency drifts of the detected signal due to the timing jitter. The higher harmonics are shifted downwards during 3 seconds of the scan time of the spectrum analyzer. Evidently, at 52 kHz, which is the theoretical position of 4th harmonic of 13 kHz fundamental, no signal exists.

jitter between the microwave signal and the femtosecond laser pulse. In Figure 7.8 the mechanism of measurement signal with lock-in amplifier is sketched assuming that the signal is jittery. In this situation, the lock-in amplifier detects the signal with

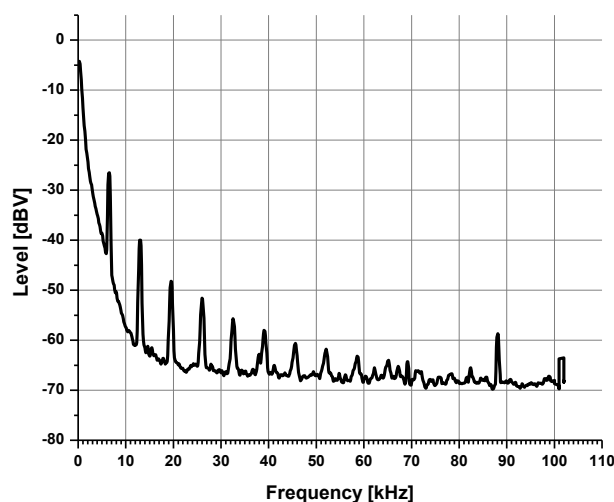


Figure 7.10 The averaged NLTL down converted signal. Jitter broadens the spectrum at higher harmonics.

some random phase which deteriorates the true sample value, especially by integration or averaging. In a worst case, the random phase shift becomes comparable with the period of the signal. Therefore, the lock-in detection results in a zero mean value averaging.

7.1.4 Jitter in the frequency domain

To investigate this hypothesis, measurements of the downconverted NLTL harmonics within a 3 second scan period were performed by the Advantest R3131A spectrum analyzer as depicted in Figure 7.9. To reduce the laser flicker noise, the reference baseband signal¹ frequency was increased and set to an arbitrary value of 13 kHz. It can be seen that at 52 kHz, which theoretically equals the 4th harmonic of the 13 kHz fundamental, no signal exists, but instead, the real 4th harmonic is shifted 5 kHz downwards. This frequency shift occurs during the 3 second of the spectrum analyzer scan time and shows the timing jitter of the signal. This circumstance for measurements with the lock-in amplifier (with detection bandwidth of 10 Hz) is extremely critical and causes large errors as demonstrated before. Furthermore, Figure 7.10 shows 100 averages of the signal recorded with the baseband HP35665A spectrum analyzer, to investigate the influence of jitter on signal averaging. As it can be seen, during averaging time the shift of the frequency for higher harmonics also broadens the harmonic bandwidth.

7.1.5 Jitter in the time domain

Figure 7.11 shows one period of a Schmidt triggered 10 kHz down converted fundamental 10 GHz signal on the oscilloscope depicting 7 picosecond of time jitter.

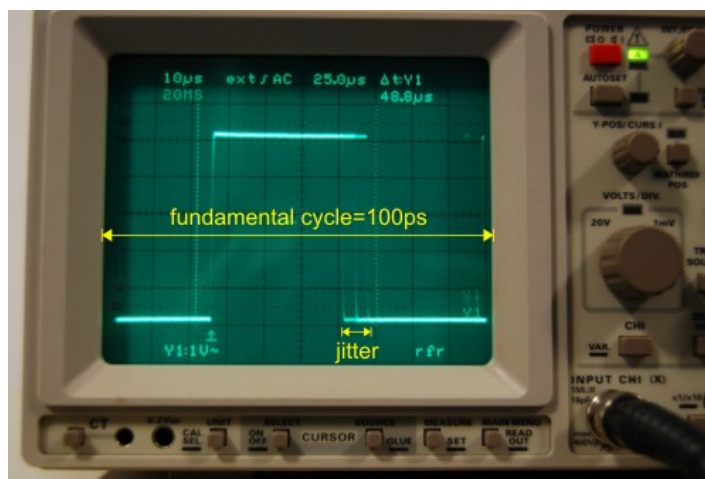


Figure 7.11 The timing jitter of the IF beat frequency (10 kHz) resulted from mixing of the laser repetition rate and a 10 GHz signal with a photoconductive switch. The yellow arrows show the RF translation of the signal. Approximately 7% of jitter in comparison to 100 ps period is observed.

¹ The signal at node 2 in Figure 7.3 which is a downconverted signal of the NLTL.

This jitter is accumulated during one scan cycle (100 μs) of the oscilloscope. Since the signal is a true baseband replica of the microwave fundamental at 10 GHz, its equivalent RF time scale is shown in picosecond on the oscilloscope. For the higher harmonics this amount of jitter is multiplied by the harmonic number and becomes very comparable to the period of the signal resulting in larger measurement errors. This kind of jitter, which is a disharmony between the microwave signal and the laser repetition rate, is the dominant source of the errors as was also previously reported in [193]. A significant effort is required to resolve fast-variant jitter to enable high sensitivity lock-in detection over the full bandwidth of the EOS system. Later on, in this and next chapter this challenge is more demonstrated in detail.

7.1.6 Characterization of the lock-in amplifier errors

To characterize other probable errors in harmonic measurements with the lock-in amplifier, measurements using a so-called clean and almost jitter-free square wave¹ signal with the amplitude of 50 mV at 3 kHz were carried out. The resulted data in comparison with spectrum analyzer measurement is shown in Figure 7.12. The diagram reveals a good agreement between these two methods up to the 21st harmonic, and for even harmonics after 22, a difference of approximately 10 dB appears. Apart from this no significant deviation between measurements with the

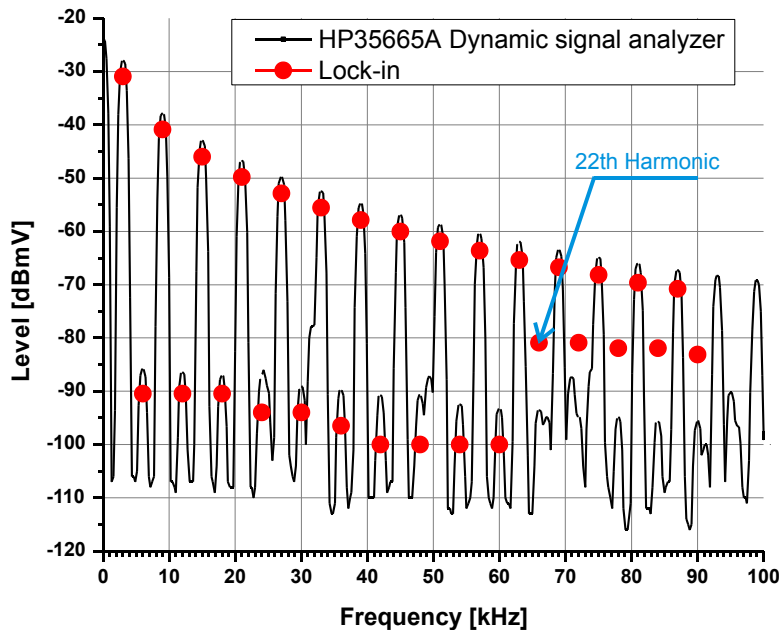


Figure 7.12 Comparison between lock-in amplifier and the spectrum analyzer measurement to characterize the lock-in malfunctioning. The input signal is a clean and almost jitter-free reference square wave at 3 kHz. There is a good agreement at most harmonics. However, after 66 kHz (22nd harmonic) there is a 10 dB of difference at -80 dBV signal level.

¹ From a commercial signal generator

lock-in amplifier and spectrum analyzer is observed. From this test it can be concluded that the errors are resulted from the jitter of the downconverted NLTL signal and not the lock-in response malfunctioning.

7.2 Synchronization techniques

In the previous sections, it was mentioned that jitter in the system can drastically reduce the EOS measurement bandwidth. It was also noticed that whenever the signal is jittery, the lock-in as a narrowband detector measures with large errors, in particular at the higher harmonics. In the following sections, common techniques to minimize jitter in the system are explained and in the end, a novel method which significantly improves the EOS performance of is introduced.

7.2.1 Free-running EOS system

In this case, no synchronization mechanism is used, and the system is running freely. For low-frequency microwave measurements and depending on the generator and laser phase noise, this system can be used, however, by increasing the frequency and in particular for the case of NLTL, where measurement at harmonics is needed, its performance significantly degrades. If the signal is too jittery, the lock-in cannot lock and due to frequency shift it hampers the efficient averaging of the signal.

7.2.2 Microwave Master- Laser Slave (MM-LS)

In this scheme, as schematically shown in Figure 7.13, using a photo switch, the reference Δf (beat signal between the microwave f_m and a harmonic of the laser repetition rate f_L) is given to a PLL system and lock with an external reference IF (f_r). The error signal from the phase detector of the PLL is then given to a motor which rotates butterfly inside the laser cavity. This rotation slightly changes the laser cavity length by making an angle between the laser path and the butterfly rod axis. This

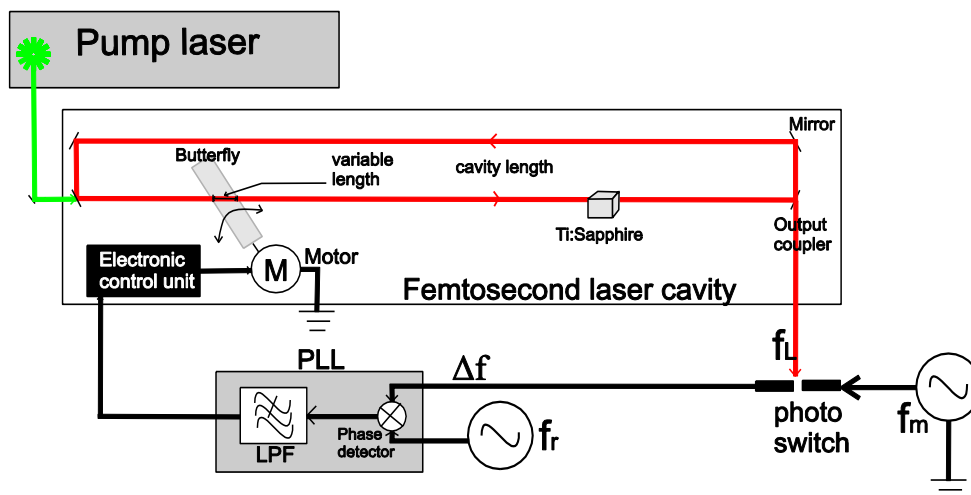


Figure 7.13 Schematic diagram of MM-LS synchronization

variation of the cavity length pushes the repetition rate of the laser to follow-up the microwave frequency synthesizer. Another approach of controlling the cavity length can be realized by mounting the laser output coupler on a linear piezo stage as addressed in [131]. However, this approach is more complicated and needs a high voltage control unit for the piezo. Since the system is electromechanical, it is slow and fails to fully follow-up a jitter faster than the system reaction time. Furthermore, ripples from a laser noise on the reference signal of the photoconductive switch can make overshooting of the system or unlock after a certain time. It is worth to mention here, that the error signal of the PLL instead of driving piezo controller can also be given to the butterfly vibrator of the femtosecond laser cavity.

7.2.3 Laser Master- Microwave Slave (LM-MS)

An alternative to the MM-LS synchronization is to lock the microwave synthesizer to the laser repetition rate by configuring the laser as a master oscillator and the

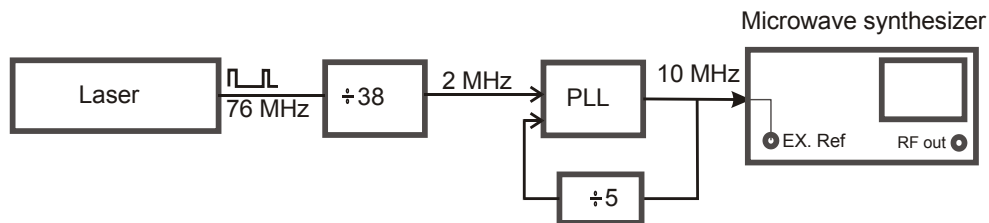


Figure 7.14 Schematic diagram of the LM-MS synchronization system

microwave synthesizer as the slave (LM-MS) which was reported in [145]. In this scheme the external reference signal (trigger) for the microwave synthesizer is derived from the laser repetition rate.

To illustrate an example, for the laser repetition rate tuned at 76 MHz, by dividing it to 38 using a programmable pre-scaler and additionally multiplying by a factor of 5 with a PLL, a 10 MHz reference signal can be achieved. This configuration

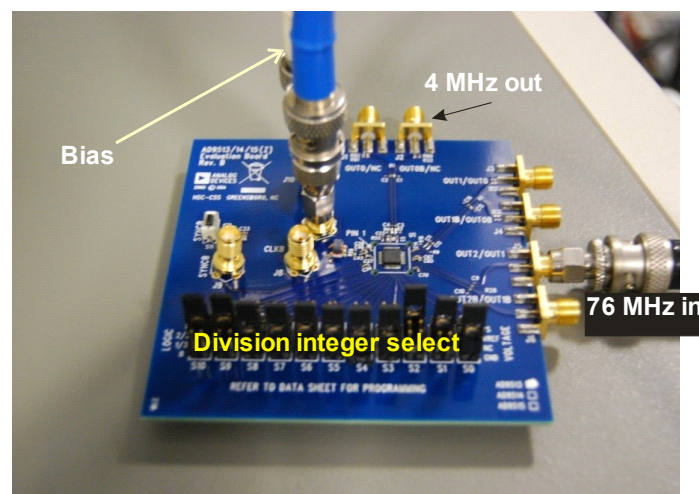


Figure 7.15 The pre-scaler circuit board used in the LM-MS configuration.

is shown in Figure 7.14. As our microwave synthesizer from Rohde & Schwarz can be synchronized with an external reference between 1-20 MHz in 1 MHz steps, our setup did not need the PLL stage. Therefore using a pre-scaler shown in Figure 7.15 with the division ratio of 19, the system can be locked at a 4 MHz (76:19) reference. To evaluate its functionality, the photo switch output signal (@10 kHz) was monitored while the system stayed synchronized and a frequency stability drift of 14 Hz was measured for several hours. Under these circumstances, the NLTL measurement performed again and compared with the free-running results as shown in Figure 7.16. Although the synchronized signal has a gain, of 7 dB for instance at the 8th harmonic, a large deviation still we have with the real microwave measurements values and hence, it cannot fulfill our requirements as a synchronization system.

7.2.4 Laser Master- Laser Slave (LM-LS)

This method which to the best of our knowledge is the newest introduced in EOS, uses the laser as both source and sampler. Since this technique is quite novel and very efficient in comparison to other methods, it is explained in detail in next chapter.

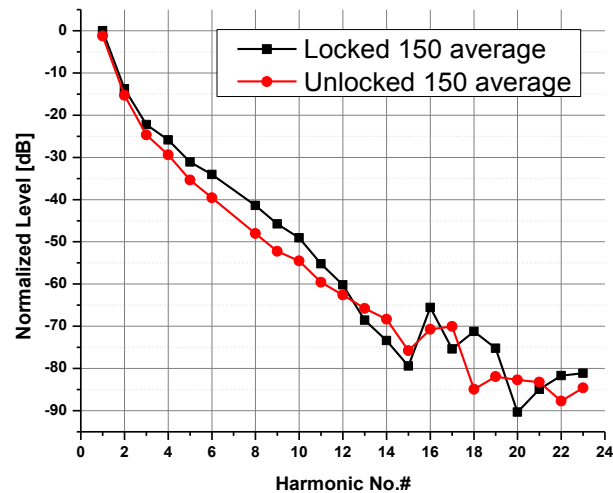


Figure 7.16 A comparisons between NLTL measurements with LM-MS synchronized setup (locked) and free-running with lock-in (unlocked: locked with jitter) signal. Despite less jitter, no significant gain with the LM-LS is achieved.

8. Laser Master-Laser Slave Synchronization

In the previous chapter, common techniques of EOS synchronization and especially two conventional methods called Laser LM-MS and MM-LS were described and it

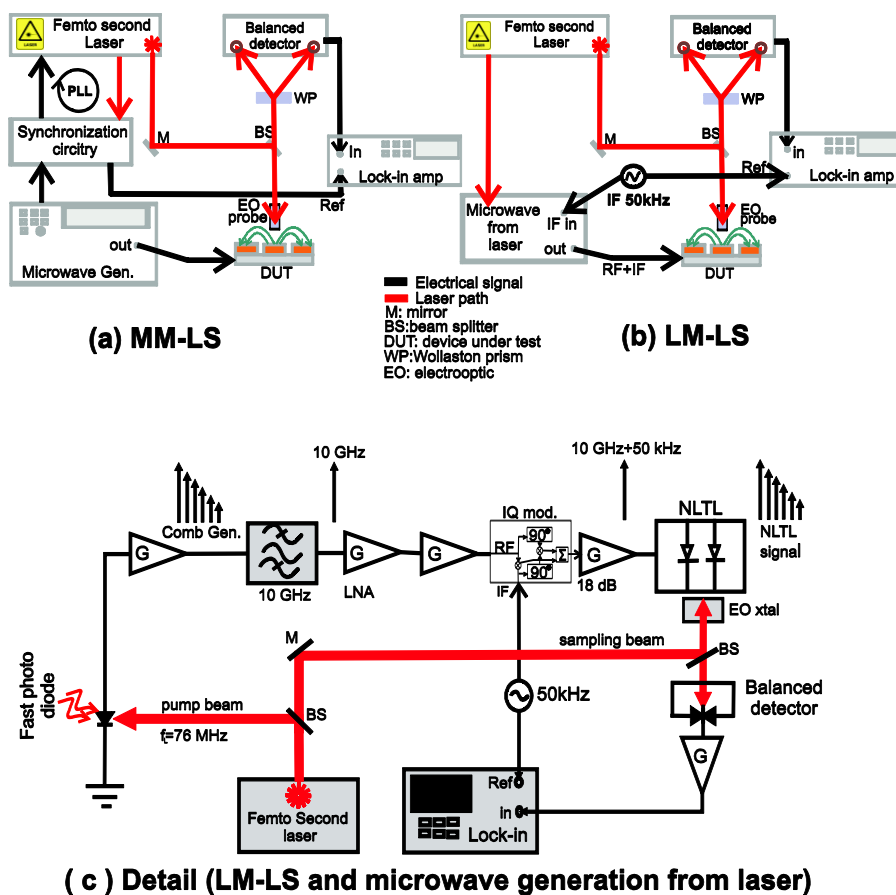


Figure 8.1 Electrooptic sampling (a) a conventional MM-LS (LM-MS) setup with PLL synchronization, (b) the LM-LS setup with a synchronization technique, whereby the laser itself generates the microwave signal directly, without a PLL loop, and (c) a detailed schematic of the LM-LS setup with the mechanism of generating microwave signal from laser to drive DUT. Reproduced with permission from [200].

was shown that they have insignificant gains in the detection of the NLTL signal at higher harmonics. For the MM-LS, it was emphasized that the electromechanical system of the laser which is controlled by a PLL is slow and cannot follow-up fast variation of a jittery signal. On the other hand, our measurement with the LM-MS did not show a significant change in comparison to free-running. With this regard, exploring a better and robust solution, capable of coping with the both slow and fast jitter is favorable. In this chapter, a new approach to resolving this long lasting problem in EOS is presented. With this approach, the relative jitter between the sampled electric signal and the sampling optical pulse is eliminated. The presented system is applicable in the characterizing of active (passive) mm-wave and THz circuits while they are under real operation e.g., with CW excitation.

8.1 Mechanism of LM-LS synchronization

To highlight the differences of LM-LS in comparison with this method, a simplified schematic diagram of MM-LS setup is portrayed in Figure 8.1 (a). In this system, the ultrafast DUT is driven by an external microwave signal generator and the EO probe samples the electric field of the circuit. As experimentally shown in Chapter 7, due to the slowness of the PLL synchronization system, the relative time jitter between microwave generator and the femtosecond laser pulse restricts the system measurement bandwidth. In the previous chapter, it was also mentioned that the presence of the jitter broadens the IF signal peaks in the frequency domain and hence, resulting in larger variation of the signal in comparison to a lock-in measurement bandwidth. This problem is a big challenge for the NLTL measurements and in particular hampers detection of the most attractive and valuable data at higher harmonics. One can imagine that 1% of jitter at the fundamental can be linearly enhanced to $n\%$ at n^{th} harmonic.

Alternatively, a new synchronization mechanism, so-called LM-LS is proposed here and the schematic of the setup is shown in Figure 8.1 (b). In contrast to the MM-

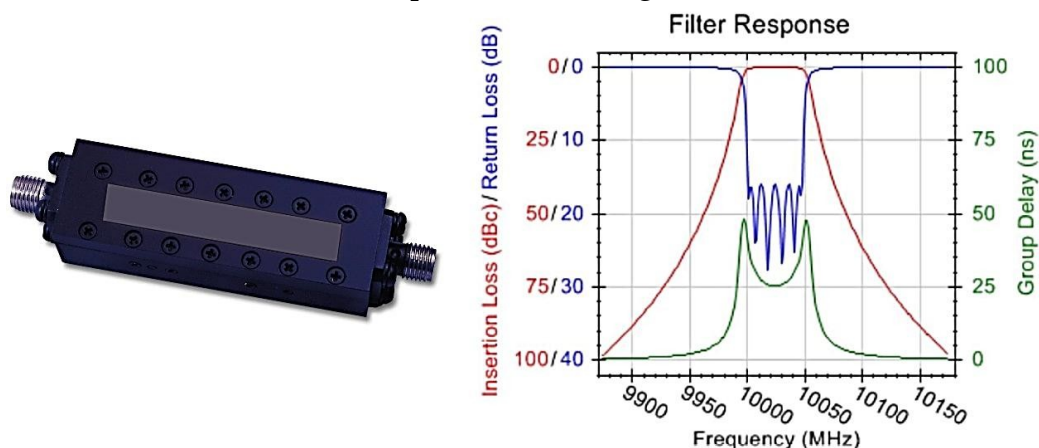


Figure 8.2 The microwave cavity filter and its frequency response. Figure from the device datasheet.

LS or LM-MS, here the *laser* itself provides a microwave signal to be fed to the DUT. Accordingly, as seen in detail in Figure 8.1 (c), a beam of the femtosecond laser pulse turns on a fast photodiode (with a $BW_{-3dB} = 3$ GHz) and generates a comb of harmonics from the laser pulse repetition rate (typically 75 MHz). By choosing a

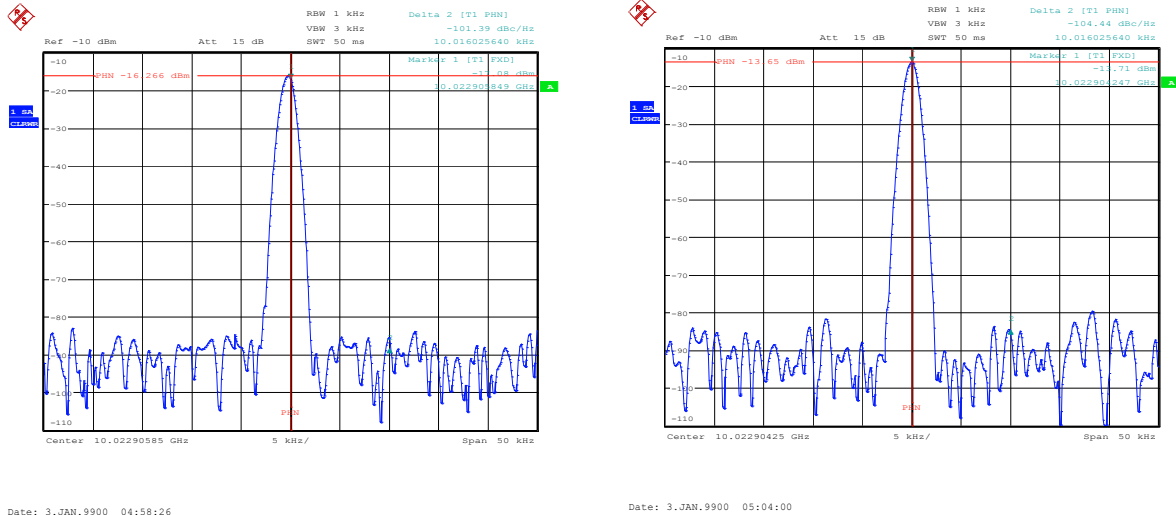


Figure 8.3 Phase noise for the laser generated signal (left) and Rohde & SFM 100 low phase noise signal generator (right).

harmonic typically close to 10 GHz and after amplification, it is then fed to the DUT. A significant advantage of this approach is that the PLL loop can fully be eliminated. To separate the 10 GHz harmonic from the comb, a rather sharp tuned microwave cavity filter with a quality factor of $Q \approx 200$ is used. As shown in the frequency response of Figure 8.2, this filter is capable of selecting the 134th harmonic of a typical 75 MHz laser repetition rate and rejects the lower and upper harmonics ($f_c \pm 75$ MHz) with approximately 55 dB of attenuation. Since by tuning the laser cavity length, the pulse repetition rate can precisely¹ be adjusted in the range of 75-76 MHz, therefore, it is possible to use an arbitrarily tuned filter and flexibly shift the desired harmonic to the filter center frequency. The level of this laser generated microwave signal, immediately after the filter, was measured at -55 dBm using a Tektronix 2755P spectrum analyzer. The signal hence was amplified to a desired level with the aid of an LNA and a chain of cascaded microwave amplifiers. As shown in Figure 8.3, the phase noise of this signal is very low and comparable to a signal from an SMF100A signal generator with -120 dBc phase noise. This signal is then delivered to the NLTL at the level of 18 dBm (see Figure 8.1 (c)). It is notable to emphasize that in the LM-LS setup both path lengths along the circuit excitation and sampling in the setup can easily be optimized to reduce the influence of their relative arrival time. The major drawback of this method can be linked to the narrowband tunability of the cavity filter which hampers selecting other frequencies for DUTs. For example, if one decides to feed DUTs at 15 GHz, he/she needs another cavity filter.

¹ With 1 Hz resolution

8.2 Providing the IF signal for superheterodyne LM-LS

Since the input microwave signal (RF) of the NLTL and the sampling laser harmonic (LO) of the EOS both are identical in the frequency, for a heterodyne detection an external IF is required. This IF signal can be brought into the setup by the following approaches.

8.2.1 The use of amplitude modulator

Although in THz TDS¹, usually, amplitude modulation is used to make an IF, for our measurements and scanning signal at harmonics, the story is different. In the LM-LS, AM modulation can be applied to both the optical and electrical paths of the setup shown in Figure 8.1 (c). In the former, to modulate the laser beam, one can either use

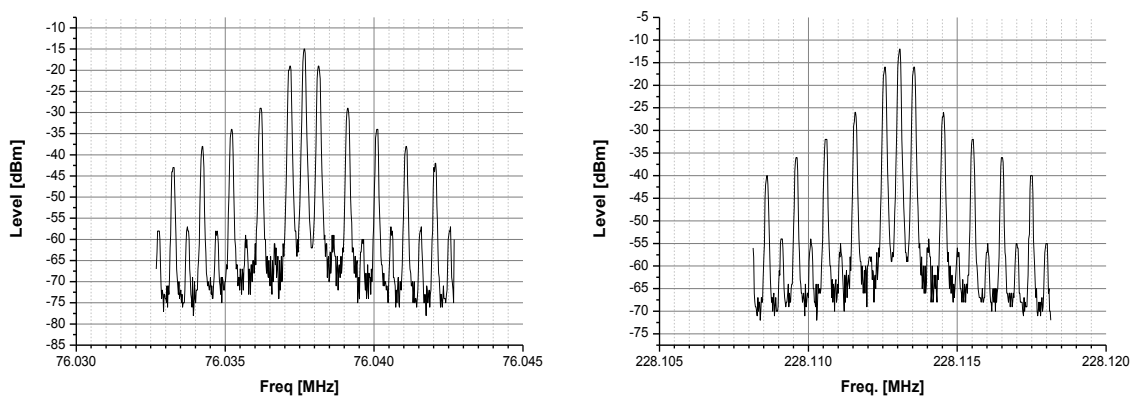


Figure 8.4 The measured signal of the photo diode after mechanical chopping of the optical beam in front . The side bands makes AM inappropriate for the NLTL input.

a mechanical chopper or an electrooptic modulator immediately before the

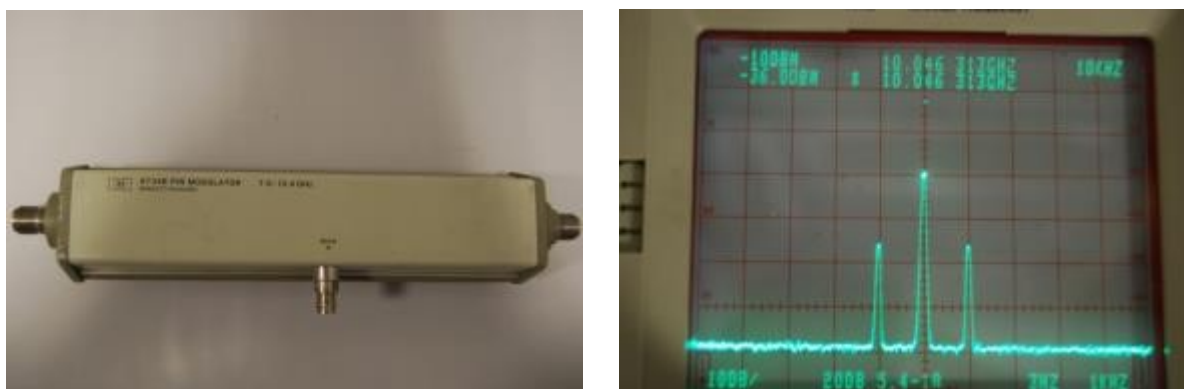


Figure 8.5 A PIN diode microwave AM modulator for X-band and the spectrum of its output signal. The sideband level is approximately -16dBc.

¹ Time domain spectroscopy

photodiode. A mechanical chopper was used, and the spectrum of the electrical signal after the photodiode at ≈ 76 MHz and 228 MHz, which are the main and the third harmonics of the laser repetition rate respectively, are measured as shown in Figure 8.4. Apparently, it can be seen that chopping of the beam creates lots of sidebands around the carrier frequency. If one feeds 134th harmonic of this signal to the NLTL, due to the nonlinearity and intermodulation effects, its response will contain a huge number of spurious sidebands. Detection of such a signal will not show the real response of the NLTL. Filtering a carrier from the side bands is also impractical as the filter needs to be extremely sharp with a very high quality factor (Q). Instead of optical chopping, AM can also be performed directly on the microwave 10 GHz signal using a PIN diode. Although this method generates a signal with much fewer sidebands (see Figure 8.5), but still AM and multi-tone input of the NLTL is problematic

8.2.2 The use of IQ modulator

Finally, it was decided to use an IQ modulator and place it before the NLTL as shown in Figure 8.1 (c). This IQ modulator, by mixing the external IF and the 10 GHz RF, provides one IF offset. The schematic diagram and mathematical expression of the mixing is shown in Figure 8.6. Although the IQ modulator also generates AM side bands, it can be controlled and minimized by tuning both the amplitude and phase of the IF (I and Q) signal. Accordingly, in our experiment, the 2nd and higher sidebands were eliminated and at the same time the first sideband level reduced around 32 dB below the carrier as depicted in Figure 8.7. In the following sections, the impact of these sidebands in the NLTL output signal which may produce artifacts and errors in the measurements is studied.

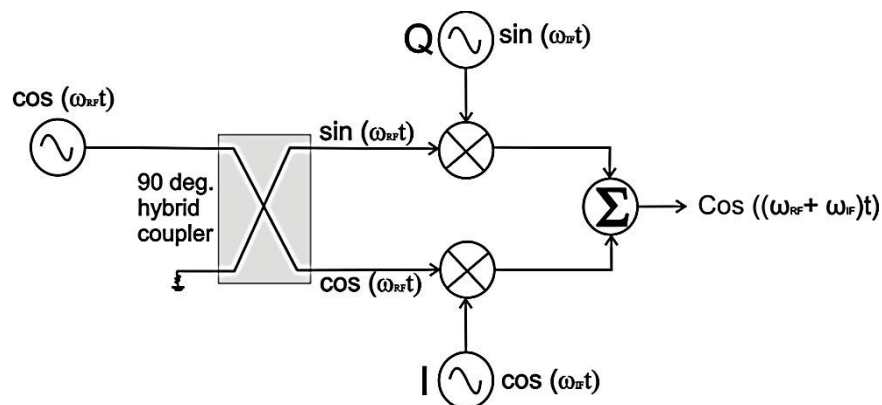


Figure 8.6 IQ modulator as frequency translator. Side bands can be minimized by adjusting the phase of I and Q IF signals and their DC offset level.

The effect of AM side bands on the NLTL signal

The operation of an NLTL as a nonlinear function for any arbitrary x input signal can mathematically be expressed with a Taylor series as

$$f(x) = \sum_{i=0}^{\infty} a_i x^i \quad (8.1)$$

Since the NLTL is a passive¹ voltage controlled phase shifter, assuming losses as a constant, the influence of sidebands can be studied under the assumption of a lossless system. In this case, from the energy conservation theory, the amount of input and output power are equal but with the different spectrum. Therefore,

$$P_{out} = P_{in} \rightarrow P_{f(x)} = P_x \quad (8.2)$$

where $P_{f(x)}$ is the sum of power for a nonlinear function shown on of the left side of

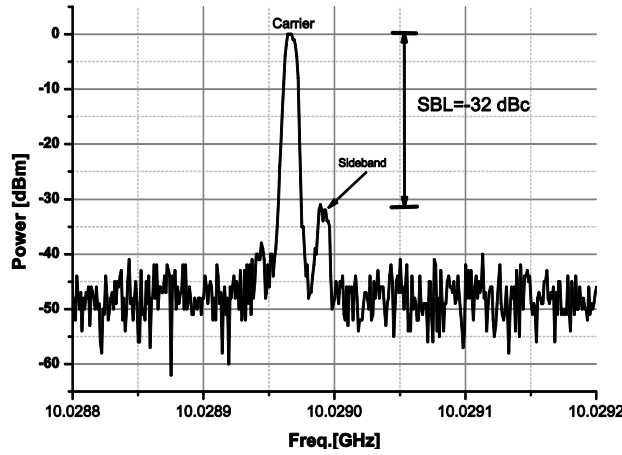


Figure 8.7 The 10 GHz signal at the output of the IQ modulator and before injecting into the NLTL. the IQ modulator beside a shift of $IF=50$ kHz generates a sideband which also has one IF space from the carrier. The level of sideband, after optimization is reduced to -32 dBc.

Reproduced with permission from [200].

Eq. (8.1) and P_x is the power of a single carrier signal applied to the input² of the device. Hence,

$$\begin{cases} x = A\cos(\omega_c t) \\ P_{f(x)} = P_x = P_C = \frac{1}{2}|A|^2 \end{cases} \quad (8.3)$$

and for a case of carrier plus a single sideband (C+SSB) with a modulation depth of m defined by

¹ Has no gain

² The initial phase for simplicity is set to zero.

$$\underbrace{A \cos(\omega_c t)}_x + \underbrace{m \cos[(\omega_c + \omega_m)t]}_{\Delta x} \quad (8.4)$$

while x and Δx are the carrier and sideband respectively, the input power spectrum is superimposed as

$$P_{x+\Delta x} = P_x + P_{\Delta x} = \frac{1}{2}|A|^2 + \frac{1}{2}|m|^2 \quad (8.5)$$

Provided that the modulation index $\left\| \frac{\Delta x}{x} \right\| = \frac{m}{A} \ll 1$ and from Eq. (8.1) and Eq. (8.4), the NLTL output for C+SSB can be approximated by

$$\begin{aligned} f(x + \Delta x) &= \sum_{i=0}^{\infty} a_i (x + \Delta x)^i = \sum_{i=0}^{\infty} a_i x^i \left(1 + \frac{\Delta x}{x}\right)^i \\ &\approx \sum_{i=0}^{\infty} a_i x^i \left(1 + i \frac{\Delta x}{x}\right) = \sum_{i=0}^{\infty} a_i x^i + \sum_{i=1}^{\infty} a_i i \Delta x x^{i-1} \\ &= f(x) + \underbrace{\sum_{i=1}^{\infty} a_i i \Delta x x^{i-1}}_{\Delta f(x)} \end{aligned} \quad (8.6)$$

as $f(x)$ reflects the only harmonics of the *carrier* with a spectrum at $(\omega_c, 2\omega_c, 3\omega_c, \dots)$, where

$$\Delta f(x) = m \cos[(\omega_m + \omega_c)t] \sum_{i=1}^{\infty} a_i i [A \cos(\omega_c t)]^i \quad (8.7)$$

represents the impact of sidebands. The spectrum of $\Delta f(x)$ contains $(\omega_c \pm \omega_m, 2\omega_c \pm \omega_m, 3\omega_c \pm \omega_m, \dots)$ frequencies, which means that only the first sideband of each carrier (harmonic) needs to be taken into account and the rest are almost suppressed. In terms of the *output* power spectrum from Eq. (8.6),

$$P_{f(x+\Delta x)} = P_{f(x)} + P_{\Delta f(x)} \quad (8.8)$$

and with substituting Eq. (8.2),

$$P_{out} = P_{in} \rightarrow P_{f(x+\Delta x)} = P_{x+\Delta x} = P_x + P_{\Delta x} \quad (8.9)$$

and from Eq. (8.2), Eq. (8.3) and Eq. (8.5) it follows:

$$P_{\Delta f(x)} = P_{\Delta x} = \frac{1}{2}|m|^2 \quad (8.10)$$

These results demonstrate that for a significantly small modulation index of m , the power of all the sidebands at the output of the NLTL equals the input sideband power and whenever the power of the sidebands in comparison to the carrier are small, the effect of sidebands at the NLTL output is negligible.

8.3 Measurements with LM-LS

With the setup synchronized with the LM-LS method, the following measurements were performed.

8.3.1 Harmonic measurement

In this experiments with manual optimization (try and error) of the IQ modulator parameters, such as IF levels and phase as well as DC offset, a C+SSB signal with RF sideband level of $SBL_{dB_c} = 20 \log(\frac{m}{A}) = -32 dB_c$, or equally $\frac{m}{A} \cong 0.025$ was achieved (see Figure 8.1 (c) and Figure 8.7). This SBL fulfills the requirement for the above mathematical assumption and hence, allows us neglecting the sideband effects in the NLTL downconverted electrooptic signal.

Using the LM-LS method, the drift frequency of IF= 10 kHz was measured at ± 3 Hz (or 3×10^{-4}) and strongly stabilized down to only a few mHz by increasing the IF to 50 kHz (drift of the order of 10^{-7}). This stability enhancement is a consequence of a reduction of the laser flicker noise which decreases with increasing the offset frequency. The results of measurements for the 65-nm CMOS NLTL are shown in Figure 8.8 demonstrating that by increasing the harmonic number a significant gain in comparison to conventional methods and free-running¹ was achieved. This gain is resulted from having a larger SNR which enables a measurement up to a bandwidth of 300 GHz (30th harmonic). To the best of our knowledge, this is the highest achieved

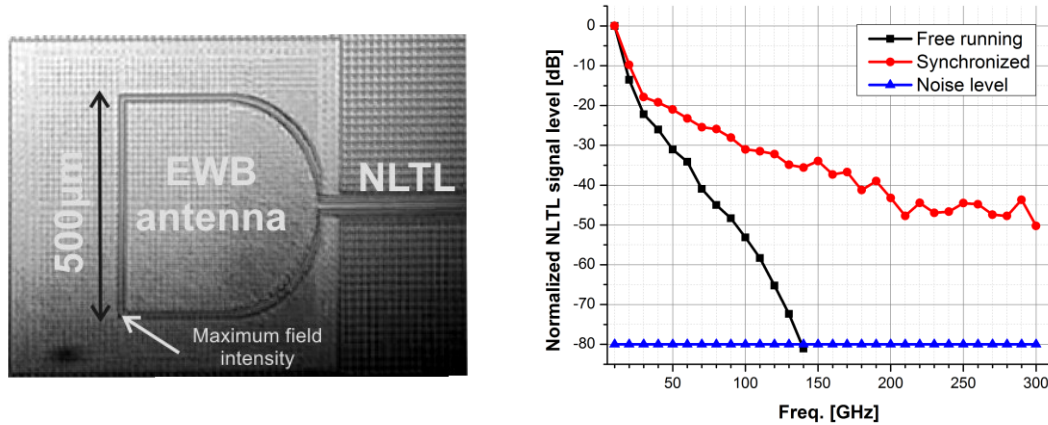


Figure 8.8 Measured signal of the on-chip antenna connected to the NLTL with the LM-LS setup and using lock-in amplifier up to 30th harmonic (300 GHz). The injected signal is 18dBm at 10 GHz. Due to decreasing jitter allows for detecting the higher harmonics with a larger SNR. The system sensitivity is restricted by shot noise level which was measured and calculated in [200] and [201].

¹ "Free-running", here refers to a state that we have jitter but the lock-in still can follow the signal and very similar to MM-LS or LM-MS methods.

bandwidth to date for EOS of electronic devices in CW mode of excitation¹. One should note that this bandwidth is mostly limited by the functionality of the DUT and not by the setup itself as in CMOS technology achieving a signal beyond this frequency is an extremely big challenge.

Having compared with the previous synchronization methods, the LM-MS configuration, in which an external trigger of the microwave generator is obtained from the laser repetition rate by frequency multiplication and division, is also investigated. Using this method, a frequency drift at IF= 10 kHz was measured at ± 25 Hz. Theoretically in comparison with ± 3 Hz drift at 10 kHz for LM-LS, SNR decreases by a factor of $-20\log\left(\sqrt{\frac{BW_{LM-MS}}{BW_{LM-LS}}}\right) = -20\log\left(\sqrt{\frac{25}{3}}\right) = -9.2\text{ dB}$ and is measured at -15 dB for the 15th harmonic. On the other side, this frequency drifts increases linearly proportional to the harmonic number and therefore, at 30th harmonic reaches to 750 Hz. According to the discussion in the previous chapter, since lock-in bandwidth is set at 10 Hz, the higher harmonics are measured with much less accuracy resulting in large deviation for the harmonics greater than 5th. Therefore, EOS must be strongly stabilized against jitter for harmonic measurements. This is crucial as the phase noise at the harmonics increases by a factor of $20\log(n)$, where n is the harmonic number and even a small drift can cause a large error at higher harmonics.

8.3.2 Longitudinal scan and the effect of relative jitter

In general, three sources of jitter including jitter from the laser, from the microwave source and the relative jitter between these two sources cause errors in the EOS measurements. Since the latter can be eliminated by the LM-LS, the mathematical description of its influence on the detected signal is explained as follows: Suppose that EOS performs measurement of a microwave signal with angular frequency ω on an NLTL (or LTL) at position A shown in Figure 8.9. A superposition² of the forward

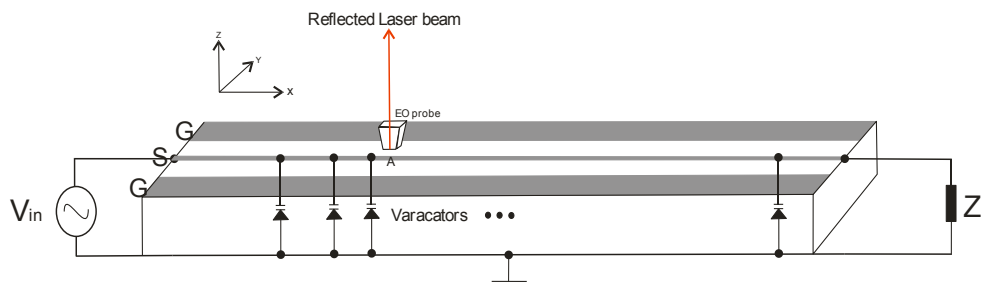


Figure 8.9 Schematic diagram of the NLTL under EOS measurements. The device is a 65nm CMOS NLTL with the length of 7.1 mm (X) and width of 63 μm (Y). Position A shows a typical measurement point. The probe not to be scaled with the device.

¹ In pulsed pump-probe EOS the bandwidth is much larger.

² Although super position is valid only for linear systems, small signals for the NLTL at higher harmonics can be approximated with a linear assumption.

(V_f) and reflected (V_r) signal from the load Z_L , seen by the EO probe, is given by $V = V_f + V_r$, where

$$V_f = |A| \cos(\omega t + \phi_m(t)) \quad (8.11)$$

and ϕ_m , is the random phase noise of the microwave generator. Correspondingly for the reflected signal

$$V_r = |\Gamma||A| \cos(\omega t + \phi_m(t + \tau) + \phi_0) \quad (8.12)$$

where Γ is the complex reflection coefficient from Z_L and τ represents one roundtrip time delay between point A and the load for this reflected signal, whereas ϕ_0 indicates the integrated phase shift of the reflected signal during this delay τ plus a phase of Γ . For EOS detection in the frequency domain, a sampling CW harmonic of the laser repetition rate, with an offset frequency of ω_{IF} given by

$$S_l = |B| \cos((\omega + \omega_{IF})t + \phi_l(t)) \quad (8.13)$$

where ϕ_l is the phase noise from the laser, mixes with the microwave signal resulting in:

$$\begin{aligned} S &= S_l \times V \\ &= k_1 \cos(\omega_{IF}t + \phi_l(t) - \phi_m(t)) \\ &\quad + k_2 \cos(\omega_{IF}t + \phi_l(t) - \phi_m(t + \tau) - \phi_0) \\ &\quad + k_3 \cos((\omega + \omega_{IF})t + \phi_l(t) + \phi_m(t)) \\ &\quad + k_4 \cos((\omega + \omega_{IF})t + \phi_l(t) + \phi_m(t + \tau) + \phi_0) \end{aligned} \quad (8.14)$$

where k_1, k_2, k_3, k_4 are constants. The baseband detection electronics rejects the high-frequency terms and the IF signal yields:

$$\begin{aligned} S_{LPF} &= k_1 \cos(\omega_{IF}t + \phi_l(t) - \phi_m(t)) \\ &\quad + k_2 \cos(\omega_{IF}t + \phi_l(t) - \phi_m(t + \tau) - \phi_0) \end{aligned} \quad (8.15)$$

This equation reveals the important role of relative jitter ($\Delta\phi = \phi_l - \phi_m$) in the measurements. In particular, for a free-running EOS (FREOS), in which an *external* microwave generator drives the DUT, uncorrelated variation of ϕ_m and ϕ_l with respect to each other, distorts the phase of the signal. In contrast in LM-LS, due to the coherency between the laser and the microwave signal, random phase in the first term of Eq. (8.15) is suppressed as $\Delta\phi(t, 0) = \phi_m(t) - \phi_l(t) \cong 0$ and only a relative phase shift at time τ i.e, $\Delta\phi(\tau) = \phi_l(t) - \phi_m(t + \tau)$, influences the signal.

A proof of this hypothesis is experimentally shown by scanning the NLTL over a long time and observing the accumulated timing jitter. For this reason, a scan is longitudinally¹ performed for 5 mm out of a 7.1 mm-long NLTL at 20 GHz (second harmonics of its input fundamental) in both LM-LS and FREOS regimes. As depicted in Figure 8.10, much less signal distortion and a clear dip (resulted from the interference of the forward and backward signals) at 2.7 mm from the load can be

¹ In the x direction from the load to generator

observed for the case of the LM-LS. Evidently, since the reflected signal for the FREOS arrives after the delay time of τ to point A, accumulation of a large random phase given in Eq. (8.15) leads to a much shorter coherence length for the interference pattern. Based on these facts the LM-LS, due to its strongly minimized jitter capability is a valuable method for ultrahigh bandwidth electrooptic analysis of active mm-wave and THz circuits.

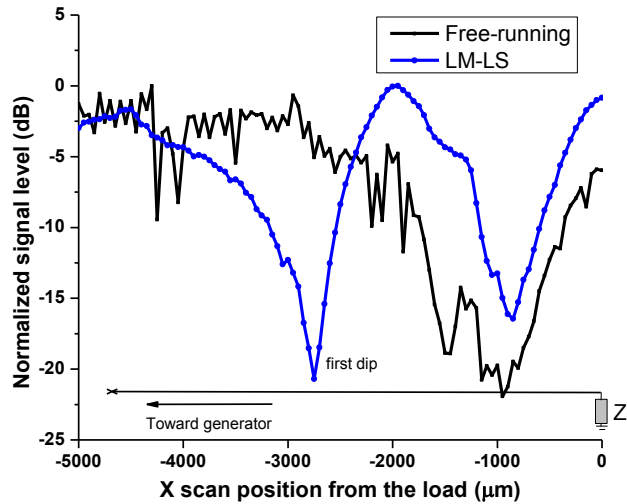


Figure 8.10 Longitudinal scanning of the NLTL at the second harmonic (20 GHz) measured with both LM-LS and FREOS. The NLTL is 7.1 mm long and terminated by an on-chip antenna. The scan range is 5 mm which starts from the terminating load Z_L (on-chip antenna) toward the generator (see Figure 8.9). Each scan step is $50 \mu\text{m}$ and the depicted signal is an average of 4 scans. A dip at 2.7 mm in LM-LS can clearly be seen due to significantly reduce of the relative jitter.

9. Optical Network Analysis

Measurements

In Chapter 3, recent advances in electronic network analyzer extension modules for the characterization of ultrafast electronic devices up to 1.1 THz were explained. It was also mentioned about the drawbacks of this approach such as challenging calibration [83], and alternatively, EOS was introduced. At this time, it is good to stress on the use of this approach for mm-wave network analysis. Although, some work such as [130], [154], [195]–[197] have demonstrated EOS for S-parameter measurements of transmission lines and passive structures, only few attention [133] have been paid to nonlinear and active devices. In this chapter, NLTL measurements and capabilities of EOS in measuring S-parameters, standing waves, effective permittivity, as well as dispersion are demonstrated.

It is necessary to mention that in contrast to works such as [97] and [140], instead of using a photoconductive pulse, here, the CW excitation of the devices is used for the characterization of active or nonlinear devices.. Because, the response of a nonlinear system to a short pulse and hence, using convolution, will not lead us to a meaningful interpretation of the system behavior. Also, the response of a nonlinear system strongly depends on the level of the applied signal to DUT and working in small or large signal regimes must be considered. This concept is also valid for electronic network analyzers as recently the large signal measurements in nonlinear systems have been presented with X-parameters instead of S-parameters [198]. The good thing is that in our EOS measurements at the signal harmonics can be performed by filtering each harmonic with a lock-in amplifier or the Fourier transformation without concerning about the complex mathematical analysis of the nonlinear system.

9.1 Device under test

Two NLTLs including a single-port device with on-chip $50\ \Omega$ load terminated, and a two-port device so called quasi-open, were subjected to the measurements (see Figure 9.1). Both these lines, excluding their bonding pads have a length of 7.1 mm

and contain uniformly incorporated 190 varactors. Also, on-chip calibration loads including short, open and $50\ \Omega$, which are connected to bonding pads¹, were characterized for further use in measurement analysis.

9.2 Scanning of the NLTLs

The DUTs are fed with a 10 GHz signal at 18 dBm of power in a fully coherent LM-LS² configuration. Each of the NLTLs was longitudinally scanned with the EO probe up to 5 mm from the load ($L=0$) towards generator in $50\ \mu\text{m}$ steps (in total 100 points). The rest 2.1 mm of the line which is close to the input pads could not be scanned due to mechanical prohibition of the GSG microwave probe housing for the EO probe (see GSG probe in Figure 9.1). The scanning procedure is as follows: the EO probe is held at $5\ \mu\text{m}$ above the NLTL at load ($L=0$) and we start to detect the signal at all harmonics up to 30th. By ending of this measurement, the probe is moved to the next step ($50\ \mu\text{m}$ towards generator) and this procedure repeats until reaching the end of scan range. At each scanning position; harmonics of the signal were measured 50 times with a lock-in time constant of 50 ms ($\text{BW}=20\ \text{Hz}$) and 6 recorded scan was finally averaged. As every scan takes approximately 500 minutes, and during this time the laser deviates with time jitter, this multiple scanning and the averaging uniformly distributes jitter over the scanned samples.

For a CPW structured device, the electric field represents the voltage, provided that the line is long enough and contains no discontinuity. This is already a case for the NLTL.. The voltage can even be precisely calculated from the integrating of the field tangential component over the CPW slot, i.e., according to $V = \int E dl$.

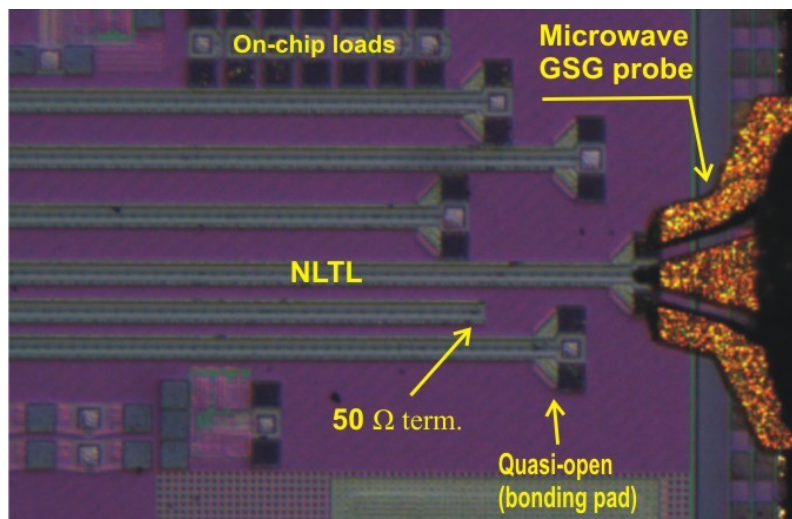


Figure 9.1 A micrograph of on-chip $50\ \Omega$ and quasi open (bonding pad) terminated NLTLs. On-chip loads including short, $50\ \Omega$, and open terminations are connected to the bonding pads.

¹ Identical to the NLTL bonding pads

² See Chapter 8 for full description.

Since EOS is a time-resolved measurement system, the measured pattern of the voltage can be attributed to either a traveling or standing wave. Therefore, a method for their discrimination is required. For this reason, the distinctive properties of standing waves are theoretically described as follows.

Properties of a standing wave

From the transmission line theory [59], the voltage of lossless line terminated with impedance Z_L is given by

$$V(z) = V_{f \max}(e^{-j\beta z} + \Gamma e^{+j\beta z}) \quad (9.1)$$

where $V_{f \max}$ is the maximum amplitude of the input wave and $\Gamma = |\Gamma|e^{j\theta}$ is the load reflection coefficient. Without losing generality, by setting $\theta=0$, and therefore, $\Gamma = |\Gamma|$, the amplitude and phase of a voltage standing wave are given by

$$\begin{cases} |V(z)| = V_{f \max} \sqrt{1 + 2|\Gamma| \cos 2\beta z + |\Gamma|^2} \\ \angle V(z) = \tan^{-1} \left(\frac{\tan(\beta z)}{VSWR} \right) \end{cases} \quad (9.2)$$

where $VSWR = \frac{1+|\Gamma|}{1-|\Gamma|} = \frac{|V(z)|_{\max}}{|V(z)|_{\min}}$. To give an illustration, the magnitude and phase pattern of a standing wave at a value of $VSWR=10$ for a 1 Vp signal is shown in Figure 9.2. This shows that: firstly, the distance between two minima (or maxima) always equals one $\lambda_g/2$, where λ_g is the guide wavelength and secondly, the phase wrap, or in other words, sharp variation of the phase *always* coincides with the

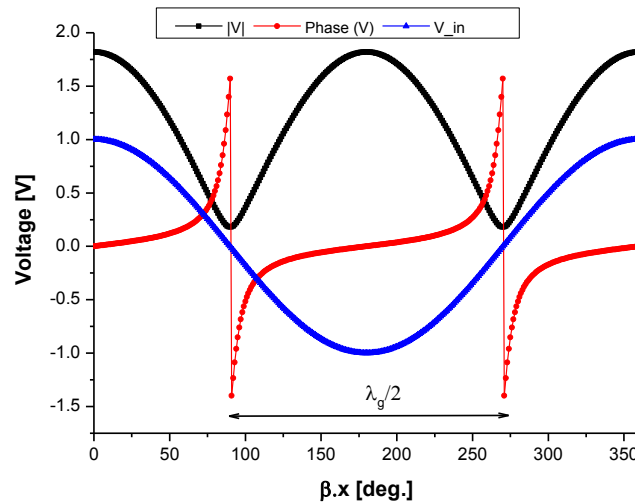


Figure 9.2 The magnitude and phase pattern of a standing wave on a transmission line.

Blue: the forward signal, Black: the standing wave magnitude superimposed from the forward and backward waves due to load mismatch for $VSWR=10$ and the red curve shows the phase of standing wave. β and x are the wave propagation constant and the distance on the line respectively.

minimums of the magnitude. These two properties are independent from the VSWR value and can be used to differentiate between a standing wave and a traveling one.

9.3 Measurement results

A comparative result for the scanning of both NLTLs at the fundamental frequency of 10 GHz (first harmonic) is shown in Figure 9.3. It should be notified that in this

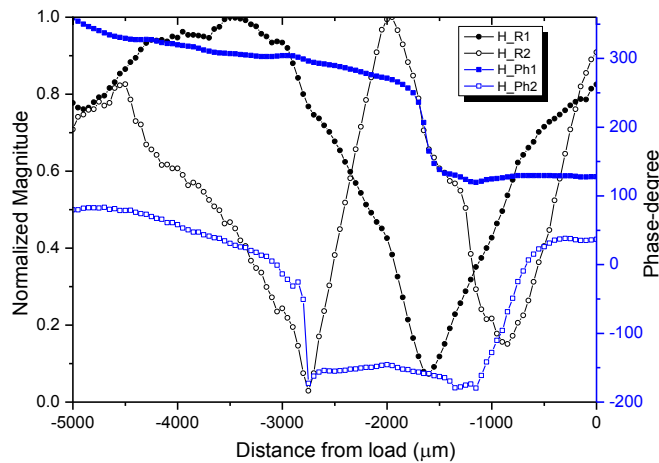


Figure 9.3 EOS longitudinal scanned magnitude and phase for the first harmonic of the NLTL signal. (H-R1, H-Ph1) for 50 Ω and (H-R2, H-Ph2) for the quasi-open line.

graph each data set¹ independently from the other was normalized to its maximum values. Apparently, it can be found that for both lines the magnitude and phase patterns are very similar in shape and more importantly, from a sharp fall in the

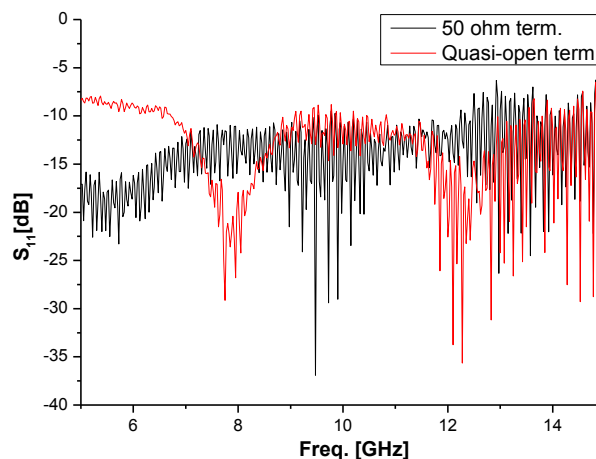


Figure 9.4 Network analyzer measured returned loss of a 50 Ω and quasi open (bonding pad) terminated NLTLs

¹ Measurement for each NLTL

phase which is coincide with the minimum of the magnitude we infer that the pattern is a standing wave.

From the $50\ \Omega$ terminated line pattern, VSWR is measured at $\frac{V_{max}}{V_{min}} = 14.2$, while, network analyzer measurement at the input port of this line at 10 GHz indicates a $VSWR=2$ (or $S_{11} \approx -10\ dB$) (see Figure 9.4). To investigate on this large difference, first we need to characterize the performance of the $50\ \Omega$ terminating load by a microwave network analyzer. The returned loss of this load, in comparison to on-chip short and open measurements is depicted in Figure 9.5.

For the on-chip $50\ \Omega$ load, a $VSWR < 1.2$, including 2 dB of power dissipation for its $40\ \mu\text{m} \times 40\ \mu\text{m}$ bonding pads [46], was measured which turns out that the origin of the large VSWR in EOS of the $50\ \Omega$ terminated NLTL cannot be attributed to imperfection of the terminating load or pads, but the NLTL itself.

An additional proof of this statement is shown in Figure 9.4 as the measured return loss at the input port of the quasi-open NLTL at 10 GHz also shows $S_{11} \approx -10\ dB$ which is close to the value for the $50\ \Omega$ terminated lines. This line was also subjected to two-port microwave measurements in which a 10 GHz signal with 18.5 dBm of power is fed at input port (port 1) and the signal measured at the output port (port 2) with another microwave GSG¹ probe. With this experiment, 6 dB of losses $S_{21} \approx -6\ dB$ is observed which is mostly due to the conversion losses from the fundamental to harmonics due to the nonlinearity of the NLTL. This reveals that for the NLTL, even with an ideal-open termination, after one round-trip of signal, faces 12 dB of losses resulting in $S_{11} \approx -12\ dB$ ($VSWR=1.67$) at the input port. This interesting result exhibits an advantage of EOS over microwave network analyzer measurement as the conversion losses in the latter can be confused with a good load matching. More interestingly, in Figure 9.3, for the quasi-open line, VSWR was measured at 7.69, which shows a better matching for the NLTL to this load than that

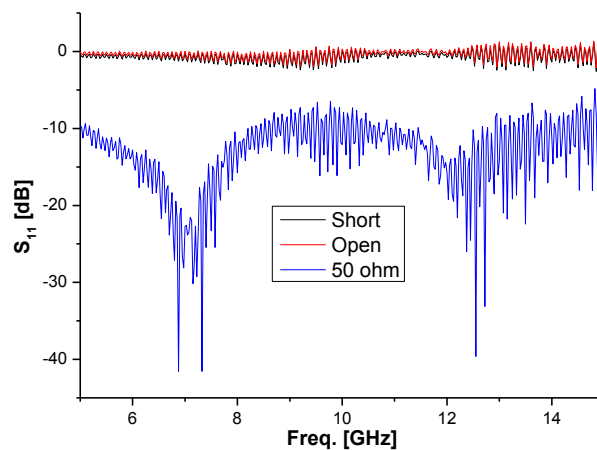


Figure 9.5 Network analyzer measured returned loss for on-chip $50\ \Omega$, short and open loads

¹ See Chapter 7.

with 50Ω termination. This may not be surprising if one takes into account that the load is a bonding pad and not a perfect open. Another reason for high VSWR of both lines may be attributed to the NLTL varactors. As mentioned in Chapter 2, the varactor capacitance of each periodic section is a function of its receiving voltage. Accordingly, by approaching the end of the line, due to losses, the varactors receive less voltage and consequently, their periodic section capacitance and impedance deviates from its designed value of 50Ω . In other words, after a certain length, the impedance of the NLTL section, for example at n th stage, tends to mismatch with its previous stage (section $n-1$). Therefore, to have a good matching between the NLTL sections over its full length, losses, as long as possible must be reduced. The Ohmic and skin effect losses of the NLTL can be minimized by shortening its length or reducing the distance between varactors [44], but the conversion losses as the aim of NLTL design, are needed. Hence, always the amount of mismatch inside the NLTL, especially for the fundamental, has to be tolerated. A strategy to face with such a challenge is to reduce the number of periodic sections, but this also degrades the performance of the NLTL leading to less fall (rise) time compression [44]. To draw a conclusion, one as a designer should find a tradeoff to optimize the NLTL length. It is also necessary to mention that the performance of NLTL in generating harmonics strongly relies on its response to the fundamental and its optimization is highly recommended.

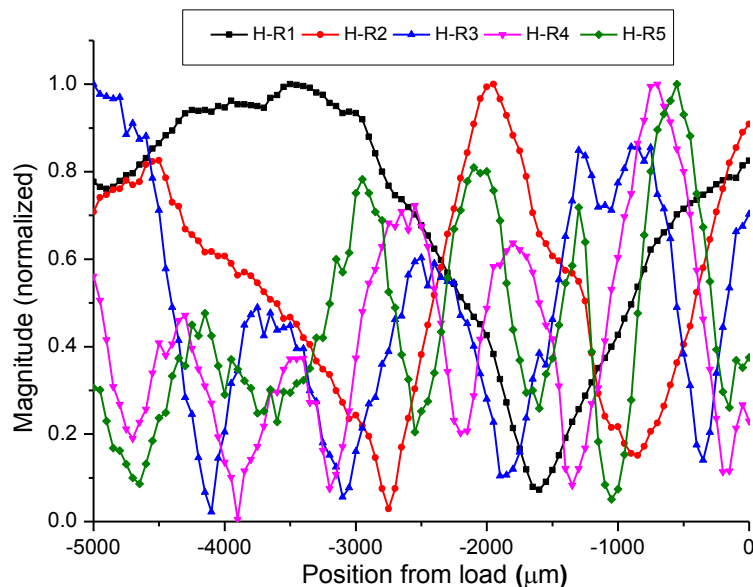


Figure 9.6 EOS measured magnitude of standing waves for the first 5 harmonics of the 50Ω terminated NLTL, $H-R_i$ indicates the magnitude for the harmonic number i , where $i=1,2,3,..$

9.3.1 VSWR for the higher harmonics

As mentioned earlier in this chapter, the line scan was also carried out for higher harmonics up to 30th. Figure 9.6 and Figure 9.7 show the magnitude and Figure 9.8 and Figure 9.9 depict the phase patterns of the standing wave for the 50 Ω terminated NLTL and the quasi-open line up to 5th harmonics (10-50 GHz). The variation of the

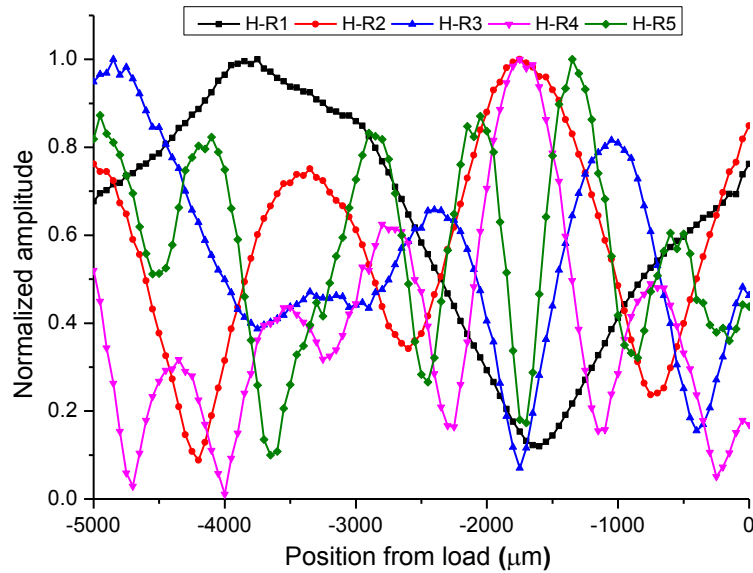


Figure 9.7 EOS measured magnitude of standing waves for the first 5 harmonics of the quasi-open terminated NLTL. H-R i indicates the magnitude for the harmonic number i , where $i=1, 2, 3,..$

local maxima and minima values in the magnitude patterns, which is more visible at 2nd and the higher harmonics, reveals a variant VSWR over the scanned length. This non-uniformity of VSWR may also be attributed to the internal mismatch caused by the different biasing of varactors by both the attenuated traveling wave, and the standing waves at the fundamental frequency.

Also at 2nd harmonic, 3 minima for the quasi-open line and 2 minima for the 50 Ω terminated one can be observed. One less minimum for the 50 Ω lines, closer to generator, shows less standing wave at the beginning of this line. This reveals that unlike the fundamental (see Figure 9.3), 2nd and the higher harmonics can be discriminated for these two lines. The response of the lines to the fundamental and higher harmonics needs to be differentiated, because, the fundamental is a high power pump signal and needs to be considered in a large signal regime while the harmonics are in small signal regime.

Taking into account a conversion loss of 6 dB for the signal reaching the end of the

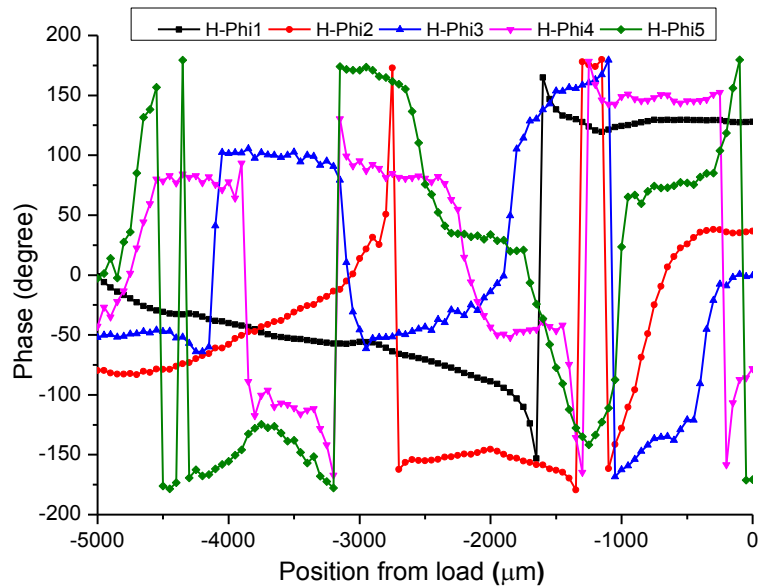


Figure 9.8 Phase of standing waves for the first 5 harmonics of the 50 Ω terminated NLTL. $H\text{-Phi}_j$ indicates the phase for the harmonic number j , where $j=1,2,3,..$

line, the reflected wave biases varactor differently from the forward wave and therefore it sees different impedance. Accordingly, the standing wave pattern should be corrected as

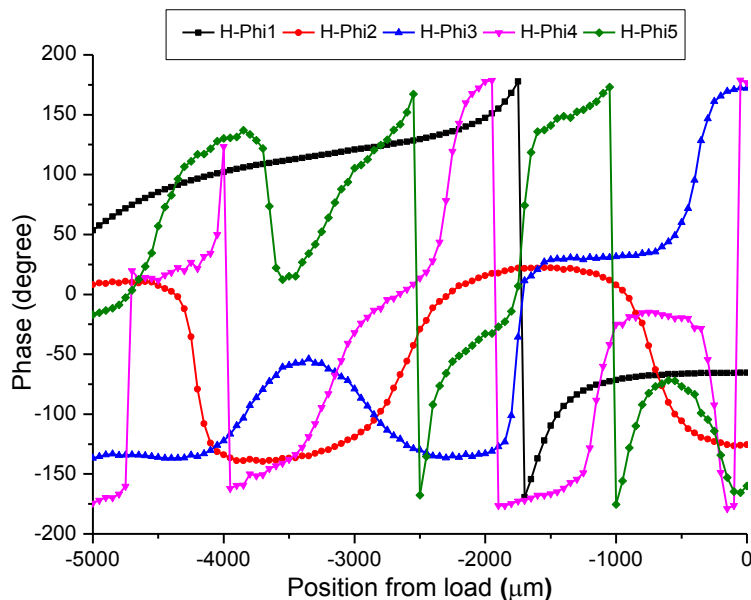


Figure 9.9 EOS measured phase of standing waves for the first 5 harmonics of the quasi-open terminated NLTL. $H\text{-Phi}_j$ indicates the phase for harmonic number j , where $j=1,2,3,..$

$$\begin{cases} V(z) = V_f \max(e^{-\gamma_f z} + \Gamma e^{+\gamma_r z}) \\ \gamma_f = \alpha_f + j\beta_f \\ \gamma_r = \alpha_r + j\beta_r \end{cases} \quad (9.3)$$

while γ_f and γ_r are large signal forward and backward propagation constants including losses respectively. This can make distortions in the standing wave

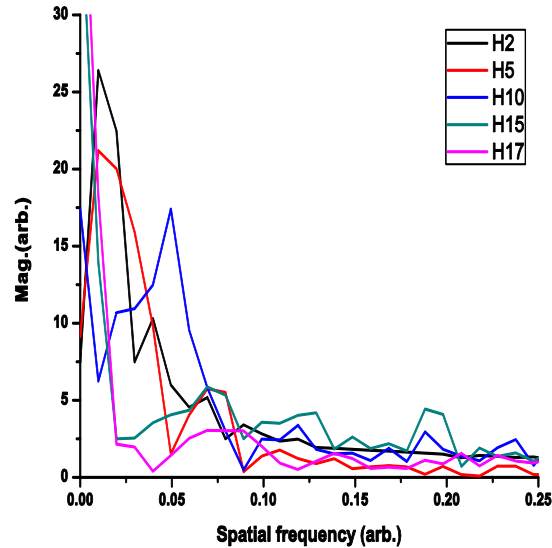


Figure 9.10 Fourier transform of $\cos(\angle V(z))$ for the 50Ω terminated NLTL. The spatial frequency not to be confused with the operation frequency of the circuit. H_i , refers to harmonic number i .

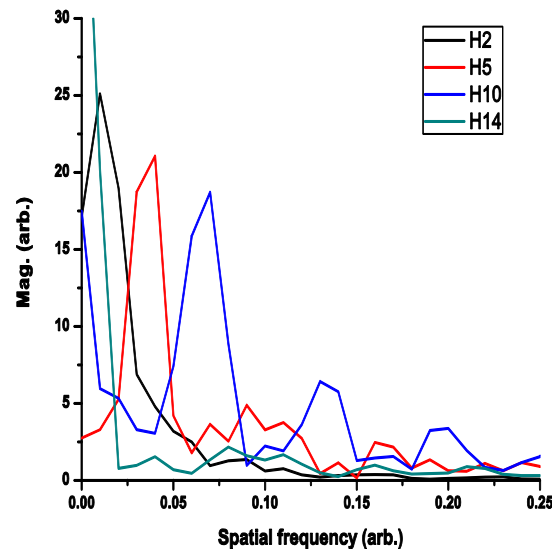


Figure 9.11 Fourier transform of $\cos(\angle V(z))$ for the quasi-open terminated NLTL. The spatial frequency not to be confused with the operation frequency of the circuit. H_i , refers to harmonic number i .

patterns. In contrary, for the higher harmonics, as they have much less power, the system tends to operate in the small signal regime and the general linear standing wave assumption leads to a good approximation. However, the fundamental standing wave also influences the standing wave at the higher harmonics by providing a bias voltage for varactors.

The distortion in the phase diagrams in Figure 9.8 and Figure 9.9, demonstrates nonlinear variation caused by the NLTL periodic sections as voltage controlled phase shifters. Also the coinciding sharp falls of the phase with the minima of the corresponding magnitudes confirm that the patterns are standing wave.

9.3.2 NLTL dispersion

The transmission lines dispersion can considerably impact the performance of an NLTL by broadening fall (rise) time of its propagating wave. Since the wavelength determines the wave propagating constant (β) and the effective permittivity (ϵ_{eff}) of the line, dispersion can be analyzed from the measured wavelength λ_{gi} at each harmonic, where $i=1, 2, 3, \dots$ is the harmonic number.

It was already mentioned that the interval between two sequential voltage minima, or two phase wraps of a standing wave pattern, equals one $\lambda_g/2$ (see Figure 9.2). This value also is an indication for the main period of a pattern. Unfortunately, due to fluctuations of the measured patterns at the higher harmonics, this period cannot be precisely measured either from the magnitude or the phase. One possible solution is to apply the Fourier transform to these patterns and find peaks corresponding to the main spatial frequency of the pattern. Alternatively, a cosine (sine) function of a fluctuated *phase* pattern, gives more visible peaks. This is mathematically true as from (9.2) the phase $\angle V(z)$ is periodic with a period of π corresponding to $z = \lambda_g/2$ and hence, $\cos(\angle V(z))$ also has the same period. The

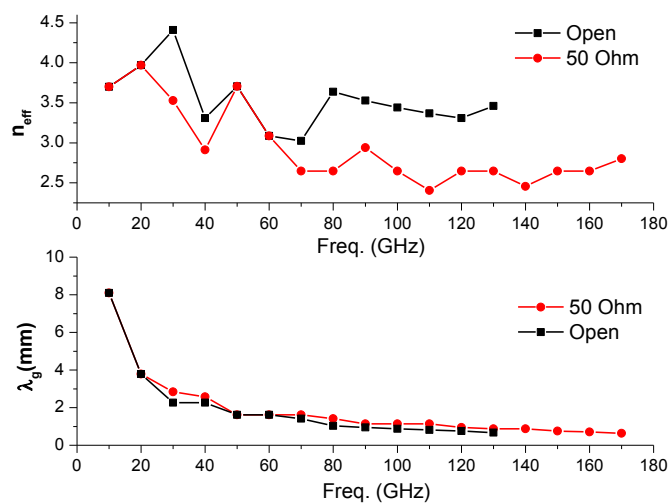


Figure 9.12 Refractive index and guide wavelength as a function of frequency at harmonics of a 10 GHz signal for both 50 Ω and quasi-open terminated NLTLs.

Fourier transform of this function for both lines is depicted in Figure 9.10 and Figure 9.11, while the horizontal axis shows an arbitrary spatial frequency. For each harmonic, one needs to find the position of the main peak and translate it to the wavelength. For the quasi-open line, the main peak for the second harmonic appears at the spatial frequency of $f=0.00125$ and referring to Figure 9.9, it corresponds to the actual $\lambda_{g2}=3.78$ mm on the line and consequently λ_{gi} can be found by reading their relative peak positions.

The result is shown in Figure 9.12 demonstrating both λ_{gi} and effective refractive index $n_{eff}(f) = \sqrt{\epsilon_r(f)_{eff}} = \frac{\lambda_{gi}}{\lambda_{g0}}$ as a function of frequency. For the quasi-open and the 50 Ω -terminated lines, up to 14th and 17th harmonics were detected respectively and detection of the higher harmonics was hampered due to low SNR and the fewer samples per cycle. The sample per cycle determines spatial resolution with respect to the signal wavelength. For example, one cycle for the 2nd harmonic contains 75 measurement samples while the 17th harmonic contains only 12. Furthermore, Figure 9.12 shows that the refractive index of the NLTL is not a linear function of frequency and varies between 2.4 to 4.4. This variation is attributed to the CMOS varactor capacitance response. Moreover, the refractive index of 3.96 at 20 GHz (2nd harmonic) represents relative permittivity of 15.68 which is 3.73 times larger than the $\epsilon_{r-eff}=4.2$ for the SiO₂ substrate¹ of the host CPW. This is not surprising as the varactors can synthetically increase the capacitance of the line in response to the voltage. Evidently, from simulations [46] the host LTL was designed with the characteristics impedance of $Z_1 = 82 \Omega$ having a capacitance of $C_{LTL}=2.93$ fF per each NLTL section. By applying a voltage with $V_{pp}=5.3$ V (or 18.5 dBm of power), each varactor adds up $C_v=6.1$ fF average capacitance to the section as depicted in Figure 9.13, and therefore, the ultimate equivalent capacitance of each periodic section is $C_{NLTL}=C_{LTL}+C_v=9.03$ pF. Since the inductance L of the line did not change in both cases, it can be said that $\frac{\epsilon_{r,NLTL}}{\epsilon_{r,LTL}} = \frac{C_{NLTL}}{C_{LTL}} = \frac{9.03}{2.93} = 3.08$ which approaches the measured value of 3.73.

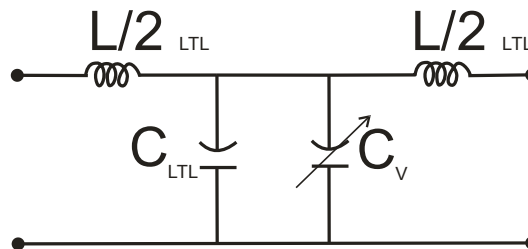


Figure 9.13. Circuit model of one NLTL periodic section.

¹ See Chapter 7

10. Photoconductive Probing vs. EOS

In Chapter 3, noncontact photoconductive (PC) probing, as a photonic approach for the application of ultrafast devices characterization was introduced. Also, some work [101], [125] which show the wideband detection of this scheme for measurement with the *pulse excitation* of circuits in the *pump-probe* detection system were also addressed. For the case of *CW excited* regime, to the best of our knowledge no work has been reported in *near field* PC probing. However, Löffler et al. [131] used PC antenna for *free-space* detection in a CW regime and Wächter et al. [126] demonstrated *near field* sensing for a frequency selective surface (FSS) at THz range in a *pump-probe* TDS. In this chapter PC probing experimental results and a comparison with EOS are demonstrated.

10.1 The photoconductive probe and the setup

A commercial [199] THz near field probe fabricated by deposition of gold on a Lt-GaAs substrate is used for PC measurements. As shown in Figure 10.1, several designs for the probe, including High Resolution (HR), High Resolution and Sensitivity (HRS), and High Sensitivity (HS) can be considered. Since dimensions of our DUT is very small (tens of μm), rather a large tip size of both HRS and HS excludes them from a high spatial resolution measurement. Therefore, the HR probe is selected at the expense of losing sensitivity. In comparison to HR, HS and HSR are

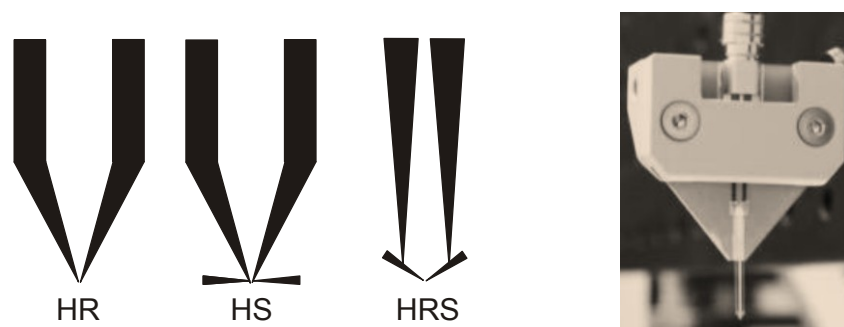


Figure 10.1 The THz near field probe and 3 tip geometry designs. Figure adapted by author from [199].

good options for far field detection as reported in [131]. The specifications of the HR and HS probes are given in Table 10.1, and a micrograph of the HR tip is shown in Figure 10.2. In this probe structure, the metallic tip senses the induced near electric field of devices and PC gate which is placed $\approx 140 \mu\text{m}$ far from the tip collects the current. This current as the response of device hence is amplified by a baseband trans-impedance (current) amplifier and then is given to a 2 MHz bandwidth lock-in amplifier. Except for the detection mechanism, the rest of the setup is similar to that in the EOS shown in Chapter 5.

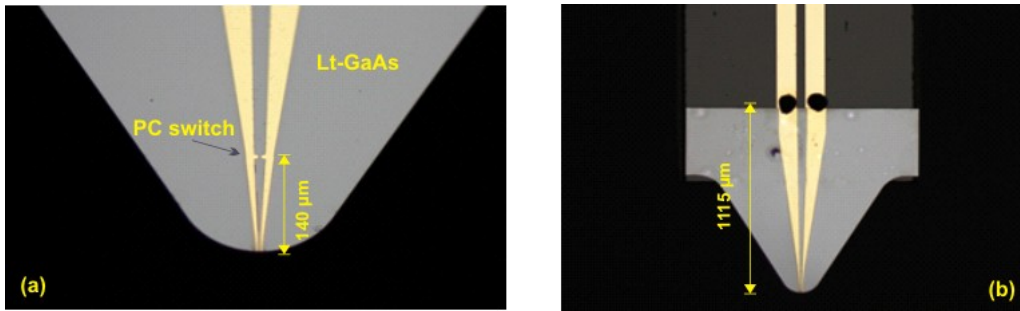


Figure 10.2 (a) A micrograph of the HR probe tip and (b) the tip in a larger field of view

Table 10.1 Specifications of the PC probe. Source from [199].

THz PC probe type →	HR	HS
Maximum spatial resolution	3 μm	100 μm
Photoconductive gap size at tip	1.5 μm	3 μm
Dark current @ 1V Bias	< 0.5 nA	< 0.4 nA
Photocurrent	> 1 μA	> 0.6 μA
Excitation wavelength (nm)	700 - 860	700- 860
Optical excitation power (mW)	< 4	< 4

10.2 Measurement results

The HR probe was mounted in a setup which is schematically shown in Figure 10.3

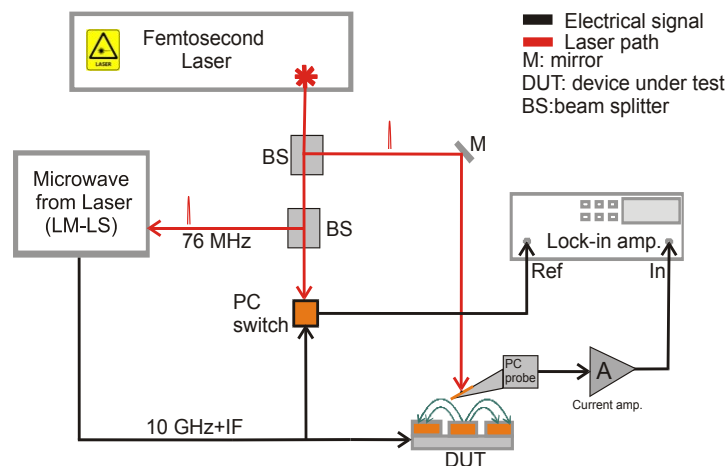


Figure 10.3 A very simplified schematic of the PC probing setup

and the following measurements were performed.

10.2.1 Harmonic scan

In a very similar way to the EOS measurements, PC probing is performed on the on-chip antenna (which terminates the NLTL) up to 300 GHz, and comparative results are shown in Figure 10.4. Apparently, it can be seen that in PC probing, by increasing

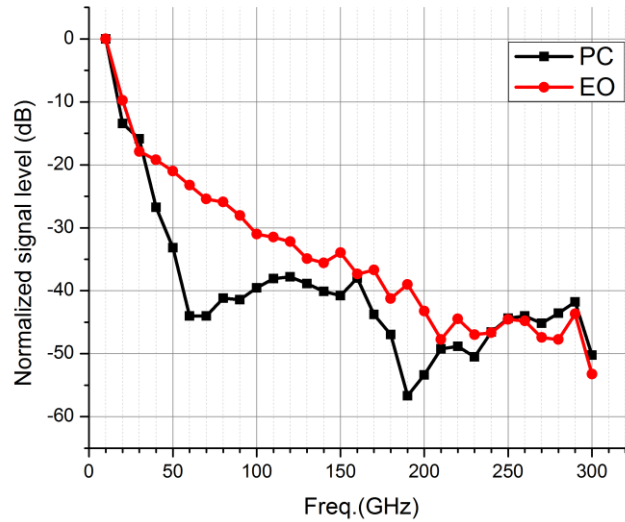


Figure 10.4 Comparison between PC and EOS probing for an NLTL up to 300 GHz

the frequency the signal level reduces which due to small SNR in the measurements. Three main sources of the measurement errors can be enumerated as: Firstly, the PC probe signal is noisier than that in EOS due to lack of balanced detector which

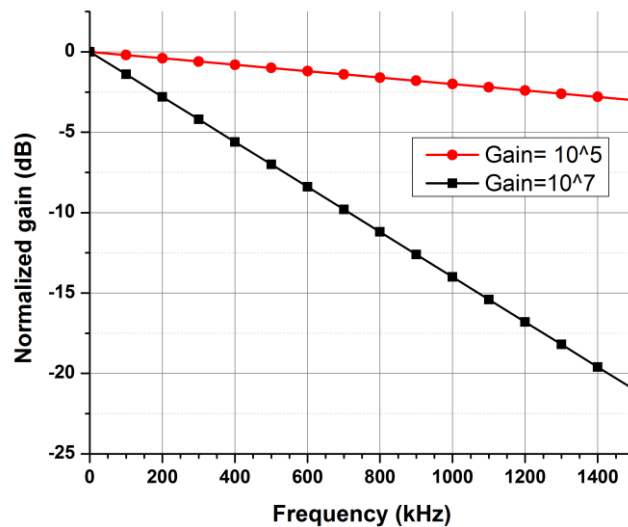


Figure 10.5 Frequency response of the current amplifier for different gains

suppresses laser amplitude noise. Secondly, for this measurements, one needs a current amplifier gain of $G=10^7$ (140 dB) which is two orders of magnitude larger than $G=10^5$ (100 dB) for the EOS. This high gain introduces larger input impedance for the trans-impedance amplifier which in conjunction with the loaded capacitance of the probe and its connected cable makes a low pass filter with frequency response shown in Figure 10.5. Assuming downconversion of the fundamental 10 GHz signal at an IF= 50 kHz, the IF= 1500 kHz represents 30th harmonic which is approximately 22 dB attenuated by the amplifier response. This attenuation can significantly decrease the SNR. The third reason may be attributed to the frequency response of the PC probe at RF which is unknown to us. Unfortunately, characterization data for the probe at these low frequencies was neither available from the manufacturer nor possible to create with our setups.

10.2.2 Transversal scan

The NLTL was scanned in transversal direction¹ and the comparative results with the EOS are shown in Figure 10.6. It can be seen that unlike the EOS, the PC probing is unable to detect a dip at the center of the scan. The reason is that the EO probe is only sensitive to the tangential components of the electric field² whereas the PC probe detects a superposition of all components. For this reason in contrast to the PC probing which cannot precisely distinguish between field components, EOS is a vector based detection system.

10.2.3 Longitudinal scan

Similar to EOS demonstrated in previous chapters, 5 mm out of 7.1 mm full length of the NLTL was longitudinally scanned and measured up to 3rd harmonic (60 GHz) of a

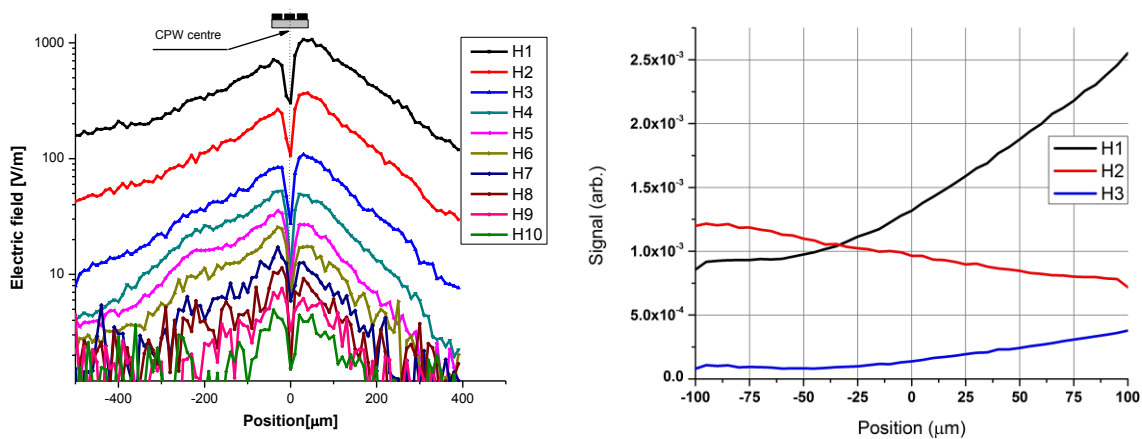


Figure 10.6 Transversal scan of the NLTL by the EOS (left) and PC probing (right)

¹ See Chapter 6 for the geometry of DUT.

² The electric field between signal and ground strips of the CPW line

20 GHz fundamental in free-running¹ regime. The result of this measurement is depicted in Figure 10.7 which in comparison to EOS shows much less amplitude resolution, as well as very less sensitivity to the phase variations of the signal. This can be caused by the far field antenna effect detection of the probe due to long electrodes of the PC probe. This theory is examined by vertically departing of the probe from the wafer and antenna in few centimeters. Surprisingly, it is observed that the signal at lower harmonics still can be detected. This also reveals another advantage of EOS for near field probing due to less affecting by crosstalk.

10.2.4 Field mapping

Near field mapping is a very interesting feature of PC and EOS measurements. To demonstrate this feature, both measurements for a 20 GHz fundamental are shown in

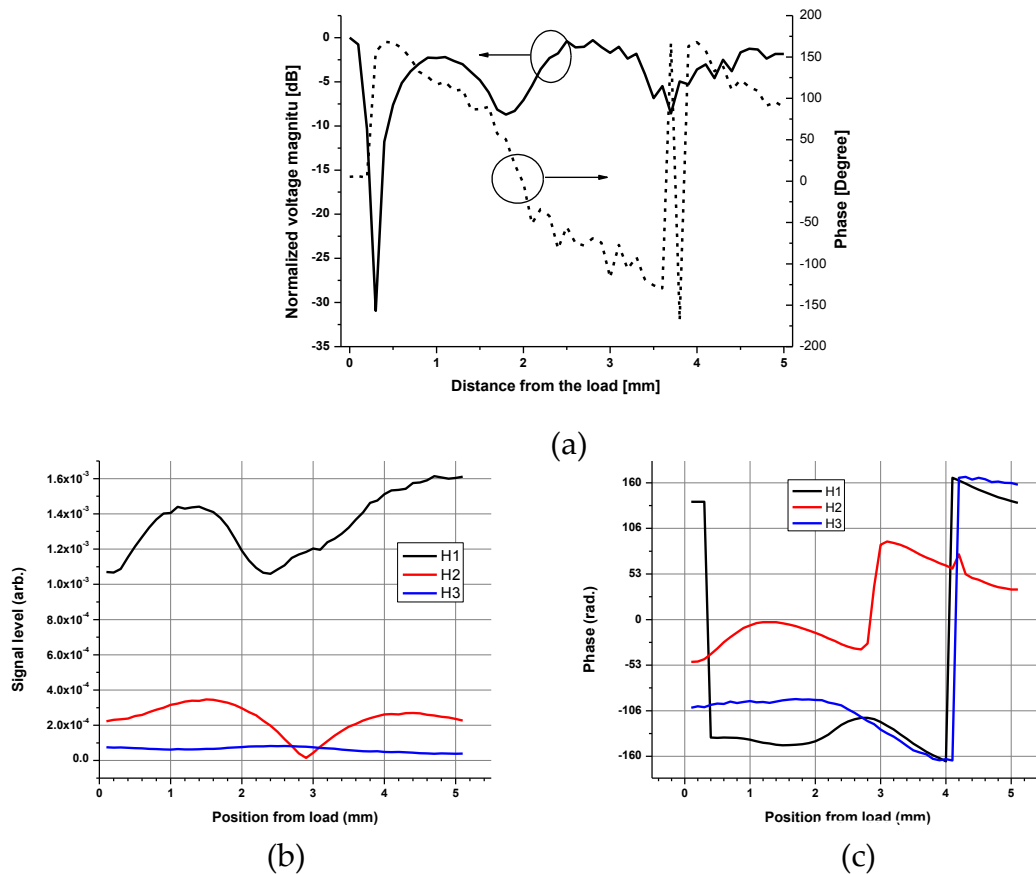


Figure 10.7 Comparison between EOS and PC probing for longitudinal scan of the NLTL terminated with an on-chip antenna. (a) EOS amplitude and phase measurement at 20 GHz in free-running mode, (b),(c) amplitude and phase of PC probing for the first 3 harmonics of the 20 GHz fundamental.

¹ In this case “free-running” means lock-in can lock with reference signal but there is no LM-LS synchronization. At first three harmonics the signal can be precisely detected in the free-running mode.

Figure 10.8. Evidently, it can be realized that EOS shows much better amplitude and phase resolution than that for the PC probing. In particular, for the case of *CW excited* circuit and with having radiation of the device from near to the far field, as the case of this on-chip antenna, the PC probe is incapable to discriminate between the near and far field. Although, such a probe at THz frequencies in time gated pump-probe has shown capability for the near field detection [126], in our microwave CW measurements the electrode arms of the probe, acting as a short antenna, and hence, significantly degrade the measurement spatial resolution. In other words, the detection of the probe is strongly dependent on the structure under test and its

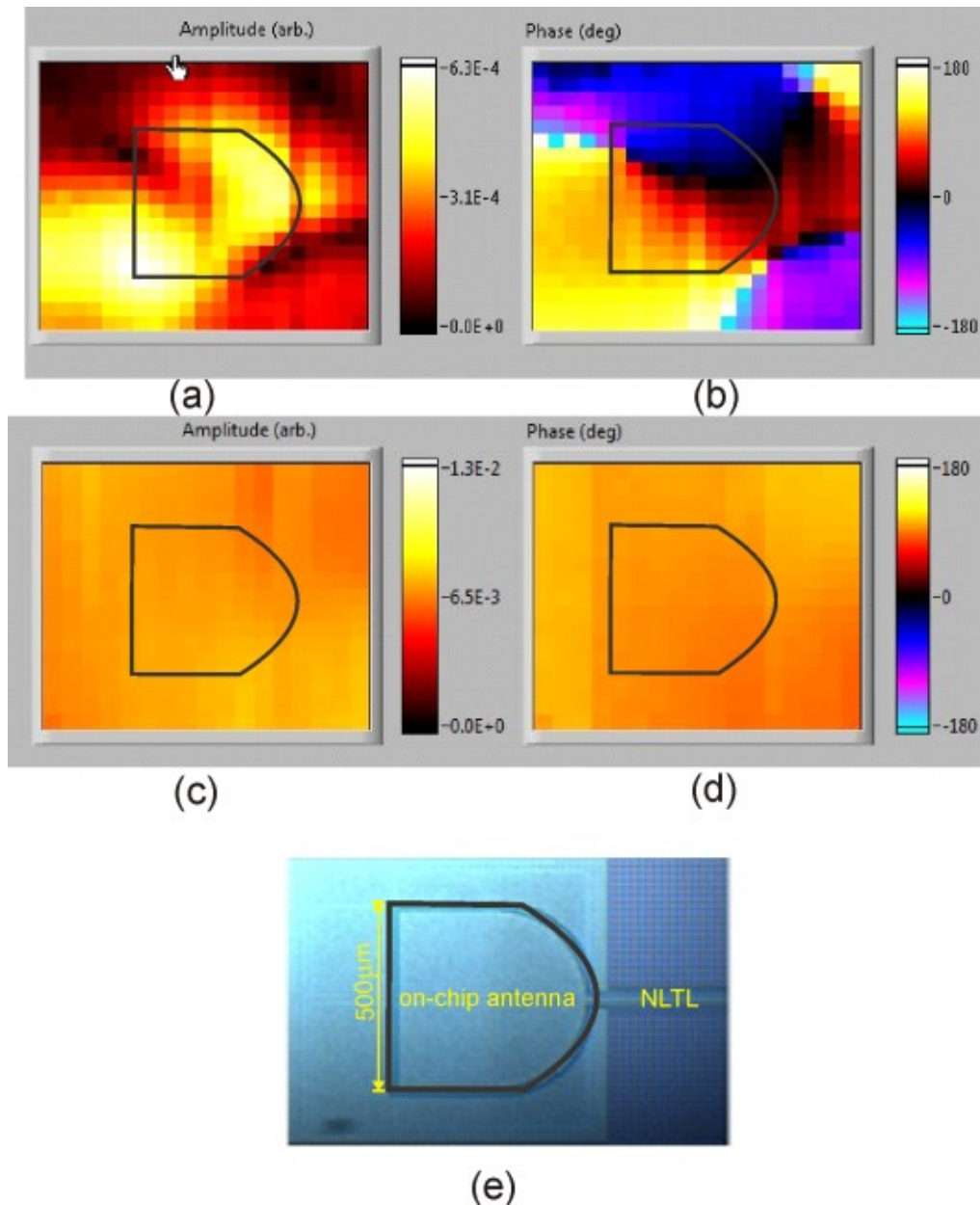


Figure 10.8 Field mapping of the on-chip antenna connected to the NLTL at 20 GHz fundamental. (a) EOS amplitude, (b) EOS phase, (c) PC amplitude, (d) PC phase and (e) a micrograph of the antenna.

mechanism of radiation. More precisely speaking, likewise [126] as long as the structure has a confined electric field and the detection mechanism is time gated (e.g. the pump-probe), the probe is a good candidate for near field detection, otherwise its performance is much weaker than an EO probe. On the other side, invasiveness of the probe due to the inductance of the metallic electrodes and mutual coupling to DUTs can potentially be high. Based on the above experimental results EOS which has already shown high resolution vectorial measurements is preferred.

11. Conclusion

The work presented here is divided into two main parts. In the first part consisting of Chapter 2, THz waves and their application are presented. Common ways of generating and detecting THz waves and the necessity for cheap and compact sources are described. The recent advances in the electronics as a demanded solution for low and medium power THz applications are reviewed in general and it has been more focused on the NLTL approach as a broadband THz source in detail.

The second part of this thesis comprehensively describes challenges and limitations in the characterization of THz device with electronic instrumentation. By concentrating on a typical state-of-the-art system, consisting of a modern network analyzer equipped with THz extension modules, capable of measuring frequencies beyond 1 THz, the performance and challenges of this approach is demonstrated. Main drawbacks of these systems such as having high complexity and cost as well as limitation in frequency band measurements are demonstrated. It is emphasized that systematic errors in electronic measurement system caused by degrees of uncertainty in calibrations and lack of precise models for devices in particular at the high frequencies of THz can degrade their achieved results. As an alternative, the photonic and optical characterization methods such as EOS and PC probing are introduced which in comparison to the electronic approach are capable of detecting several or even tens of THz bandwidth, much far beyond today's electronic devices operational frequency range. Additionally two common methods of EOS including internal and external sampling with their advantages and disadvantages are also reviewed, and it is mentioned that due to ease of use and implementing, as well as freedom in selecting devices more applicability, the external EOS probing is preferred for on-wafer measurements.

Following-up with the EOS, in Chapter 4 its theory and principle of operation are described in detail and based on results published in the literature, and our simulation, it is demonstrated that how a suitable electrooptic crystal for the application of THz circuit characterization can be selected. As a useful evaluation criterion, the invasiveness of the most commonly used electrooptic crystals in probing of the near field of the devices is compared.

In Chapter 5, an EOS setup consisting of a freely positionable EO probe mounted on an XYZ stage, a rotary wafer station and a very high resolution vision system for DUTs is introduced. The setup is specified with properties such as having a very good sensitivity and a large dynamic range, as well as an ultra-broadband measurement bandwidth.

Since as the first plan of the experimental setup, a fiber pigtailed EO probe was used, challenges of using this probe in measurements are explained and finally, it was decided to evolve the setup to non-pigtailed solution. This approach, has resolved drawbacks of the former plan while retained its advantages.

To assess the measurement setup bandwidth and its capabilities, it is necessary to have an ultra-broadband electronic DUT. By a flashback to Chapter 2 and recognizing NLTL as a broadband THz electronic source, it was decided to use such a device which was fabricated in 65-nm CMOS technology and provided by our ULTRA project partners. For detection of the highest frequency radiated from this device and characterize the device functionalities, different known synchronization techniques such as LM-MS and MM-LS are tried.

During this exploration, and by facing with prohibiting challenges such as jitter in the system, the initial setup was able to measure only at first 5 harmonics of the NLTL signal without having a large deviation from the real values measured by on-wafer microwave probing technique. By analyzing the results, hidden sources of the measurement errors are figured out. Following this procedure, by replacing the lock-in amplifier in the setup with a low-frequency spectrum analyzer and self-referencing method, up to 200 GHz (20th harmonic of a 10 GHz input signal) for the NLTL was detected.

The influence of jitter in measurements is comprehensively investigated. Amongst the three kinds of jitter including jitter from the laser as a sampling pulse, jitter from the microwave generator as a signal source, and relative jitter between these two, the latter is distinguished as the main source of the measurement errors and studied in detail. It is demonstrated that the other types of jitter which are caused by the instruments used, can be slightly optimized by choosing the IF signal in the heterodyne system far from the DC. Looking for a solution to resolve the relative jitter, finally, a novel solution called laser master- laser slave (LM-LS) is introduced. In this technique, which in EOS for the first time is presented in this work, the femtosecond pulse of the laser with the help of photodiode generates a microwave signal which is then fed to the DUT. At the same time the laser pulse samples with the sampling EO probe. Due to the full coherency of this detection, the amount of jitter in the system is extremely reduced that enables to measure the NLTL up to 300 GHz (30th harmonic of the input 10 GHz fundamental). This achievement is not only far beyond 50 GHz that the preliminary measured with other conventional synchronization techniques, but also can be demonstrated as a very good record for CMOS semiconductor technology measurement bandwidth.

Moreover, with the help of experimental results, advantages of EOS over electronic measurement approach are demonstrated. It is shown that EOS can carry out continuous ultra-broadband measurements without the need for change in the setup components during measurements, or deal with sophisticated calibrations. EOS is also capable of measuring the near field mapping of devices as a useful tool for detecting their malfunctioning. In this work, this feature is demonstrated by scanning of the NLTL in all longitudinal, transversal, vertical and two dimensional schemes. Interestingly, the longitudinal scan can also be used for measurement of the S-parameters, VSWR, and the internal behaviors of the NLTL. It is also demonstrated that unlike a linear transmission system, a unique VSWR number cannot be defined for the NLTL as the varactors are voltage dependent and response to a signal which varies over the scan range. This is an interesting result which may not be achieved by microwave probing. Also, internal features of devices like high conversion losses can be confused with a good matching at the input port for the case microwave a network analyzer, while EOS scanning can distinguish them. Transversal EOS scan also can demonstrate near field effects such asymmetry of the field distribution for the NLTL or non-desired modes.

In the last chapter of this work, a so-called near field photoconductive probe is used as an alternative for EOS to detect the NLTL signal. In comparison with EOS, it is demonstrated that in the photoconductive probing the SNR can be smaller than that in EOS as is shown for the scanning of the NLTL harmonics. Not only RF, but also the effect of baseband electronic in the measurement such as using a very high gain current amplifier is studied. This shows that after downconversion of the NLTL signal, detecting the higher harmonics can be hampered by loading the amplifier with the capacitance of cables and hence, acting as a lowpass filter. It is also mentioned that EOS by detecting all harmonics with almost a flat response takes advantages over PC probing which can be influenced by the frequency response of the photoconductive antennas used. For the case of NLTL characterization which needs CW excitation, it is concluded that the PC near field probe can also detect the far field with its metallic arms and drastically affect the measurements. Evidently, from near field mapping, it is figured out that EOS shows better phase and amplitude sensitivity, a better spatial resolution and good vectorial detection performance; therefore, it is preferred over the photoconductive probing method.

Bibliography

- [1] "Agilent." [Online]. Available: <http://www.keysight.com>.
- [2] J. Valdmanis, "Picosecond and subpicosecond optoelectronics for measurements of future high speed electronic devices," *Electron Devices Meet.*, pp. 597–600, 1983.
- [3] "ULTRA project." [Online]. Available: <http://www2.teknik.uu.se/ultrac/start.asp>.
- [4] X. Hu, L. Tripodi, M. K. Matters-Kammerer, S. Cheng, and A. Rydberg, "65-nm CMOS Monolithically Integrated Subterahertz Transmitter," *IEEE Electron Device Lett.*, vol. 32, no. 9, pp. 1182–1184, Sep. 2011.
- [5] "TSMC." [Online]. Available: <http://www.tsmc.com/english/default.htm>.
- [6] P. de Maagt, P. H. Bolivar, and C. Mann, "Terahertz science, engineering and systems from space to earth applications," *Encycl. RF Microw. Eng. Ed. by K. Chang. John Wiley Sons, Inc., ISBN 0-471-27053-9*, 2005.
- [7] D. Van Der Weide, "Applications and Outlook for Terahertz," *Opt. photonic news*, pp. 49–53, 2003.
- [8] P. H. Siegel, "Terahertz technology," *IEEE Trans. Microw. Theory Tech.*, vol. 50, no. 3, pp. 910–928, Mar. 2002.
- [9] M. Y. Glyavin *et al.*, "A 670 GHz gyrotron with record power and efficiency," *Appl. Phys. Lett.*, vol. 101, no. 15, p. 153503, 2012.
- [10] G. P. Gallerano and S. Biedron, "OVERVIEW OF TERAHERTZ RADIATION SOURCES," in *FEL*, 2004, pp. 216–221.
- [11] V. Bratman and M. Glyavin, "TERAHERTZ GYROTRONS: DEVELOPMENT AND APPLICATIONS," in *Kharkiv Young Scientists Conference on radiophysics, electronics, photonics and biophysics*, 2011.
- [12] P. D. Coleman, "Reminiscences on selected millennium highlights in the quest for tunable terahertz-submillimeter wave oscillators," *IEEE J. Sel. Top. Quantum Electron.*, vol. 6, no. 6, pp. 1000–1007, 2000.
- [13] Y. U. Jeong *et al.*, "High power table-top THz free electron laser and its application," *IRMMW-THz Conf.*, 2009.
- [14] C. H. Lee, Ed., *Picosecond optoelectronic devices*. Academic Press Inc, 1984.
- [15] D. Mittleman, *Sensing with Terahertz Radiation*. Berlin Heidelberg: Springer, 2003.
- [16] S. L. Dexheimer, *Terahertz spectroscopy: principles and applications*. CRC Press, 2007.
- [17] Z. Y. Zhao, S. Hameau, M. Voos, and J. Tignon, "THz generation by optical rectification and competition with other nonlinear processes," in *AIP Conference Proceedings*, 2007.
- [18] K. Wynne and J. J. Carey, "An integrated description of terahertz generation through optical rectification, charge transfer, and current surge," *Opt.*

- Commun.*, vol. 256, no. 4–6, pp. 400–413, Dec. 2005.
- [19] G. Scalari *et al.*, “THz and sub-THz quantum cascade lasers,” *Laser Photonics Rev.*, vol. 3, no. 1–2, pp. 45–66, Feb. 2009.
- [20] S. Kumar, “Recent Progress in Terahertz Quantum Cascade Lasers,” vol. 17, no. 1, pp. 38–47, 2011.
- [21] A. Valavanis *et al.*, “Terahertz quantum cascade lasers with >1 W output powers,” *Electron. Lett.*, vol. 50, no. 4, pp. 309–311, Feb. 2014.
- [22] “laser world.” [Online]. Available: <http://www.laserfocusworld.com/>.
- [23] “Resolve magazine.” [Online]. Available: <http://www.lehigh.edu/engineering/news/resolve/2011/vol2/a-breakthrough-for-thz-lasers-2.html>.
- [24] M. Reddy *et al.*, “Monolithic Schottky-collector resonant tunnel diode oscillator arrays to 650 GHz,” *IEEE Electron Device Lett.*, vol. 18, no. 5, pp. 218–221, 1997.
- [25] S. Iezekiel, Ed., *Microwave Photonics: Devices and Applications*. John Wiley & Sons, Inc., 2009.
- [26] “Virginia diodes.” [Online]. Available: www.vadiodes.com.
- [27] “RPG.” [Online]. Available: <http://www.radiometer-physics.de>.
- [28] A. Maestrini *et al.*, “Design and Characterization of a Room Temperature All-Solid-State Electronic Source Tunable From 2.48 to 2.75 THz,” *IEEE Trans. Terahertz Sci. Technol.*, vol. 2, no. 2, pp. 177–185, Mar. 2012.
- [29] L. A. Samoska, “An overview of solid-state integrated circuit amplifiers in the submillimeter-wave and THz regime,” *IEEE Transactions on Terahertz Science and Technology*, vol. 1, no. 1, pp. 9–24, 2011.
- [30] M. Urteaga *et al.*, “InP HBT Integrated Circuit Technology for Terahertz Frequencies,” *2010 IEEE Compd. Semicond. Integr. Circuit Symp.*, pp. 1–4, Oct. 2010.
- [31] T. B. Reed, Z. Griffith, P. Rowell, M. Field, and M. Rodwell, “A 180mW InP HBT Power Amplifier MMIC at 214 GHz,” *2013 IEEE Compd. Semicond. Integr. Circuit Symp.*, pp. 1–4, Oct. 2013.
- [32] M. Seo *et al.*, “InP HBT IC technology for terahertz frequencies: Fundamental oscillators Up to 0.57 THz,” *IEEE J. Solid-State Circuits*, vol. 46, no. 10, pp. 2203–2214, 2011.
- [33] V. Jain *et al.*, “1.0 THz f_{max} InP DHBTs in a refractory emitter and self-aligned base process for reduced base access resistance,” in *69th Annual Device Research Conference (DRC)*, 2011, vol. 96, no. 2, pp. 271–272.
- [34] M. J. W. Rodwell *et al.*, “THz Indium Phosphide Bipolar Transistor Technology,” in *Compound Semiconductor Integrated Circuit Symposium (CSICS)*, 2012 IEEE, 2012, pp. 8–11.
- [35] J. Park, “Fully Integrated Silicon Terahertz Transceivers for Sensing and Communication Applications,” 2013.
- [36] J. B. Hacker, Y. M. Lee, H. J. Park, J.-S. Rieh, and M. Kim, “A 325 GHz InP HBT Differential-Mode Amplifier,” *IEEE Microw. Wirel. Components Lett.*, vol. 21, no. 5, pp. 264–266, 2011.

- [37] A. Tessmann, A. Leuther, R. Loesch, M. Seelmann-Eggebert, and H. Massler, "A metamorphic HEMT S-MMIC amplifier with 16.1 dB gain at 460 GHz," *Tech. Dig. - IEEE Compd. Semicond. Integr. Circuit Symp. CSIC*, 2010.
- [38] A. Tessmann *et al.*, "A 600 GHz low-noise amplifier module," *2014 IEEE MTT-S Int. Microw. Symp.*, pp. 1–3, 2014.
- [39] U. J. Lewark, A. Tessmann, H. Massler, A. Leuther, T. Zwick, and I. Kallfass, "An active 600 GHz frequency multiplier-by-six S-MMIC," *2013 IEEE MTT-S Int. Microw. Symp. Dig.*, pp. 1–3, Jun. 2013.
- [40] W. Deal, X. B. Mei, K. M. K. H. Leong, V. Radisic, S. Sarkozy, and R. Lai, "THz monolithic integrated circuits using InP high electron mobility transistors," *IEEE Trans. Terahertz Sci. Technol.*, vol. 1, no. 1, pp. 25–32, 2011.
- [41] R. Lai *et al.*, "Sub 50 nm InP HEMT Device with Fmax Greater than 1 THz," in *Electron Devices Meeting, 2007. IEDM 2007. IEEE International, 2007*, vol. 3, pp. 609–611.
- [42] "Fraunhofer." [Online]. Available: <https://www.fraunhofer.de/>.
- [43] M. Tonouchi, "Cutting-edge terahertz technology," *Nat. Photonics*, pp. 97–105, 2007.
- [44] M. Rodwell, D. Bloom, and B. Auld, "Nonlinear transmission line for picosecond pulse compression and broadband phase modulation," *Electron. Lett.*, 1987.
- [45] J. Bostak, D. Van der Weide, D. Bloom, and B. A. Alud, "All-electronic terahertz spectroscopy system with terahertz free-space pulses," *J. Opt. Soc. Am. B*, vol. 11, no. 12, pp. 2561–2565, 1994.
- [46] L. Tripodi, M. Matters-Kammerer, and D. Van Goor, *Extremely wideband CMOS circuits for future THz applications*. Springer, 2012.
- [47] M. K. Matters-Kammerer, L. Tripodi, R. van Langevelde, J. Cumana, and R. H. Jansen, "RF Characterization of Schottky Diodes in 65-nm CMOS," *IEEE Trans. Electron Devices*, vol. 57, no. 5, pp. 1063–1068, May 2010.
- [48] M. J. W. Rodwell, M. Kamegawa, R. Yu, M. Case, E. Carman, and K. S. Giboney, "GaAs nonlinear transmission lines for picosecond pulse generation and millimeter-wave sampling," *IEEE Trans. Microw. Theory Tech.*, vol. 39, no. 7, pp. 1194–1204, Jul. 1991.
- [49] M. Case, "Nonlinear Transmission Lines for Picosecond Pulse, Impulse and Millimeter-Wave Harmonic Generation," 1993.
- [50] M. Li, R. G. Harrison, R. E. Amaya, J. Duchamp, P. Ferrari, and N. G. Tarr, "CMOS Varactors in NLTL Pulse-Compression Applications," in *2nd European Microwave Integrated Circuits*, 2007, no. October, pp. 607–610.
- [51] D. Leblebici and Y. Leblebici, *Fundamental of High-Frequency CMOS Analog Integrated Circuits*. Cambridge University Press, 2009.
- [52] F. Yu, K. G. Lyon, and E. C. Kan, "Harmonic Generation from Integrated Nonlinear Transmission Lines for RFID Applications," in *Microwave Symposium Digest (MTT)*, 2010, pp. 844–847.
- [53] A. B. Kozyrev, K. Hongjoon, and D. W. van der Weide, "Observation of

- the Parametric Amplification in Nonlinear Left-Handed Transmission Line Metamaterials," in *Antennas and Propagation Society International Symposium, IEEE*, 2006, pp. 4129–4132.
- [54] A. B. Kozyrev et al., "Higher harmonic generation and parametric instabilities in left-handed nonlinear transmission lines," *IEEE Antennas Propag. Soc. Int. Symp.*, pp. 209–212, 2005.
- [55] A. B. Kozyrev and D. W. van derWeide, "Nonlinear transmission lines in left-handed media," in *IEEE MTT S Digest*, 2004, pp. 317–320.
- [56] A. B. Kozyrev and D. W. Van Der Weide, "Nonlinear Wave Propagation Phenomena in Left-handed Transmission-line Media," *IEEE Trans. Microw. Theory Tech.*, vol. 53, no. 1, pp. 238–245, 2005.
- [57] A. Kozyrev, H. Kim, and D. W. Van Der Weide, "Active Left-Handed Transmission Line Media," in *IEEE MTT-S International Microwave Symposium Digest*, 2006, pp. 432–435.
- [58] I. Wolff, *Coplanar microwave integrated circuits*. John Wiley & Sons, Inc., 2006.
- [59] D. M. Pozar, *Microwave Engineering*, 3rd ed. John Wiley & Sons, Inc., 2005.
- [60] M. J. W. Rodwell et al., "Active and nonlinear wave propagation devices in ultrafast electronics and optoelectronics," *Proc. IEEE*, vol. 82, no. 7, pp. 1037–1059, Jul. 1994.
- [61] D. W. van der Weide, "Delta-doped Schottky diode nonlinear transmission lines for 480-fs, 3.5-V transients," *Appl. Phys. Lett.*, vol. 65, no. 7, p. 881, 1994.
- [62] M. Y. Frankel, S. Gupta, and J. A. Valdmanis, "Terahertz Attenuation and Dispersion Characteristics of Coplanar Transmission Lines," *IEEE Trans. Microw. Theory Tech.*, vol. 39, no. 6, pp. 910–916, 1991.
- [63] F. Martin, "Modelling Soliton Pulses in Nonlinear Transmission Lines for Millimeter Wave Generation," *30th Eur. Microw. Conf. 2000*, no. 1, pp. 1–4, Oct. 2000.
- [64] J. R. Thorpe, D. P. Steenson, and R. E. Miles, "Harmonic Generation using Soliton Effects I o n Nonlinear Transmission Lines," in *High Frequency Postgraduate Student Colloquium*, 1997, no. September.
- [65] F. Martin, "EFFECTS OF NON-LINEAR CAPACITANCE ON SOLITON WAVE PROPAGATION IN NLTLs FOR MILLIMETER WAVE MULTIPLICATION," in *2nd International Conference on Microwave and Millimeter Wave Technology*, 2000, pp. 485–488.
- [66] D. S. Ricketts et al., "On the Self-Generation of Electrical Soliton Pulses," *IEEE J. Solid-State Circuits*, vol. 42, no. 8, pp. 1657–1668, 2007.
- [67] C. Tiofack, A. Mohamadou, T. Kofané, and F. Ndzana, "SHAPE CHANGING COLLISIONS OF BRIGHT SOLITONS IN NONLINEAR ELECTRICAL TRANSMISSION LATTICES," 2008.
- [68] F. Martín and X. Oriols, "Understanding soliton wave propagation in nonlinear transmission lines for millimeter wave multiplication," *Int. J. Infrared Millimeter Waves*, 2001.
- [69] K. Narahara, "Characterization of Nonlinear Transmission Lines for Short

- Pulse Amplification," *J. Infrared, Millimeter, Terahertz Waves*, pp. 411–421, Dec. 2009.
- [70] D. Ricketts, X. Li, and D. Ham, "Electrical soliton oscillator," *Microw. Theory Tech.*, vol. 54, no. 1, pp. 373–382, 2006.
- [71] S. Ben Mbarek *et al.*, "Investigations of room temperature bolometers for THz applications," *35th Int. Conf. Infrared, Millimeter, Terahertz Waves*, pp. 1–2, 2010.
- [72] Y. Wang, Z. Zhao, Z. Chen, and L. Wang, "Characterization of Golay detector for the absolute power measurement of terahertz radiation," *2012 37th Int. Conf. Infrared, Millimeter, Terahertz Waves*, pp. 1–2, Sep. 2012.
- [73] P. L. Richards, "Bolometers for infrared and millimeter waves," *J. Appl. Phys.*, vol. 76, no. 1, p. 1, 1994.
- [74] "Anritsu." [Online]. Available: <http://www.anritsu.com>.
- [75] "Rohde & Schwarz." [Online]. Available: <http://www.rohde-schwarz.com>.
- [76] J. Hesler, Y. Duan, B. Foley, and T. Crowe, "THz Vector Network Analyzer Measurements and Calibration," *Int. Symp. Sp. Terahertz Technol.*, pp. 381–320, 2010.
- [77] "OML." [Online]. Available: <http://www.omlinc.com/>.
- [78] "Cascade probes." [Online]. Available: <http://www.cmicro.com/>.
- [79] N. S. B. and R. M. W. M. F. Bauwens, N. Alijabbari, A. W. Lichtenberger, "A 1.1 THz micromachined on-wafer probe," in *2014 IEEE MTT-S International Microwave Symposium (IMS2014), Tampa, FL, 2014*, pp. 1–4.
- [80] "GGB probes." [Online]. Available: <http://www.ggb.com/>.
- [81] VDI, "High Dynamic Range Transceivers." [Online]. Available: www.vadiodes.com.
- [82] D. F. Williams, J. A. Jargon, and P. D. Haie, "The Impact of Characteristic Impedance on Waveform Calibrations."
- [83] D. F. Williams, "500 GHz - 750 GHz Rectangular-Waveguide Vector-Network-Analyzer Calibrations," *Trans. Terahertz Sci. Technol.*, vol. 1, no. 1, pp. 1–14, 2011.
- [84] A. R. Kerr, "Mismatch Caused by Waveguide Tolerances , Corner Radii , and Flange Misalignment," 2010.
- [85] M. Kahrs, "50 years of RF and microwave sampling," *IEEE Trans. Microw. Theory Tech.*, vol. 51, no. 6, pp. 1787–1805, Jun. 2003.
- [86] M. S. Shakouri, H. Matsuura, B. a. Auld, and D. M. Bloom, "Active Probes for Millimeter-Wave On-Wafer Measurements," *38th ARFTG Conf. Dig.*, pp. 62–67, Dec. 1991.
- [87] M. S. Shakouri, A. Black, B. A. Auld, and D. M. Bloom, "500GHz GaAs MMIC PROBE," *Electron. Lett.*, vol. 29, no. 6, 1993.
- [88] R. Y. Yu, M. Reddy, J. Pusl, S. T. Allen, M. Case, and M. J. W. Rodwell, "Millimeter-wave on-wafer waveform and network measurements using active probes," *IEEE Trans. Microw. Theory Tech.*, vol. 43, no. 4, pp. 721–729, Apr. 1995.
- [89] O. Wohlgemuth *et al.*, "A NLTL-Based Integrated Circuit for a 70-200 GHz VNA System," in *28th European Microwave Conference, 1998*, 1998, vol. 1, pp.

- 104–107.
- [90] A. W. YU, R. Y., CASE, M. KAMEGAWA, M. SUNDARAM, M. RODWELL, M. J. W. GOSSARD, "275GHz 3-MASK INTEGRATED GaAs SAMPLING CIRCUIT," *Electron. Lett.*, vol. 26, no. 13, pp. 949–951, 1990.
- [91] M. J. W. Rodwell, R. Yu, P. Reddy, S. Allen, and U. Bhattacharya, "Active probes for on-wafer millimeter-wave network analysis," in *Proceedings of Conference on Precision Electromagnetic Measurements Digest*, 1994, p. 8.
- [92] O. Wohlgemuth, M. J. W. Rodwell, R. Reuter, J. Braunstein, and M. Schlechtweg, "Active probes for 2-port network analysis within 70-230 GHz," *1999 IEEE MTT-S Int. Microw. Symp. Dig. (Cat. No.99CH36282)*, vol. 4, pp. 1635–1638, 1999.
- [93] O. Wohlgemuth *et al.*, "An integrated circuit for network analysis within 50-200 GHz," in *1998 IEEE Sixth International Conference on Terahertz Electronics Proceedings. THZ 98. (Cat. No.98EX171)*, 1998, pp. 113–116.
- [94] K. Noujeim, J. Martens, and T. Roberts, "Frequency-Scalable Vector Network Analyzers," in *ARMMS*, 2011.
- [95] Chi H. Lee, Ed., *Picosecond optoelectronic devices*. Elsevier, 1984.
- [96] D. E. Cooper and S. c. Moss, "Picosecond Optoelectronic Measurement of the High-Frequency Scattering Parameters of," *IEEE J. Quantum Electron.*, vol. QE-22, no. 1, pp. 94–100, 1986.
- [97] H. Heiliger, G. Vortmeier, and H. Kurz, "External photoconductive sampling up to 1 THz," *Lasers and Electro-Optics*, vol. 2294, no. 1996, pp. 2–3, 1998.
- [98] M. C. Beard, G. M. Turner, and C. a. Schmuttenmaer, "Subpicosecond carrier dynamics in low-temperature grown GaAs as measured by time-resolved terahertz spectroscopy," *J. Appl. Phys.*, vol. 90, no. 12, p. 5915, 2001.
- [99] K. Ma, R. Urata, D. A. B. Miller, and J. S. Harris, "Low Temperature Growth of GaAs on Si Substrates for Ultra-fast Photoconductive Switches," *MRS Proc.*, vol. 768, no. 6, pp. 800–804, 2003.
- [100] a. Hussain and S. R. Andrews, "Dynamic range of ultrabroadband terahertz detection using GaAs photoconductors," *Appl. Phys. Lett.*, vol. 88, no. 14, p. 143514, 2006.
- [101] R. K. Lai, J.-R. Hwang, T. B. Norris, and J. F. Whitaker, "A photoconductive, miniature terahertz source," *Appl. Phys. Lett.*, vol. 72, no. 24, p. 3100, 1998.
- [102] G. David *et al.*, "Photoconductive probing and computer simulation of microwave potentials inside a SiGe MMIC," *1998 Top. Meet. Silicon Monolith. Integr. Circuits RF Syst. Dig. Pap. (Cat. No.98EX271)*, pp. 187–191, 1998.
- [103] J. Coutaz, "Semiconductor materials for ultrafast photoswitches," *Acta Phys. Pol. A*, vol. 2, no. 4 95, 2002.
- [104] J. Hwung, H. Chen, J. F. Whitaker, J. V Rudd, and A. A. Mi, "An Ultrafast Photoconductive Sampling Gate Integrated with a JFET Amplifier," in *Lasers and Electro-Optics Society Annual Meeting*, 1995, pp. 331–332.
- [105] K. Ogawa, J. Allam, N. de B. Baynes, J. R. a. Cleaver, T. Mishima, and I. Ohbu, "Ultrafast characterization of an in-plane gate transistor integrated with

- photoconductive switches," *Appl. Phys. Lett.*, vol. 66, no. 10, p. 1228, 1995.
- [106] M. B. Ketchen *et al.*, "Generation of subpicosecond electrical pulses on coplanar transmission lines," *Appl. Phys. Lett.*, vol. 48, no. 12, p. 751, 1986.
- [107] T. Pfeifer and H. Heiliger, "High-frequency on-wafer testing with freely positionable silicon-on-sapphire photoconductive probes," *IEEE MTT-S Dig.*, 1995.
- [108] M. Beard, G. Turner, and C. Schmuttenmaer, "Transient photoconductivity in GaAs as measured by time-resolved terahertz spectroscopy," *Phys. Rev. B*, vol. 62, no. 23, pp. 15764–15777, Dec. 2000.
- [109] M. Y. Frankel, J. F. Whitaker, G. a. Mourou, F. W. Smith, and A. R. Calawa, "High-voltage picosecond photoconductor switch based on low-temperature-grown GaAs," *IEEE Trans. Electron Devices*, vol. 37, no. 12, pp. 2493–2498, 1990.
- [110] F. W. Smith *et al.*, "Picosecond GaAs-based photoconductive optoelectronic detectors," *Appl. Phys. Lett.*, vol. 54, no. May 2015, pp. 890–892, 1989.
- [111] S. Kono, M. Tani, and K. Sakai, "Detection of up to 60 THz with an LT-GaAs photoconductive antenna," in *CLEO*, 2001, pp. 102–103.
- [112] M. D. Feuer, S. C. Shunk, P. R. Smith, M. C. Nuss, and N. H. Law, "100 GHz wafer probes based on photoconductive sampling," *IEEE Photonics Technol. Lett.*, vol. 5, no. 3, pp. 361–364, Mar. 1993.
- [113] M. Y. Frankel, "500-GHz characterization of an optoelectronic S-parameter test structure," *IEEE Microw. Guid. Wave Lett.*, vol. 4, no. 4, pp. 118–120, Apr. 1994.
- [114] C. H. Hung, H.-L.A.; Polak-Dingels, P.; Webb, K.J.; Smith, T.; Huang, H.C.; Lee, "Millimeter-Wave Monolithic Integrated Circuit Characterization by a Picosecond Optoelectronic Technique," *IEEE Microw. Theory Tech.*, vol. 37, no. 8, pp. 1223–1231, 1989.
- [115] M. Y. Frankel, J. F. Whitaker, and G. a. Mourou, "Optoelectronic transient characterization of ultrafast devices," *IEEE J. Quantum Electron.*, vol. 28, no. 10, pp. 2313–2324, 1992.
- [116] M. C. Feuer, M.D.; Shunk, S.C.; Smith, P.R.; Law, N.H.; Burrus, C.A.; Nuss, "Broadband Optoelectronic Wafer Probing," in *High Speed Semiconductor Devices and Circuits*, 1993, pp. 485–493.
- [117] S. L. Huang, E. A. Chauchard, C. H. Lee, H. A. Hung, T. T. Lee, and T. Joseph, "On-Wafer Photoconductive Sampling of MMICs," *IEEE Microw. Theory Tech.*, vol. 40, no. 12, pp. 2312–2320, 1992.
- [118] J. R. Hwang, H. J. Cheng, J. F. Whitaker, and J. V Rudd, "Photoconductive sampling with an integrated source follower/amplifier," *Appl. Phys. Lett.*, vol. 68, no. 11, pp. 1464–1466, 1996.
- [119] P. T. Matloubian, M.; Rosenbaum, S.E.; Fetterman, Harold R.; Greiling, "Wide-band millimeter wave characterization of sub-0.2 micrometer gate-length AlInAs/GaInAs HEMTs," *Microw. Guid. Wave Lett. IEEE*, vol. 1, no. 2, pp. 32–34, 1991.
- [120] D. Matloubian, M.; Fetterman, H.; Kim, M.E.; Oki, A.; Camou, J.; Moss, S.; Smith, "Picosecond optoelectronic measurement of S parameters and optical

- response of an AlGaAs/GaAs HBT," *Microw. Theory Tech. IEEE Trans.*, vol. 38, no. 5, pp. 683–686, 1990.
- [121] R. W. Eisenstadt, W.R.; Hammond, R.B.; Dutton, "On-Chip Picosecond Time-Domain Measurements for VLSI and Interconnect Testing Using Photoconductors," *Electron Devices, IEEE Trans.*, vol. 32, no. 2, pp. 364–369, 1985.
- [122] T. Webb, K.J.; Chauchard, E.A.; Polak-Dingels, P.; Lee, C.H.; Hung, H.-L.; Smith, "A time-domain network analyzer which uses optoelectronic techniques," in *IEEE MTT-S International Microwave Symposium Digest*, 1989, pp. 217–220.
- [123] J. F. Whitaker, "Advances in optically-based sampling for diagnostics of microwave digital and analog circuits," in *Pacific Rim Conference on Lasers and Electro-Optics*, 1999, vol. 3, pp. 787–788.
- [124] J. F. Williamson, S.L.; Al-Hemyari, K.; Cheng, H.J.; Hwang, J.-R.; Nees, J.A.; Whitaker, "Picosecond photoconductive probe," in *IEEE Lasers and Electro-Optics Society Annual Meeting*, 1996, pp. 184–185.
- [125] R. K. Lai, J. Hwang, J. Nees, T. B. Norris, and J. F. Whitaker, "A fiber-mounted, micromachined photoconductive probe with 15 nV/Hz^{1/2} sensitivity," *Appl. Phys. Lett.*, vol. 69, no. September, pp. 1843–1845, 1996.
- [126] M. Wächter, M. Nagel, and H. Kurz, "Tapered photoconductive terahertz field probe tip with subwavelength spatial resolution," *Appl. Phys. Lett.*, vol. 95, no. 4, p. 41112, 2009.
- [127] M. Nagel, A. Safiei, T. Pletzer, and H. Kurz, "Active Terahertz near-field probes for high-resolution free-carrier density imaging applications," *37th Int. Conf. Infrared, Millimeter, Terahertz Waves*, vol. 2, pp. 1–2, Sep. 2012.
- [128] M. Nagel, C. Matheisen, A. Deninger, and H. Kurz, "Continuous-wave terahertz near-field spectroscopy and imaging with a micro-machined photomixer probe-tip," *Infrared, Millimeter, Terahertz Waves (IRMMW-THz)*, *37th Int.*, 2012.
- [129] M. J. W. Rodwell, M. Riaziat, K. J. Weingarten, D. M. Bloom, and L. Ginzton, "Internal Microwave Propagation and Distortion Characteristics of Travelling-Wave Amplifiers Studied by Electro-Optic Sampling," in *MTT-S International Microwave Symposium Digest*, 1986, vol. 86, pp. 333–336.
- [130] R. Majidi-Ahy, B. A. Auld, and D. M. Bloom, "100 GHz on-wafer S-parameter measurements by electrooptic sampling," *IEEE MTT-S Int. Microw. Symp. Dig.*, pp. 0–3, 1989.
- [131] T. Löffler, T. Pfeifer, H. G. Roskos, H. Kurz, and D. W. van der Weide, "Stable optoelectronic detection of free-running microwave signals with 150-GHz bandwidth," *Microelectronic Engineering*, vol. 31, no. 1–4, pp. 397–408, 1996.
- [132] M. Weiss and M. Crites, "Time-domain optical sampling of nonlinear microwave amplifiers," in *IEEE MTT-S Digest*, 1999.
- [133] T. Pfeifer *et al.*, "Optoelectronic on-chip characterization of ultrafast electric devices: Measurement techniques and applications," *IEEE J. Sel. Top. Quantum*

- Electron.*, vol. 2, no. 3, pp. 586–603, 1996.
- [134] G. A. Whitaker, J.F.; Valdmanis, J.A.; Jackson, T.A.; Bhasin, K.B.; Romanofsky, R.; Mourou, “External electro-optic probing of millimeter-wave integrated circuits International,” in *IEEE MTT-S Digest*, 1989, pp. 221–224.
- [135] J. Valdmanis and G. Mourou, “Subpicosecond electrooptic sampling: Principles and applications,” *IEEE J. Quantum Electron.*, vol. 22, no. January, pp. 69–78, 1986.
- [136] D. M. Weingarten, K.J.; Majidi-Ahy, R.; Rodwell, M.J.W.; Auld, B.A.; Bloom, “Microwave Measurements of GaAs Integrated Circuits Using Electrooptic Sampling,” *Microw. Symp. Dig. IEEE MTT-S Int.*, pp. 887–880, 1987.
- [137] M. Y. Frankel, R. H. Voelker, and J. N. Hilfiker, “Coplanar transmission lines on thin substrates for high-speed low-loss propagation,” *IEEE Trans. Microw. Theory Tech.*, vol. 42, no. 3, pp. 396–402, Mar. 1994.
- [138] R. H. Voelker, M. Y. Frankel, and C. G. Sentelle, “Study and characterization of optoelectronic photoconductor-based probes,” *IEEE Trans. Microw. Theory Tech.*, vol. 44, no. 2, pp. 331–337, 1996.
- [139] M. Y. Frankel, J. F. Whitaker, G. A. Mourou, J. A. Valdmanis, C. Science, and A. Arbor, “ULTRAHIGH-BANDWIDTH VECTOR NETWORK ANALYZER BASED ON EXTERNAL ELECTRO-OPTIC SAMPLING,” vol. 35, no. 3, pp. 325–332, 1992.
- [140] M. Y. Frankel, “Optoelectronic techniques for ultrafast device network analysis to 700 GHz,” *Optical and Quantum Electronics*, vol. 28, no. 7, pp. 783–800, 1996.
- [141] G. A. Frankel, M.Y.; Gupta, S.; Valdmanis, J.A.; Mourou, “Picosecond pulse formation by transmission line discontinuities,” *Electron. Lett.*, vol. 25, no. 20, pp. 1363–1365, 1989.
- [142] H. Heiliger *et al.*, “Thin-film microstrip lines for MM and sub-MM/wave on-chip interconnects,” in *IEEE MTT-S Digest*, 1997, vol. 2, pp. 421–424 vol.2.
- [143] T. Pfeifer, H. Heiliger, H. G. Roskos, and H. Kurz, “Generation and Detection of Picosecond Electric Pulses with Freely Positionable Photoconductive Probes,” *IEEE Trans. Microw. Theory Tech.*, vol. 43, no. 12, pp. 2856–2862, 1995.
- [144] K. Giboney and S. Allen, “Picosecond measurements by free-running electro-optic sampling,” *Photonics Technol. ...*, vol. 6, no. 1, pp. 5–7, 1994.
- [145] J. F. David, G.; Yang, K.; Katehi, L.P.B.; Whitaker, “Electro-optic imaging of millimeter-wave field distributions,” *IEEE Lasers Electro-Optics Soc. Annu. Meet.*, pp. 217–218, 1998.
- [146] D.-J. Lee and J. F. Whitaker, “Bandwidth enhancement of electro-optic field sensing using photonic down-mixing with harmonic sidebands,” *Opt. Express*, vol. 16, no. 19, p. 14771, Sep. 2008.
- [147] C. Chen and J. F. Whitaker, “vector sensor using cadmium manganese telluride,” *Opt. Express*, vol. 18, no. 12, pp. 12239–12248, 2010.
- [148] D.-J. Lee and J. F. Whitaker, “Bandwidth enhancement of electro-optic sensing using high-even-order harmonic sidebands,” *Opt. Express*, vol. 17, no. 17, p. 14909, Aug. 2009.

- [149] D.-J. Lee, N.-W. Kang, J.-H. Choi, J. Kim, and J. F. Whitaker, "Recent advances in the design of electro-optic sensors for minimally destructive microwave field probing," *Sensors (Basel)*, vol. 11, no. 1, pp. 806–24, Jan. 2011.
- [150] J. F. Deibel, J.A.; Whitaker, "A Fiber-Mounted Polymer Electro-Optic-Sampling Field Sensor," in *IEEE Lasers and Electro-Optics Society, The 16th Annual Meeting of*, 2003, pp. 786–787.
- [151] C.-C. Chen and J. F. Whitaker, "Combined Electro/Magneto-Optic Field Probe Using Cadmium Manganese Telluride," *LEOS 2007 - IEEE Lasers Electro-Optics Soc. Annu. Meet. Conf. Proc.*, pp. 118–119, Oct. 2007.
- [152] S. Chandani, "Fiber-based probe for electrooptic sampling," *Photonics Technol. Lett. IEEE*, vol. 18, no. 12, pp. 1290–1292, 2006.
- [153] L. Meignien, J. Mangeney, P. Crozat, L. Duvillaret, and M. Hanna, "Two-port vectorial terahertz electro-optic sampling system," *Appl. Phys. Lett.*, vol. 92, no. 13, p. 131103, 2008.
- [154] J. F. Kyoung Yang, David, G., Jong-Gwan Yook, Papapolymerou, I., Katehi, L.P.B., Whitaker, "Electrooptic mapping and finite-element modeling of the near-field pattern of a microstrip patch antenna," *IEEE Trans. Microw. Theory Tech.*, vol. 48, no. 2, pp. 288–294, 2000.
- [155] T. Nagatsuma, N. Sahri, A. Hirata, Y. Rope, and A. Sasaki, "Millimeter-Wave Network Analyzers Based on Photonic Techniques," in *IEEE MTT-S Digest*, 2002, pp. 1497–1500.
- [156] T. Nagatsuma, "Photonic measurement technologies for high-speed electronics," *Meas. Sci. Technol.*, vol. 13, no. 11, pp. 1655–1663, Nov. 2002.
- [157] B. H. KOLNER and D. M. BLOOM, "DIRECT ELECTRO-OPTIC SAMPLING OF TRANSMISSION-LINE SIGNALS PROPAGATING ON A GaAs SUBSTRATE," in *ELECTRONICS LETTERS*, 1984, vol. 20, no. 20, pp. 818–819.
- [158] E. K. W. Mertina, A. Leyka, T. Novaka, G. Davidb, D. Jägerb, "Characterization of a MMIC by direct and indirect electro-optic sampling and by network analyzer measurements," *Microelectron. Eng.*, vol. 24, no. 1–4, pp. 377–384, 1994.
- [159] S. Seitz *et al.*, "Characterization of an external electro-optic sampling probe: Influence of probe height on distortion of measured voltage pulses," *J. Appl. Phys.*, vol. 100, no. 11, p. 113124, 2006.
- [160] W. Mertin, C. Roths, F. Taenzler, and E. Kubalek, "Probe tip invasiveness at indirect electro-optic sampling of MMIC," *1993 IEEE MTT-S Int. Microw. Symp. Dig.*, pp. 1351–1354, 1993.
- [161] E. K. W. Mertin, C. Bohm, L. J. Balk, "TWO-DIMENSIONAL FIELD MAPPING IN MMIC-SUBSTRATES BY ELECTRO-OPTIC SAMPLING TECHNIQUE," in *IEEE MTT-S Digest*, 1992, pp. 1443–1446.
- [162] X. J. Tian, D. M. Zhang, W. Sun, K. X. Chen, H. Yang, and M. B. Yi, "Direct fault detection and analysis of GaAs IC's chip on wafer," *IEEE Asia-Pacific Conf. Circuits Syst.*, pp. 806–808, 2000.
- [163] B. J. Thompson, Ed., *Ultrafast Lasers: Technology and Applications*. New York, USA: Marcel Dekker Ltd, 2003.

- [164] Coherent Co., *Operator's Manual: The Coherent Mira Seed Laser*. 2002.
- [165] L. Krainer, R. Paschotta, M. Moser, and U. Keller, "77 GHz soliton modelocked Nd:YVO₄ laser," *Electron. Lett.*, vol. 36, no. 22, p. 1846, 2000.
- [166] U. Keller, "Recent developments in compact ultrafast lasers," *Nature*, vol. 424, no. August, pp. 831–838, 2003.
- [167] D. G. S. Bob D. Guenther, *Encyclopedia of Modern Optics*. Academic Pr Inc., 2004.
- [168] P. Yariv, Amnon and Yeh, *Optical waves in crystals*. New York, USA: John Wiley & Sons, Inc., 1983.
- [169] P. Yariv, Amnon and Yeh, *Photonics: Optical Electronics in Modern Communications (The Oxford Series in Electrical and Computer Engineering)*. Oxford University Press, Inc., 2006.
- [170] Shun Lien Chuang, *Physics of optoelectronic devices*. New York, USA: John Wiley & Sons, Inc., 1995.
- [171] L. Duvillaret, S. Riolland, and J. Coutaz, "Electro-optic sensors for electric field measurements. I. Theoretical comparison among different modulation techniques," *J. Opt. Soc. Am. B*, vol. 19, no. 11, p. 2692, 2002.
- [172] J. A. Deibel, "A Study of Nonlinear Optical Polymers for Use in Ultrafast Electro-Optic Sampling Measurements," The University of Michigan, 2004.
- [173] M. E. Jacob, M.V.; Hartnett, J.G.; Mazierska, J.; Krupka, J.; Tobar, "Lithium tantalate - a high permittivity dielectric material for microwave communication systems," in *Conference on Convergent Technologies for the Asia-Pacific Region*, 2003, pp. 1362–1366.
- [174] J. Frankel, M.Y.; Whitaker, J.F.; Mourou, G.A.; Valdmanis, "Experimental characterization of external electrooptic probes," *Microw. Guid. Wave Lett. IEEE*, vol. 1, no. 3, pp. 60–62, 1991.
- [175] M. A. H. A . J . VICKERS, R . TESSER, R . DUDLEY, "Fabry-Pe'rot enhancement of external electro-optic sampling," *Opt. Quantum Electron.*, vol. 29, pp. 661–669, 1997.
- [176] M. Walther, K. Jensby, S. R. Keiding, H. Takahashi, and H. Ito, "Far-infrared properties of DAST," *Opt. Lett.*, vol. 25, no. 12, p. 911, Jun. 2000.
- [177] M. Jazbinsek, L. Mutter, and P. Gunter, "Photonic Applications With the Organic Nonlinear Optical Crystal DAST," *IEEE J. Sel. Top. Quantum Electron.*, vol. 14, no. 5, pp. 1298–1311, 2008.
- [178] M. Stillhart, M. Jazbinsek, A. Schneider, and P. Guenter, "Organic Crystals for THz Wave Applications," *Proc. Symp. Photonics Technol. 7th Framew. Progr.*, vol. 4, no. 1, pp. 226–229, 2006.
- [179] X. Zheng *et al.*, "Electro-optic sampling system with a single-crystal 4-N,N-dimethylamino-4'-N'-methyl-4-stilbazolium tosylate sensor," *Appl. Phys. Lett.*, vol. 82, no. 15, p. 2383, 2003.
- [180] J. Luo and A. K.-Y. Jen, "Highly Efficient Organic Electrooptic Materials and Their Hybrid Systems for Advanced Photonic Devices," *IEEE J. Sel. Top. Quantum Electron.*, vol. 19, no. 6, pp. 42–53, Nov. 2013.
- [181] G. Gaborit, G. Martin, L. Duvillaret, J.-L. Coutaz, R. Hierle, and J. Zyss,

- "Electrooptic probe based on an organic microcavity," *IEEE Photonics Technol. Lett.*, vol. 17, no. 10, pp. 2140–2142, Oct. 2005.
- [182] A. Nahata, D. H. Auston, C. Wu, and J. T. Yardley, "Generation of terahertz radiation from a poled polymer," *Appl. Phys. Lett.*, vol. 67, no. 10, p. 1358, 1995.
- [183] H.-J. Cheng, J. F. Whitaker, K. J. Herrick, N. Dib, and L. P. B. Katehi, "Electro-Optic-Probe system response: experiment and simulation," *25th Eur. Microw. Conf. 1995*, pp. 151–154, Oct. 1995.
- [184] L. Duvillaret, S. Riolland, and J.-L. Coutaz, "Electro-optic sensors for electric field measurements. II. Choice of the crystals and complete optimization of their orientation," *J. Opt. Soc. Am. B*, vol. 19, no. 11, p. 2704, Nov. 2002.
- [185] "Nufern Co." [Online]. Available: <http://www.nufern.com/>.
- [186] D. E. Aspnes, "Recombination at semiconductor surfaces and interfaces," *Surf. Sci.*, vol. 132, no. 1–3, pp. 406–421, 1983.
- [187] F. Hilbk-kortenbruck, "Raum- und Zeitanalyse der Abstrahlung neuartiger Höchsfrequenzemitter im GHz- und THz-Bereich," der Rheinisch-Westfälischen Technischen Hochschule Aachen, 1998.
- [188] E. Treacy, "Optical pulse compression with diffraction gratings," *IEEE J. Quantum Electron.*, vol. 5, no. 9, pp. 454–458, 1969.
- [189] P. H. Jamshidifar, M.; Spickermann, G.; Schäfer, H.; Bolivar, "200-GHz bandwidth on wafer characterization of CMOS nonlinear transmission line using electro-optic sampling," *Microw. Opt. Technol. Lett.*, vol. 54, no. 8, pp. 1858–1862, 2012.
- [190] L. Tripodi *et al.*, "Broadband CMOS Millimeter-Wave Frequency in 3-D Chip-Scale Packaging," vol. 60, no. 12, pp. 3761–3768, 2012.
- [191] G. Zhao, R. N. Schouten, N. van der Valk, W. T. Wenckebach, and P. C. M. Planken, "Design and performance of a THz emission and detection setup based on a semi-insulating GaAs emitter," *Rev. Sci. Instrum.*, vol. 73, no. 4, p. 1715, 2002.
- [192] L. Tripodi, "First design and layout of the NLTL, driving circuitry, sampling head and antenna," ULTRA project periodic report, 2008.
- [193] K. S. Giboney, S. T. Allen, M. J. W. Rodwell, and J. E. Bowers, "Picosecond Measurements by Free-Running Electro-Optic Sampling," *IEEE Photonics Technol. Lett.*, vol. 6, no. 11, pp. 1353–1355, 1994.
- [194] "Hittite microwave." [Online]. Available: <https://www.hittite.com/>.
- [195] R. Majidi-Ahy, K. Weingarten, M. Riaziat, D. M. Bloom, and B. A. Auld, "Electrooptic sampling measurement of dispersion characteristics of slot line and coplanar waveguide (coupled slot line) even and odd modes," 1988., *IEEE MTT-S Int. Microw. Symp. Dig.*, pp. 301–304, 1988.
- [196] D.-J. Lee, J.-Y. Kwon, J.-G. Lee, and N.-W. Kang, "Mismatch analysis using pulsed electro-optic sampling at KRISS," *2012 Conf. Precis. Electromagn. Meas.*, pp. 448–449, Jul. 2012.
- [197] Z. H. Zhu *et al.*, "Electro-optic measurement of standing waves in a GaAs coplanar waveguide," *Appl. Phys. Lett.*, vol. 50, no. 18, p. 1228, 1987.

- [198] M. M. David E. Root, Jan Verspecht, Jason Horn, *X-Parameters: Characterization, Modeling, and Design of Nonlinear RF and Microwave Components*. Cambridge University Press, 2013.
- [199] "AMO GmbH." [Online]. Available: <http://www.amo.de/>.
- [200] M. Jamshidifar and P. H. Bolívar, "Diminishing relative jitter in electrooptic sampling of active mm-wave and THz circuits.," *Opt. Express*, vol. 21, no. 4, pp. 4396–404, 2013.
- [201] M. Jamshidifar, G. Spickermann, H. S. Eberwein, and P. H. Bolívar, "Low-Jitter Electrooptic Sampling of Active mm-Wave Devices up to 300 GHz," in *the 43rd European Microwave Conference*, 2013, pp. 752–754.



Mehran Jamshidifar received his B.Sc. in electrical engineering in 2000. After several years of work experience, in 2005 he graduated with master degree with excellent mark in electrical engineering from Urmia University of Iran. His master thesis was on fractal miniaturization of microstrip patch antennas. From 2005 to 2008, he was a senior engineer for radio networks planning and optimization in Mobile Telecommunication Co. of Iran. Enthusiastic to learn new areas of science, in the end of 2008 he moved to Germany and since that time has been working as a research assistant towards his Ph. D degree in electrical engineering in the Institute of High Frequency and Quantum Electronics at the University of Siegen.

THz waves, with the electromagnetic spectrum between millimeter-waves and optics, are nowadays widely used in applications such as material inspection, medicine, astronomy and etc. Optical based systems for generating THz waves are usually bulky and inefficient at the frequencies below 1THz. Alternatively, all-electronics THz approach is promising to facilitate the future availability of THz waves in cheap, compact and industrial solutions. A milestone in reaching this goal is the characterization of devices, and therefore, electrooptic sampling (EOS) is a superior solution. EOS, in comparison to the electronic characterization approaches offers a much broadband and faster measurement system with reduced systematic errors from system calibrations. Moreover, non-contact near-field probing allows for producing high resolution images of devices.

The aim of this work is to demonstrate EOS for the characterization of mm-wave and THz electronic devices. Accordingly, an experimental setup, featured with a large dynamic range, high sensitivity, and high spatial resolution for imaging is introduced. A 65-nm CMOS Nonlinear Transmission Line (NLTl) is then chosen as a broadband device under test. In the preliminary measurement phase, jitter of the system is recognized as the major prohibiting factor in achieving a full measurement bandwidth for the device. As a solution, a fully coherent synchronization technique, called Laser Master Laser Slave (LM-LS) is used which extremely enhances the system detection bandwidth from 50 GHz up to 300 GHz, restricted by the device fabrication technology i.e., the CMOS. It is also shown that EOS non-contact probing of nonlinear devices can detect features which may not be seen by electronic measurement instrumentation at device ports. In the end, results of photoconductive probing are compared with EOS in terms of detection bandwidth and image resolution.